TESIS DE LA UNIVERSIDAD DE ZARAGOZA

2021

30

Emin Istif

Nanostructured Polythiophene Hybrid Charge-Transfer Complexes

Departamento

Ingeniería Química y Tecnologías del Medio Ambiente

Director/es

Benito Moraleja, Ana M.
Maser, Wolfgang K.

ISSN 2254-7606

Prensas de la Universidad Universidad Zaragoza

ISSN 2254-7606

Universidad Zaragoza
1542

Tesis Doctoral

NANOSTRUCTURED POLYTHIOPHENE HYBRID CHARGE-TRANSFER COMPLEXES

Autor

Emin Istif

Director/es

Benito Moraleja, Ana M.
Maser, Wolfgang K.

UNIVERSIDAD DE ZARAGOZA

Ingeniería Química y Tecnologías del Medio Ambiente

2018

NANOSTRUCTURED POLYTHIOPHENE HYBRID CHARGE-TRANSFER COMPLEXES

TESIS DOCTORAL

Emin Istif

2018

CONSEJO SUPERIOR DE INVESTIGACIONES CIENTÍFICAS (CSIC)

INSTITUTO DE CARBOQUÍMICA

NANOSTRUCTURED POLYTHIOPHENE HYBRID CHARGE-TRANSFER COMPLEXES

Memoria presentada en el marco del Programa de Doctorado de Ingeniería Química y Tecnologías del Medio Ambiente de la Universidad de Zaragoza, para optar al grado de Doctor por:

Emin Istif

Septiembre 2018

Directores:

Wolfgang Maser

Ana Maria Benito Moraleja

Wolfgang Maser y Ana María Benito Moraleja

Investigadores Científicos del Consejo Superior de

Investigaciones Científicas

CERTIFICAN

Que la Memoria, titulada

“Nanostructured polythiophene hybrid charge transfer complexes”

ha sido realizada bajo nuestra dirección en el Instituto de Carboquimica de Zaragoza (CSIC) por D. Emin Istif, autorizando su presentación.

Y para que así conste, firmamos el presente certificado en Zaragoza, a 28 de septiembre de 2018

Dr. Wolfgang Maser

Dra. Ana María Benito Moraleja

Acknowledgement

First and foremost, I am deeply grateful to my supervisors Dr. Wolfgang K. Maser and Ana M. Benito for giving me the great opportunity of working on this project, for their guidance, feedbacks, patience and supports. I greatly appreciated the freedom they allowed me to pursue different projects without any objection.

Additionally, I would like to express my appreciation to Ana Santidrián and Lorenzo Vallan who made my time in Zaragoza, Brighton and in the laboratory great.

Thank you very much, Ana Santidrián, for all your help with any challenges that I encountered.

I would like to thank my friends and colleagues in Instituto de Carboquímica, José Miguel González Domínguez, Sandra Victor, Eduardo Colom, Alejandro Anson and Enrique García Bordejé for their friendly environment and useful discussion in group meetings. I would also like to thank my officemate Laura Díez Martín.

I would like to thank to Javier Hernandez-Ferrer for carrying out electrochemical and photoelectrochemical characterization of my materials.

I would like to thank to Esteban Urriolabeitía from University of Zaragoza for all his help for NMR analysis.

I would like to acknowledge Elisa Palacios-Lidón and Jaime Colchero from University of Murcia for KPM characterizations of the materials and fruitful collaboration.

I would like to express my sincere gratitude to Dr. Nikos Tagmatarchis and his group for their worthy collaboration during my secondment in National Hellenic Research Foundation, Greece. Especially, I would like thank to Antonia Kagkoura and Ruben Canton-Vitoria for their patience, time, help and enjoyful time in Athens.

I would also like to thank Prof. Alan Dalton and his group for their collaboration during my secondment in University of Sussex. Especially, I would like to thank Manuela Meloni and Giuseppe Fratta, for all their help and friendly atmosphere both inside and outside the laboratory. I would like to thank Dr. Matthew Large for AFM characterization of the materials.

During my PhD, I also spent a month in Jean Rouxel Institute of Materials in Nantes, and I am very thankful to Dr. Jean-Luc Duvail, Dr. Chris Ewels, Elodie Babu and Daniel Funes for their help and collaborative works.

I would like to thank all members of the Enabling Excellence network for creating the best possible teamwork and for fruitful collaborations.

Most of all, I am indebted to my parents, Aysel and Ahmet Istif, and my brother Mehmet and my sister Hulya for their love and continuous support up to this point in my life. I would like to express my greatest gratitude to Beste Orhan who is my wife, my love and my soulmate, for her love, endless support and wonderful moments we have shared together.

Lastly, I would like to acknowledge to European Union's Horizon 2020 research and innovation program for its funding under the Marie Skłodowska-Curie grant agreement No 642742.

Content

List of Figures

List of Tables

List of Schemes

LIST OF ABBREVIATIONS AND ACRONYMS

2D: Two dimensional

AFM: Atomic Force Microscopy

AM-SFM: Amplitude modulation mode scanning force microscopy

BF-STEM: Bright-field scanning transmission electron microscopy

BHJ: Bulk Heterojunction

BOC: Butoxycarbonyl

CNT: Carbon nanotube

cAFM: Conductive atomic force microscopy

CPs: Conjugated Polymers

CPNs: Conjugated Polymer Nanoparticles

CT: Charge transfer

CV: Cyclic voltammetry

D/A: Donor-Acceptor

DC: Direct-current

DMF: Dimethylformamide

DLS: Dynamic light-scattering

EDS: Energy-dispersive X-ray spectroscopy

FTO: Fluorine-doped tin oxide

FTIR: Fourier-transform infrared spectroscopy

GO: Graphene Oxide

HOMO: Highest occupied molecular orbital

HAADF-STEM: high-angle annular dark-field scanning transmission electron microscopy

HRTEM: High resolution transmission electron microscopy

HCI: Hydrochloric acid

ITO: Indium tin oxide

KPFM: Kelvin Probe Force Microscopy

LUMO: Lowest unoccupied molecular orbital

MWCNT: Multi-walled carbon nanotube

NMR: Nuclear magnetic resonance

OLED: Organic light emitting diodes

OPV: Organic photovoltaic cell

OSC: Organic solar cell

P3HT: Poly (3-hexyl thiophene)

$P3HT_{NPs}$: Poly (3-hexyl thiophene) nanoparticles

PANI: Polyaniline

PATs: Poly (3-alkylthiophene)s

PC-AFM: Photoconductive atomic force microscopy

PEDOT: Poly(3,4-ethylenedioxythiophene)

PPV: Poly(p-phenylene vinylene)

PTh: Polythiophene

PFM : Piezoresponse force microscopy

PEC: Photoelectrochemical characterization

PCBM: Phenyl-C61-butyric acid methyl ester

SEC: Size exclusion chromatography

SFM: Scanning force microscopy

SP: Surface potential

SPV: Surface photovoltage

STEM: Scanning transmission electron microscopy

SWCNT: Single-walled carbon nanotube

TEM: Transmission electron microscopy

TMDs: Transition metal dichalcogenides

THF: Tetrahydrofuran

TGA: Thermogravimetric analysis

UV–Vis: Ultraviolet–visible spectroscopy

QDs: Quantum dots

XPS: X-ray photoelectron spectroscopy

ABSTRACT

Conjugated polymers (CPs) exhibit unique electronic and optoelectronic properties due to their extended π orbitals along the polymer chain. They possess large absorption cross sections, reveal high fluorescence efficiencies and show remarkable charge transport characteristics. These properties render CPs as ideal candidates for synthesizing novel donor-acceptor (D/A) charge transfer complexes with various nanostructures of interest for optoelectronic applications. The well-known example based on electron-donating conjugated polymers in combination with electron accepting fullerene derivatives underlines the importance of CPs role in D/A hybrids for potential applications for thin film plastic electronics i.e. organic solar cells, organic light-emitting diodes, organic field effect transistors, chemical sensors and biosensors and flexible displays. Here, an efficient charge transfer in conjugated polymer based D/A complexes depends on the optimization of some important parameters such as i) proper adjustment of HOMO and LUMO energy levels of the D/A materials and ii) the morphology of the blend system for fine-tuning of the D/A interfaces for achieving optimal exciton dissociation and charge transport.

Additionally, concerning environmental awareness, the fabrication of D/A complexes from environmentally-friendly solutions, compatible with large-area coating or printing technologies is a key requirement for their commercial implementation .

In order to advance in the development of the variety of D/A hybrid structures and environmentally-friendly processing condition, this thesis focuses on synthesis of water based nanohybrids as D/A complexes and the elucidation of the electronic interaction among the D/A units by spectroscopic techniques such as UV-visible spectroscopy, photoluminescence spectroscopy, time resolved photoluminescence and Raman spectroscopy techniques. On the other hand, the electrochemical and photoelectrochemical properties of hybrids were also investigated in order to gain important insights on the thin film device performance.

Chapter 1 provides the general context and summarizes the general background information of (CPs), conjugated polymer nanoparticles (CPNs) and their donor-acceptor charge transfer complexes including methods of preparation and physical properties.

Chapter 2 describes the synthesis and characterization of a novel water-based self-assembled nanohybrid, which consists of poly (3-hexylthiophene) nanoparticles ($P3HT_{NPs}$) and graphene

oxide (GO). $P3HT_{NPs}$ and $P3HT_{NPs}$-GO complexes were synthesized by an in-situ re-precipitation technique. Morphological characterization reveals that the formation of $P3HT_{NPs}$ is successfully accomplished exhibiting particles sizes in the range of 50 to 200 nm. In the case of $P3HT_{NPs}$-GO complexes the morphological studies reveal the presence of $P3HT_{NPs}$ in intimate contact with micrometer sized GO sheets. Importantly,, spectroscopic characterization of the samples demonstrates that GO changes the optical properties of $P3HT_{NPs}$ by influencing the crystalline packing of poly (3-hexylthiophene) (P3HT) chains in the forming $P3HT_{NPs}$ from H to H/J aggregates during the self-assembly process. Furthermore, π-π interface interactions between the $P3HT_{NPs}$ and GO sheets are established resulting in the creation of $P3HT_{NPs}$-GO D/A charge-transfer complexes. This work demonstrates that the electronic and optoelectronic properties of conjugated polymer nanoparticles can be tuned by GO. Moreover, properties established in liquid phase are maintained in the form of films. Thus, thin film properties do not depend anymore on external processing parameters. Photoelectrochemical studies additionally underline the value $P3HT_{NPs}$-GO thin films as photoactive thin layer materials with improved performance. Combined with the possibility to process these charge-transfer hybrids from water-based dispersions renders $P3HT_{NPs}$-GO charge transfer complexes of special interest for the development of improved thin film optoelectronic applications.

Chapter 3 focuses on photogenerated charge-transfer properties on individual nanoobjects of $P3HT_{NPs}$-GO hybrids by employing Kelvin Probe Force Microscopy under dark and illuminated conditions. By mapping the local surface potential (SP) in darkness, a substructure is resolved which clearly indicates the presence of aggregate domains within the polymer nanoparticles. In addition, surface photovoltage (SPV) measurements on individual $P3HT_{NPs}$ nanoparticles and $P3HT_{NPs}$-GO complexes were performed to sheed light on the photoinduced charge generation and charge recombination mechanisms at the different nanoscale interfaces. This study is of great relevance for the improved understanding of the overall functionality thin film layers composed of individual nanoscale objects and thus for providing feedback for further optimizing the optoelectrical performance of thin film devices.

Chapter 4 covers the self-assembly of novel core−shell nanoensembles consisting of 100 nm $P3HT_{NPs}$ as core and semiconducting CdTe quantum dots ($CdTe_{QDs}$) as shell. The nanoensemble structure was accomplished by employing a re-precipitation approach. The morphology and composition of $CdTe_{QDs}/P3HT_{NPs}$ nanoensembles were confirmed by high-resolution scanning transmission microscopy and dynamic light-scattering studies. The

interaction between the outer amorphous part of the $P3HT_{NPs}$ core and the $CdTe_{QDs}$ shell is confirmed by optical characterization and photoluminescence spectra. These exhibit effective quenching of the characteristic photoluminescence of $CdTe_{QDs}$ at 555 nm, accompanied by simultaneous increase in the emission of $P3HT_{NPs}$ at 660 and 720 nm, suggesting the existence of photoinduced charge-transfer processes. Additionally, the electrochemical response on films further supports the findings of a stabilized $CdTe_{QDs}/P3HT_{NPs}$ core−shell system in the solid state. Photoelectrochemical assays on $CdTe_{QDs}/P3HT_{NPs}$ films show a reversible on−off photoresponse at a bias voltage of +0.8 V with a 3 times increased photocurrent compared to $CdTe_{QDs}$. This study shows that the unique core−shell configuration is directly related with the donor-acceptor behavior and charge separation.

Finally, *Chapter 5* focuses on the preparation, characterization, and photophysical and electrochemical properties of water-dispersible polythiophene/layered transition metal dichalcogenide ensembles. The positive charges on functionalized molybdenum disulfide (MoS_2) and tungsten disulfide (WS_2), due to the presence of ammonium units, were exploited to electrostatically bring in contact a newly synthesized water-dispersible polythiophene derivative bearing a carboxylate moiety. This yields in water soluble polythiophene/MoS_2 and water soluble polythiophene/WS_2 ensembles. The electronic interactions between the materials within the nanoensembles were characterized firstly by absorption and photoluminescence titration assays. Efficient photoluminescence quenching of polythiophene emission by MoS_2 and WS_2 within nanoensembles, in combination with time-resolved photoluminescence assays, were observed and attributed to photoinduced electron/energy transfer from photoexcited polythiophene to MoS_2 or WS_2. The ensembles show enhanced photocurrent in comparison with individual exfoliated materials, especially in case of WS_2. This further confirms that electron transfer between the negatively charged polymer and the positively charged transition metal dichalcogenides is taking place. All these results consistently reveal the advantageous function of electrostatic interactions between the negatively charged polymer and the positively charged transition metal dichalcogenides not only for the realization of the nanoensembles but also for succeeding efficient electronic communication.

RESUMEN

Los polímeros conjugados (PC) presentan notables propiedades electrónicas y optoelectrónicas debido a sus orbitales π extendidos a lo largo de la cadena del polímero. Poseen una gran sección eficaz de absorción, mostrando un transporte de carga adecuado y una alta eficacia de fluorescencia. Estas propiedades hacen de los PC candidatos ideales para sintetizar complejos de transferencia de carga dador-aceptor (D/A) con varias nanoestructuras de alto interés en aplicaciones optoelectrónicas. El ejemplo bien conocido de los materiales basados en polímeros conjugados dadores de electrones en combinación con derivados de fullereno, subraya la importancia de los PC en compuestos D/A para aplicaciones de plástica electrónica en película delgada, como son las celdas solares orgánicas, diodos de emisión de luz, transistores de efecto de campo, sensores químicos y biosensores y pantallas flexibles. Aquí, la eficiencia en la transferencia de carga en complejos D/A basados en polímeros conjugados depende de la optimización de algunos parámetros importantes tales como i) los niveles de energía HOMO y LUMO de los materiales y ii) la morfología del sistema de mezcla para el ajuste fino de la interfaz D/A para lograr una disociación de excitones y un transporte de carga óptimos.

Además, en lo que se refiere a la sostenibilidad ambiental, la fabricación de los complejos D/A con disoluciones respetuosas con el medio ambiente y compatibles con tecnologías de recubrimiento o impresión de grandes superficies serían puntos clave para su implementación comercial.

Para avanzar en el desarrollo de estructuras compuestas D/A, sintetizadas en condiciones de sostenibilidad con el medio ambiente, esta tesis se centra en la síntesis de nanohíbridos D/A solubles en medios acuosos y en la elucidación de la interacción electrónica entre las unidades D/A mediante técnicas espectroscópicas tales como espectroscopía UV-visible, espectroscopia de fotoluminiscencia, fotoluminiscencia de resolución temporal y técnicas de espectroscopía Raman. Por otro lado, las propiedades electroquímicas y fotoelectroquímicas de los nanohíbridos también se investigaron con el fin de obtener información importante sobre el funcionamiento del dispositivo de película delgada.

El Capítulo 1 proporciona un contexto general y resume la información fundamental de los PC, las nanopartículas de polímero conjugado y sus complejos de transferencia de carga D/A, así como los métodos de preparación y sus propiedades físicas.

El capítulo 2 describe la síntesis y caracterización de un nuevo nanohíbrido soluble en agua obtenido por ensamblado, que consiste en nanopartículas de poli (3-hexiltiofeno) ($P3HT_{NPs}$) y óxido de grafeno (GO). Los materiales $P3HT_{NPs}$ y $P3HT_{NPs}$-GO se sintetizaron mediante la técnica de reprecipitación in-situ. La caracterización morfológica revela que la formación de $P3HT_{NPs}$ se lleva a cabo con éxito, exhibiendo éstas, tamaños de partícula en el rango de 50 a 200 nm. En el caso de los complejos $P3HT_{NPs}$-GO, los estudios morfológicos revelan la presencia de $P3HT_{NPs}$ en intimo contacto con las láminas de GO de tamaño micrométrico. Por otra parte, la caracterización espectroscópica de las muestras demuestra que GO cambia las propiedades ópticas de las nanopartículas $P3HT_{NPs}$ al influir en el empaquetamiento cristalino de las cadenas de poli (3-hexiltiofeno) (P3HT) en las $P3HT_{NPs}$ formadas, pasando de agregados H a H/J durante el proceso de autoensamblado. Además, se establecen interacciones interfaciales π-π entre las $P3HT_{NPs}$ y las láminas de GO que dan como resultado la formación de complejos de transferencia de carga D/A $P3HT_{NPs}$-GO. Este trabajo demuestra que las propiedades electrónicas y optoelectrónicas de las nanopartículas de polímeros conjugados se pueden ajustar mediante la adicción de GO. Además, las propiedades que se han establecido en fase líquida se mantienen al formar películas. Por lo tanto, las propiedades de las películas ya no dependen de los parámetros de procesado externos. Por otra parte, los estudios fotoelectroquímicos ponen en valor el uso de películas de $P3HT_{NPs}$-GO como capa fotoactiva con mejor funcionalidad. Todo esto combinado con la posibilidad de procesar estos híbridos de trasferencia de carga usando dispersiones acuosas evidencia su especial interés para el desarrollo de aplicaciones optoelectrónicas en película fina.

El Capítulo 3 se enfoca en las propiedades de transferencia de carga fotogeneradas en nanoobjetos individuales de los híbridos $P3HT_{NPs}$-GO empleando la técnica de fuerza de sonda Kelvin (KPM) en condiciones de oscuridad e iluminación. Al mapear el potencial de superficie local (SP) en la oscuridad, se resuelve una subestructura que claramente indica la presencia de dominios de agregados dentro de las nanopartículas de polímero. Además, se aplicaron mediciones de fotovoltaje de superficie (SPV) en nanopartículas individuales y el complejo $P3HT_{NPs}$-GO que arrojaron luz sobre la generación de carga fotoinducida y sobre los mecanismos de recombinación de carga en las diferentes interfaces a nanoescala. Este estudio tiene un impacto importante en la mejor comprensión de la funcionalidad general de capas de película delgada compuestas de objetos individuales a nanoescala y proporciona, por

tanto, feedback para la optimización del funcionamiento optoelectrónico de los dispositivos de película delgada.

El Capítulo 4 estudia la formación de nuevas nanopartículas con estructura core-shell mediante autoensamblado. Estas nanopartículas están formadas por $P3HT_{NPs}$ de 100 nm que forman el núcleo y puntos cuánticos semiconductores de CdTe ($CdTe_{QDs}$) que forman la capa externa de la particula core-shell. Estas estructuras se sintetizaron mediante el empleo de una técnica de reprecipitación. La morfología y composición de los nanoensamblados $CdTe_{QDs}/P3HT_{NPs}$ se analizaron mediante microscopía electrónica de transmisión de alta resolución y estudios dinámicos de dispersión de la luz. La interacción entre la parte amorfa externa de las nanopartículas $P3HT_{NPs}$ que forman el núcleo y los puntos cuánticos nanométricos $CdTe_{QDs}$ situados en la corteza de la estructura core-shell se confirma en los análisis de espectroscopía óptica y de fotoluminiscencia en los que se observa simultáneamente la extinción de la banda fluorescencia a 550 nm característica de $CdTe_{QDs}$ y el aumento en la emisión de $P3HT_{NPs}$ a 660 y 720 nm, evidenciando la existencia de procesos de transferencia de carga fotoinducidos. Al mismo tiempo, la respuesta electroquímica del material en forma de película respalda la presencia de un sistema core-shell de $CdTeQ_{Ds}$/ $P3HT_{NPs}$ estabilizado en el estado sólido. Los ensayos fotoelectroquímicos en películas $CdTe_{QDs}/P3HT_{NPs}$ muestran una foto-respuesta reversible on-off a una tensión de polarización de +0.8 V con una fotocorriente tres veces mayor que la de los CdTeQDs. Este estudio prueba que la configuración única core-shell está directamente relacionada con el comportamiento dador-aceptor y la separación de carga.

Finalmente, el Capítulo 5 se enfoca en la síntesis, caracterización y propiedades fotofísicas y electroquímicas de híbridos de dicalcogenuros metales de transición laminados y politiofeno soluble en agua. Las cargas positivas que proporcionan las unidades de amonio en el disulfuro de molibdeno funcionalizado (MoS_2) y el disulfuro de tungsteno (WS_2), se conectan electrostáticamente con las cargas negativas de un nuevo politiofeno soluble en agua que fue sintetizado con grupos terminales carboxilato en la cadena alquílica del anillo de tiofeno. Se forman así híbridos politiofeno/MoS_2 y politiofeno/WS_2 solubles en agua. Las interacciones electrónicas entre los materiales dentro de los nano-ensamblados se caracterizaron primero mediante ensayos de valoración de absorción y fotoluminiscencia. Se observó una extinción en fotoluminiscencia de la emisión del politiofeno al unirse a MoS_2 (o WS_2). Estos estudios junto a los ensayos de fotoluminiscencia resuelta en el tiempo indicaron que existe una transferencia de electrones/energía fotoinducida desde el politiofeno fotoexcitado a MoS_2 (o

WS_2). Asimismo, en condiciones fotoelectroquímicas específicas, los ensamblados híbridos muestran una mejora de la fotocorriente en comparación con los materiales individuales exfoliados, especialmente en el caso de WS_2, lo que también corrobora la transferencia de electrones entre el polímero y los dicalcogenuros de metal de transición. Todos estos resultados ratifican de manera precisa la ventaja de aprovechar las interacciones electrostáticas entre el polímero cargado negativamente y los dicalcogenuros de metal de transición con carga positiva no solo para la formación de los nanoensamblados, sino también para establecer una comunicación electrónica eficiente exitosa.

1. LITERATURE OVERVIEW

1.1. Conjugated Polymers (CPs)

Conjugated polymers (CPs) are special class of polymers possessing alternating single and conjugated double bonds in their chemical structure. On the backbone of a conjugated polymer, the π electrons are effectively delocalized along the polymer chain, leading to one unpaired π-electron per carbon atom, which allows for charge transport along the polymer chain. Consequently, they exhibit intrinsic semiconducting or conducting behaviour.[1]

In 1977s, Shirakawa, MacDiarmid, and Heeger demonstrated that the conductivity of conjugated polymers can be controlled by doping,[2, 3] thus opening a whole new world for fundamental studies and application possibilities in the field of optoelectronics and beyond. For their ground-breaking discovery, the authors were awarded with the Nobel prize in Chemistry in 2000.

The concept of doping is a unique process for conjugated material, which distinguish conjugated polymers from all other types of polymers. During the doping process, small conductivity of a semiconducting conjugated polymer can be reached up to the metallic conducting regime. Moreover, the control of doping level allows optimizing the properties of conjugated polymer, which is important for their applications.[4-6]

Polyacetylene is the first synthesized conjugated polymer, has led to abundance of research in the field of synthesis of CPs derivatives such as polythiophene (PTh), polyaniline (PANI), poly (p-phenylene vinylene) (PPV) etc. (Figure 1.1).

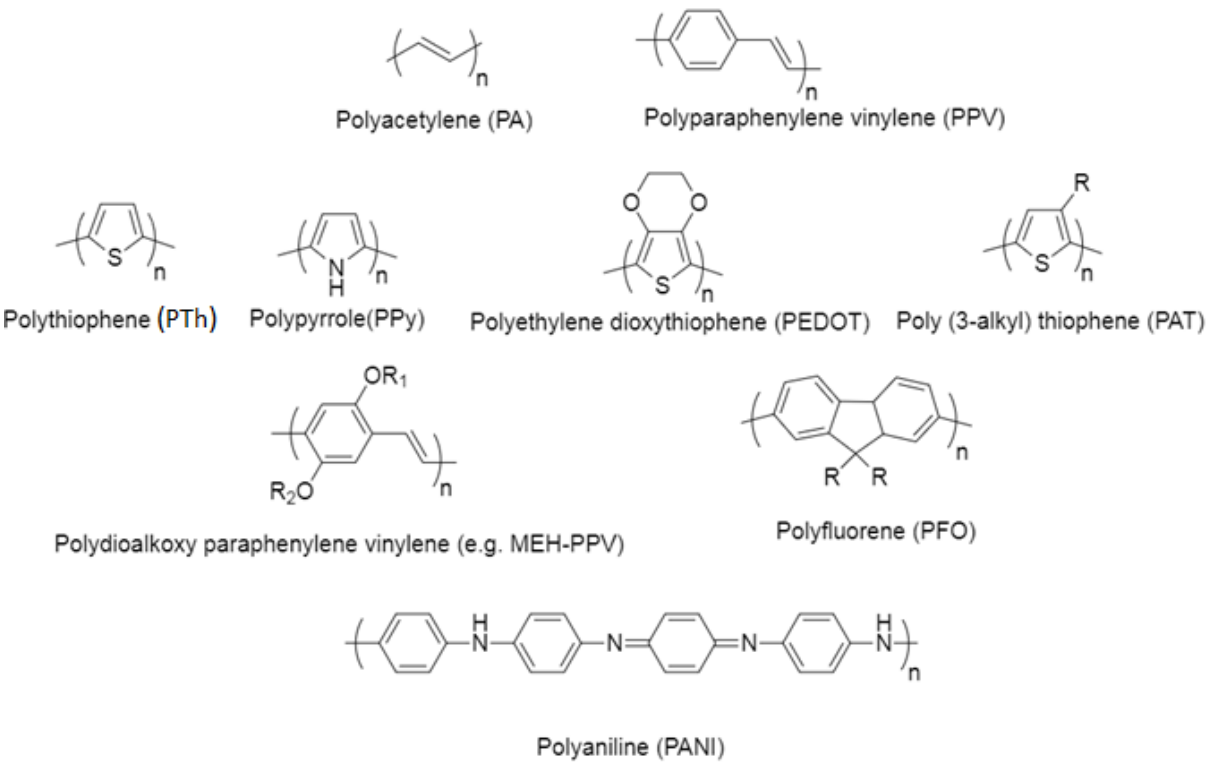

Figure 1.1 Some examples of conjugated polymers.

Since CPs have the ability to absorb and emit light they raise expectations within the field of optoelectronic applications such as, organic photovoltaic cell (OPV), organic light emitting diodes (OLED), electrochromic devices, smart windows, flexible display technologies. (Figure 1.2) Besides, CPs finds application in the field of transistors, supercapacitors and sensors due to their conductivity and sensing properties.[7, 8, 10]

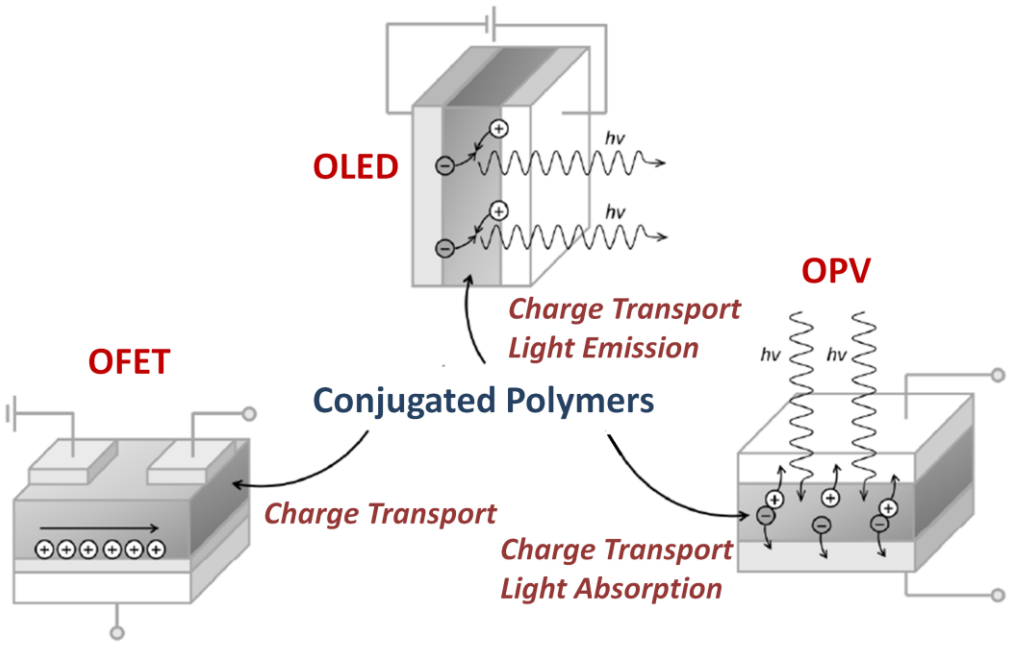

Figure 1.2. Application fields of conjugated polymers in organic electronics and the importance of charge creation and charge transport.[9]

Moreover, CPs exhibit environmental stability and are solution processable materials which is important for high volume processing and their use in large area applications. The solubility parameters depend on the polymer structure as well as on the morphology of the CPs. Introducing alkyl moieties or different organic groups can change the solubility of CPs and it can improve the processing condition of the polymer. For instance, introducing a side chain to the polymer backbone with a charged group results in water soluble CPs. On the other hand, changing the morphology of the CPs could lead to different processing conditions from different solvent range.

1.2. Conjugated Polymer Nanoparticles

Nanoparticles derived from conjugated polymers have attracted widespread attention for a number of reasons such as their ease of synthesis, tunable properties, low toxicity and environmentally friendly processing conditions for device fabrication.[11, 12] These nanoscale materials offer a great opportunity to use them in wide variety of applications such as optoelectronic devices, photonics, fluorescence imaging and photothermal therapy in biological application. [12, 13]

Conjugated polymer nanoparticles (CPNs) are also referred to as colloidal dispersions of lyophobic polymer chains. The first colloids of CPNs were produced by aqueous oxidative

polymerization of polyacetylene and polypyrrole.[14] Since then, many studies focus on achieving CPNs in aqueous media.[11-15.] The water dispersibility of CPNs receives increased interest since it facilitates environmentally friendly processing conditions for optoelectronic device fabrication [16-19] and for their use in biological applications.[20-22] In order to obtain water dispersible or soluble conjugated polymer, one strategy consists in the synthesis of polymers with hydrophilic or ionic side chains.[23] However, the presence of the side chains causes a decrease in the quantum yield and favors the disorganization of the polymer chain due to the repulsion of charges located on the ionic side chain. To overcome this undesirable situation, nanostructuration offers a great advantage since this preserves the intrinsic optical and electronic properties of conjugated polymers.

CPs can be converted to CPNs by different approaches such as mini-emulsion or re-precipitation technique. Miniemulsion technique in most cases involves a mixture of two immiscible liquid phases (for example, oil and water), which implies the use of one or more surfactants. On the other hand, re-precipitation technique entails the rapid injection of a polymer solution (organic solvent) into an excess volume of a marginal solvent that is miscible with the organic solvent.

1.2.1. Synthesis of Conjugated Polymer Nanoparticles

1.2.1.1. Miniemulsion technique

The miniemulsion technique is a widely used technique for the synthesis of CPNs. To prepare CPNs, the appropriate amount of polymer is dissolved in an organic solvent, which is immiscible with water followed by the injection of the polymer solution into an aqueous solution of a proper surfactant. Subsequently, ultrasonication of the mixture forms a stable miniemulsion containing small droplets of the polymer solution. Next, evaporation of the organic solvent leads to the formation of a stable dispersion of polymer nanoparticles in water. (Figure 1.3) A wide range of nanoparticles sizes (from 30 nm to 500 nm) can be obtained with miniemulsion technique, depending on the polymer solution concentration, surfactant and sonication time and power.[12, 24]

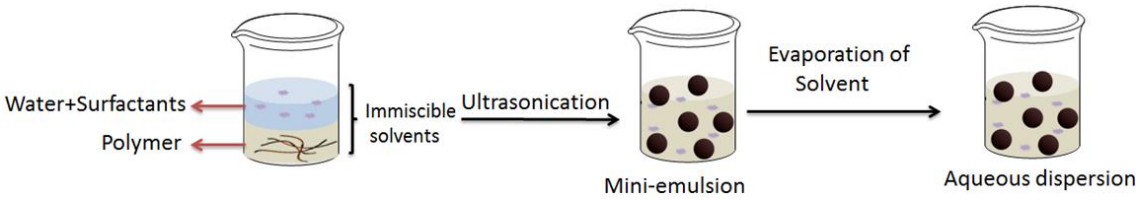

Figure 1.3. Preparation of CPNs by mini-emulsion approach

Since the mini emulsion technique can be employed as a post polymerization process it also can be applied during the polymerization process itself. For example, this approach was employed for the preparation of nanoparticles of poly (3,4-ethylenedioxythiophene) (PEDOT), polyacetylene and poly(thiophene- 3-yl-acetic acid).[25]

1.2.1.2. Re-precipitation technique

Another important route to obtain CPNs is the so-called re-precipitation technique, which is illustrated in figure 1.4. This technique involves three steps: (i) dissolving the polymer into a selective solvent, (ii) rapid injection of polymer solution into excess amount of a marginal solvent (water), which has to be completely miscible with the selective solvent, and (iii) removal of the organic solvent by evaporation to leave behind water dispersible nanoparticles. During the second step, rapid diffusion of the selective solvent into the marginal solvent decreases the solvent quality for polymer chains and they tend to avoid entering in contact with water. In order to achieve minimum exposure, they fold and assemble into spherical nanoparticles, before becoming into contact with the water phase.[26]

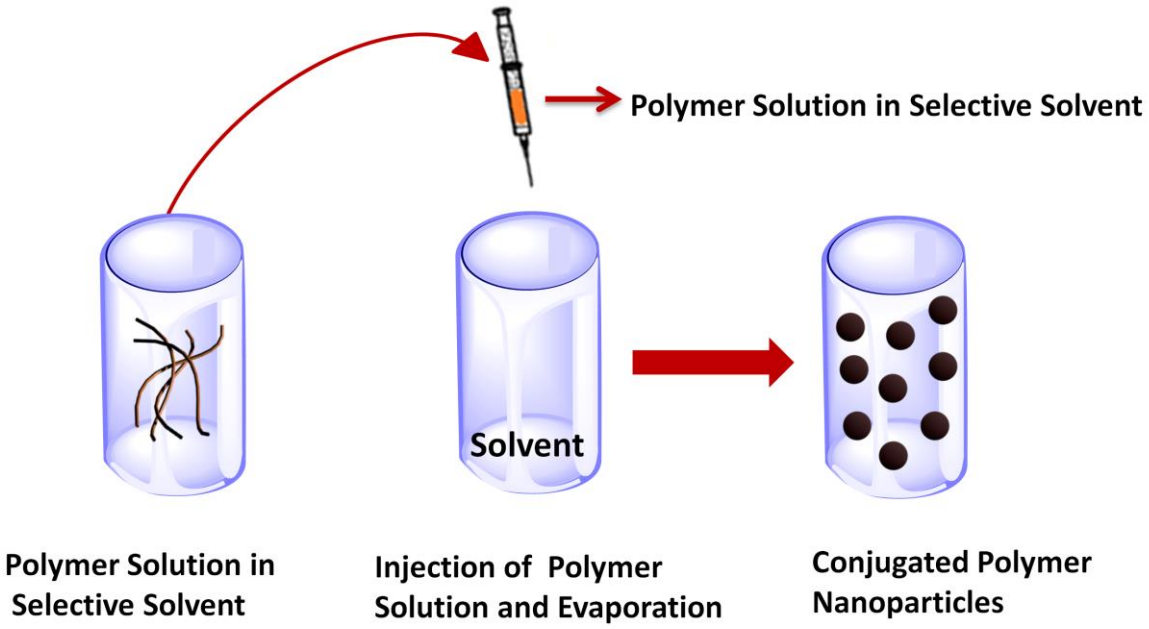

Figure 1.4. Preparation of CPNs by re-precipitation approach.

Through the re-precipitation method, 3-150 nm spherical CPNs can be prepared. The concentration of the polymer, solvent type and molecular weight of the polymer can also play a role for the size range.[12]

The re-precipitation technique further is of great value to create self-assembled functional CPNs based hybrid materials. For instance, poly (3-hexyl thiophene) nanoparticles ($P3HT_{NPs}$) have been combined with a phenyl-C61-butyric acid methyl ester (PCBM) as an acceptor material resulting in the fabrication of core-shell nanoparticles. Further characterization of the nanostructure reveals that the emission of $P3HT_{NPs}$ was found quenched indicating the development of photo-induced electron transfer phenomena from the nanoparticles to the fullerene derivative.[27]

1.3. Polythiophenes

Polythiophenes (PTh) are prominent members of the family of conjugated polymer and consist of repeating units of thiophene, which can be described as a sulphur heterocycle. PTh receive remarkable interest for optoelectronic device applications due to their large absorption cross section, photo and electroluminescent behavior. Moreover, they exhibit high environmental stability of its (un)doped states, ease of structural modification, and solution processability. [1,7, 8]. The chemical structure of polythiophene is shown in figure 1.5.

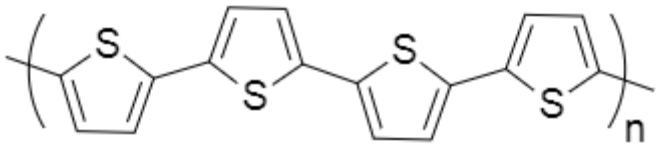

Figure 1.5. Chemical structure of unsubsituted polythiophene

Non-substituted PTh is very limited for possible applications because of its poor solubility due to its extended π-conjugated structure.[28]

However, soluble and processable PTh, which contain alkyl moieties on the thiophene repeating unit can be synthesized. (Figure 1.6)

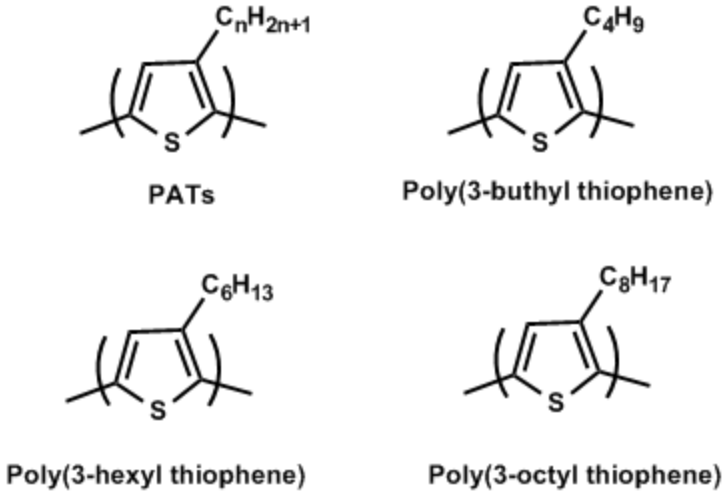

Figure 1.6. General formula for PATs and the chemical structures of mostly used PATs

Usually alkyl chains are incorporated into the third position of thiophene monomer and the the resulting alkyl modified polymer is called poly (3-alkylthiophene)s (PATs). These types of polythiophenes thus are highly soluble and processable. Besides, due to their improved solubility in organic solvents, full characterization of the polymer by spectroscopic methods such as ^{1}H NMR and ^{13}C NMR etc. can be easily achieved.

The asymmetry of 3-substituted alkyl thiophenes results in three possible couplings when two monomers are linked between the 2- and the 5-positions. These couplings can be combined into four distinct triads; (Figure 1.7).

- 2,5': Head–tail (HT), coupling.
- 2,2': Head–head (HH), coupling.
- 5,5': Tail–tail (TT), coupling

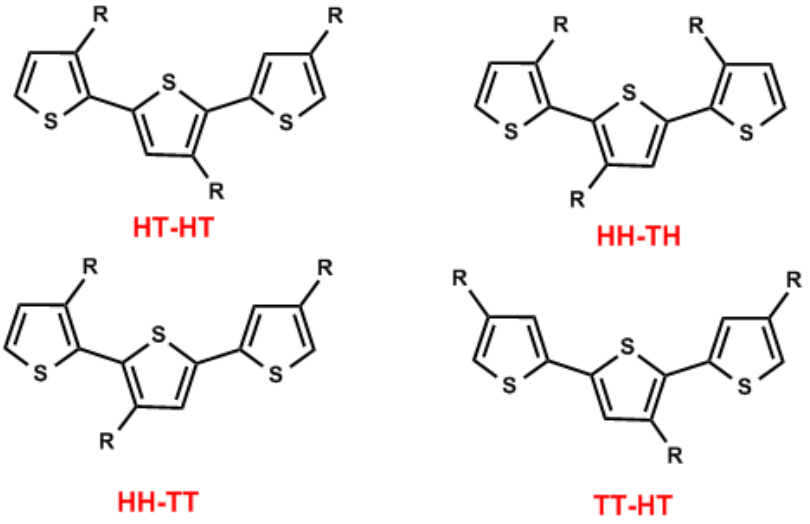

Figure 1.7. The four possible triads resulting from coupling of 3-substituted thiophenes.

The different triads are distinguishable by NMR spectroscopy, and the degree of regio-regularity can be thus estimated.

The regio-regularity of 3-substituted alkyl thiophenes considerably affects their optical and electronic properties. Among these triads, HT-HT coupling presents a regio-regular system. In case of regio-regular PATs, the polymer tends to create quasi crystalline domains in solid state or in solution and this enhances the intermolecular interaction between the polymer chains. Therefore, regio-regular PAT exhibits higher electron mobility and better charge separation in comparison to regio-random PAT.

Several methods have been studied in order to synthesize regio-regular PATs. One of the well-known techniques is Grignard metathesis polymerization, which is a very quick and easy method for the synthesis of regioregular, head-to-tail coupled PATs. This method involves two steps. In the first step 2,5-dibromo-3-alkylthiophene is treated with a variety of alkyl and vinyl Grignard reagents. The second step comprises the introduction of a catalytic amount of Ni(dppp)Cl_2. This method offers HT-HT couplings with a regio-regularity higher than 95%.[29]

1.3.1. Poly (3-hexyl thiophene): Electron donor material

Regio-regular poly (3-hexylthiophene) (P3HT) is a particular PAT. P3HT has become an exemplary semiconducting polymer for a variety of opto-electronic applications due to its ease of processing conditions from solution, as well as promising electronic and optoelectronic properties.

Moreover, regio-regular P3HT exhibits a strong tendency to aggregate into crystalline domains, which are formed by multiple π-stacked P3HT polymer chains. The crystalline domains determine intra- and intermolecular interactions of P3HT, which are critical for their charge transport properties across overall polymer network.

P3HT is also widely used as a donor material for the fabrication of donor-acceptor (D/A) charge-transfer complexes such as D/A hybrids, blends or heterojunctions. Due to its excellent electron donor properties together with its high absorption coefficient, it is possible to achieve an effective matching of energy levels with various acceptor molecules and lower the energy bandgap with respect to other conjugated polymer derivatives. The resulting hybrids of P3HT form suitable D/A complexes of interest as photoactive layer in optoelectronic device applications.[30]

A typical example of photoactive layer in organic photovoltaic cell is a bulk heterojunction of P3HT and PCBM with P3HT acting as a donor and a prominent nanocarbon material, namely phenyl-C61-butyric acid methyl ester (PCBM), acting as an acceptor (P3HT:PCBM).[31] However, there are many on-going research studies, which focus on increasing the power conversion efficiency in organic solar cell by complementing the donor molecules with other acceptor molecules such as carbon nanomaterials or inorganic counterparts.[32]

1.4. Aggregation in P3HT

The term "aggregate" refers to self-assembled highly ordered structures consisting of multiple π-stacked P3HT polymer chains. This can be observed either when P3HT is casted from solution phase into solid thin films or in nanoparticles and nanowires dispersed in solutions. These highly ordered domains are embedded in an amorphous (disordered polymer chains) matrix and the behavior is usually referred to as semi-crystallinity.[33] Two types of aggregate structures are described in literature. Depending on the alignment of the polymer chains they are referred to as H or J aggregates. In case of H aggregates, polymer chains are aligned parallel and are identified by inter-chain coupling while J aggregates show head-to-tail alignment of polymer chain and are identified by intra-chain coupling. (Figure 1.8)

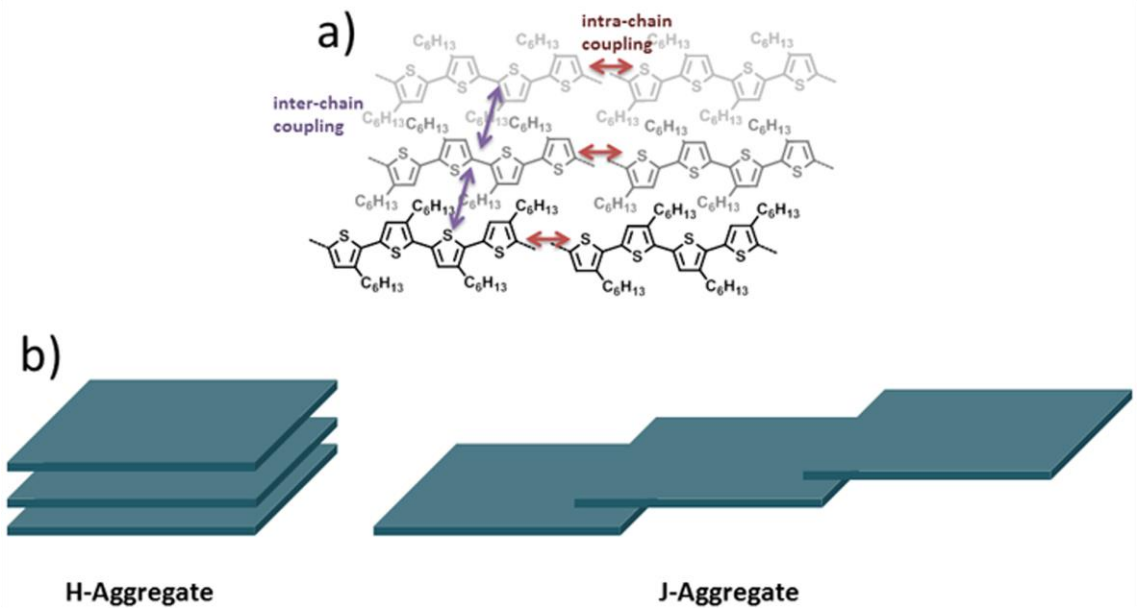

Figure 1.8. a) Charge transport path of P3HT in case of intra-chain coupling and inter-chain coupling, b) Typical arrangements of H- and J-aggregates for a π –conjugated molecule

The nature of the aggregates plays an essential role for efficient charge carrier transport and charge separation in polymer-based electronic devices. In optoelectronic devices, donor and acceptor materials should assemble at lengths scales of a few nanometers for efficient charge separation.[34] Therefore, the aggregate structure facilitates the close contact between the donor and acceptor units. On the other hand, disordered domains are unfavorable for efficient charge transport across the polymer chains since they do not offer efficient pathways for charge transport.[35] Charge transport in P3HT aggregates may occur either along the polymer backbone (intrachain transport), or in π-stacking direction (interchain transport). Intra-chain coupling of P3HT chains promotes an extended conjugation length, which creates continuous pathways for charge transport. Thus, charges can travel efficiently through to neighbor polymer chains without being trapped in disordered domains thus being carried effectively towards the external electrodes of the devices.

In addition, different coupling type in P3HT can be distinguished by photophysical features using the UV-Vis absorption spectrum as well as the photoluminescence spectrum.

While disordered P3HT chains show broad featureless optical absorption, the crystalline structure exhibits series of vibronic peaks ($A_{0\text{-}2}$, $A_{0\text{-}1}$, $A_{0\text{-}0}$). The $A_{0\text{-}0}$ vibronic transition is controlled by the type of exciton coupling in crystalline aggregates.

Spano and coworkers[36, 37] modeled the vibronic transitions using a Frank-Condon fit under different coupling conditions to reproduce absorption spectra. The model offers the ability to

use absorption spectra to gain a general idea of the aggregate structure within a sample. (Figure 1.9)

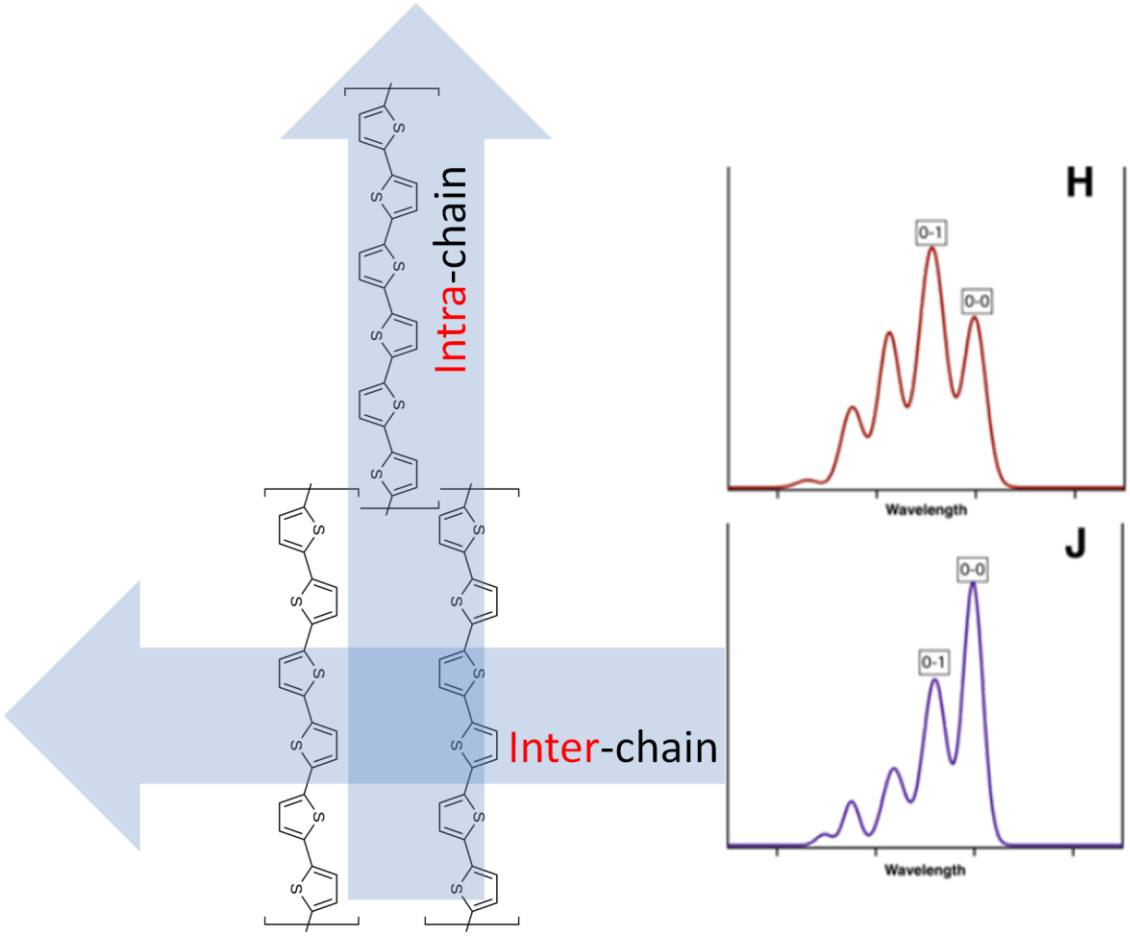

Figure 1.9. (left) Molecular depiction of thiophene packing with arrows in the direction of interchain (H-aggregate) and intrachain (J-aggregate) coupling. (right) Recreated absorption spectra of pure H and J aggregates of P3HT with 0-0 and 0-1 transition peaks.[24]

The intensity ratio of the $A_{0\text{-}0}$ and the $A_{0\text{-}1}$ vibronic transitions is related to the excitonic coupling constant according to

$$\frac{A_{0-0}}{A_{0-1}} = \frac{(1-0.96Jo/Ep)^2}{(1+0.292Jo/Ep)^2} \quad (1)$$

where J_0 is the coupling constant and E_p is the energy of the coupled phonon.

In general, a ratio of $A_{0\text{-}0}/ A_{0\text{-}1}$ greater than 1 suggests a dominance of J-aggregates (intra-chain coupling), and a ratio lower than 1 suggests a dominance of H-aggregates (inter-chain coupling). As explained above, the formation of P3HT aggregates can be established either in thin film or in solution;

1.4.1. Formation of P3HT aggregates in thin films

Regio-regular P3HT shows a semi-crystalline fraction of highly ordered π–π stacked polymer chains with a typical stacking distance of 3.8 Å, and a less ordered amorphous fraction when it is deposited on a substrate from solution.[38] However, several parameters influence the aggregation behavior, including the choice of solvent and the film preparation method, as well as the structural properties of P3HT such as molecular weight and regio-regularity. Recently, many studies focus on the creation of polymer aggregates in solution by changing solvent parameters instead of using post-treatements such as thermal annealing. For example, chloroform ($CHCl_3$) is a "good" solvent for well-dissolving P3HT, as indicated by a broad band absorbance in UV-vis and the absence of vibronic peaks. The processed film from $CHCl_3$ solution exhibits a poor intra-chain ordering. However, thin film deposition of P3HT from toluene results in enhanced intrachain order. Here toluene acts as a "poor", "marginal" solvent for P3HT therefore inducing aggregation in solution.[39-43] Also, binary solvent approaches have been studied to control the aggregation of P3HT. This is achieved by addition of a poor or marginal solvent to the P3HT solution in a good solvent. An example study shows that marginal solvents are promoting the growth of P3HT aggregates in solution. Subsequent thin film deposition facilitates the preservation of the aggregated domains in the thin film.[40]

Lastly, an alternative method for tuning the aggregates of P3HT has been reported recently by Neto et. al.[44] The work describes a photo induced approach for tuning the crystalline behavior of P3HT in solution. They also report that the morphological and physical properties of the aggregated P3HT solution is preserved in spin coated films with a high degree of crystallinity.

1.4.2. Formation of aggregates in P3HT nanoparticles

In the case of P3HT nanoparticles ($P3HT_{NPs}$), the polymer chains self-assemble into well-defined crystal packing structures within the polymer nanoparticle, which are established during liquid phase processing. Furthermore, this intrinsic property remains unaltered in thin films. Labastide et. al.[94] confirm the semicrystalline nature of the $P3HT_{NPs}$ by high-resolution transmission electron microscopy (HRTEM) images and results show that the $P3HT_{NPs}$ are actually polycrystalline with multiple crystalline domains that are nonuniformly oriented.

The aggregation within the polymer nanoparticle can be also tuned. Nagarjuna et. al.[45] used a binary solvent mixture approach for tuning the aggregation of P3HT nanoparticles. The

results show that internal aggregate structure of P3HT within polymer nanoparticles can be tuned by solvent mixtures during liquid phase preparation of $P3HT_{NPs}$.

1.5. Donor-Acceptor Charge-Transfer Complexes

A charge-transfer complex (CT complex) or electron-donor-acceptor complex is an association of two or more molecules whereby a fraction of electronic charge is transferred between them. An electron is transferred from the so-called electron donor (D) molecule (molecule with a relatively low ionization potential, which is the energy required to remove an electron from the highest occupied molecular orbital (HOMO)), to the electron receiving species, the so-called the electron acceptor (A) molecule (molecule with a relatively high electron affinity, which is the energy released when filling the lowest unoccupied molecular orbital (LUMO)).

The charge transfer from D to A can be induced by light. In this case, the donor absorbs the photon and an electron from the HOMO of the donor is excited to the LUMO of the acceptor since the energy levels of the acceptor are lower than the ones of the donor. Photo induced electron transfer can be identified in the absorption spectrum by a red-shift or by quenching of photoluminescence of the donor component (Figure 1.10).[8]

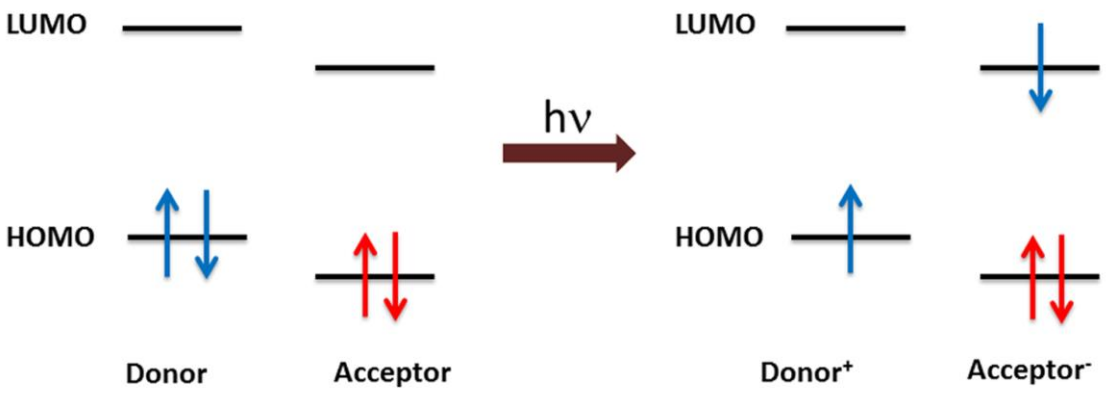

Figure 1.10. Schematic illustration of photo-induced charge transfer process

The synthesis of D/A complexes is of great interest for improvement of the performance of optoelectronic devices such as organic solar cells (OSC), since the photoactive layer of organic solar cell is constituted of D/A complexes. The working principle of an OSC includes six important steps:

1. Absorption of a photon.
2. Diffusion of the exciton to the D-A interface.
3. Charge transfer from the donor to the acceptor.
4. Charge separation
5. Charge transport of holes and electrons through donor and acceptor phase, respectively.
6. Charge extraction at the respective electrode interfaces.

As explained above, by light absorption an electron is excited from the HOMO into the LUMO which leaves a hole in the HOMO. Thus, an excited coulomb-bound electron-hole pair, a so-called exciton, is formed. Thus, it is important to choose a donor photoactive compound with a large absorption cross-section. Then, the exciton should reach the D/A interface within the lifetime of the exciton before relaxation occurs. In order to obtain free charge carriers, charge transfer from the donor to the acceptor and subsequent charge separation is necessary. This can only take place in close proximity (10-20 nm) to the D/A interfaces. Finally, the separated holes and electrons are transported through the donor and acceptor phase, respectively, towards the electrodes.[46]

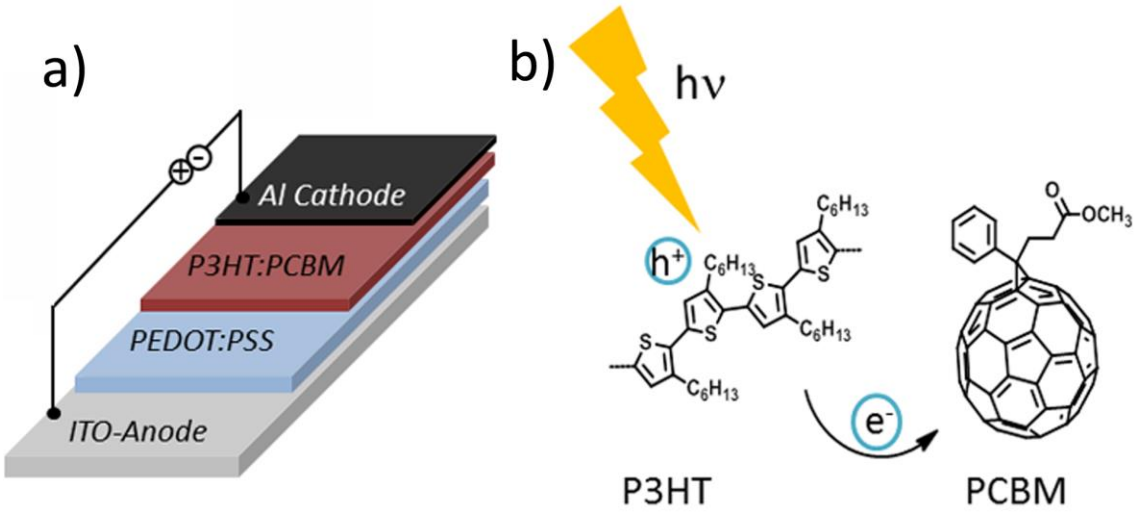

Figure 1.11. a) Representation of archetype organic solar cell of P3HT:PCBM bulk heterojunction, and b) charge transfer mechanism.

The improvement of the device performance of OSC highly depends on tuning of the D/A properties. Enhancement of the OSC performance can be achieved by selection of the appropriate donor and acceptor species with respect to their HOMO and LUMO levels.

Furthermore, tuning the morphology of the D/A mixture by controlling polymer aggregates can improve the charge transport and charge separation, which further have a direct impact on the OSC efficiency.

Besides, the development of environmental friendly processing conditions by designing water based D/A pairs is also favorable to avoid the use of toxic organic solvents in the fabrication of OSCs.

1.6. Acceptor Materials

1.6.1. Carbon nanostructures

Carbon can create various nanostructures such as fullerenes (C_{60}), carbon nanotubes, graphene and etc. (Figure 1.12) with remarkable electronic, optical, mechanical and thermal properties. The discovery of fullerenes in 1985 drew the attention of scientists in carbon science to explore the unusual and exciting properties of carbon nanomaterials. This was followed by the discovery of multi-walled carbon nanotubes (MWCNT) in 1991 and single-walled carbon nanotubes (SWCNT) in 1993 and the isolation of an atomic thin sheet of sp^2 bonded carbon atoms arranged in a hexagonal network, i.e. graphene in 2004

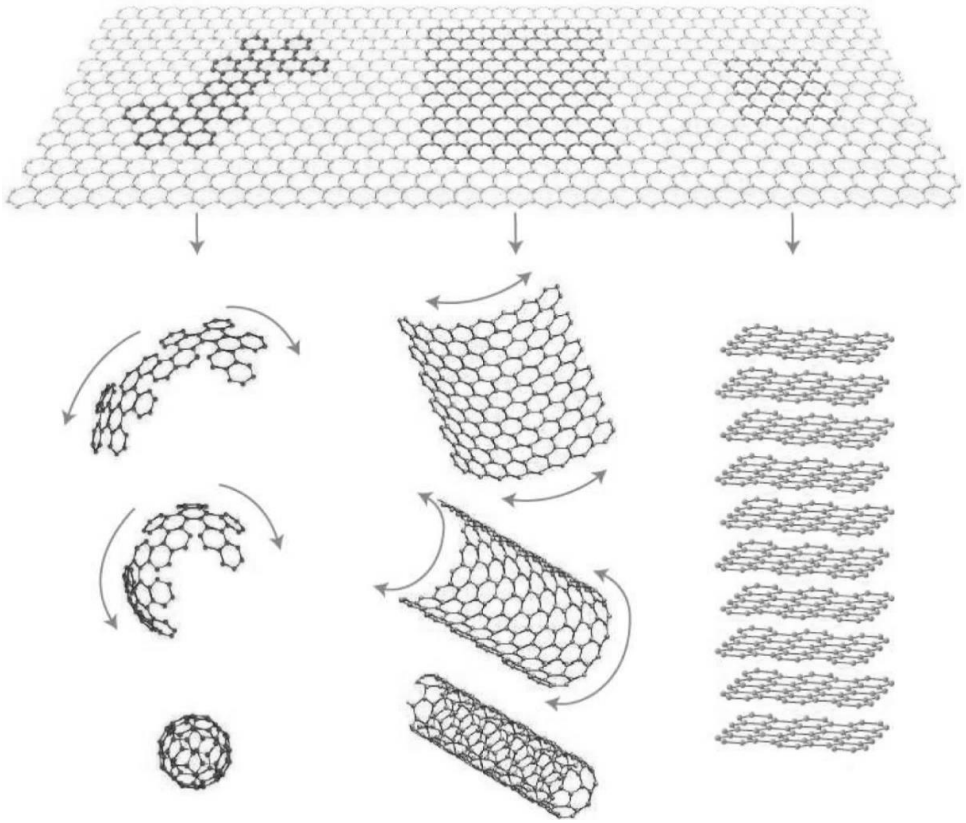

Figure 1.12. Graphene (2D) sheet can be wrapped up into (OD) fullerene, rolled into (1D) carbon nanotube and stacked into (3D) graphitic structure. (Nature Materials 2007, 6 (3), 183-191)[95]

In particular, C_{60}, carbon nanotube (CNT) and graphene consist of sp^2 carbon atoms, which pave the way for their application at the macroscopic level for electronics and optoelectronics. Among these carbon nanostructures, graphene represents the building block of other important allotropes such as, fullerene (wrapped graphene sheets containing 12 isolated pentagonal defects), CNT (rolled form of graphene), and stacked graphitic planes (stacked graphene).[47]

The next sections in this chapter focus on the description of the structure, properties and electron accepting properties in optoelectronic applications of C_{60}, CNT and graphene nanostructures.

1.6.1.1. Fullerene

Fullerenes represent the hollow spherical allotropic form of nanocarbon structures, created by the presence of 12 isolated pentagonal defects in the hexagonal honeycomb sheet of sp^2 bonded carbons. The most prominent member of the family of is C_{60} or Buckminsterfullerene, discovered in the mid-1980s.[48] The finding of closed hollow spherical carbon structures and their isolation opened novel pathways for chemistry on

curved carbon surfaces as well as inside confined spaces, for which H. Kroto, R. Smally and R. Curl were wared in 1996 with the Nobel Prize in Chemistry.

C_{60} has a cage-like fused-ring structure, made of 20 hexagonal and 12 pentagonal rings. Each carbon atom is bonded to three others and is sp2 hybridized. While the oxidation of fullerene is irreversible, C_{60} undergoes six reversible one-electron reductions to C^{6-}_{60}. The first reduction needs around 1,0V (Fc/Fc^{+}), indicates that C_{60} is moderately electron acceptor. Besides, C_{60} tends to avoid the double bonds in the pentagonal rings, therefore, it readily reacts with electron rich species.[49] This electron acceptor properties make the C_{60} a promising material for using in optoelectronic applications such as OSC. Although, C_{60} is an efficient electron acceptor, the chemical modification of fullerenes has made possible to enhance even more its electron acceptor ability and improve the limited solubility of pristine C_{60}. Therefore, many research studies focus on functionalization of fullerenes.

For example, Hummelen et al[50] synthesized the [6,6]-Phenyl C_{61} butyric acid methyl ester ($PC_{61}BM$) for the first time (Figure 1.13), which is largely used in OSC fabrication, due to its high solubility in aromatic solvents and a very efficient electron acceptor compared to pristine C_{60}.[51]

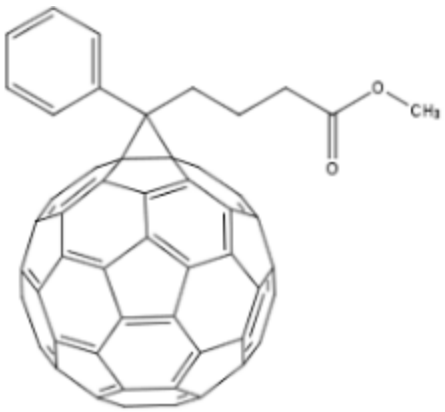

Figure 1.13. Chemical structure of $PC_{61}BM$

The combination of a donor polymer and an acceptor-PCBM as photoactive layer is one of the most widely used systems for OSC fabrication due to the ultrafast photo-induced electron transfer from the polymer to the fullerene. Photo-induced charge transfer from the conjugated polymer to the fullerene was first identified by Sariciftci et al.[52] They showed the potential of new carbon allotrope, fullerene (C_{60}), in the field of organic solar cells.

Yu et al.[53] introduced for the first time $PC_{61}BM$ in bulk heterojunction OSC, which triggers the development in the field of polymer-$PC_{61}BM$ based OSC. They studied the effect of combining soluble $PC_{61}BM$ derivatives with a polymer and reported the enhancement of charge separation, carrier mobility and energy conversion efficiency due to the formation of a bicontinuous D-A network.

Bulk heterojunction OSC made of regioregular P3HTas donor and PCBM as acceptor exhibit efficient device performance. The high efficiency of these devices is due to the crystalline stacking of P3HT in the the solid state packing, which results in reduced recombination and enhanced hole mobility.[54]

1.6.1.2. Carbon nanotubes

In 1991 S. Ijıma (re-)discovered carbon nanotubes (CNTs) by examining a specially synthesized carbon sample in a high resolution electron microscope (HRTEM). He clearly described these objects as one-dimensional new allotrope form of carbon with a cylindrical structure.[55] CNTs are classified into single wall carbon nanotubes (SWCNT) and multi-wall carbon nanotubes (MWCNT) (Figure 1.14). SWCNT can be visualized by rolling up graphene sheet to form a seamless cylinder. The diameter of SWCNT typically ranges between 0,5 nm to 2 nm and its length varies in the range from 10 nm to 1 cm.

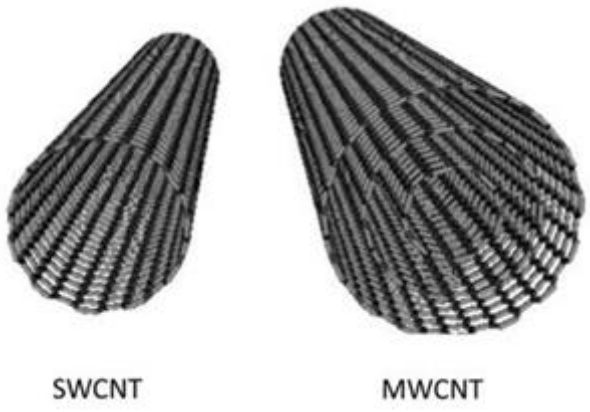

Figure 1.14. Classical model structure of SWCNT and MWCNT

The properties of SWNTs depend on their size and arrangement of the carbon atoms. For instance, the direction in which the graphene sheet is rolled up to form the nanotube is very important for its electronic properties. This direction is defined by the so-called chiral vector, which determines the character metalic or semi-conducting of SWNTs.[56]

On the other hand, MWCNTs consist of multiple concentrically rolled-up layers of graphene sheets. Since the number of concentric tubes (number of walls) within a MWCNT may vary from 2 to 50 with an interlayer distance of 0.34 nm approximately its electronic performance either metallic or semiconducting is difficult to predict due to the effect of the tube-tube inner interactions.[57] In this case, the overall electrical conductivity of MWCNTs depends on its diameter. [58]

The outstanding electronic properties of CNTs allow their use in wide variety of potential applications. Metallic CNTs have been proposed as ideal nano-conductors while semiconducting CNTs can be used in field effect transistors (FET) thanks to their ballistic electron transport properties.[59] The electronic properties of CNTs can be also employed in field-emission displays,[60] gas-sensors,[61] electrochemical biosensors[62] as well as in energy storage applications such as improved supercapacitor[63,64] and Li-ion batteries.[65]

Furthermore, due to their electron acceptor properties[66] the combination of SWNT with electron-donor molecules is considered of great promise for optoelectronic applications. For instance, a theoretical study shows that semiconducting SWCNTs (s-SWCNT) display ultrafast charge transfer when they are combining with P3HT, and it has been suggested that they can act as efficient acceptors at the interface of P3HT.[67]

Besides, an experimental study demonstrates that P3HT/sSWCNT heterojunctions can generate photocurrent from photons absorbed both in the P3HT and in the s-SWCNT.[68]

One should take into account that in case of OSC applications of CNTs, the presence of metallic CNTs limits the device performance because metallic CNTs enhance electron-hole recombination.[69] For this reason, an additional step for sorting metallic and semiconducting CNTs its necessary to use them in OSC applications.

Semiconducting single-walled carbon nanotubes can be sorted by wrapping the CNTs with conjugated polymers due to strong $\pi - \pi$ stacking interaction. This approach is of great interest for electronic and optoelectronic applications because the conjugated polymers such as polyfluorenes or P3HT are selective for semiconducting-CNTs. Wang et.al.[70] reported a high-yield method to sort semiconducting –SWNTs with regio-regular P3HT. Furthermore, the sorting process selectively enriches smaller-diameter SWNTs with larger bandgaps, which is ideal for solar cell applications.

1.6.1.3. Graphene

Graphene is a crystalline single layer of graphite, which consists of sp^2-hybridized carbon atoms arranged in a two-dimensional lattice with remarkable thermal, mechanical and electronic properties. Andre Geim and Konstantin Novoselov[8,71] for the first time isolated single graphene layers by mechanical exfoliation of highly-oriented pyrolytic graphite in 2004, and after that the two scientists were awarded the 2010 Nobel Prize in Physics.

Graphene exhibits delocalized π orbitals in a plane structure, which creates a path where the electrons can move freely through the continuous conjugated electron clouds in both sides of the graphene flake. This makes graphene a zero band gap semiconductor with carrier mobilities as high as $2x10^5$ $cm^2V^{-1}s^{-1}$ at a carrier density of 10^{12} cm^{-2}. Electrons can flow through graphene more easily than even through copper.[72]

Moreover, a single layer of graphene shows 97.7 % of optical transparency in the visible range, and the transparency decreases linearly with the increasing number of the layers.[73] This feature is intrinsically coupled to the electronic and mechanical properties of graphene and thus reveals its value to make it an ideal candidate for use in flexible electronics.

For instance, graphene can be a unique candidate to construct a transparent electrode for photovoltaic devices and flexible display technologies due to its high electrical conductivity, high carrier mobility, and high optical transmittance in the visible range of the spectrum.[74]

On the other hand, since graphene is a zero band gap material, its application in optoelectronic devices as an active layer is limited. However, chemically modified graphene exhibits suitable acceptor behavior for an active layer in OSC.[75] The most widely used chemically functionalized derivatives of graphene are graphene oxide (GO) and reduced graphene oxide (rGO), which show semiconducting behavior. The details on GO structure and its properties are explained in the next chapter of this thesis.

1.6.2. Quantum dots (QDs)

Quantum dots (QDs) can be described as a zero-dimensional, nanometer-scale semiconducting nanoparticles or nanocrsytals. QDs are quite versatile materials due to their size-dependent physicochemical properties and, particularly, their ability of tunable absorption and emission of light.

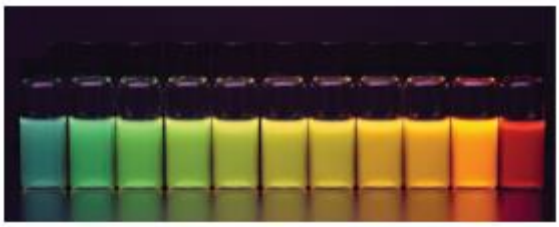

Figure 1.15. Quantum dots emitting different colours from violet to deep red (Annu. Rev. Anal. Chem. 2013. 6, 143–62) [96]

The optical properties of QDs, such as absorption and emission, are governed by the quantum confinement effect. This effect is related with the particle size and the exciton Bohr radius. The exciton Bohr radius can be described as the average distance between the photoexcited electron into the conduction band and the hole left behind in the valence band.

Due to small size of QDs, the electrons are confined in a small space and when the radius of the QDs is smaller than the exciton Bohr radius, quantization of the energy levels occurs. The discrete quantized energy levels of quantum dots let them behave rather like atoms than bulk semiconducting materials and for this reason they are even described as 'artificial atoms'. While the size of the crystal decreases, the difference in energy between the highest valence band and the lowest conduction band usually increases. More energy is required to excite the QDs and consequently, they exhibit shift from red to blue in the emission spectrum. As a result of this phenomenon, quantum dots can emit any color of light from the same material simply by changing the size of quantum dots. (Figure 1.16) [76, 77]

Quantum dots can be classified into different types based on their composition and structure. For instance, the *core type* QDs are uniformly composed of chalcogenides (selenides, sulphides or tellurides) and metals like cadmium lead or zinc, for example CdTe, CdSe, PbS etc. Another type of QDs are the so-called as core-shell type QDs. These quantum dots consist of small regions of one material embedded in another with a wider band gap. For example, quantum dots with CdSe in the core and ZnS in the shell.

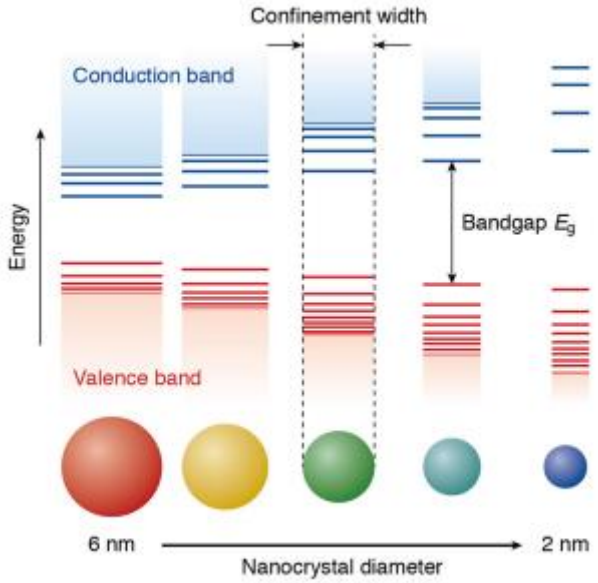

Figure 1.16. The electronic structure of quantum dots varies with the size of the dot. (Top Curr Chem (Z), 2016, 374, 5)[97]

Moreover, QDs can be an ideal material for managing energy-conversion processes and participate in a variety of photoelectrochemical, electronic, and optoelectronic applications upon photoexcitation.[78-82] Especially, among these potential applications, QDs gained popularity in photovoltaic devices and display technologies in recent years. On the other hand, the ease of processability makes the QDs also important for device structuring due to its solubility in organic solvents or water (when capped with ionic surfactant molecules). For instance, they can be easily incorporated into conjugated polymers, which are soluble in the same solvents from which both can be directly coated onto the corresponding surfaces by solution based processing methods.

1.6.3. Two dimensional transition metal dichalcogenides (2D-TMDs)

Two-dimensional (2D) materials have attracted significant interest due to their unique properties: they can be obtained by liquid phase exfoliation process on individual or few layer nanosheets, they are chemically versatile and exhibit electronic bandgaps that depend on the crystal symmetry, composition and phase., leading to a broad range of optoelectronic properties. This is the reason of their increase interest for potential applications in the last years.[83]

The family of TMDs is composed of nearly 40 different compounds such as molybdenum disulfate (MoS_2), tungsten disulfate (WS_2), tantalum(IV) sulfide (TaS_2), Titanium disulfide

(TiS_2), Tungsten diselenide (WSe_2), molybdenum diselenide ($MoSe_2$), etc.[84] As shown in the periodic table in figure 1.17, the highlighted transition metals and chalcogens are the elements that are predominately crystalized into layered structures.

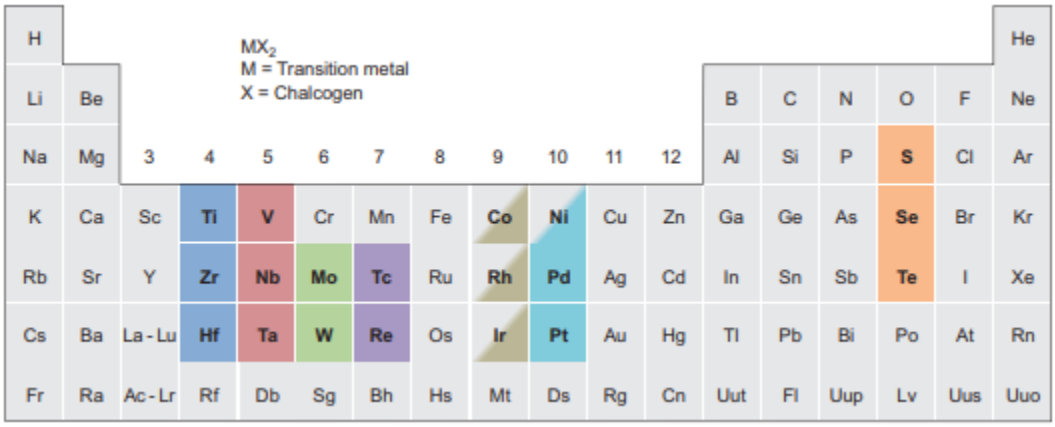

Figure 1.17. Chemical composition of layered transition metal dichalcogenides (LTMDs). The general chemical formula for LTMDs is given by MX2, where M and X denote the transition metal and chalcogen elements, respectively. The S, Se, Te elements that are highlighted IVB, VB, VIB, VIIB, IXB and XB elements are common choices for the transition metal elements. Partial highlights for Co, Rh, Ir and Ni indicate that only some of the dichalcogenides form layered structures. (Nat Chem., 2013 5(4), 263-75)[84]

The electronic properties of the 2D-TMDs depend on the configuration of the transition metals and chalcogen elements. For instance, the dichalcogenides are wide bandgap semiconductors with metal elements from Group 4B and 6B, and narrow bandgap semiconductors with metal elements from Group 7B.

Additionally, the electronic and optical properties of 2D-TMDs depend strongly on the thickness of the 2D-TMDs (number of layers). To date, several synthetic methods have been developed to prepare single- and few-layered 2D-TMDs nanosheets, namely, mechanical cleavage, chemical vapor deposition (CVD), wet-chemical synthesis, chemical or electrochemical Li-intercalation and exfoliation as well as liquid phase exfoliation in different solvents.[85]

For example, the exfoliation effect on the TMDs properties can be clearly seen in case of MoS_2. The bandgap of bulk MoS_2 is about 1.3 eV while that of single-layered MoS_2 is 1.8–1.9 eV. Thus it shows an indirect-to-direct bandgap transition as the thickness decreased to a single layer.[86]

Also, the electronic band structures of TMDs influence their optical properties. For instance, increasing bandgap energy in MoS_2 results in changes in photoconductivity, absorption spectra and photoluminescence. From bulk to monolayer, MoS_2 shows an increase of photoluminescence quantum yield by a factor of up to 10^4.[87]

Another unique properties of monolayer or few-layer MoS_2 include a large excitonic binding energy and strong electron-exciton interactions. The optical absorption spectrum of MoS_2 shows two main peaks corresponding to exciton bands, the so-called A and B excitons. (Figure 1.18)

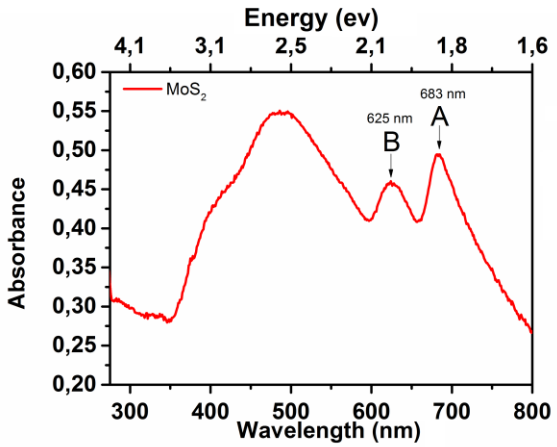

Figure 1.18. The optical absorption spectrum of MoS_2 in DMF

Therefore, due to their ultrathin thickness, 2D structure and bandgap, these 2D TMDs nanosheets present unique physical, chemical, optical, and electronic properties compared with their bulk counterparts.[88] Based on these properties, several studies has been reported including field-effect transistors (FETs),[89] broad-band photodetectors,[90] light-harvesting devices[91] chemical sensors[92, 93.] Also, their direct bandgaps in the visible range and electron accepting properties make them attractive material for thin-film solar cells and also for flexible transparent optoelectronics.

1.7. References

1. T. P. Kaloni, P. K. Giesbrecht, G. Schreckenbach and M. S. Freund, Polythiophene: From Fundamental Perspectives to Applications, *Chem. Mater.*, 2017, *29* (24), 10248–10283.

2. C. K. Chiang, C. R. Fincher Jr., Y. W. Park, A. J. Heeger, H. Shirakawa, E. J. Louis, S. C. Gau, and A. G. MacDiarmid, *Phys. Rev. Lett.* 39, 1098 (1977).

3. H. Shirakawa, E.J. Louis, A.G. MacDiarmid, C.K. Chiang and A.J. Heeger, Synthesis of electrically conducting organic polymers: halogen derivatives of polyacetylene, (CH)x *J Chem. Soc .Chem. Comm.* (1977) 579

4. A. G. MacDiarmid, "Synthetic Metals": A Novel Role for Organic Polymers (Nobel Lecture), *Angew. Chem. Int. Ed*. 2001, 40, 2581 ± 2590

5. H. Shirakawa, The Discovery of Polyacetylene Film: The Dawning of an Era of Conducting Polymers (Nobel Lecture). *Angew. Chem. Int. Ed.* 2001, 40, 2574- 2580

6. A.J. Heeger, Semiconducting and Metallic Polymers: The Fourth Generation of Polymeric Materials (Nobel Lecture). *Angew. Chem. Int. Ed.* 2001, 40, 2591- 2611

7. Shotheim ,T. A, Elsenbaumer ,R. L, Reynolds , J. R, Handbook of Conducting Polymers. Marcel Dekker , New York , 1998.

8. M. Geoghegan, G. Hadziioannnou, Polymer Electronics, *Oxford University Press*, Oxford, UK, 2013

9. D. Mori, Development of Polymer Blend Solar Cells Composed of Conjugated Donor and Acceptor Polymers, Kyoto University, PhD Thesis, 2015

10. D. T. McQuade, A. E. Pullen and T. M. Swager, Conjugated Polymer-Based Chemical Sensors, Chem. Rev., 2000, 100 (7), 2537–2574.

11. J. Pecher and S. Mecking, Nanoparticles of Conjugated Polymers, *Chem. Rev*. 2010, 110, 6260–6279.

12. D. Tuncel and H. V. Demir, Conjugated Polymer Nanoparticles, *Nanoscale*, 2010, 2, 484–494.

13. Y. K. Choi, D. Lee, S. Y. Lee, T. J. Shin, J. Park and D. J. Ahn, Conjugated Polymer Nanoparticles in Aqueous Media by Assembly with Phospholipids via Dense Alkyl Chain Packing, *Macromolecules* 2017, 50, 6935−6944.

14. Landfester, K., 'Miniemulsion Polymerization and the Structure of Polymer and Hybrid Nanoparticles', *Angew. Chem. Int. Ed.*, vol. 48, no. 25, pp. 4488-4507, 2009.

15. Landfester, K, 'Semiconducting Polymer Nanospheres in Aqeous Dispersion Prepared by a Miniemulsion Process', *Adv. Mater*., vol 22, no 9, pp. 651-656, 2002.

16. T. Piok, S. Gamerith, C. Gadermaier, H. Plank, F. P. Wenzl, S. Patil, R. Montenegro, T. Kietzke, D. Nehrer, U. Scherf, K. Landfester and E. J. W. List, Organic Light-Emitting Devices Fabricated from Semiconducting Nanospheres, *Adv. Mater*., 2003, 15, 800

17. T. Kietzke, D. Nehrer, K. Landfester, R. Montenegro, R. G€untner and U. Scherf, Novel approaches to polymer blends based on polymer nanoparticles, *Nat. Mater*., 2003, 2, 408

18. T. Kietzke, D. Nehrer, M. Kumke, R. Montenegro, K. Landfester and U. Scherf, A Nanoparticle Approach To Control the Phase Separation in Polyfluorene Photovoltaic Devices, *Macromolecules*, 2004, 37, 4882

19. G. Mauthner, K. Landfester, A. Kock, H. Br€uckl, M. Kast, C. Stepper and E. J. W. List, Inkjet printed surface cell light-emitting devices from a water-based polymer dispersion, *Org. Electron*., 2008, 9, 164

20. N. A. A. Rahim, W. McDaniel, K. Bardon, S. Srinivasan, V. Vickerman, P. T. C. So and J. H. Moon, Conjugated Polymer Nanoparticles for Two-Photon Imaging of Endothelial Cells in a Tissue Model, *Adv. Mater*., 2009, 21, 3492.

21. J. H. Moon, W. McDaniel, P. MacLean and L. E. Hancock, Live-Cell-Permeable Poly(p-phenylene ethynylene)*Angew. Chem., Int. Ed.*, 2007, 46, 8223.

22. P. Howes, R. Thorogate, M. Green, S. Jickells and B. Daniel, Synthesis, characterisation and intracellular imaging of PEG capped BEHP-PPV nanospheres, *Chem. Commun*., 2009, 2490.

23. C. Zhu, L. Liu, Q. Yang, F. Lv, and S. Wang, Water-Soluble Conjugated Polymers for Imaging, Diagnosis, and Therapy, *Chem. Rev*. 2012, 112, 4687−4735.

24. A. D., Desiree, Impact of Fabrication Parameters on the Internal Structure of Poly(3-hexylthiophene) Nanoparticles, 2015, *University of Massachusetts – Amherst*, Doctoral Dissertations, May 2014 - current. 515. http://scholarworks.umass.edu/dissertations_2/515

25. H. W. Ryu, Y. S. Kim, J. H. Kim and I. W. Cheong, Direct synthetic route for water-dispersible polythiophene nanoparticles via surfactant-free oxidative polymerization, *Polymer* 55 (2014) 806-812.

26. E. Istif, A. Kagkoura, J. Hernandez-Ferrera, A.Stergiou, T. Skaltsas, R. Arenal, N. Tagmatarchis, A. M. Benito, W.K. Maser, Self-assembled core-shell CdTe/poly(3-

hexylthiophene) nanoensembles as novel donor-acceptor light harvesting systems, *ACS Appl. Mater. Interfaces*, 2017, 9, 44695−44703.

27. S. Chambon, C. Schatz, V. Sebire, B. Pavageau, G. Wantza and L. Hirsch, Organic semiconductor core–shell nanoparticles designed through successive solvent displacements, *Mater. Horiz*., 2014, 1, 431–438

28. B. X. Valderrama-García, E. Rodríguez-Alba, E. G. Morales-Espinoza, K. M. Chane-Ching and E. Rivera, Synthesis and Characterization of Novel Polythiophenes Containing Pyrene Chromophores: Thermal, Optical and Electrochemical Properties, *Molecules*, 2016, 21, 172

29. R. S. Loewe, P. C. Ewbank, J. Liu, L. Zhai, and R. D. McCullough Regioregular, Head-to-Tail Coupled Poly(3-alkylthiophenes) Made Easy by the GRIM Method: Investigation of the Reaction and the Origin of Regioselectivity, *Macromolecules*, 2001, 34, 4324-4333

30. B. Xu, S. Noh, and B. C. Thompson, Fine Tuning of Polymer Properties by Incorporating Strongly Electron-Donating 3-Hexyloxythiophene Units into Random and Semi-random Copolymers, Macromolecules 2014, 47, 5029−5039

31. M. T. Dang, L. Hirsch, G, Wantz, P3HT:PCBM, Best Seller in Polymer Photovoltaic Research, *Adv. Mater.*, 2011, 23, 3597

32. I. Monnaie,Structure creation of P3HT in solution, Eindhoven: Technische Universiteit Eindhoven, PhD Thesis, 2015.

33. M. K. L. Zellmeier, Characterization of hybrid solar cells prepared from poly-thiophenes and silicon, Humbolt Universitat zu Berlin, PhD Thesis, 2016.

34. D. Venkataraman, Serkan Yurt, B. Harihara Venkatraman and Nagarjuna Gavvalapalli, Role of Molecular Architecture in Organic Photovoltaic Cells, J. Phys. Chem. Lett. 2010, 1, 947–958

35. M. Chang, G. T. Lim, B. Park, and E. Reichmanis, Control of Molecular Ordering, Alignment, and Charge Transport in Solution-Processed Conjugated Polymer Thin Films, *Polymers*, 2017, 9, 212.

36. Spano, F. C. Modeling disorder in polymer aggregates: The optical spectroscopy of regioregular poly(3-hexylthiophene) thin films. *J. Chem. Phys.* 2005, 122, 234701.

37. Spano, F. C. Absorption in regio-regular poly(3-hexyl)thiophene thin films: Fermi resonances, interband coupling and disorder, *Chem. Phys*. 2006, 325, 22–35.

38. N.Seidler, G. M. Lazzerini, G. Li Destri, G. Marletta and F. Cacialli, Enhanced crystallinity and film retention of P3HT thin-films for efficient organic solar cells by use of preformed nanofibers in solution, *J. Mater. Chem. C*, 2013,1, 7748-7757.

39. L. Xue, X. Gao, K. Zhao, J. Liu, X. Yu and Y. Han, The formation of different structures of poly(3-hexylthiophene) film on a patterned substrate by dip coating from aged solution, *Nanotechnology*, 2010, 21, 145303.

40. F. Machui, S. Langner, X. Zhu, S. Abbott, C. J.Brabe, Determination of the P3HT:PCBM solubility parameters via a binary solvent gradient method: Impact of solubility on the photovoltaic performance, *Solar Energy Materials & Solar Cells*, 100 (2012) 138–146

41. C. E. Johnson, D. S. Boucher, Poly(3-hexylthiophene) aggregate formation in binary solvent mixtures: An excitonic coupling analysis, *J. Polym. Sci. Part B Polym. Phys.* 2014, 52, 526–538

42. S. Hu, O. Dyck, H. Chen, Y.Hsiao, B. Hu, G. Duscher, M. Dadmun and B. Khomami, The impact of selective solvents on the evolution of structure and function in solvent annealed organic photovoltaics, *RSC Adv*. 2014, 4, 27931

43. P.Y. Chen, A.Rassamesard, H.L. Chen, and S.A. Chen, Conformation and Fluorescence Property of Poly(3-hexylthiophene) Isolated Chains Studied by Single Molecule Spectroscopy: Effects of Solvent Quality and Regioregularity, *Macromolecules*, 2013, 46 (14), pp 5657–5663

44. N. M. Barbosa Neto, M. D. R. Silva, P. T. Araujo, R. N. Sampaio, Photoinduced Self-Assembled Nanostructures and Permanent Polaron Formation in Regioregular Poly(3-hexylthiophene), *Adv. Mater*. 2018, 30, 1705052

45. G.Nagarjuna, M. Baghgar, J. A. Labastide, D. D. Algaier, M. D. Barnes, and D. Venkataraman, Tuning Aggregation of Poly(3-hexylthiophene) within Nanoparticles, *ACS Nano*, 2012, 6 (12), 10750–10758

46. D. Reitzenstein, Donor-Acceptor Conjugated Polymers for Application in Organic Electronic Devices, Julius-Maximilians-Universität Würzburg, 2010.

47. Geim, A. K.; Novoselov, K. S., The rise of graphene. *Nature Materials* 2007, *6* (3), 183-191.

48. H. W. Kroto, J. R. Heath, S. C. O'Brien, R. F. Curl, and R. E. Smalley, "C60: Buckminsterfullerene," *Nature*, 1985, 318, 162-163.

49. (Buckminsterfullerene, C_{60}. University of Bristol. Chm.bris.ac.uk (1996-10-13). Retrieved on 2011-12-25.)

50. J. C. Hummelen, B. W. Knight, F. LePeq, F. Wudl, J. Yao, and C. L. Wilkins, "Preparation and characterization of fulleroid and methanofullerene derivatives," The *Journal of Organic Chemistry*, vol. 60, pp. 532-538, 1995.

51. R. Ganesamoorthy, G. Sathiyan and P. Sakthivel, Review: Fullerene based acceptors for efficient bulk heterojunction organic solar cell applications, *Solar Energy Materials & Solar Cells* 161 (2017) 102–148.

52. N.S. Sariciftci, L. Smilowitz, A.J. Heeger and F. Wudl, Photoinduced electron transfer from a conducting polymer to buckminsterfullerene, Science 258 (1992) 1474–1476.

53. G. Yu, J. Gao, J.C. Hummelen, F. Wudl and A.J. Heeger, Polymer photovoltaic cells: enhanced efficiencies via a network of internal donor-acceptor heterojunctions, *Science,* 1995 270, 1789–1791.

54. S. Günes, H. Neugebauer and N.S. Sariciftci, Conjugated polymer-based organic solar cells, *Chemical Reviews*, 2007, Vol. 107, 4, 1324.

55. S. Iijima, "Helical microtubules of graphitic carbon," *Nature*, vol. 354, pp. 56-58, 1991.

56. I. Iezhokin, Carbon nanotube electronics, University of Groningen, *Master thesis*, 2011.

57. P. R. Bandaru, Electrical Properties and Applications of Carbon Nanotube Structures. *Journal of Nanoscience and Nanotechnology* 2007, *7* (4-1), 1239-1267.

58. J. Li, R. Stevens, L. Delzeit, H. T. Ng, A. Cassell, J. Han and M. Meyyappan, Electronic properties of multiwalled carbon nanotubes in an embedded vertical array. *Applied Physics Letters* 2002, *81* (5), 910-912.

59. S. J, Tans, A.R.M. Verschueren and C. Dekker, Room-temperature transistor based on a single carbon nanotube. *Nature* 1998, *393* (6680), 49-52.

60. W. B. Choi,D. S. Chung, J. H. Kang, H. Y. Kim, Y. W. Jin, I. T. Han, Y. H. Lee, J. E. Jung, N. S. Lee, G. S. Park and J. M. Kim, Fully sealed, high-brightness carbon-nanotube field-emission display. *Applied Physics Letters* 1999, *75* (20), 3129-3131.

61. I. Sayago, E. Terrado, M. Aleixandre, M. C. Horrillo, M. J. Fernandez, J. Lozano, E. Lafuente, W. K. Maser, A. M. Benito, T. M. Martinez, J. Gutierrez and E. Munoz, Novel selective sensors based on carbon nanotube films for hydrogen detection. *Sensors and Actuators B-Chemical* 2007, *122* (1), 75-80.

62. C. B. Jacobs, M. J. Peairs and B. J. Venton, Review: Carbon nanotube based electrochemical sensors for biomolecules. *Analytica Chimica Acta* 2010, *662* (2), 105-127.

63. D. N. Futaba, K. Hata, T. Yamada, T. Hiraoka, Y. Hayamizu, Y. Kakudate, O. Tanaike,H. Hatori, M. Yumura and S. Iijima, Shape-engineerable and highly densely packed single-walled carbon nanotubes and their application as super-capacitor electrodes. *Nat Mater* 2006, *5* (12), 987-994.

64. H. Pan,J. Li and Feng, Y., Carbon Nanotubes for Supercapacitor. *Nanoscale Research Letters* 2010, *5* (3), 654-668.

65. A. L. M. Reddy, M. M. Shaijumon, S. R. Gowda and P. M. Ajayan, Coaxial MnO2/Carbon Nanotube Array Electrodes for High-Performance Lithium Batteries. *Nano Letters* 2009, *9* (3), 1002-1006.

66. D. M. Guldi, G. M. A. Rahman, F. Zerbetto and M. Prato, Carbon Nanotubes in Electron Donor−Acceptor Nanocomposites, *Acc. Chem. Res.*, 2005, *38* (11), pp 871–878

67. Y. Kanai and J. C. Grossman, Role of Semiconducting and Metallic Tubes in P3HT/Carbon-Nanotube Photovoltaic Heterojunctions: Density Functional Theory Calculations, *Nano Lett.*, 2008, *8* (3), pp 908–912

68. S. Ren, M. Bernardi, R. R. Lunt, V. Bulovic, J. C. Grossman, and S. Gradečak, Toward Efficient Carbon Nanotube/P3HT Solar Cells: Active Layer Morphology, Electrical, and Optical Properties, Nano Lett. 2011, 11, 5316–5321

69. E. Kymakis, E. Koudoumas, I. Franghiadakis and G. A. J. Amaratunga, Post-fabrication annealing effects in polymer-nanotube photovoltaic cells. *J. Phys. D: Appl. Phys.* 39, 1058–1062 (2006).

70. H. Wang, G. I. Koleilat, P. Liu, G. Jiménez-Osés, Y.-C. Lai, M.l Vosgueritchian, Y. Fang, S. Park, K. N. Houk, and Z. Bao, *High-Yield Sorting of Small-Diameter Carbon Nanotubes for Solar Cells and Transistors*, *ACS Nano*, 2014, *8* (3), pp 2609–261.

71. K. S. Novoselov, A. K. Geim, S. V. Morozov, D. Jiang, Y. Zhang, S. V. Dubonos, I. V. Grigorieva and A. A. Firsov, Electric Field Effect in Atomically Thin Carbon Films, *Science*, 2004, 306, 666

72. X. Du, I. Skachko, A. Barker and E. Y. Andrei, Approaching ballistic transport in suspended graphene, *Nat Nano*, 2008, 3, 491-495.

73. R. R. Nair, P. Blake, A. N. Grigorenko, K. S. Novoselov, T. J. Booth, T. Stauber, N. M. R. Peres and A. K. Geim, Fine structure constant defines visual transparency of graphene. *Science*, 2008, 320, 1308

74. Y. W. Zhu, S. Murali, W. W. Cai, X. S. Li, J. W. Suk, J. R. Potts and R. S. Ruoff, Graphene and Graphene Oxide: Synthesis, Properties, and Applications, *Adv. Mater.* 2010, 22, 3906

75. Z. Liu, Q. Liu, Y. Huang, Y. Ma, S. Yin, X. Zhang, W. Sun and Y. Chen, Organic Photovoltaic Devices Based on a Novel Acceptor Material: Graphene*, *Adv. Mater. 2008, 20, 3924–3930.*

76. A. D. Yoffe, Semiconductor quantum dots and related systems: Electronic, optical, luminescence and related properties of low dimensional systems, *Advances in Physics*, 2001, 50(1), 1.

77. M.A. Kastner, Artificial Atoms, *Physics Today*, 1993, 46(1), 24.

78. U. Resch-Genger, M. Grabolle, S. Cavaliere-Jaricot, R. Nitschke, T. Nann, Quantum Dots Versus Organic Dyes as Fluorescent Labels. *Nat. Methods,* 2008, 5, 763−775

79. S. Kundu and A. Patra, Nanoscale Strategies for Light Harvesting. *Chem. Rev*. 2017, 117, 712−757.

80. Q. Han, R. Wang, B. Xing, T. Zhang, M.S. Khan, D. Wu and Q. Wei, Label-free Photoelectrochemical Immunoassay for CEA Detection Based on CdS Sensitized WO3@BiOI Heterostructure Nanocomposite, *Biosens. Bioelectron*. 2018, 99, 493−499.

81. X. Michalet, F. Pinaud, L. A. Bentolila, J.M. Tsay, S. Doose, J.J. Li, G. Sundaresan, A.M. Wu, S.S. Gambhir and S. Weiss, Quantum Dots for Live Cells, in Vivo Imaging, and Diagnostics. *Science* 2005, 307, 538−544.

82. K. Meng, G. Chen, G and K.R. Thampi, Metal Chalcogenides as Counter Electrode Materials in Quantum Dot Sensitized Solar Cells: A Perspective, *J. Mater. Chem. A* 2015, 3, 23074−23089.

83. Y. L. Huang, Y. J. Zheng, Z. Song, D. Chi, T. S. W. Andrew and S. Y. Quek, The Organic-2D Transition Metal Dichalcogenide Heterointerface, *Chem. Soc. Rev*., 2018, 47, 3241—3264.

84. M. Chhowalla, H. S. Shin, G. Eda, L. J. Li, K. P. Loh and H. Zhang, The Chemistry of Two-Dimensional Layered Transition Metal Dichalcogenide Nanosheets, *Nat Chem.*, 2013 5(4), 263-75.

85. Y. Hu, Y. Huang, C. Tan, X. Zhang, Q. Lu, M. Sindoro, X. Huang, W.Huang, L. Wang and H. Zhang, Two-Dimensional Transition Metal Dichalcogenide Nanomaterials for Biosensing Applications, *Mater. Chem. Front*., 2017, 1, 24-36.

86. K. F. Mak, C. Lee, J. Hone, J. Shan and T. F. Heinz, Atomically Thin MoS_2: A New Direct-Gap Semiconductor, *Phys. Rev. Lett*., 2010, 105, 136805.

87. Q.H. Wang, K. K. Zadeh, A. Kis, J. N. Coleman and M. S. Strano, Electronics and Optoelectronics of Two-Dimensional Transition Metal Dichalcogenides, *Nature Nanotechnology*, 2012, 7, 699–712, 2012.

88. Y. Hu, Y. Huang, C. Tan, X. Zhang, Q. Lu, M. Sindoro, X. Huang, W.Huang, L. Wang and H. Zhang, Two-Dimensional Transition Metal Dichalcogenide Nanomaterials for Biosensing Applications, *Mater. Chem. Front*., 2017, 1, 24-36.

89. B. Radisavljevic, A. Radenovic, J. Brivio, V. Giacometti and A. Kis, Single-layer MoS2 transistors, *Nat. Nanotechnol*., 2011, 6, 147–150.

90. C. Xie, C. Mak, X. Tao and F. Yan, Photodetectors Based on Two-Dimensional Layered Materials Beyond Graphene, *Adv. Funct. Mater*., 2017, 27, 1603886.

91. L. Britnell, R. M. Ribeiro, A. Eckmann, R. Jalil, B. D. Belle, A. Mishchenko, Y. J. Kim, R. V. Gorbachev, T. Georgiou, S. V. Morozov, A. N. Grigorenko, A. K. Geim, C. Casiraghi, A. H. Castro Neto and K. S. Novoselov, Strong Light-Matter Interactions in Heterostructures of Atomically Thin Films, *Science*, 2013, 340, 1311–1314.

92. F. K. Perkins, A. L. Friedman, E. Cobas, P. M. Campbell, G. G. Jernigan, and B. T. Jonker, Chemical Vapor Sensing with Monolayer MoS2, *Nano Lett*., 2013, 13 (2), 668–673.

93. Z. Hu, Z. Wu, C. Han, J. He, Z. Ni and W.Chen, Two-Dimensional Transition Metal Dichalcogenides: Interface and Defect Engineering, *Chem. Soc. Rev*., 2018,47, 3100-3128.

94. J.A. Labastide, M.Baghgar, I.Dujovne, B. H. Venkatraman, D. C. Ramsdell, D. Venkataraman, and M. D. Barnes, Time- and Polarization-Resolved Photoluminescence of Individual Semicrystalline Polythiophene (P3HT) Nanoparticles, *J. Phys. Chem. Lett.*, 2011, *2* (17), 2089–2093.

95. A. K. Geim and K. S. Novoselov, The Rise of Graphene, *Nature Materials* 2007, 6 (3), 183-191.

96. B.A. Kairdolf, A. M. Smith, T. H. Stokes, M. D. Wang, A. N. Young and S. Nie, Semiconductor quantum Dots for Bioimaging and Biodiagnostic pplications, *Annu. Rev. Anal. Chem*, 2013,6,143-62.

97. F. T. Rabouw, C. M. Donega, Excited-State Dynamics in Colloidal Semiconductor Nanocrystals, *Top Curr Chem (Z)*, 2016, 374, 5

2. SELF-ASSEMBLED P3HT$_{NPs}$/ GO DONOR-ACCEPTOR CHARGE-TRANSFER COMPLEXES

2.1. Abstract

D/A charge-transfer complexes are of critical importance for the development of optoelectronic devices such as OSC. In this chapter, a novel charge-transfer complex consisting of an electron donor $P3HT_{NPs}$ and an electron acceptor GO is described. An in-situ re-precipitation approach of P3HT in the presence of GO is used for the first time to create $P3HT_{NPs}$/GO hybrids D/A charge-transfer complexes. During the self-assembly process and formation of $P3HT_{NPs,}$ GO changes the crystalline packing of P3HT chains from H to H/J aggregates, which in turn improve the electronic and optical properties of $P3HT_{NPs}$. Concomitantly, π–π interface interactions between the $P3HT_{NPs}$ and GO sheets are established resulting in the creation of $P3HT_{NPs}$–GO charge-transfer complexes

The characterization of the hybrid was performed both in liquid and thin films. Importantly, their optoelectronic properties, preestablished in the liquid phase, are retained when processed into thin films from the stable aqueous dispersions which is crucial for the fabrication of improved optoelectronic thin film devices.

2.2. Introduction

2.2.1. Graphene oxide

Graphene oxide (GO) is a chemically derived and highly defective form of graphene that combines regions of conjugated sp^2 carbon atoms and of sp^3 carbon containing randomly distributed oxygen functional groups, which are covalently bonded to its basal plane and edges (Figure 2.1). These organic functional groups comprise, epoxy (C-O-C) and hydroxyl (C-OH) groups bonded to the basal plane and carbonyl (C=O) and carboxylic acid (COOH) moieties on the edges.[1-4] They are responsible for establishing electrostatic repulsion effect, rendering hydrophilic colloidal solutions of GO. The presence of functional groups and sp^2 domains offer great promise to modify the electronic and optical properties of GO. For example, Mkhoyan et. al.[5] suggest that controlled oxidation processes allow for the tunability of the electronic and mechanical properties of GO. These render GO an amphipilic molecular platform of great interest as semiconducting interface material.

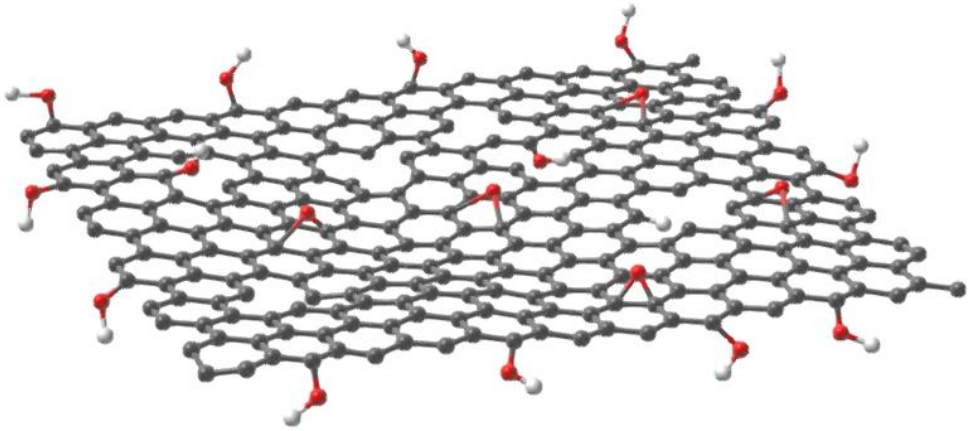

Figure 2.1. Schematic representation of graphene oxide with oxygen functional groups and defects. The grey, red and white atoms represents carbon, oxygen and hydrogen respectively

Current methods for the synthesis of GO are mostly based on oxidation-intercalation methods for graphite developed by Brodie,[6] Staudenmaier[7], and Hummers[8] to obtain graphite oxide material. Here, the type of oxidation method, reducing agents and applied chemical route offers different graphite oxide materials with different chemical surface. Higher content of oxygen functional groups can be achieved by longer and harsher oxidation treatments. Once a method is selected for the synthesis of graphite oxide, subsequent exfoliation results in monolayer or few layers GO. The most common exfoliation technique is the sonication of graphite oxide in water. Moreover, applying a centrifugation procedure after the exfoliation can offer control on the size and number of layers of the GO.

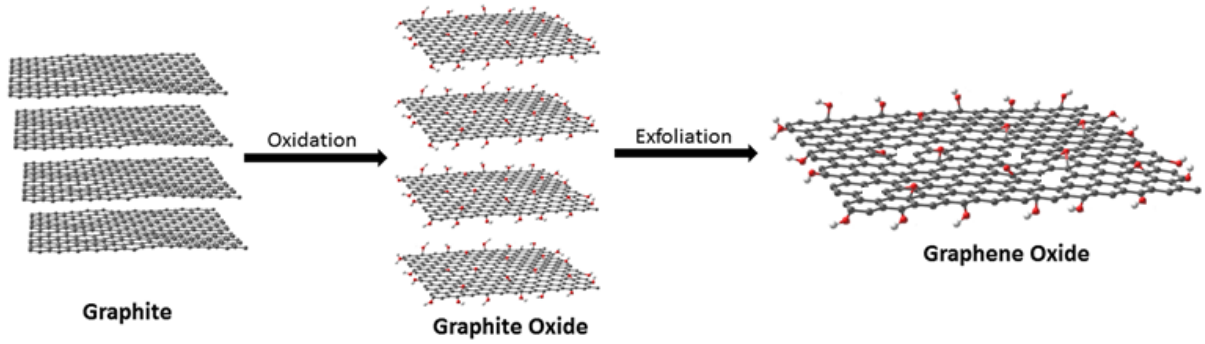

Figure 2.2. Synthesis of GO

Due to the oxidation of graphite oxide, the interlayer space between the layers is more than twice compared to graphite. While graphite shows an interlayer spacing of 0.336 nm, XRD analysis has reported values of 0.88 nm for graphite oxide.[1] Consequently, graphite oxide exhibits a lower Van der Waals interactions when compared to graphite and it makes possible to obtain single layer GO sheets via exfoliation by sonication of graphite oxide.

Processed from solution into thin films, GO can be used as a thin film electronic charge transport layer for optoelectronic application.[9,10] On the other hand, ease functionalization of GO makes it unique to tune the properties depending on the desired application such as optoelectronics[10, 11, 18] biodevices or as a drug-delivery material.[12] For instance, Yoon et. al. developed a sensor with functionalized GO, which can detect a very low level of cancer cells in a blood sample.[13]

As a result of its unique semiconducting and optoelectronic properties as well as due to its environmentally friendly processing possibilities, GO is a nanomaterial of special interest to wide variety of applications in the field of sensing and optoelectronic device.

2.2.2. Graphene oxide-conjugated polymer interactions

The combination of GO with CPs offers an attractive route for the development of organic electronic device structures, such as organic field effect transistors, light-emitting devices, and solar cells. Due to the chemically versatile structure of GO, this combination can take place by covalent or non-covalent interactions, such as electrostatic, hydrogen bonding and π–π interaction. The interaction of GO with CPs thus affects their optical properties, such as absorption and photoluminescence. This in turn may be based on energy or charge transfer processes creating suitable CPs-GO combination is thus of interact for organic electronic device fabrication. For instance, Wang et. al. [14] reported a GO-P3HT hybrid established via π–π interaction and leading to effective quenching of P3HT emission properties based on energy transfer from P3HT to GO. In another study, Valles et. al. reported in situ polymerization of PANI in the presence of GO to create charge transfer complexes.[15]

The fabrication of devices using CPs-GO charge transfer complexes were also reported by many research groups. Liu et. al. reported the blend of solution-processable GO functionalized with phenyl isocyanate as an acceptor with P3HT as a donor material. They show that adding graphene to the P3HT induces a large quenching effect of the photoluminescence of the P3HT, which indicates electron/energy transfer from the P3HT to the graphene. Moreover, this blend uses as a photoactive layer in bulk heterojunction OSC. [16] Yu et. al. reported that P3HT is chemically grafted onto carboxylic groups of graphene oxide (GO) via esterification reaction and the fabrication of OSC was achieved by using this material with a good yield of power conversion efficiency.[17]

As a result of this overview, CPs-GO hybrids could offer a new outlook for the organic electronic applications, due to the versatile chemical structure of GO, tunable electronic and optoelectronic properties and ease of processing conditions,

In the present work, we explore the established interactions between GO sheets and P3HT nanoparticles during an in situ re-precipitation process carried out in aqueous dispersions. The hybrid materials were investigated by optical spectroscopic techniques, which reveal that GO has strong impact on the internal aggregate structure of P3HT$_{NPs}$. Moreover, electronic communication such as charge transfer between GO and P3HT$_{NPs}$ is elucidated by Raman spectroscopy, cyclic voltammetry and photoelectrochemistry experiments. The findings serve as guide for the design of optoelectronic components with superior properties compatible with environmentally friendly processing possibilities.

2.3. Experimental Section

2.3.1. Materials

3-hexyl thiophene, [1,3-Bis(diphenylphosphino)propane] dichloronickel(II)] (Ni(dppp)Cl2), tert-BuMgCl (1M THF solution), dry DMF, THF, N-Bromosuccinimide, acetonitrile, HCl were purchased from Sigma-Aldrich and were used as received. THF was distilled over benzophenone and sodium. $NaClO_4$ was dried overnight at 130^0C in vacuum oven before use. Graphene oxide in aqueous dispersion (4mg/mL) was acquired from Graphenea S.L. (San Sebastian, Spain) and used as received without any further treatment.

2.3.2. Characterization techniques

- ^{1}H-NMR spectra were recorded in $CDCl_3$ solutions at 25 ºC on a Bruker AV500 spectrometer (δ in ppm and J in Hz) at a ^{1}H NMR operating frequency of 500.13 MHz.
- UV/Vis absorption spectra from dispersions and from films spray coated on cleaned glass substrates were recorded on a Shimadzu UV-2401 PC spectrophotometer. The concentrations of the dispersions and film thicknesses were carefully adjusted to obtain comparable optical densities for the π-π* absorption band for each of the series of dispersions and films.
- Photoluminescence emission spectra were recorded on a Horiba Jobin Yvon Fluoromax-P, from dispersions used in UV-Vis spectroscopy using a 10 mm path-length quartz cuvette and from films spray coated on cleaned silicon oxide substrates.

Raman spectroscopy was performed on the films coated on silicon oxide substrates using a Horiba Jobin-Yvon HRLAB HR 800 UV apparatus (λexc= 785 nm).

- Transmission electron microscopy (TEM) images were acquired in a JEOL microscope model 2000 FXII at an acceleration potential of 200 kV. Aqueous dispersions were drop-cast on lacey carbon TEM grids followed by a room temperature drying process to evaporate the aqueous solvent.
- Atomic force microscopy (AFM) images on films drop-casted on Si/SiO_2 substrates (previously cleaned with isopropanol and treated with ozone cleaner for 10 min) were obtained with a Bruker Dimension Icon®, in Scanasyst® mode using a PFQNE-AL ® tip with a 5 nm diameter. Images were taken with a 512 sampling/line resolution at a frequency of 1 Hz. Scanasyst mode is a proprietary PeakForce Tapping ® mode developed by Bruker that employs automatic optimization algorithms to actively check image quality and consequently chooses the most appropriate amplitude, frequency and amplitude set-point values.
- Molecular weight distributions of the samples were determined by size exclusion chromatography (SEC) using a Waters system, composed of a Waters 1515 isocratic pump, a set of three μ-Styragel mixed bed columns (having a porosity range of 102 to 106 Å), a Waters 2414 refractive index detector (equilibrated at 40ºC) and controlled through Breeze software. Tetrahydrofuran was the mobile phase, used at a flow rate of 1.0 mL/min at 30 ºC. The setup was calibrated with linear polystyrene standards having narrow polydispersity and average molecular weights in the range of 1200 to 929,000 g/mol. The samples were readily soluble in the mobile phase. Concentrations in the range 2-4 mg/mL were used for analysis.
- The electrochemical experiments were performed with a Autolab PGSTAT302N potentiostat. Cyclic voltammetry (CV) of hybrids were carried out under nitrogen in a three- electrode cell using 0.1 M $NaClO_4$ in dry acetonitrile as a supporting electrolyte. Scan rates of 100 mV/s were employed. Glassy carbon, platinum plate and silver/silver chloride were used as working electrode, counter electrode and reference electrode, respectively. The samples were drop-casted on the glassy carbon electrode. For hybrids and GO films 10 continuous pre-cycles in the range of -1.5 to 1.2 V were applied to obtain stable CV responses.
- Photoelectrochemical measurements were carried out on samples spray-coated on FTO substrates covering an area of 1 cm^2. Placed in the three-electrode

electrochemical cell as working electrode, they were illuminated through a quartz window by a 150 W Xenon arc lamp (LOT-Oriel GmbH, Germany). On-off cyclic voltammetry at a scan rate of 0.02 $V \cdot s^{-1}$ was carried out by intermittently interrupting the pass of the light beam with a frequency of about 0.3 Hz. Further experimental set-up details are identical to those used for the electrochemical experiments.

2.3.3. Synthesis and characterization of Poly (3-hexyl) thiophene (P3HT)

P3HT was synthesized using a Grignard metathesis polymerization, which is well known synthesis method to obtain high regioregular index. The synthesis route towards the polymer started with the bromination of 3-hexyl thiophene (Scheme 1). For the bromination, 1.5 g (9 mmol) 3-hexyl thiophene were dissolved in 25 mL of dry DMF in round a bottom flask and placed in an ice bath. Afterwards, 3.2 g (18 mmol) N-Bromosuccinimide (NBS) were dissolved in 10 mL of dry DMF in another vial and added portion-wise to the round bottom flask and stirred for in 15 min under inert atmosphere. During the synthesis, the reaction flask was covered with aluminum paper to protect it from light. After 1 h the ice bath was removed and the reaction stirred overnight at room temperature. For purification, the reaction vessel poured onto cold water and extracted three times with diethyl ether. (50 mL x 3). The separated organic phase was washed with brine and water then organic phase was dried over Na_2SO_4 and filtered. Organic solvent and remaining 3-hexyl thiophene was removed under vacuum at 90^0C. (Yield: 80%). The synthesized 2,5-dibromo-3-hexylthiophene was characterized by ^{1}H-NMR technique. (Figure 2.3)

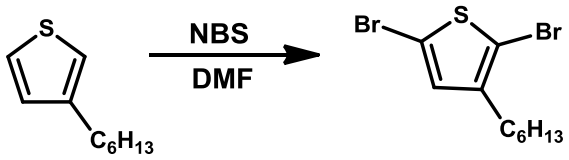

Scheme 2.1. Synthesis of 2,5-dibromo-3-hexylthiophene

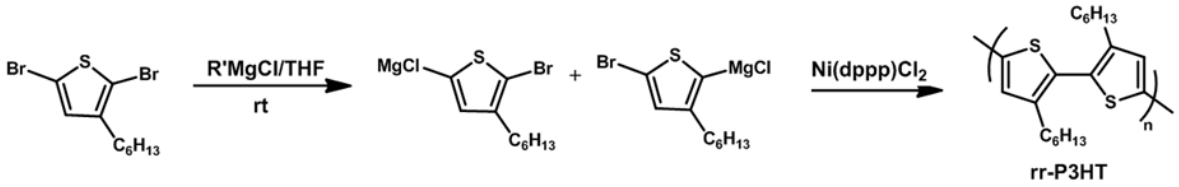

Scheme 2.2. Synthesis of regio-regular poly (3-hexyl) thiophene (P3HT)

Next, 2,5-dibromo-3-hexylthiophene was used for P3HT synthesis in the presence of Ni(dppp)Cl_2 catalyst using Grignard metathesis polymerization. The polymerization reaction took place under inert atmosphere and all the glassware were dried by flame gun. In a flame dried schlenk flask, 1g (3 mmol) 2,5-dibromo-3-hexylthiophene was dissolved in 6 mL of freshly dried THF and 2.9 mL (2.9 mmol) t-BuMgCl (1M THF solution) was added with a syringe under inert atmosphere. The reaction mixture was stirred at room temperature for 3h. Subsequently, 64mg (0.12mmol) of [1,3-Bis(diphenylphosphino)propane]dichloronickel(II) (Ni(dppp)Cl_2) were added to initiate the polymerization and stirred 30 min at room temperature. The polymerization was stopped by adding 2 ml of 5N HCl. After precipitation in methanol, the polymer was filtered into a Soxhlet thimble and extracted with methanol over-night to wash away unreacted monomer and low molecular weight impurities. The pure polymer was obtained by dissolving polymer in chloroform and precipitate in methanol. 300 mg of the polymer were obtained. Regioregularity index of P3HT (92% head-to-tail conformation) was calculated by comparing the integrations of the ^{1}H-NMR peaks at δ 2.8 ppm (head-to-tail) and 2.6 ppm (head-to-head) (Figure 2.3b). Molecular weight (8100) and polydispersity of P3HT (1.19) were obtained by SEC technique. (Figure 2.4)

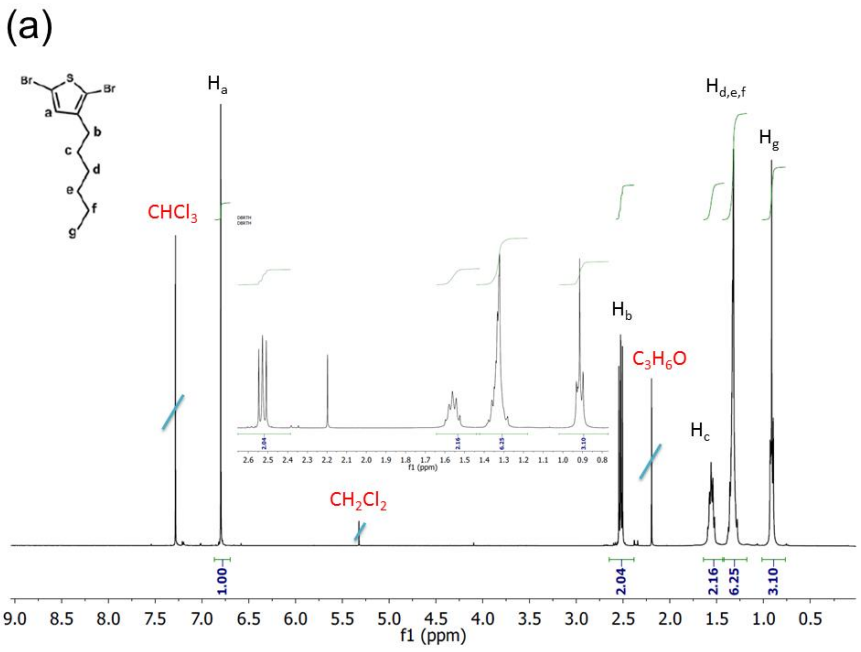

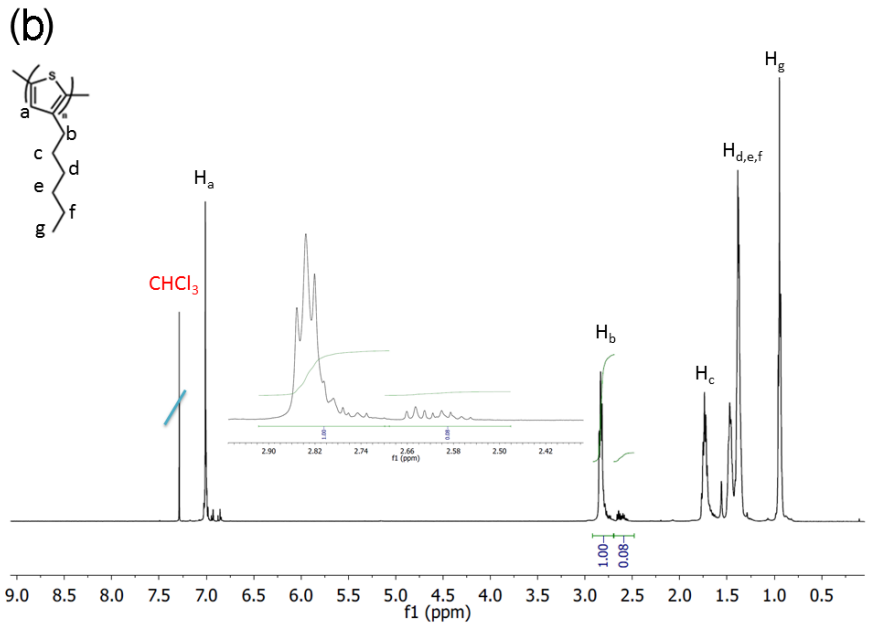

Figure 2.3. ^{1}H-NMR spectrum of a) 2,5-dibromo-3-hexylthiophene and b) P3HT recorded in $CDCl_3$ solution

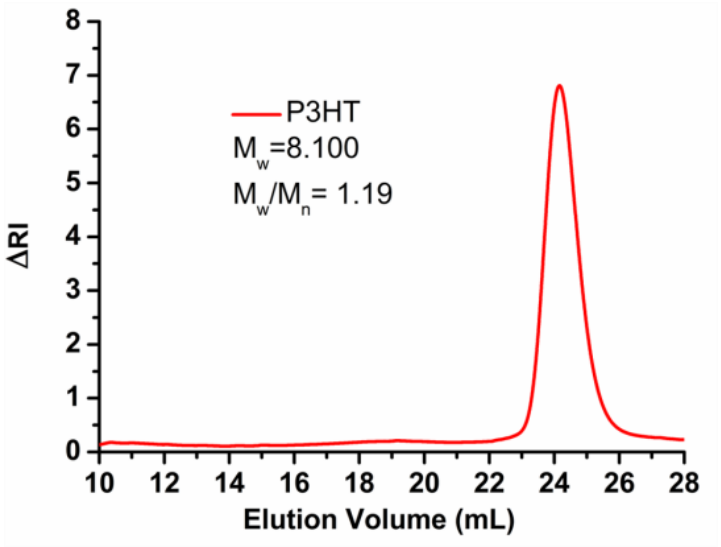

Figure 2.4. Molecular weight and polydispersity of P3HT.

2.3.4. Characterization of GO

Firstly, GO was characterized by FTIR in order to obtain information on its chemical structure (Figure 2.5). FTIR spectra were recorded on a Bruker Vertex 70 instrument in the range of 3500 cm^{-1} to 500 cm^{-1}. The GO dispersion was freeze-dried and mixed with KBr to prepare a pellet. GO exhibits a broad band centered at 3423 cm^{-1}, comprising the O–H stretch modes related to C–OH and COOH functional groups located on the GO sheets. The absorption peak at 1730 cm^{-1} is assigned to the C=O stretching of carboxylic groups and the peak at 1625 cm^{-1}

is related to sp^2-hybridized C=C groups (asymmetric vibrational stretching mode). The two peaks at about 1217 cm^{-1} and 1051 cm^{-1} correspond to C–O stretching vibrations and the peak at 830 cm^{-1} to C-O-C bending mode.[19,20]

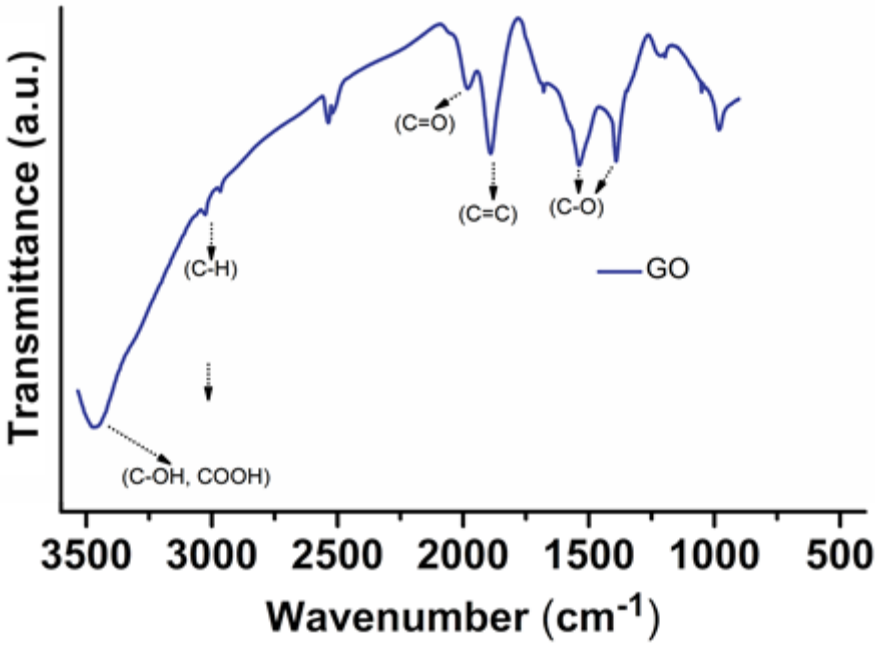

Figure 2.5. FTIR spectra of GO

Raman measurement was carried out on films in order to further investigate the vibrational modes of GO. GO was deposited on Si/SiO_2 substrate (previously cleaned by piranha solution and isopropanol) by spray coating. GO shows two broad bands at 1598 cm^{-1} and 1318 cm^{-1}, (Figure 2.6) corresponding to the G-band (tangential C-C stretch modes of graphene sheets) and the D-band (related to defects, i.e. the presence of sp^3 hybridized carbon in the oxidized graphene sheets), respectively.[21]

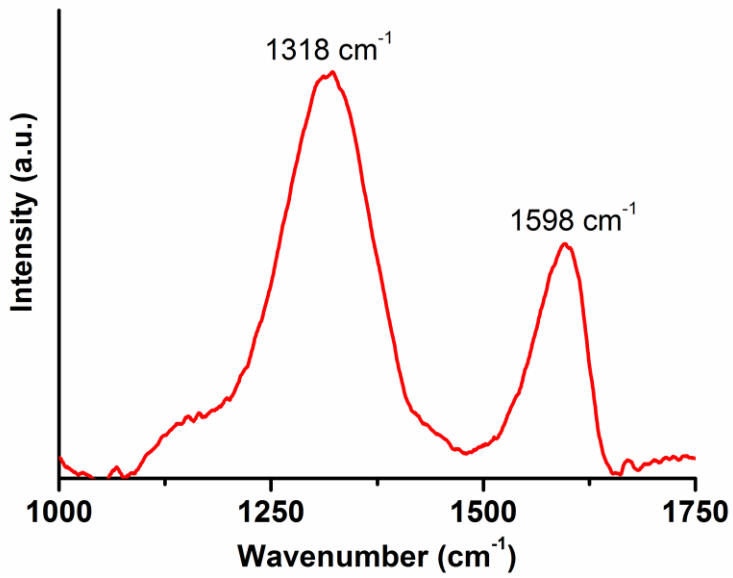

Figure 2.6. Raman spectra of GO.

Lastly, X-ray photoelectron spectroscopy (XPS) was performed to reveal the elemental compositions and chemical states of GO. XPS measurements were performed with a Phoibos 150 analyzer (SPECS GmbH, Berlin, Germany) in ultra-high vacuum conditions (base pressure 3 x 10-10 mbar). A monochromatic Al Kα X-ray source (1486.74 eV) was used to probe the film samples spray-coated on FTO substrates. The XPS C1s core shell spectrum of GO (Figure 2.7) reveals the existence of a large variety of oxygen functional groups, such as hydroxyl, epoxy, carboxylic and carbonyl groups attached to the GO sheets, composed of sp^2 and sp^3 domains.[4,19]

The de-convolution results are summarized in Table 2.1, while the overall elemental composition is listed in Table 2.2.

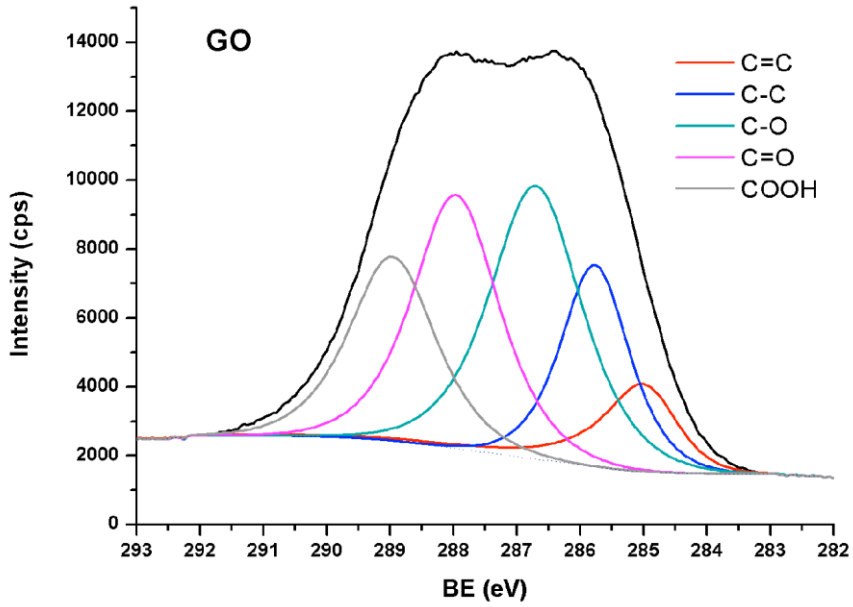

Figure 2.7. XPS C1s core shell spectrum of GO film and best fit for de-convolution into components (C=C, C-C, C-O, C=O and COOH).

Table 2.1 De-convolution of XPS C1S spectrum of GO: Peak positions and contribution to the overall spectrum. (Fitting: Subtraction of a Shirley background, use of GL70 line-shape, and max. FWHM of 1.6 eV)

C1s	C=C	C-C	C–O	C=O	COOH	π-π*
Binding energy (eV)	284.8	285.8	286.7	288.0	288.9	290.1
Contribution (at %)	4.05	24.14	25.15	23.93	20.11	1.63

Table 2.2. Elemental composition of GO as calculated from survey spectra

Elemental Composition	C (at %)	O (at %)	N (at %)	S (at %)	C/O	C/S
GO	69.49	28.89	1.62	0	2.41	-

2.3.5. Synthesis of P3HT nanoparticles (P3HT$_{NPs}$) and P3HT$_{NPs}$-GO hybrids

The formation of P3HT$_{NPs}$ and P3HT$_{NPs}$-GO hybrid nano-assemblies were accomplished by an in-situ reprecipitation process involving rapid injection of P3HT in THF to an excess

volume of water dispersion of GO. Figure 2.8 illustrates the in-situ re-precipitation approach and the resulting stable water dispersions containing the P3HT$_{NPs}$ (left-hand route) and P3HT$_{NPs}$-GO nanohybrid (right-hand route).

P3HT was added to THF in a concentration of 1mg/mL and left to dissolve under magnetic stirring overnight at room temperature. The polymer solution (2 ml) was injected into 10 ml of water under vigorous stirring. Then, a tip sonicator was used for 3 min and the remaining THF was evaporated via a vacuum evaporator at 35 ^{0}C. Lastly, the dispersion was filtered.

In the case of P3HT$_{NPs}$-GO hybrid materials, a similar procedure was applied. The polymer solution (2 mL) was injected into an aqueous solution of GO under vigorous stirring (2 mg in 10 mL, 1 mg in 10 mL and 0.5 mg in 10 mL). In order to increase the dispersibility a tip sonicator was used for 3 min. Remaining THF was evaporated via a vacuum evaporator operating at 35 ^{0}C. The dispersions were filtered and supernatant used for further experiments. The samples were obtained using the following P3HT : GO weight ratios 1 : 0.25 (C3); 1 : 0.5 (C2), and 1 : 1 (C1). Sample denomination is given in parenthesis.

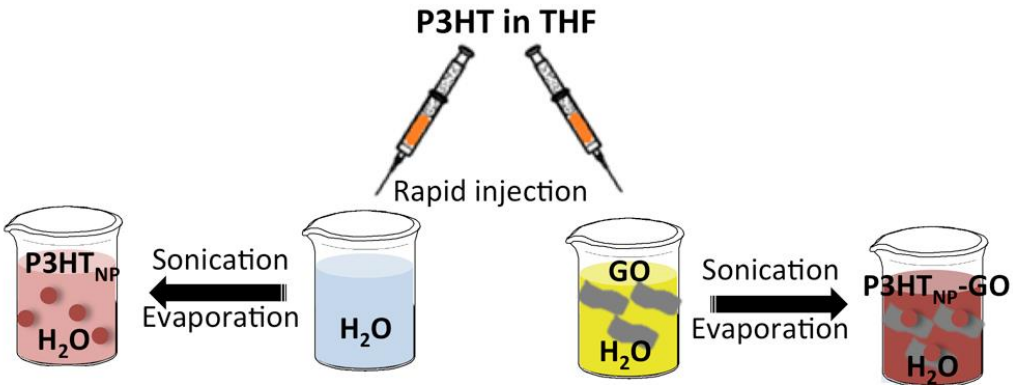

Figure 2.8. Self-assembly of P3HT$_{NPs}$ and P3HT$_{NPs}$-GO nanohybrids.

2.4. Results and Discussion

The formation of P3HT$_{NPs}$-GO hybrid nano-assemblies was accomplished by an in-situ re-precipitation method. Figure 2.9 shows the stable water dispersions of P3HT$_{NPs}$ and P3HT$_{NPs}$-GO nanohybrids. During the reprecipitation process, rapid diffusion of THF solution into the water leads to coiling-up of the polymer chains. By minimizing their surface energy they induce the formation of P3HT$_{NPs}$. Taking advantage of this process, as well as of the excellent water dispersibility of GO, a novel in-situ re-precipitation process was applied for the first time to develop novel P3HT$_{NPs}$-GO hybrid material.

Figure 2.9. Dispersions of P3HT$_{NPs}$ (1st flask left) and P3HT$_{NPs}$-GO (5th flask right). P3HT$_{NPs}$ were obtained by injection of P3HT dissolved in THF (flask in the middle) in water (2nd flaks from left). P3HT$_{NPs}$-GO were obtained by injection of P3HT dissolved in THF in aqueous dispersion of GO (4th flaks from left).

2.4.1. Morphological characterization

The morphology of the P3HT$_{NPs}$ and P3HT$_{NPs}$-GO hybrid nano-assemblies were studied by transmission electron microscopy (TEM) and atomic force microscopy (AFM). Firstly, AFM and TEM images (Figure 2.10) proved that nanoparticle fabrication (P3HT$_{NPs}$) via reprecipitation process was successfully accomplished. The images show spherical P3HT nanoparticles with sizes in the range of 50 to 200 nm.

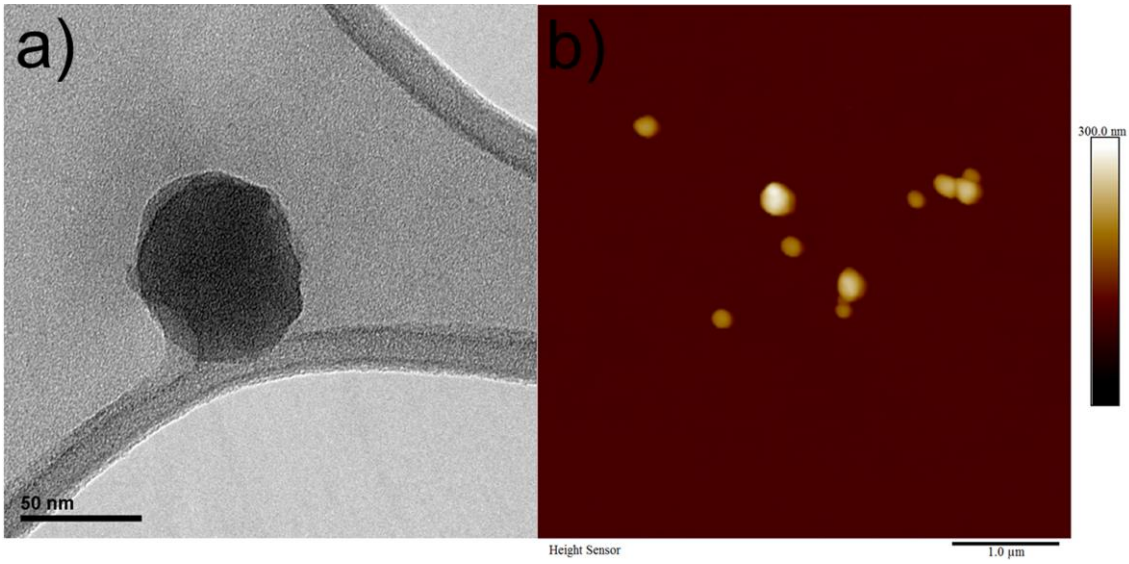

Figure 2.10. a) TEM images of spherical P3HT$_{NPs}$ and b) AFM images of spherical P3HT$_{NPs}$

Moreover, size distribution of P3HT$_{NPs}$ nanoparticles obtained from analysis of AFM topography images shows that more than 90% of the 63 analyzed P3HT$_{NPs}$ nanoparticles have a particle size between 50 and 200 nm. (Figure 2.11)

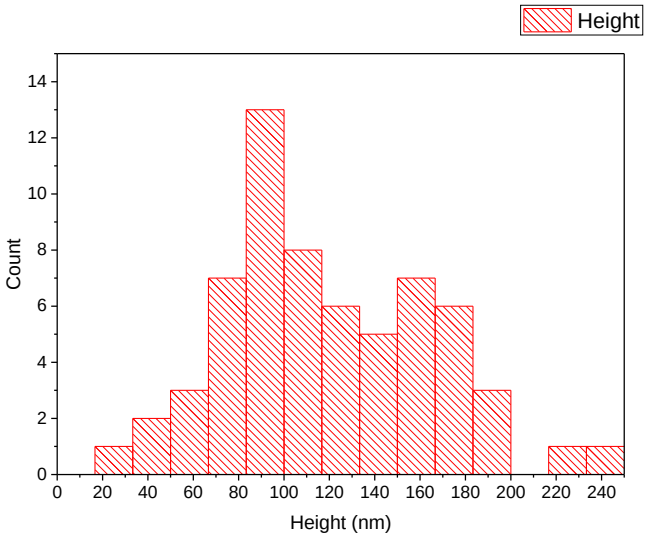

Figure 2.11. Size distribution of P3HT$_{NPs}$.

Next, the morphological characterization of P3HT$_{NPs}$-GO hybrid nano-assemblies were also studied by TEM and AFM. Figure 2.12 shows that P3HT$_{NPs}$ are equally formed in the aqueous GO dispersions. The TEM image shows that P3HT$_{NPs}$ and GO are in close contact and P3HT$_{NPs}$ is always seen on the wrinkled sheets of GO, indicating the formation of P3HT$_{NPs}$-GO hybrid material. Also, AFM studies suggest a deposition of the forming P3HT$_{NPs}$ onto the micrometer sized GO sheets. However, agglomeration of P3HT$_{NPs}$ on the GO sheet can be recognized through the AFM images and this might correlate with the established $\pi-\pi$ interface interaction between the aromatic structure of P3HT$_{NPs}$ and sp^2 domains of GO.

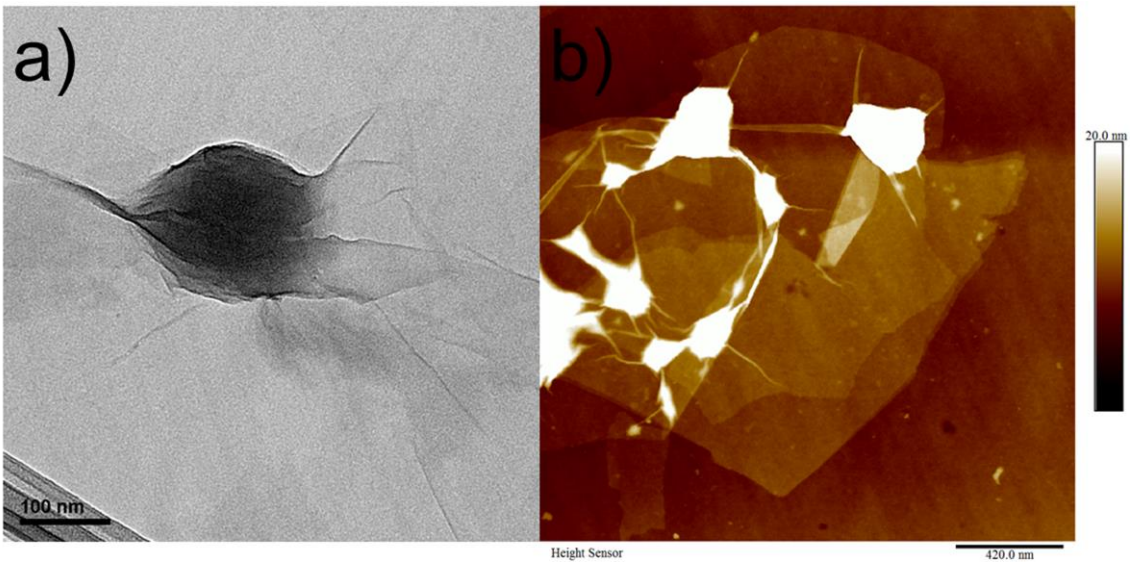

Figure 2.12. Morphology of and P3HT$_{NPs}$-GO samples. TEM and AFM images of P3HT$_{NPs}$-GO (a, b) (at lowest GO concentration C3).

Moreover, AFM characterization has been done on a larger scale (4µm) in order to obtain information on P3HT$_{NPs}$ distribution on GO sheets. In figure 2.13, the AFM topography image shows that most of the P3HT$_{NPs}$ nanoparticles are uniformly deposited on GO sheets. Enlarged zone A and B topography images also shows that the GO wrinkles are induced by P3HT$_{NPs}$ deposition

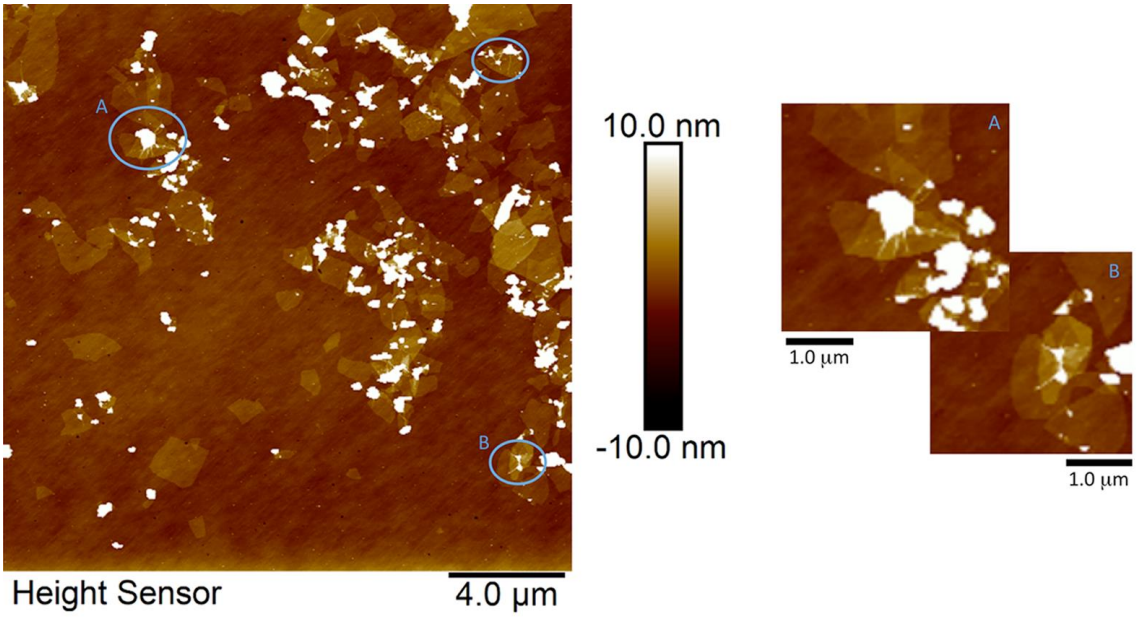

Figure 2.13. (Left) AFM topography image of P3HT$_{NPs}$-GO (at lowest GO concentration C3. (Right) Enlarged zones A and B.

2.4.2. Optical properties of P3HT$_{NPs}$ and P3HT$_{NPs}$-GO hybrids

Firstly, UV-Vis absorption spectroscopy was used to monitor the changes in P3HT$_{NPs}$ after the nanoparticle formation. The spectrum of P3HT$_{NPs}$ in water is compared with P3HT solution in THF (P3HT$_{THF}$) in order to see the effect of morphological changes on absorption features (Figure 2.14). P3HT$_{THF}$ shows a broad band absorption, in the range from 300 to 550 nm which is correspond to π–π* transition absorption. This broad band absorption is due to the purely amorphous, non-aggregated polymer structure. In case of P3HT$_{NPs}$ water dispersion the π–π* transition absorption maxima red shifted around 100nm. Additionally, three new peaks are observed around 515nm, 551nm and 601 nm. Three vibronic A$_{0-n}$ peaks (n=1, 2, 3, whereby refers to the number of vibrational quanta coupled to the electronic transition) are identified at the low energy side of the π–π* transition band, where A$_{0-0}$ corresponds to the lowest energy transition. These vibronic peaks indicated the presence of crystalline P3HT aggregates within the polymer nanoparticles, induced by the insolubility of P3HT in water.

The distinct difference between amorphous absorption band and one with vibronic transition of P3HT absorption provides valuable structural information about the polymer nanoparticle.

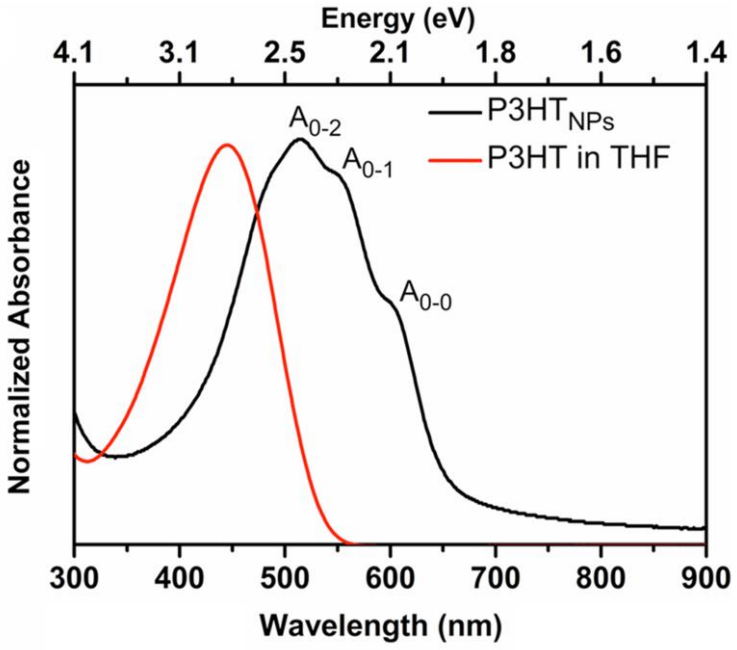

Figure 2.14. Absorption spectrum of P3HT in THF and P3HT$_{NPs}$ in aqueous solution.

Using the A$_{0-0}$/A$_{0-1}$ intensity ratios offers an easy approach to estimate the interchain excitonic coupling (explained in Chapter1 in details), which is governed largely by intrachain order according to the model introduced by Spano.[22-24]

Exploiting the equation 1, the A_{0-0}/A_{0-1} intensity ratios and J_0 exciton coupling constants of $P3HT_{NPs}$ reveal an A_{0-0}/A_{0-1} ratio of 0.72.

Equation 1: $$\frac{A_{0-0}}{A_{0-1}} = \frac{(1-0.96Jo/Ep)^2}{(1+0.292Jo/Ep)^2}$$

Being lower than 1, this value indicates the presence of weakly coupled H-aggregates with a corresponding J_0 exciton coupling constant of +22 meV. (Using a value of 0.18eV for *Ep* [22-24])

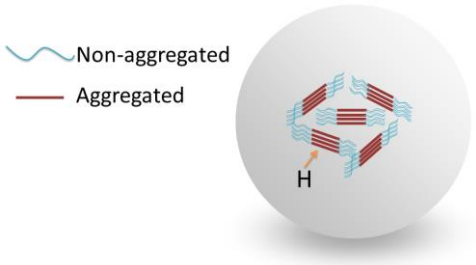

Figure 2.15. Schematic illustration of aggregated (red lines) and non-aggregated (blues wavy lines) domains within P3HT$_{NPs}$.

In the case of $P3HT_{NPs}$-GO hybrids nano-assemblies, UV-vis absorbance spectrum shows an important enhancement of the A_{0-0}/A_{0-1} intensity ratio in the dispersed state. The A_{0-0}/A_{0-1} intensity ratio values close to 1 and resulting in coupling constants as low as 2 meV. (Figure 2.16a) While this still is lower than 1 and indicates the presence of weakly coupled H-aggregates, GO clearly induces the formation of highly planar P3HT chains in the $P3HT_{NPs}$. The changes on intensities of A_{0-0}-A_{0-1} peaks were also followed by a redshift of the vibronic peaks by about 30 meV. (Figure 2.16a)

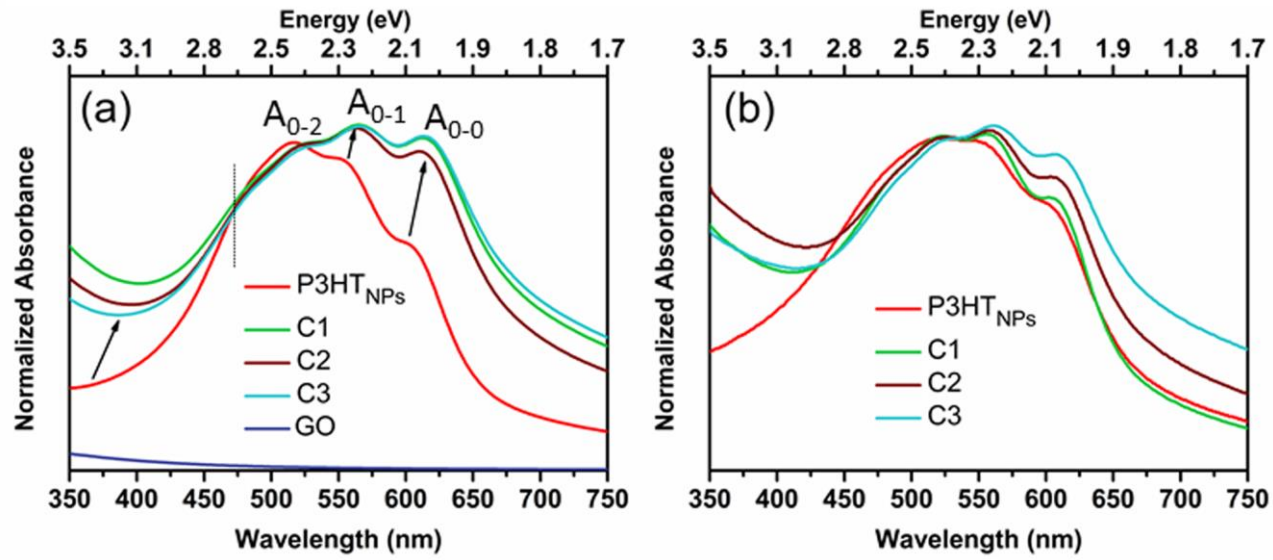

Figure 2.16. Absorption spectra of P3HT$_{NPs}$ and P3HT$_{NPs}$-GO samples (labeled Cn, where increasing n denotes decreasing GO concentration) taken from (a) aqueous dispersions and (b) thin films. The spectra are normalized to the intensity of the A0-2 vibronic peak. featur eless spectrum of an aqueous dispersion of GO is included in (a).

The remarkable changes on the vibronic peaks intensities are already achieved at the lowest amount of GO (C3) and it suggest that GO induces the formation of highly planar P3HT H/J like aggregates (H-aggregates with reduced interchain coupling, also called H/J aggregates) within the P3HT$_{NPs}$ (Figure 2.17). The role of GO can be attributed to a "good" solvent additive for the conjugated polymer during the formation of P3HT$_{NPs}$, as indicated in the work of Barnes and Venkataraman[25], who pointed out that the use of "marginal" and "good" solvent mixtures in the self-assembly process increase the A_{0-0}/A_{0-1} ratio in pure P3HT$_{NPs}$. On the other hand, GO sheets also can act as two- dimensional surfactant templates and induce a higher planarity of the internal P3HT chains. This lowers the surface tension at the interface of the P3HT$_{NPs}$ and the GO sheets and contributes to stabilize the P3HT$_{NPs}$-GO hybrid structure.

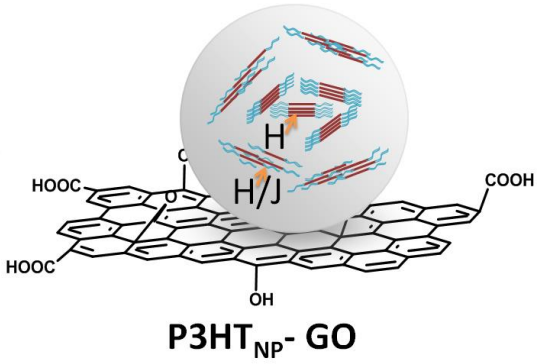

Figure 2.17. Schematic illustration of GO effect on the aggregated domains within P3HT$_{NPs}$ (red lines) and non-aggregated (blues wavy lines) domains within P3HT$_{NPs}$.

On the contrary, in can be seen from figure 2.19 that the already formed aggregation structure of P3HT$_{NPs}$ cannot be modified upon subsequent mixing with a water dispersion of GO (ex-situ mixing illustrated in figure 2.18). This clearly proves that GO has strong impact on the aggregation structure during the rapid liquid phase re-precipitation process.

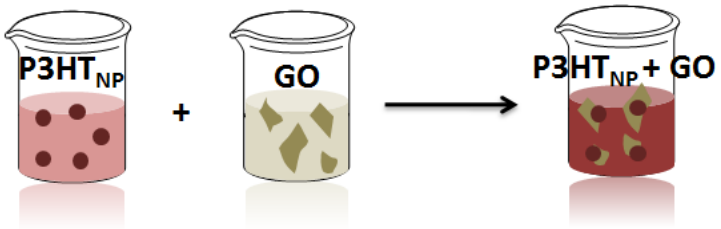

Figure 2.18. Schematic illustration of ex-situ mixing process.

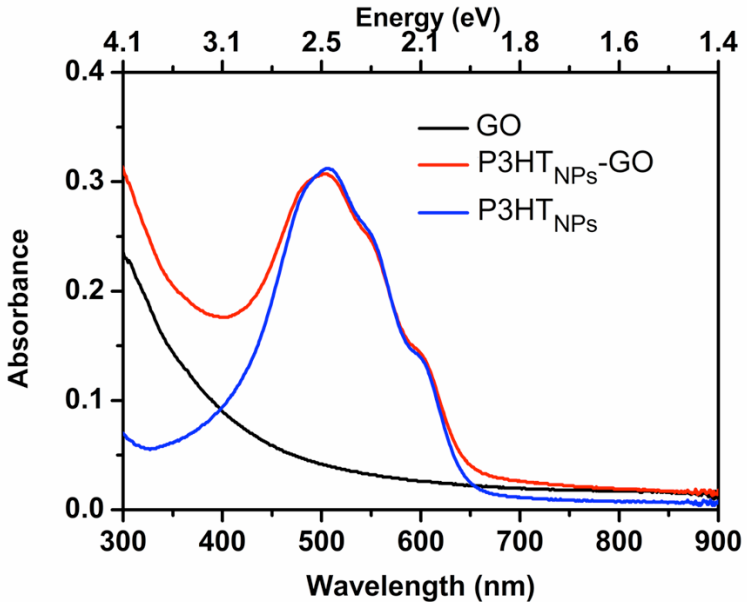

Figure 2.19. Comparison of UV-Vis spectra for GO, P3HT$_{NPs}$, and P3HT$_{NPs}$-GO obtain upon ex-situ mixing of P3HT$_{NPs}$ and GO.

Moreover, looking at the high-energy side of the absorption spectrum P3HT$_{NPs}$-GO samples, which is attributed to disordered P3HT chains in the P3HT$_{NPs}$, a redshift of the minima by about 0.4 to 0.5 eV was observed. Also, the vibronic peaks and the π–π* transition absorption maxima shifted to lower energy, (shifts are summarized in figure 2.20b and 2.20c). This suggests the existence of favorable interface interactions between the GO sheets and P3HT$_{NPs}$. The existence of an isosbestic point in figure 2.16a at about 475 nm (2.61 eV) nicely illustrates the convergence of both effects, increasing the intensity of vibronic peaks and shifted absorption peaks.

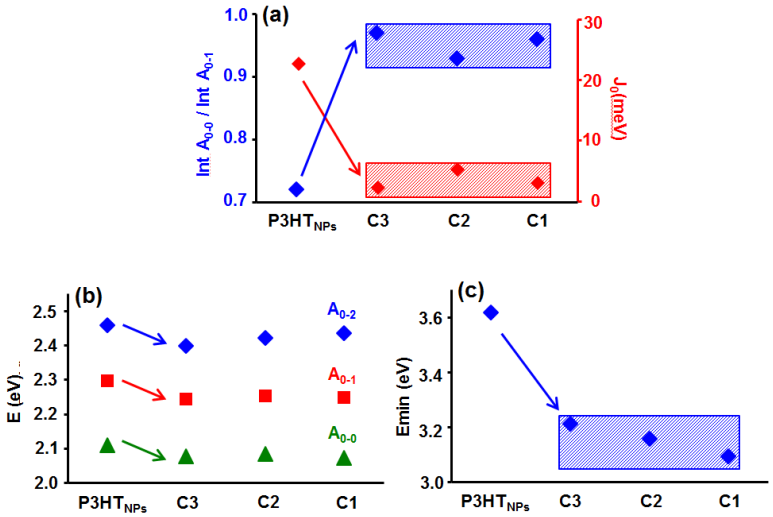

Figure 2.20. Intensity ratio of vibronic A_{0-0} to A_{0-1} transitions (blue) and excitonic coupling constant J_0 (red). (a) Energy position of the A_{0-2}, A_{0-1}, A_{0-0} vibronic transitions. (b) Energy position of the minima at the high-energy side of the π-π* band.(c)

The thin film absorption features of the P3HT$_{NPs}$ and P3HT$_{NPs}$-GO were investigated as well. The thin film absorption spectrum essentially maintains the features acquired in the dispersion state. (Figure 2.16b) This refers to the presence of the vibronic structure, the enhancement of the A_{0-0} to A_{0-1} intensity ratio and the redshift of the high energy peaks in the nanohybrids preserve in thin films, while the respective values may somewhat differ from the case of dispersions. This also shows that solvent evaporation effects do not play a significant role during the thin film formation.

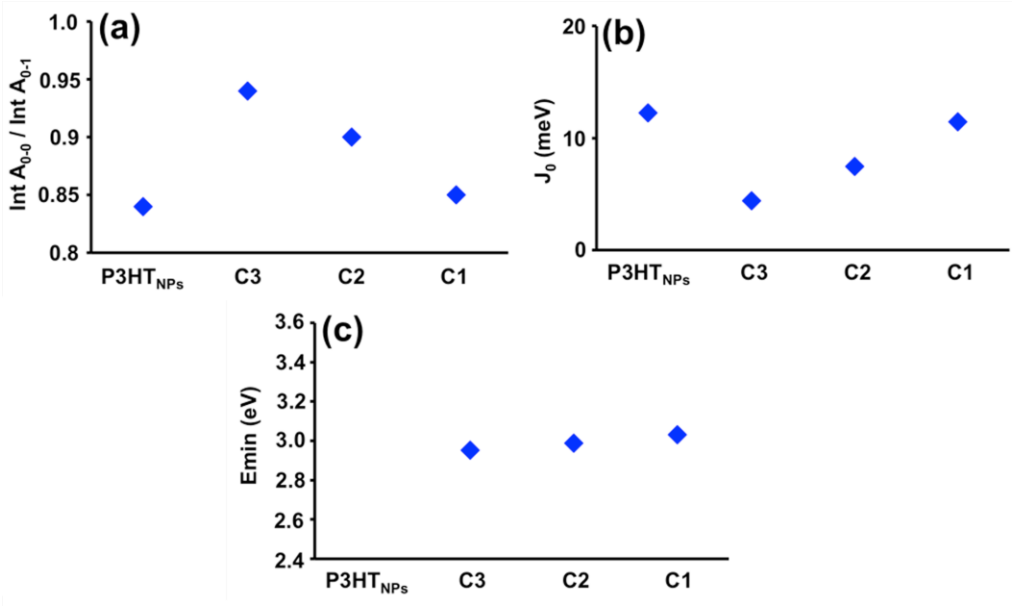

Figure 2.21.Values derived from the UV-Vis absorption spectrum of thin films of P3HT$_{NPs}$ and P3HT$_{NPs}$- GO (Cn, n = 3, 2, 1, from lowest to highest GO concentration, respectively). (a) Intensity ratio of the vibronic A0-0 to A0-1 transitions, (b) exciton coupling constant J_0 calculated from the A_{0-0} to A_{0-1} intensity ratios according to eq. (1), and (c) position of the minima at the high energy side of π-π* band.

Next, valuable complementary information on aggregation and interaction effects is obtained from steady-state photoluminescence studies. The spectra of P3HT$_{NPs}$ and the P3HT$_{NPs}$-GO series exhibit a broad emission ranging from 600 to 800 nm, both in dispersion and solid state. This is composed of two well defined vibronic bands located at about 650 nm (1.90 eV) and 710 nm (1.75 eV) with an intensity ratio of about 1.35, accompanied by a not well defined third band at about 800 nm (1.55 eV) of very low intensity (Figure 2.22). These well-defined peaks originate from aggregates as the only emitting species for P3HT. [26-29]

As we seen from the absorption spectra, P3HT$_{NPs}$ and P3HT$_{NPs}$-GO clearly exhibit the presence of H-aggregates in P3HT$_{NPs}$, which are the origin of the photoluminescence spectra. Additionally, existence of the disordered (amorphous) P3HT chain in P3HT$_{NPs}$ can be identified by the broadness of the vibronic transitions.[26, 27, 29]

Looking at the photoluminescence spectra in dispersion, it can be clearly seen that P3HT$_{NPs}$-GO samples essentially show the same features as the bare P3HT$_{NPs}$, except with negligible changes in the positions of the vibronic peaks (Figure 2.22e). However, a remarkable increase of the emission intensity of up to 50 % with respect to the corresponding P3HT$_{NPs}$ is observed and the enhancement is proportional with the decreasing amount of GO in P3HT$_{NPs}$-GO. (Figure 2.22a and 2.22c).

This uncommon feature actually correlates with the results obtained from absorption spectroscopy. Here an important enhancement of H-aggregates (i.e. H-aggregates with reduced interchain coupling, also called H/J aggregates) is seen already for the lowest GO concentration. At the lowest concentrations it facilitates the enhanced formation of H aggregates, which, towards the periphery of the nanoparticles, adopt a more H/J-like character. Thus, a larger overall volume of H-aggregates is available in the nanoparticles contributing to the enhancement of the photoluminescence. At higher GO concentrations the emission intensity is reduced, but still remaining higher compared to the bare P3HT$_{NPs}$. The lowering in intensity is explained by a decreased GO solvent effect, i.e. a less effective formation of H aggregates and/or by a reduced dispersibility upon the increase of GO in the aqueous dispersion.

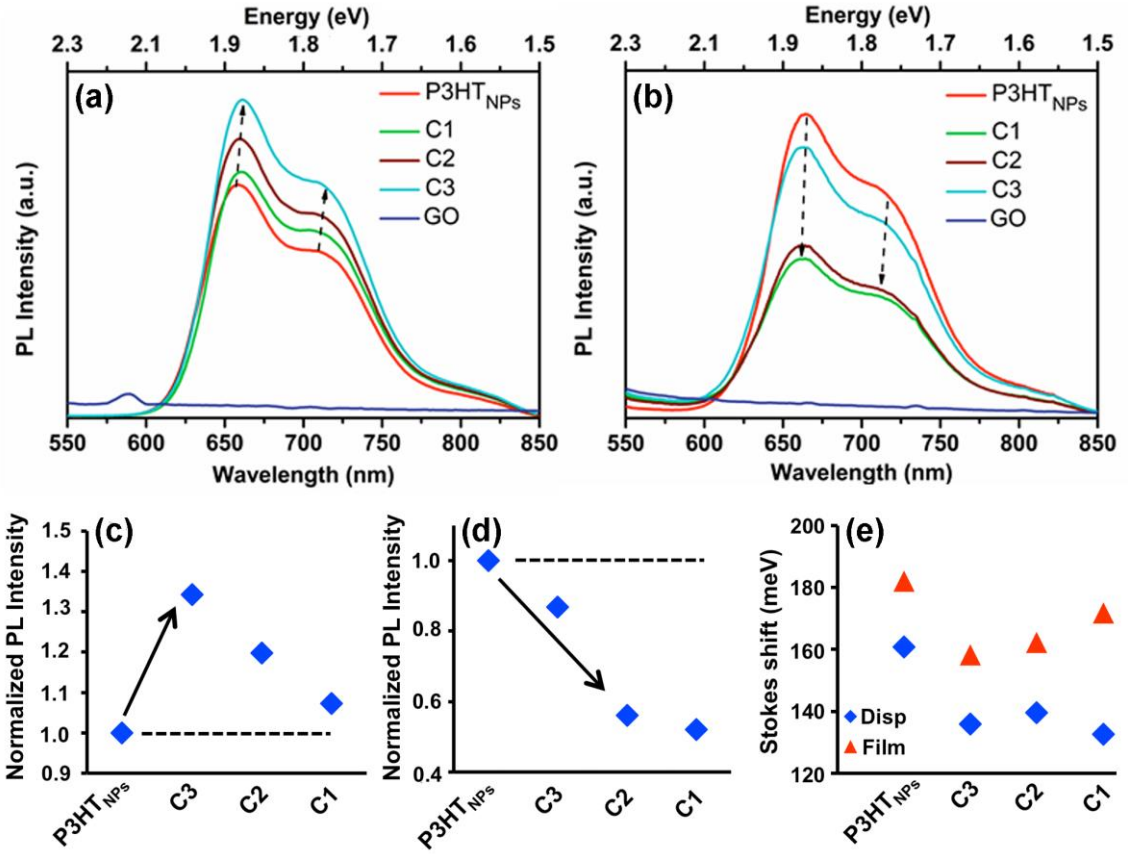

Figure 2.22. Photoluminescence emission spectra (λexc = 490 nm) of GO, P3HT$_{NPs}$ and P3HT$_{NPs}$-GO samples (labeled Cn, n=3, 2, 1, from lowest to highest GO concentration, respectively) for aqueous dispersions (a) and thin films (b). Normalized integrated photoluminescence intensities for dispersions (c) and thin films (d). Stokes shifts (e) as determined from the energy differences of the position of the high energy photoluminescence band maximum and the position of the low energy A$_{0-0}$ vibronic transition.

A completely opposite situation is observed for the case of the corresponding thin films where significant quenching by up to 50 % is observed in terms of P3HT$_{NPs}$ –GO thin films with

increased amounts of GO. (Figure 2.22b and 2.22d). While in dispersion the emission intensity enhancement arises by the enhanced H-character of the $P3HT_{NPs}$ due to the performance of GO as a "good" solvent, in thin films the emission behavior is dominated by the intimate contact between GO sheets and $P3HT_{NPs}$ due to (non-isotropic) deposition process. The interface established between GO and $P3HT_{NPs}$ due to π-π stacking, results in the formation of photo-induced charge-transfer complex which can be characterized by the quenching of the fluorescence emission of $P3HT_{NPs}$ in thin films. Additionally, the shifts in the absorption spectra also reflect the photo-induced charge-transfer properties between $P3HT_{NPs}$ and GO.

Raman measurements were also carried out for the film of $P3HT_{NPs}$, $P3HT_{NPs}$-GO and GO (on Si/SiO_2 substrate) using an excitation wavelength of 785 nm to investigate further the interaction between the GO and $P3HT_{NPs}$ (Figure 2.23a). In the range from 1000 to 1750 cm^{-1}, $P3HT_{NPs}$ exhibit two dominant sharp peaks at around 1445 cm^{-1} and 1380 cm^{-1}, assigned to the symmetric C=C (C_α=C_β) and C–C (C_β–C_β) ring stretch modes of the thiophene ring, respectively.[30]

On the other hand, GO shows two broad bands at 1598 cm^{-1} and 1318 cm^{-1}, corresponding to the G-band (tangential C-C stretch modes of graphene sheets) and the D-band (related to defects, i.e. the presence of sp^3 hybridized carbon in the oxidized graphene sheets), respectively.[21]

The $P3HT_{NPs}$-GO samples are characterized by the broad G and D band of GO since the $P3HT_{NPs}$ peaks are in superposition with the GO. The GO related bands (G and D) are clearly visible in the $P3HT_{NPs}$-GO nanohybrids already at the lowest GO concentration and they are comparable with the bare GO. From the Raman spectra, it can be clearly seen a shift of about 10 cm^{-1} for the G band of the GO, (Figure 2.23a and 2.23b), to lower wavenumbers already for the lowest content of GO. This shift suggests electron injection from P3HT chains to GO, as also reported for reduced graphene oxide or carbon nanotubes.[31, 32] Thus, the Raman results further support that charge-transfer is taking place at the interface between $P3HT_{NPs}$ and GO, which act as electron donor and acceptor, respectively. Furthermore, the intensity ratio of the C=C to C–C ring stretch modes (Figure 2.23c), analyzed from background subtracted spectra, reveals a clear decrease with increasing GO concentration. This is consistent with an enhanced quinoid character, as consequence of an effective charge-transfer.

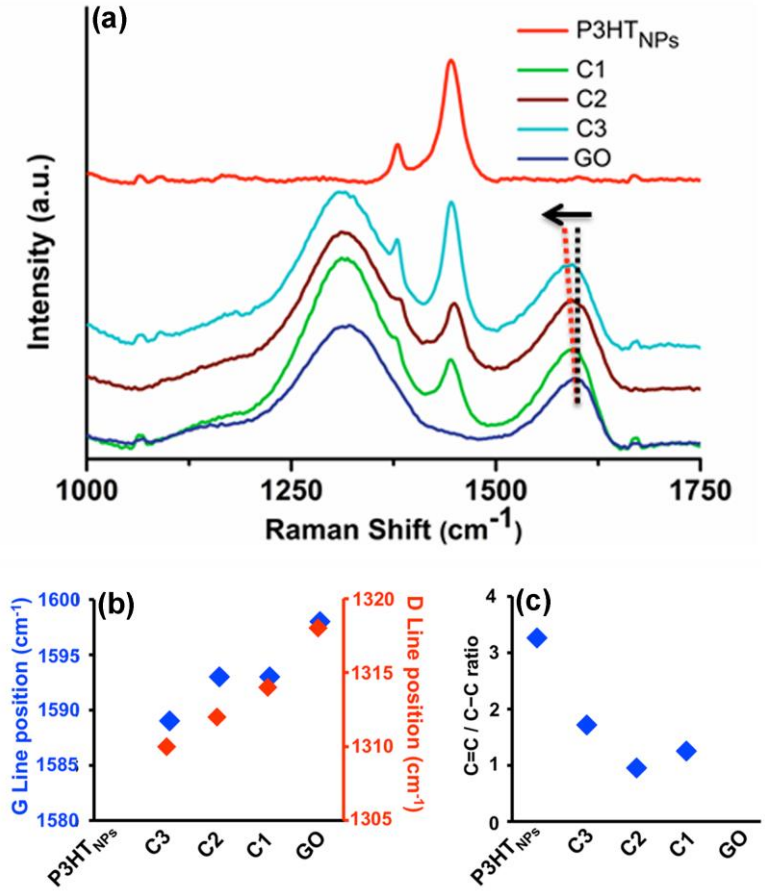

Figure 2.23. (a) Raman spectra (λexc = 785 nm) of films of P3HT$_{NPs}$ and P3HT$_{NPs}$-GO hybrid (labeled Cn, n=3, 2, 1, from lowest to highest GO concentration, respectively), (b)Position of G and D line, (c) Intensity ratio of P3HT C=C/C–C ring stretch mode.

2.4.3. XPS and FTIR characterization

XPS analysis was also performed in order to further investigate the interaction between the two materials. The XPS S2p core shell spectra of P3HT$_{NPs}$ and P3HT$_{NPs}$-GO were also carried out from their spray coated thin films on FTO and the spectra are shown in figure 2.24. The S2p region can be de-convoluted into four peaks. A S2p$_{3/2}$ and S2p$_{1/2}$ doublet centered at 164.0 and 165.3 eV, which corresponds to the sulfur atom in the heterocyclic ring (C-S-C) of P3HT. A broad band centered around 170 eV is associated to the existence of partially positively charged sulfur ($S^{\delta+}$) atoms and can be de-convoluted into two components. While the presence of positively charged sulfur atoms in P3HT$_{NPs}$ may be related to charge transfer to the FTO substrate.[33,34] However, its enhanced intensity in the P3HT$_{NPs}$-GO most likely is related to charge transfer from P3HT to GO, leaving behind a positively charged S atom which, in turn, enabled interaction with oxygen groups of the GO sheet, as further suggested by FTIR results (Figure 2.25). Results of the de-convolution of the spectra are summarized in

table 3 while the overall elemental composition is listed in table 4. The XPS C1s core shell spectrum of GO is shown in figure 2.7. In section "characterization of GO"

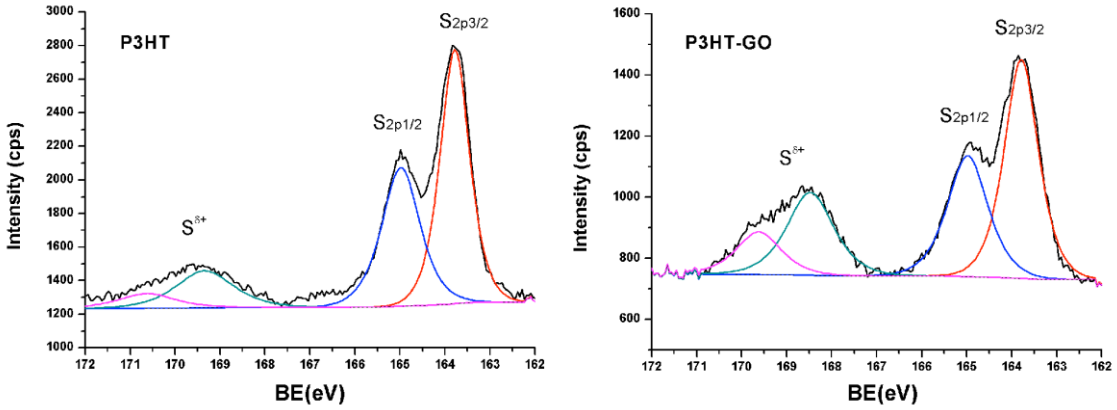

Figure 2.24. XPS S2p core shell spectra of films of P3HT$_{NPs}$ (left) and P3HT$_{NPs}$-GO (C3) (right) and best fits of de-convolution into components.

Table 2.3. De-convolution of XPS S2p spectra of P3HT$_{NPs}$ and P3HT$_{NPs}$-GO: Peak positions and contribution to overall spectra.

S2p	S2P$_{3/2}$	S2P$_{1/2}$	S1$^{\delta+}$	S2$^{\delta+}$	S1$^{\delta+}$+ S2$^{\delta+}$
Binding Energy (eV)	164.0	165.3	169.6	170.9	---
P3HT$_{NPs}$(at %)	47.36	33.79	13.5*	5.36*	18.86
P3HT$_{NPs}$-GO (at %)	41.25	26.98	21.24*	10.53*	31.77

Table 2.4. Elemental composition of P3HT$_{NPs}$ and P3HT$_{NPs}$-GO as calculated from survey specta

Elemental Composition	C (at %)	O (at %)	N (at %)	S (at %)	C/O	C/S
P3HT$_{NPs}$	77.51	16.71	0	5.79	4.64	13.39
P3HT$_{NPs}$-GO	75.76	24.42	0	2.82	3.10	26.87

In summary, XPS studies reveal the presence of positively charged sulfur atoms in the P3HT chains of the P3HT$_{NPs}$-GO as a result of the charge transfer process via the established π-π interface interactions.

Moreover, the FTIR spectroscopy measurement was carried out for P3HT$_{NPs}$- P3HT$_{NPs}$-GO and bare GO samples to elucidate the sulfur-oxygen group interaction which appeared on XPS results. (Figure 2.25)

GO exhibits a broad band centered at 3423 cm^{-1}, comprising the O–H stretch modes related to C–OH and COOH functional groups located on the GO sheets. The peak at 1730 cm^{-1} is assigned to the C=O stretching of carboxylic groups and the peak at 1625 cm^{-1} is related to sp^2-hybridized C=C groups (asymmetric vibrational stretching mode). The two peaks at about 1217 cm^{-1} and 1051 cm^{-1} correspond to C–O stretching vibrations and the peak at 830 cm^{-1} to C-O-C bending mode.[19]

On the other hand, P3HT reveals three important IR absorption regions associated to vibrational modes of the P3HT thiophene rings (1450 - 1510 cm^{-1}, and 820 cm^{-1}) and alkyl side chains (2800 to 3000 cm^{-1}). At 1459 cm^{-1} and 1512 cm^{-1} the C=C stretch vibrations of the thiophene rings appear (symmetric and antisymmetric, respectively). The band at 821 cm^{-1} corresponds to the out-of skeleton C-H bending mode on the thiophene ring. The band located between 2855 and 2920 cm^{-1} is caused by the CH_2 stretching modes (symmetric and antisymmetric, respectively) belonging to the alkyl side-chains. The band at 2959 cm^{-1} corresponds to the antisymmetric CH_3 stretching modes.[35]

In the case of P3HT$_{NPs}$-GO a new pronounced vibrational band appears in the region of the C–O stretching modes of GO appears at 1140 cm^{-1}. Its relative intensity increases with the amount of GO. This unique fingerprint, only observable in the P3HT$_{NPs}$-GO samples indicates that the interaction between P3HT$_{NPs}$ and GO may involve the interaction between oxygen atoms from C-O related groups on the GO sheet and the positively charged sulfur atoms of P3HT chains, as we discussed on XPS S2p spectra, as consequence of the charge transfer from P3HT$_{NPs}$ to GO vía effective π-π interface interactions.

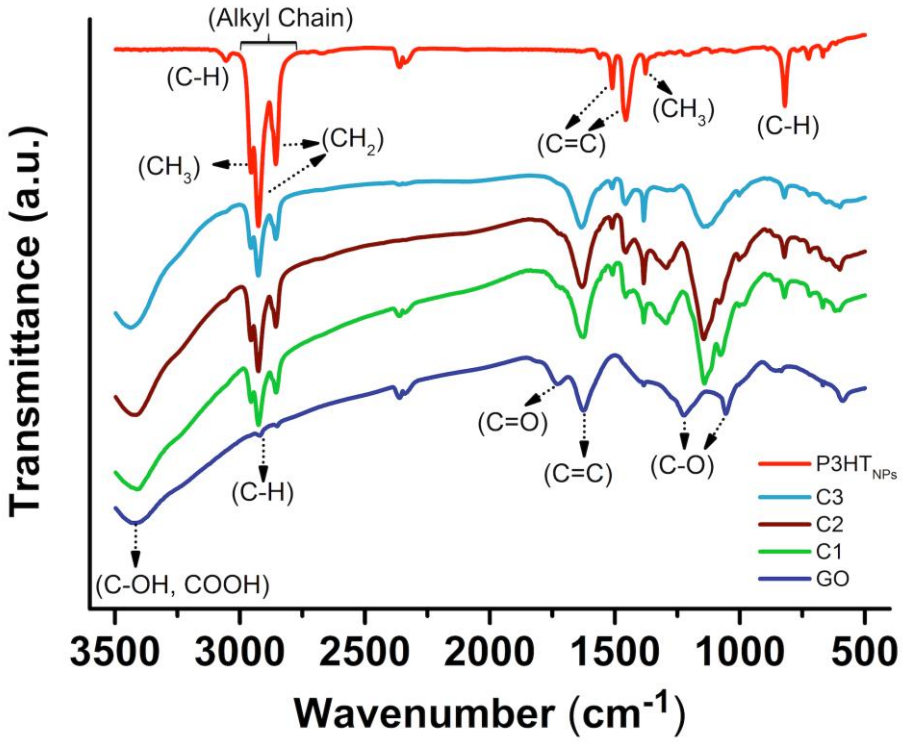

Figure 2.25. FTIR spectra of GO, P3HT$_{NPs}$, P3HT$_{NPs}$-GO (labeled Cn, n = 3, 2, 1, from lowest to highest GO concentrations, respectively).

2.4.4. Electrochemical characterization of P3HT$_{NPs}$ and P3HT$_{NPs}$-GO hybrids

Next, in order to focus on the electrochemical properties and the HOMO and LUMO energy levels of the materials, cyclic voltammetry (CV) studies are performed. Besides, CV studies also further provided valuable complementary information on the properties of aggregation and charge-transfer.

First, for the case of hybrids, reproducible CV curves revealing only P3HT related features were acquired after applying 10 continuous pre-cycles in the range of -1.5 to 1.2 V. Because, GO gets effectively reduced in the potential range from - 0.4 to -2.0 V.

For this, the CV curves of the P3HT$_{NPs}$-GO samples obtained after applying 10 continuous pre-cycles in the range of -1.5 to 1.2 V.

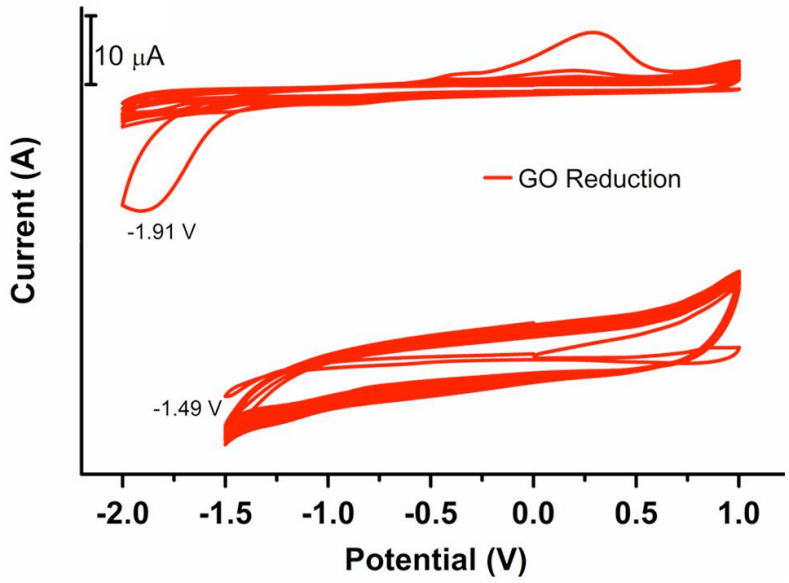

Figure 2.26. Electrochemical reduction of graphene oxide after 10 pre-cycle.

Figure 2.26 shows the reduction of GO in two different potential range. In the potential range between -1.5 to 1.0 V GO does not show a sharp reduction peak which means reduction of GO is not efficiently completed and GO does not exhibit reversible CV curves. On the other hand, if the potential window is set to a wider range like -2.0 to 1.0 V, the sharp reduction peak in the first cycle are observed clearly at -1.9 V. The continuous cycles exhibit reversible stable CV curves as well.

Then the P3HT$_{NPs}$-GO nanohybrids were also reduced by applying 10 continuous pre-cycles in the range of -1.5 to 1.2 V. The case for C3 is represented in figure 2.27a as example. In case of hybrid material, we observed that the reduction of GO takes place at more positive potentials in the hybrids compared to GO alone. (Figure 2.27b) It shows the reduction peak value at -1.35 V for C3 while it is -1.90 V for GO. This is an important indication of strong charge transfer, whereby P3HT acts as electron donor in case of P3HT$_{NPs}$-GO nanohybrid materials.

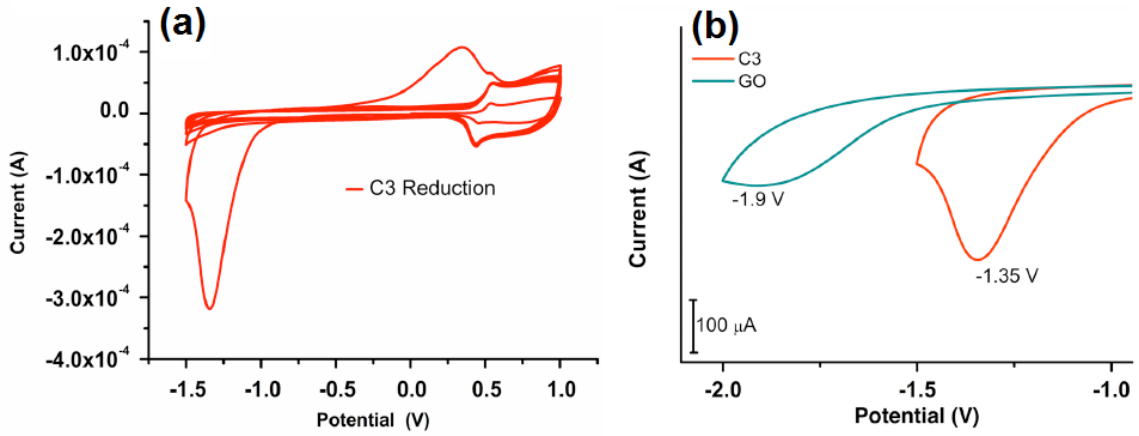

Figure 2.27. (a) Electrochemical reduction of P3HT$_{NPs}$-GO at lowest GO concentration (C3). (b) Comparison of the first electrochemical reduction cycle of GO and P3HT$_{NPs}$-GO (C3).

Once we obtained the reversible stable CV curves for GO and P3HT$_{NPs}$-GO hybrids, the electrochemical features were analyzed for all the samples. (Figure 2.28) The CV response of P3HT$_{NPs}$ is characterized by two oxidation peaks located at about 0.55 and 0.85 V. The lower one is attributed to the presence of aggregated P3HT chains and the higher one to amorphous or a mixture of amorphous and aggregated P3HT chains.[36]

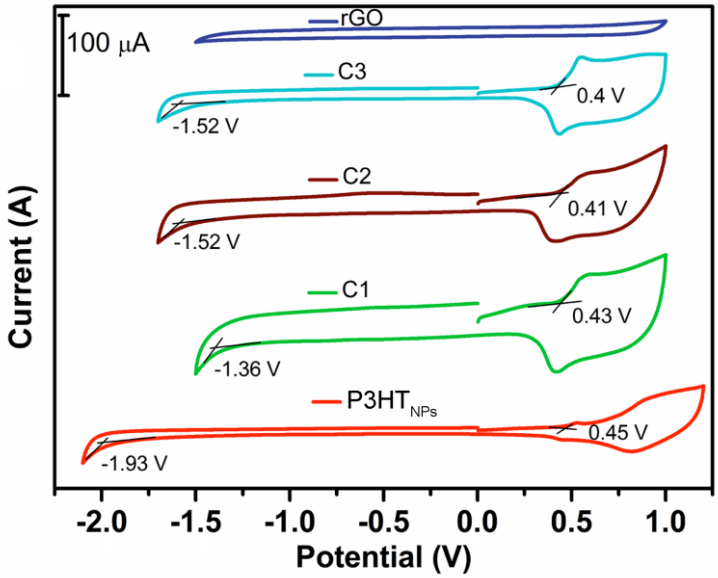

Figure 2.28. Cyclic voltammograms of films of P3HT$_{NPs}$, GO and P3HT$_{NPs}$-GO samples (labeled Cn, n=3, 2, 1 from lowest to highest GO concentration, respectively). Potential values are given with respect to Ag/AgCl used as reference electrode. Values of on-set oxidation and reduction positions are indicated.

The onset-value of the oxidation and reduction peaks (indicated in Figure 2.28), determined as the crossing point of the slopes of the peaks with the background current, are used to calculate the HOMO and LUMO energy levels of P3HT and the corresponding energy gap. The HOMO, LUMO and electrochemical bandgap values are summarized in table 5.

Table 2.5. Energy values for HOMO and LUMO levels and derived energy bandgaps, determined from the on-set values of the oxidation and the reduction peaks, for P3HT$_{NPs}$ and P3HT$_{NPs}$-GO samples (labelled Cn, n=3, 2, 1 from lowest to highest GO concentration).

Sample	E_{HOMO} [eV][a]	E_{LUMO} [eV][a]	E_{gap} [eV][b]
P3HT$_{NPs}$	-5.05	-2.67	2.38
C3	-5.00	-3.08	1.92
C2	-5.01	-3.08	1.93
C1	-5.03	-3.24	1.79

[a] ((E_{HOMO} =-(E_{onset} (ox) + 4.6) [eV])[37] (E_{LUMO} = -(E_{onset} (red) + 4.6) [eV][37]

[b] ((E_{gap} = E_{LUMO}-EH_{OMO}))

For the P3HT$_{NPs}$-GO samples a significant enhancement of the low oxidation peak with respect to the high oxidation peak indicates a significant increase of aggregated P3HT chains. This can be clearly seen already for the lowest concentration of GO. An accompanying downshift of the oxidation on-set potential (HOMO level) by about 50 meV further underlines the enhancement of aggregated P3HT domains with respect to the original P3HT$_{NPs}$. This situation fully coincides with the observation in absorption spectroscopy where intensity changes and redshifts of the vibronic modes by several tens of meV confirm the presence of enhanced amounts of H/J aggregates in the P3HT$_{NPs}$ of the P3HT$_{NPs}$-GO nanohybrids.

Looking at the reduction on-set potentials (LUMO levels) considerable shifts of 400 to 500 meV towards more positive potentials for the lowest GO concentration are observed, progressing by several tens of meV for higher GO concentrations. This fully coincides with the redshifts of the minima in the low-energy shoulder in absorption spectroscopy, which are attributed to the π-π interface interactions of GO sheets with the disordered P3HT chains located at the surface of the P3HT$_{NPs}$. Effective interface interactions (discernable by lower absolute values of the on-set reduction potential), which are the origin of charge-transfer processes as witnessed by photoluminescence and Raman spectroscopy, coupled to the enhancement of H/J domains (notable by lower absolute values of the on-set oxidation potential), lead to an important decrease of the HOMO-LUMO energy gap in P3HT$_{NPs}$-GO nanohybrids with respect to the original P3HT$_{NPs}$. This further is accompanied by an enhancement of the overall current response with increasing GO concentration. These

observations consistently suggest the formation of stabilized P3HT$_{NPs}$-GO charge-transfer complexes with reduced excitonic coupling, achieved during the synthesis in the liquid state and maintained in the solid state.

2.4.5. Photoelectrochemical characterization of P3HT$_{NPs}$ and P3HT$_{NPs}$-GO hybrids

Photoelectrochemistry is the study of electrochemistry at the semiconductor/electrolyte interface under illumination of visible and UV light. Since semiconductor (active layer) materials have energy band gaps, they are able to generate a pair of electron and hole for each absorbed photon if the energy of the photon is higher than the band gap energy of the semiconductor.

The electron-hole pair formation occurs at the interface between the semiconductor and a solution upon absorption of light leads to oxidation or reduction reactions of solution species.[38] When a semiconductor comes into contact with a solution (redox species), in order to maintain the electrostatic equilibrium a charge transfer process that occur between the semiconductor and a solution phase, if formal redox potential of redox species (solution) lies inside semiconductor band gap. The main reason to use the electrical potential also in this photocatalytic system is reduce the number of recombination processes between the electrons and the holes. Since, in photocatalysis, the electron-hole pair suffers from fast recombination processes. In this case photoelectrochemistry, allows an increase in the yield of light's conversion into chemical energy.

Since the promising properties of P3HT$_{NPs}$-GO nanohybrids in dispersion preserved in thin films, the photoelectrochemical features were carried out on samples which spray-coated on FTO substrates covering an area of 1 cm^2 in order to obtain important insights on the thin film device performance. The samples placed in the three-electrode electrochemical cell as working electrode, they were illuminated through a quartz window by a 150 W Xenon arc lamp. A scheme explaining the working mechanism is illustrated in figure 2.29.

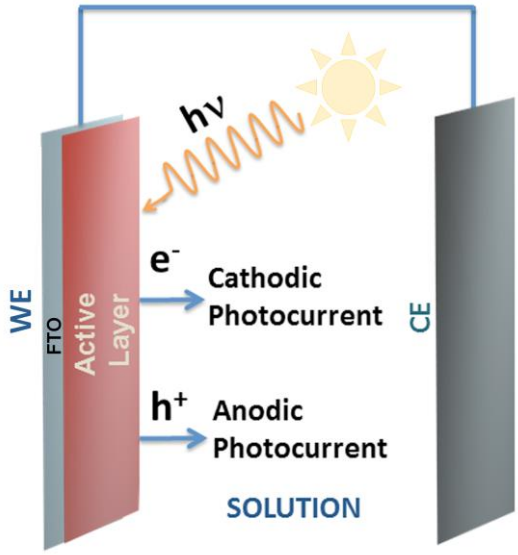

Figure 2.29. Photoelectrochemical cell composed of a photoactive thin film layer (red layer) spray-coated on FTO (grey layer) operating as working electrode (WE) and electrically connected to a counter-electrode (CE). The electrodes are immersed in an electrolyte solution.

Figure 2.29 shows that upon illumination of the photoactive layer an electron-hole pair is created and two possible pathways (or a combination thereof) can occur,

a) Transfer of photo-generated electrons from the active layer into the solution resulting in a *cathodic photocurrent*. The system is operating as a photocathode.
b) Transfer of photo-generated holes from the active layer into the solution resulting in an *anodic photocurrent*. The system is operating as a photoanode.

In order to understand the interaction and charge-transfer interaction between the P3HT$_{NPs}$ and GO, the photocurrent ($I_{light\ on}$ - $I_{light\ off}$) as a function of the applied potential for the cathodic and anodic branch (I-V curves) for the P3HT$_{NPs}$ based films were performed and are shown in figure 2.30.

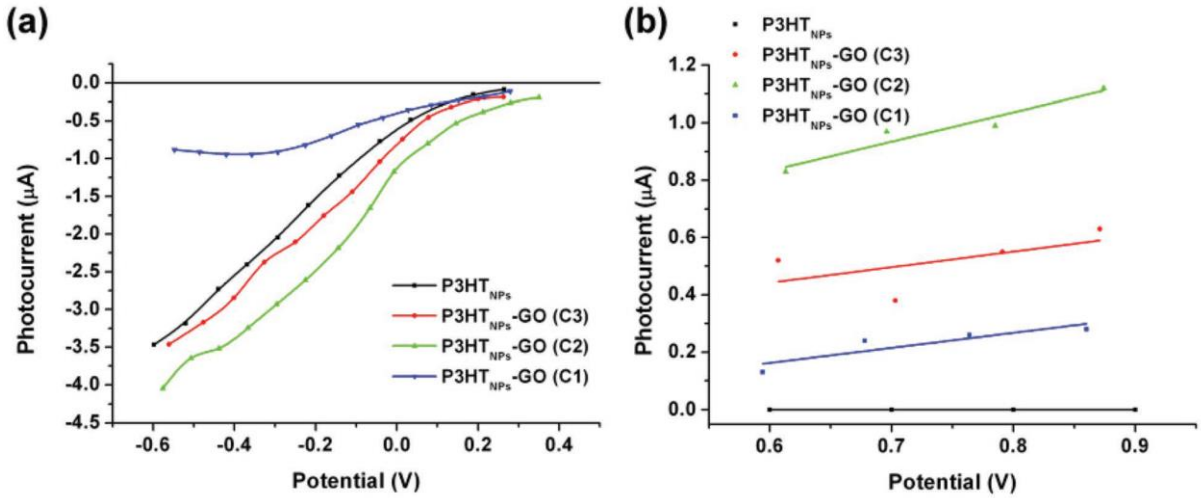

Figure 2.30. Photocurrent ($I_{light\ on}$ - $I_{light\ off}$) as a function of the applied voltage for P3HT$_{NPs}$ and P3HT$_{NPs}$-GO films (labeled Cn, n=3, 2, 1 from lowest to highest GO content) showing the (a) cathodic and (b) anodic branch.

It can be seen in figure 2.30a that a bare P3HT$_{NPs}$ film exhibits an overall photocathodic response, whereby electrons from P3HT$_{NPs}$ are transferred to the solution and photoanodic response is not detected. This behavior is consistent with the p-type semiconducting nature of P3HT. In addition, P3HT$_{NPs}$-GO nanohybrid materials show enhanced photocurrent for both, the cathodic and the anodic branch, in case of low and intermediate content of GO (C3 and C2, respectively). This indicates improved charge separation in the P3HT$_{NPs}$-GO films and favorable charge transfer to the solution.

However, for P3HT$_{NPs}$-GO films with the highest GO content (C1) the photocurrent both anodic and cathodic branches considerably decreases (for the cathodic branch it even falls below the values of P3HT$_{NPs}$) suggesting that charge separation and transfer is effectively blocked in films with highest content of GO. This clearly shows that enhanced photo-induced charge-transfer can be achieved by carefully adjusting the GO content in the P3HT$_{NPs}$-GO nanohybrids. An illustrative demonstration of the photoelectrochemical cell operation is depicted in figure 2.31.

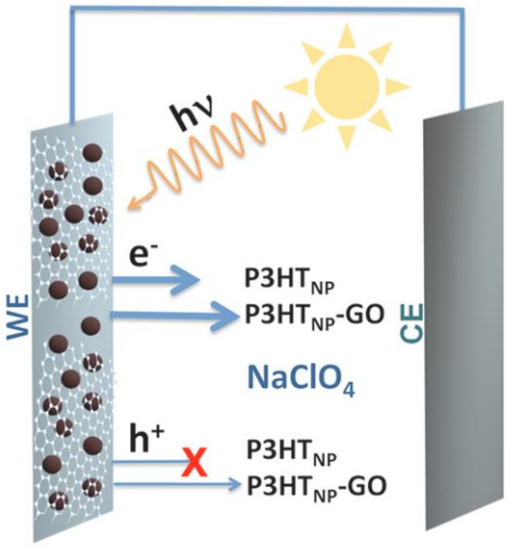

Figure 2.31. Scheme of photoelectrochemical cell indicating the improved operation when using P3HT$_{NPs}$-GO.

These finding shows that photo-induced charge-transfer can be achieved by carefully adjusting the GO content in the P3HT$_{NPs}$-GO systems. GO has a synergistic effect on P3HT$_{NPs}$ by important enhancement effects on the photocurrent responses. According to the results, P3HT$_{NPs}$-GO charge-transfer complexes can be integrated to thin film devices where P3HT$_{NPs}$-GO contributes as a photoactive layer.

2.5. Conclusion

In the present chapter, self-assembled P3HT$_{NPs}$-GO nanostructures have been successfully synthesized by applying a novel in situ reprecipitation approach, in which P3HT assembles into nanoparticles (P3HT$_{NPs}$) with sizes of 50–200 nm, being in intimate contact with surrounding GO sheets. Following all optical, electrochemical and photoelectrochemical characterization, game-changing role of GO is showed for the first time the in tuning the excitonic behavior of conjugated polymer nanoparticles and the efficient formation of P3HT$_{NPs}$–GO charge-transfer complexes.

During the self-assembly process GO plays the role of a “good” solvent additive in the marginal water phase resulting in a significant enhancement of the planarity of the P3HT chains in the formation of P3HT$_{NPs}$. This results in a change of the crystalline packing of the internal P3HT chains from an original H-type toward an H/J aggregate structure, which can be followed by UV-vis spectroscopy techniques. In case of, P3HT$_{NPs}$–GO nanostructures

exhibits excitonic coupling constants as low as 2 meV, favoring charge separation along the P3HT chains.

Furthermore, establishment of effective π–π interface interactions between the $P3HT_{NPs}$ and the GO sheets enables the formation of stable $P3HT_{NPs}$–GO charge-transfer complexes, which are characterized by quenching of photoluminescence emission in thin films and electrochemistry as well. Electrochemical studies showed energy bandgaps, as a function of GO content, are lowered by up to 0.5 eV, with respect to $P3HT_{NPs}$.

Moreover, in order to have more insights for the thin film device performance, photoelectrochemical characterization was performed. The findings show that enhanced photoinduced charge transfer can be achieved by carefully adjusting the GO content in the $P3HT_{NPs}$–GO nanostructures.

The results herein show that our synthesis approach leads to novel $P3HT_{NPs}$-GO donor-acceptor hybrid assemblies with tunable optoelectronic properties and environmental-friendly processing characteristics thus may provide a base for the design of improved functional nanomaterials of interest for thin film photovoltaic or sensing devices.

2.6. References

1. W. Gao, L. B. Alemany, L. Ci, and P. M. Ajayan, "New insights into the structure and reduction of graphite oxide," *Nat Chem*, 2009, 1, 5, 403–408.

2. K. P. Loh, Q. Bao, G. Eda, and M. Chhowalla, "Graphene oxide as a chemically tunable platform for optical applications," *Nature Chemistry*, 2010, 2, 12, 1015–1024,

3. G. Eda and M. Chhowalla, Chemically derived graphene oxide: towards large-area thin-film electronics and optoelectronics. *Adv. Mater*. 2010, 22, 2392.

4. D. R. Dreyer, S. Park, C. W. Bielawski, and R. S. Ruoff, "The chemistry of graphene oxide," *Chem. Soc. Rev*., 2009, 39, 1, 228–240.

5. K. A. Mkhoyan, A. W. Contryman, J. Silcox, D. A. Stewart, G, Eda, C, Mattevi, S. Miller and M. Chhowalla, Atomic and Electronic Structure of Graphene-Oxide, *Nano Lett.*, 2009. 9, 3.

6. B. C. Brodie, On the Atomic Weight of Graphite. Philosophical Transactions of the Royal Society of London ,1859, 149, 249-259.

7. L. Staudenmaier, Verfahren zur Darstellung der Graphitsäure. Berichte der deutschen chemischen Gesellschaft 1898, 31 (2), 1481-1487.

8. W. S. Hummers, R. E. Offeman, Preparation of Graphitic Oxide. *Journal of the American Chemical Society* 1958, 80 (6), 1339.

9. H.J. Kim, D. Kim, S. Jung, S. N. Yi, Y. J. Yun, S. K. Chang, and D. H. Ha, Charge Transport in Thick Reduced Graphene Oxide Film, *J. Phys. Chem. C*, 2015, 119, 51, 28685–28690

10. J. Liu, M. Durstock and L. Dai, Graphene oxide derivatives as hole- and electron-extraction layers for high-performance polymer solar cells, *Energy Environ. Sci*. 2014, 7, 1297.

11. Q. Liu, Z. Liu, X. Zhang, L. Yang, N. Zhang, G. Pan, S. Yin, Y. Chen and J. Wei, Polymer Photovoltaic Cells Based on Solution-Processable Graphene and P3HT, *Adv. Funct. Mater*. 2009,19,894–904.

12. J. Liu, L. Cui and D. Losic, Graphene and graphene oxide as new nanocarriers for drug delivery applications, *Acta Biomaterialia*, 2013, 9, 12, 9243-9257.

13. H. J. Yoon, T. H. Kim, Z. Zhang, E. Azizi, T. M. Pham, C. Paoletti, J. Lin, N. Ramnath, M. S. Wicha, D. F. Hayes, D. M. Simeone and S. Nagrath, Sensitive capture of circulating tumour cells by functionalized graphene oxide nanosheets, *Nature Nanotechnology*, 2013, 8, 735–741.

14. S. Wang, C. T. Nai, X. Jiang, Y. Pan, C. Tan, M. Nesladek, Q. Xu and K. P. Loh, Graphene Oxide–Polythiophene Hybrid with Broad-Band Absorption and Photocatalytic Properties, *J. Phys. Chem. Lett*., 2012, 3, 17, 2332–2336.

15. C. Vallés, P. Jiménez, E. Muñoz, A. M. Benito, and W. K. Maser, Simultaneous Reduction of Graphene Oxide and Polyaniline: Doping-Assisted Formation of a Solid-State Charge-Transfer Complex, *J. Phys. Chem. C*, 2011, 115, 21, 10468–10474

16. Q. Liu, Z. Liu, X. Zhang, L. Yang, N. Zhang, G. Pan, S. Yin, Y. Chen and J. Wei, Polymer Photovoltaic Cells Based on Solution-Processable Graphene and P3HT, *Adv. Funct. Mater*. 2009,19,894–904

17. D. Yu, Y. Yang, M. Durstock, J. B. Baek, and L. Dai, Soluble P3HT-Grafted Graphene for Efficient Bilayer Heterojunction Photovoltaic Devices, *ACS Nano*, 2010, 4 (10), pp 5633–5640.

18. X.Zhuang, Y. Chen, G. Liu, P.Li, C. Zhu, E. Kang, K. Noeh, B. Zhang, J. Zhu and Y. Li, Conjugated-Polymer-Functionalized Graphene Oxide: Synthesis and Nonvolatile Rewritable Memory Effect, *Adv. Mater*. 2010, 22, 1731–1735.

19. J. D. Núñez, A. M. Benito, S. Rouzière, P. Launois, R. Arenal, P.M. Ajayan, W.K.Maser, Graphene oxide–carbon nanotube hybrid assemblies: cooperatively strengthened OH···OC hydrogen bonds and the removal of chemisorbed water, *Chem. Sci.*, 2017 8, 4997.

20. E. Pretsch, T. Clerc, J. Seibl, W. Simon, Tabellen zur Strukturaufklärung organischer Verbindungen mit spektroskopischen Methoden, Springer Verlag, Berlin-Heidelberg-New-York, 1976.

21. A. C. Ferrari and J. Robertson, Interpretation of Raman spectra of disordered and amorphous carbon, *Phys. Rev. B*, 2000, 61, 14095.

22. F. C. Spano, Modeling disorder in polymer aggregates: the optical spectroscopy of regioregular poly(3-hexylthiophene) thin films.*J. Chem. Phys*. 2005, 122, 234701

23. J. Clark, C. Silva, R. H. Friend and F. C. Spano, Role of Intermolecular Coupling in the Photophysics of Disordered Organic Semiconductors: Aggregate Emission in Regioregular Polythiophene, *Phys. Rev. Lett*. 2007, 98, 206406.

24. J. Clark, J.-F. Chang, F. C. Spano, R. H. Friend and C. Silva, Determining exciton bandwidth and film microstructure in polythiophene films using linear absorption spectroscopy, *Appl. Phys. Lett*. 2009, 94, 163306.

25. G. Nagarjuna, M. Baghgar, J. A. Labastide, D. D. Algaier, M. D. Barnes, D. Venkataraman, Tuning aggregation of poly(3-hexylthiophene) within nanoparticles, ACS Nano 2012, 6, 10750.

26. K. Tremel and S. Ludwigs, Morphology of P3HT in Thin Films in Relation to Optical and Electrical Properties, *Adv. Polym. Sci*. 2014, 265, 39. 23,

27. F. C. Spano and C. Silva, H- and J-aggregate behavior in polymeric semiconductors, *Annu. Rev. Phys. Chem*. 2014, 65, 477.

28. M. Baghgar and M. D. Barnes, Work Function Modification in P3HT H/J Aggregate Nanostructures Revealed by Kelvin Probe Force Microscopy and Photoluminescence Imaging. *ACS Nano* 2015, 9, 7105.

29. E. T. Niles, J. D. Roehling, H. Yamagata, A. J. Wise, F. C. Spano, A. J. Moulé and J. K. Grey, J-Aggregate Behavior in Poly-3-hexylthiophene Nanofibers, *J. Phys. Chem. Lett.* 2012, 3, 259.

30. W. C. Tsoi, D. T. James, J. S. Kim, P. G. Nicholson, C. E. Murphy, D. D. C. Bradley, J. Nelson and J.S. Kim, The nature of in-plane skeleton Raman modes of P3HT and their correlation to the degree of molecular order in P3HT:PCBM blend thin films.*J. Am. Chem. Soc*. 2011, 133, 9834.

31. Q. Su, S. Pang, V. Alijani, C. Li, X. Feng, K. Müllen, Composites of Graphene with Large Aromatic Molecules, *Adv. Mater*. 2009, 21, 3191.

32. A. Bakour, F. Geschier, M. Baitoul, J. Wéry, F. Massuyeau, E. Faulques, Photoexcitations in fully organic nanocomposites of poly(3-hexylthiophene) and multiwalled carbon nanotubes, *Mater. Chem. Phys*. 2016, 171, 83.

33. S. Takemura, H. Kato, Y. Nakajima, Photoelectron studies of electrochemical diffusion of conducting polymer/transparent conductive metal oxide film interfaces, *Appl. Surf. Sci*. 1999, 144-145, 360.

34. H. Liang and X. Li, Visible-induced photocatalytic reactivity of polymer–sensitized titania nanotube films, *Appl. Cat. B* 2009, 86, 8-17.

35. D. M. DeLongchamp, R. J. Kline, D. A. Fischer, L. J. Richter, M.F. Toney, Molecular Characterization of Organic Electronic Films, *Adv. Mater*. 2011, 23, 319.

36. S. Sweetnam, K. R. Graham, G. O. Ngongang Ndjawa, T. Heumüller, J. A. Bartelt, T. M. Burke, W. Li, W. You, A. Amassian, M. D. McGehee, Characterization of the Polymer Energy Landscape in Polymer:Fullerene Bulk Heterojunctions with Pure and Mixed Phases, *J. Am. Chem. Soc*. 2014, 136, 14078.

37. S. Trasatti, The absolute electrode potential: an explanatory note, *Pure Appl. Chem.* 1986, 58, 955.

38. A. J. Bard, Photoelectrochemistry, *Science* , 1980, 207, 4427, 139-144.

3. NANOSCALE PHOTOGENERATED CHARGE-TRANSFER STUDY OF P3HT$_{NPs}$/GO COMPLEXES

3.1. Abstract

Electronic properties of donor-acceptor charge transfer complexes play an essential role for their integration in optoelectronic device structures. However, the electronic properties of these complexes such as photogenerated excitons and transport pathways can be strongly affected by changes in the morphology. For this reason, nanoscale characterization techniques exhibit outstanding tools for the characterization of blend materials. In this chapter, Kelvin Probe Force Microscopy (KPFM) is used to investigate the P3HT$_{NPs}$–GO nanohybrids formation which is discussed in Chapter 2. Two different synthesis approaches (in-situ and ex-situ) have been used to elucidate the morphology effect on the electronic properties. By mapping the local surface potential (SP) in darkness, the aggregate sub-structure of P3HT$_{NPs}$ is resolved. In addition, surface photovoltage (SPV) measurements on individual nanoparticles and hybrid materials shed light on the photoinduced charge generation and charge recombination mechanisms at the different interfaces. This work has been carried out in collaboration with Elisa Palacios-Lidón and Jaime Colchero from University of Murcia who are expert on AFM characterization techniques.

3.2. Introduction

3.2.1. Atomic force microscopy

Atomic force microscopy (AFM) or scanning force microscopy (SFM) is a microscopic technique which allows imaging of sample surface at the nanometer scale.[1] AFM technique is able to probe wide range of materials from conducting to insulating materials regardless of their transparency, stiffness and synthetic or natural properties. AFM is also generally used to image samples under atmospheric conditions which makes it attractive as a characterization tool.

AFM operates by measuring force between a probe and the sample. A sample is probed by a tip which is around a few microns long and less than 100 Å in diameter attached to the free end of a cantilever (100-200 μm long). The sample and the tip exert forces on each other, which results in deflecting the cantilever. Then the deflection of cantilever, is measured by a detector and processed by a computer to create the surface morphology of the sample.

There are various methods for detecting the motion of the cantilever with nanometer scale accuracy like tunneling current measurement, optical deflection technique, fiber interferometry and piezoresistive methods.[2]

Typically, the deflection of the cantilever is detected by measuring the displacement of a laser beam reflected from the back side of the cantilever using a position sensitive photodetector. As the cantilever deflects, the position of the laser beam shifts and can be detected by photodetectors.

The force associated with the cantilever deflection is an interatomic force such as Van der Waals forces, capillary forces, chemical bonding, electrostatic forces, magnetic forces etc. and they depend on the nature of the samples and tips. Additionally, depending on the distance between the tip and the sample, different operating modes can be used for AFM characterization and the most common by used are contact and non-contact modes.[3]

In contact mode AFM, tip creates very soft contact with the sample. The tip is brought into the sample around few Å and in this distance the electronic clouds of the tip and the sample's atoms strongly repel each other, which results in a strong repulsive force between them. Due to the forces between the tip and sample, the imaging of the morphology of the samples can be done.

In non-contact mode AFM, the tip of the cantilever does not contact the sample surface.[4] Non-contact mode measures surface topography by utilizing the long range attractive inter-atomic interactions (van der Waals, electrostatic) between the tip and a sample surface.

Based on material properties, several AFM techniques has been developed to provide more insights of the material properties. The techniques can be categorized due to the contact or non-contact mode of AFM. For instance, electrostatic force microscopy (EFM).[5] Kelvin probe force microscopy (KPFM)[6] and magnetic force microscopy (MFM)[7] are the non contact mode techniques. On the other hand, conductive-AFM (cAFM)[8] piezoresponse force microscopy (PFM)[9] and electrochemical strain microscopy (ESM) are contact mode AFM techniques.

3.2.2. Basic principle of Kelvin probe microscopy and its applications in material science

Kelvin probe force microscopy (KPFM) is a non-contact dynamic atomic force microscopy (AFM) based technique that measures contact potential difference (V_{CPD}) between a probing tip and a sample.

The CPD can be identified the difference between the work-function of the tip (Φt) and work function of the sample (Φs). The work function of a sample or a tip represents the minimal energy required to remove one electron from its Fermi level (ε_v) to vacuum (ε_f).

In KPFM technique, when an AFM tip is brought close to the sample surface, electrons will flow from a material of lower work function to a material of higher work function, until equilibrium established. For $\Phi t > \Phi s$, electrons transfer from the sample to the tip, and vice versa for $\Phi t < \Phi s$. Along with the electron flow, some net surface charge is formed on the surface of the tip and the sample which generate the contact potential difference (V_{CPD}).

In KPFM, the contact potential difference between the AFM tip and the sample can be determined as;

Equation (2): $$V_{CPD}= \Phi_t-\Phi_s)/e$$

where e is the electronic charge) and Φ_t and Φ_s are the work functions of the tip and sample, respectively.

During the KPFM scanning, the external direct-current (DC) voltage can be applied and electrostatic force between the tip and the sample adjust to zero thus the tip vibration becomes minimized. In this case DC voltage cancels the contact potential difference and enables determining of the work function of the sample from Equation 2, if the work function of the tip is known from scanning a reference sample.[3]

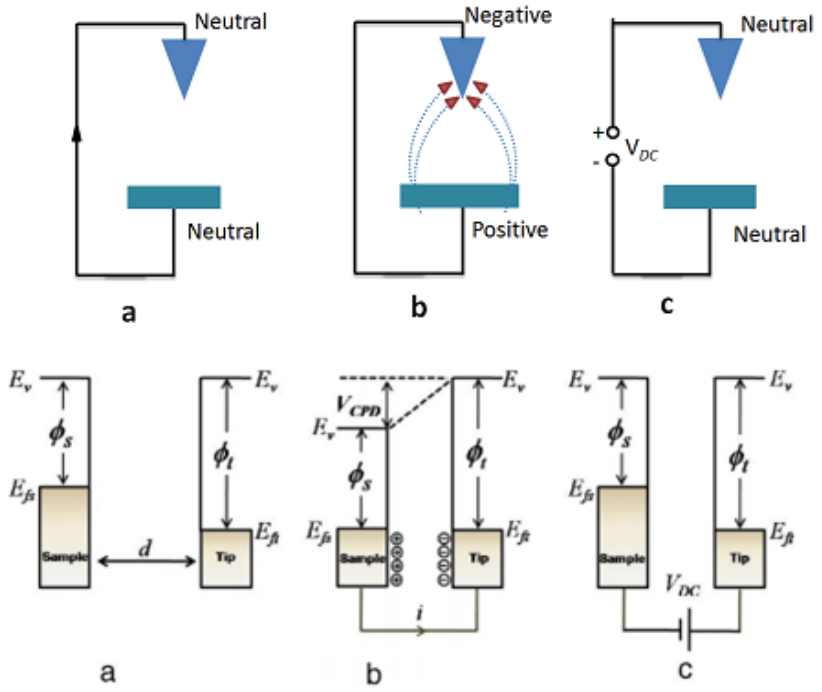

Figure 3.1 . Schematic sketches of energy levels of tip and sample: a) the tip and the sample are not in contact; b) the tip and the sample are in electrostatic contact; c) an external voltage Vdc is applied to the cantilever.[10]

In parallel to the developments in materials science, KPFM has become an important characterization technique especially for topography and local work function relation at the nanometer scale. Thus, KPFM helps to gain insight about the morphology and electrical properties relations of materials in order to optimize them for better efficiencies on possible optoelectronic applications. On the other hand, KPFM enables the imaging of surface potential of a broad range of materials including semiconductors[11], carbon nanostructures[12], conductive polymers[13], metallic nanostructure[14] and even for devices such as solar cells [15, 16] by measuring the local contact potential difference between a conductive AFM tip and the sample based on electrostatic interactions.

For instance, Hoppe et. al. reported a comprehensive work about KPFM study on a classical organic solar cell system consisting of conjugated polymer and PCBM in order to identify distinct differences in the energetics on the surface of chlorobenzene and toluene cast blend films. The KPFM method provides the information of topography and local work function at the nanometer scale and they confirmed nanomorphology of the bulk heterojunction system is strongly related with the electron transport toward the cathode in the solar cell configuration. [13]

Another KPFM study is reported on graphene–polythiophene blends. KPFM is used as tool to investigate the surface potential of rGO, P3HT and source–drain contacts in nanometric scale is measured. Besides, the work function of rGO were calculated by KPFM and results show the work function of rGO depends strongly on the number of layers.[17]

Lastly, in-depth study on the surface potential changes of P3HT/(titanium dioxide)TiO_2 nanorods (NRs) bulk heterojunction thin films has been reported by Wu et. al.[18] The surface potential mappings of P3HT/TiO_2 NRs bulk heterojunction films by Kelvin probe force microscope reveal important insight for optimizing the various parameters such as interlayer structures, processing solvents, P3HT molecular weights and ligands on TiO_2 NRs for high performance heterojunction photovoltaic devices.

In conclusion, KPFM is a useful nanoscale characterization technique to investigate the relations between the morphology and electronic properties for various types of materials. Also, it helps as a useful guide for the fabrication of high performance devices.

3.2.3. Surface photovoltage

Optoelectronic properties of the photoactive materials can be also studied by AFM technique in nanoscale resolution. Two main AFM based technique has been developed in this field; photocurrent and photovoltage measurements. Firstly, photoconductive atomic force microscopy (PC-AFM) was presented by Sakaguchi et. al[19] using conductive AFM to measure the photocurrent of organic thin films. This technique has also been used to map the photocurrent in an organic photovoltaic blend with 20 nm resolution.[20, 21]

On the other hand, surface photovoltage (SPV) is a widely used nondestructive and contactless characterization technique[22] which has been used to study the electronic properties of electroactive materials such as nanostructured p–n junctions (bulk heterojunctions) using inorganic, organic or mixtures of inorganic and organic materials.[23] SPV mainly used for determining the the minority carrier diffusion length of semiconductors. For this reason, SPV characterization is one of the most important technique since the transport of minority carriers determines the behavior of the p-n junctions which is key element for optoelectronic devices such as organic solar cells.

One of the main approaches to measure SPV is combining KPFM technique with controlled illumination offers to characterize optoelectronic properties of the samples on a nanometer length scale. 23 In contrast to PC-AFM, SPV-KPFM is a contactless technique (without

contact between the sample and the AFM tip) which based on analyzing the illumination-induced changes of the surface voltage. In other words, SPV refers to the change of CPD under illumination.[24]

This method requires two steps to measure SPV. The first measurement is performed under dark conditions to obtain the CPD_{dark} of the material. Subsequently, KPFM measurement is repeated under illumination to measure the $CPD_{illumination}$. Hence, the net difference between the two measurements is referred to as surface photovoltage ($SPV = CPD_{dark} - CPD_{illumination}$) whereby a nonzero SPV indicates redistribution of photogenerated free charges.[25]

Using the SPV method by combining KPFM technique provides useful information about photoinduced effects at the nanoscale. In this way, the properties such as the surface dipole, the carrier density and carrier diffusion length, etc can be obtained.[23] Besides, it exhibit better understanding for the relations between surface photovoltage and morphology of the materials which is crucial for fabrication of semiconductor devices consist of materials such as nanocomposites, hybrids or bulk heterojunctions.

Rogero et. al. [26] reported a nanoscale-resolved surface photovoltage maps of hybrid material (porphyrin functionalized polycrystalline ZnO) by KPFM in darkness and under illumination which allows detection of spatial variations in the surface photovoltage and surface potential, studying the photoactivity of the different regions individually.

In another study, Chiesa et. al. [27] present a microscopic study of photoinduced charge generation in polyfluorene-based photovoltaic structures and it exhibits the strong correlation between surface photovoltage and blend morphology. They also found in their blend films, the highest surface photovoltage found in the regions where a simple bilayer structure is present. Integration of the film to the device structure suggesting that an efficient conduction path for photogenerated electrons is significant for achieving a high device efficiency.

This chapter, focuses on the nanoscale photo-generated of our novel hybrids materials P3HT$_{NPs}$–GO nanohybrids which are described in Chapter 2. Moreover, we investigate the surface photovoltage-morphology correlation as well by using different approaches for the material preparation.

3.3. Experimental Section

3.3.1. Materials

3-hexyl thiophene, [1,3-Bis(diphenylphosphino)propane] dichloronickel(II)] (Ni(dppp)Cl2), tert-BuMgCl (1M THF solution), dry DMF, THF, N-Bromosuccinimide, acetonitrile, HCl were purchased from Sigma-Aldrich and were used as received. THF was distilled over benzophenone and sodium. $NaClO_4$ was dried overnight at 130^0C in vacuum oven before use. Graphene oxide in aqueous dispersion (4mg/mL) was acquired from Graphenea S.L. (San Sebastian, Spain) and used as received without any further treatment.

3.3.2. Characterization

Scanning force microscopy measurements where carried on using a home-made SFM mounted on an inverted optical microscope (Nikon Eclipse TE2000-E) that allows controlled sample illumination at ambient conditions. Image acquisition and processing was performed with freely available WSxM software. Topography and SP images were acquired simultaneously with Platinum coated silicon tips (Olympus, k = 3 N/m and f = 75 kHz) are used. Amplitude modulation mode (AM-SFM) was used for topography feedback while KPFM was operated in frequency modulation mode (FM-KPFM). All the measurements were performed at very low reduction amplitudes (Aset/Afree ≈ 0.9-0.95), which implies a non-contact, highly non-perturbative low interaction mode, needed to acquire quantitative low noise SP.[28]

3.3.3. Determination of surface potential (SP)

In our set-up, we define the SP as the (experimental) voltage needed to minimize electrostatic tip-sample interaction when the tip is grounded and the sample voltage U_{sample} is controlled by the feedback of the KPFM controller: $SP=U_{sample} - U_{tip} = U_{sample}$, since the tip is grounded. Then, the difference between the tip and the sample voltage corresponds to $SP=(\Phi_{sample} - \Phi_{tip})/e$ where Φ_{sample} and Φ_{tip} are the sample and the tip work functions respectively and *e* is the magnitude of the electron charge (positive number). In a SP image, a positive *SP* therefore corresponds to a sample with higher work function than the tip and thus to a material which is more electronegative as compared to the tip. If the tip is stable during data acquisition then the Pt tip can be considered a stable reference electrode and changes in the measured SP can be directly correlated with local changes of the surface potential/electronegativity of the sample.

Therefore, a larger (brighter) SP corresponds to a smaller work function or positively charged region and vice versa.

3.3.4. Determination of surface photovoltage (SPV)

To study photo-induced processes by means of the SPV, a sample region kept in darkness (SP^{dark}) was illuminated through the ITO substrate using a collimated monochromatic green LED (λ=535 nm). To illuminate the sample a "two pass" scanning line method is used.[23]

The illumination protocol of this method therefore involves cyclic periods of illumination and darkness (about 1s each). From the data acquired during this "two pass" technique, two (almost) simultaneous images are reconstructed, one in darkness ("off" image) and the other one under illumination ("on" image). Thus, if electro-optical processes are much faster than the line scanning time (typically 1-2s), the "two pass" protocol is equivalent to acquire two SP images, one always in darkness (SP^{dark}=SP^{off}) and another one always with illumination (SP^{on}=SP^{on}_{cont}). However, if processes slower than the line scanning time occur, these two set of images are not equivalent. Keeping this in mind and defining SPV=SP^{on}-SP^{dark}, we can decompose the SPV in a fast (SPV^{fast}=SP^{on}-SP^{off}) and a slow (SPV^{slow}= SP^{off}-SP^{dark}) contributions, that give valuable information of the time scale of the photo-generated charge excitation and recombination processes that are taking place.

3.3.5. Synthesis and characterization of P3HT

Synthesis and characterization details of P3HT were shown in chapter 2. The same P3HT batch was used for the experiments in this chapter.

3.3.6. P3HT$_{NPs}$ preparation

The P3HT synthesized according to Chapter 2 (section 2.3.3) with a regioregularity of 92%, a molecular weight of 8100, and a polydispersity index of 1.19 was added to THF in a concentration of 1 mg/mL and left to dissolve under magnetic stirring overnight at room temperature. The polymer nanoparticle synthesized via re-precipitation technique. 2 mL solution of P3HT in THF (1mg/mL was) was rapidly injected into deionized water (10 mL). The resulting solution sonicated with a tip sonicator for 3 min. Subsequently, remaining THF evaporated via vacuum evaporator at 35 °C. Then the final solution filtered and results stable aqueous dispersion of P3HT$_{NPs}$. Final concentration of P3HT$_{NPs}$ was 0.2 mg/mL.

3.3.7. In-situ P3HT$_{NPs}$-GO preparation

P3HT$_{NPs}$-GO sample was prepared via in-situ re-precipitation technique according to the procedure in Chapter 2 (section 2.3.5).[29] 2 mL of polymer solution (1mg/mL) in THF was injected into an aqueous solution of GO (0.5 mg in 10 mL) under vigorous stirring. Further steps were followed like described in preparation of P3HT$_{NPs}$. Then the final solution filtered and results stable aqueous dispersion of in-situ P3HT$_{NPs}$-GO sample. (Figure 3.2a)

3.3.8. Ex-situ P3HT$_{NPs}$-GO preparation

In order to keep the same concentration with in-situ P3HT$_{NPs}$-GO samples, P3HT$_{NPs}$ (0.2 mg/mL) were mixed 25% of GO by weight under magnetic stirring for 30 min. The final solution results stable aqueous dispersion of ex-situ P3HT$_{NPs}$-GO sample. (Figure 3.2b)

3.3.9. Thin film preparation

1 mL stock solutions of in-situ P3HT$_{NPs}$-GO, ex-situ P3HT$_{NPs}$-GO and P3HT$_{NPs}$ were diluted to 5 mL with deionized water in order to avoid the agglomeration of the nanostructures in thin film. Bare GO was also diluted to a final concentration 0.01 mg/mL. The diluted samples were spray coated on ultraflat indium tin oxide (ITO) substrate (previously cleaned with isopropanol several times) which placed on a heating plate (65 °C). The covering a surface area was of 0.5 cm × 0.5cm. (The spray gun passed maximum 5 times over the substrate).

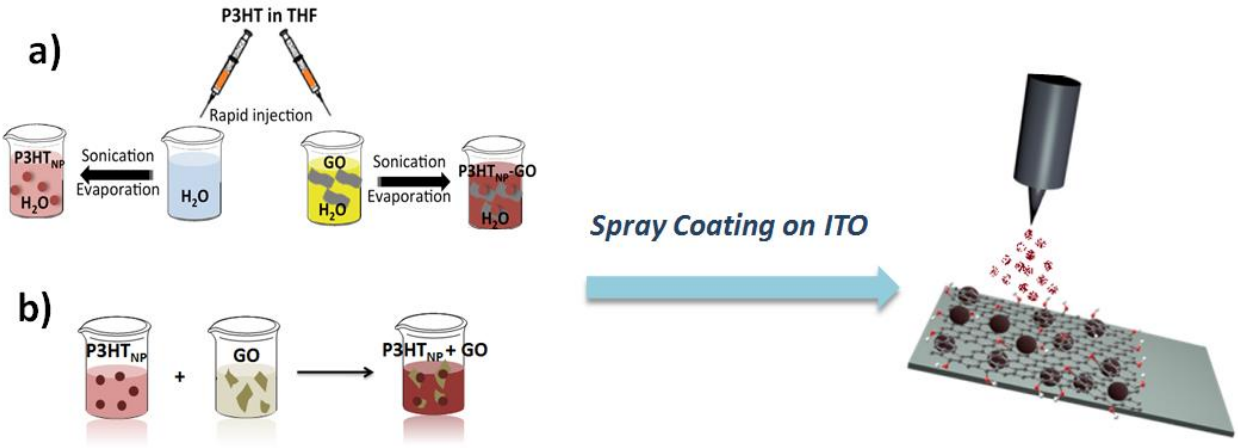

Figure 3.2. a) The preparation of in-situ P3HT$_{NPs}$ –GO samples, b) the preparation of ex-situ P3HT$_{NPs}$ –GO samples and subsequent deposition on ITO substrate.

3.3.10. Topography and SKPM dark experiments of P3HT$_{NPs}$ and GO

Firstly, the topography of P3HT$_{NPs}$ and GO sheets, which are deposited on ITO were characterized. The topography of GO (Figure 3.3) shows a discontinuous film of staked GO sheets with a lateral size around several micrometers (which correlates with our previous AFM characterizations in chapter 2) and the sheet high is about 1.7 nm in good agreement with previous values reported in the literature. [30]

Besides, the GO sheets are clearly distinguished in the corresponding (Scanning Kelvin Probe Microscopy) SKPM image (Figure 3.3) appearing as large brighter regions compared to the ITO reference. Moreover, surface potential (SP) differences (ΔSP) relative to ITO substrate depends on the layers of the GO. For one layer GO ΔSP is ($\Delta SP_{GO}^{1} = 80mV$) for two ($\Delta SP_{GO}^{2} = 60mV$) or for more than two layers of GO ($\Delta SP_{GO}^{>2} = 20mV$) are found. (Figure 3.4) This indicates that the GO reduces the ITO work function generating a positive surface dipole pointing outside.

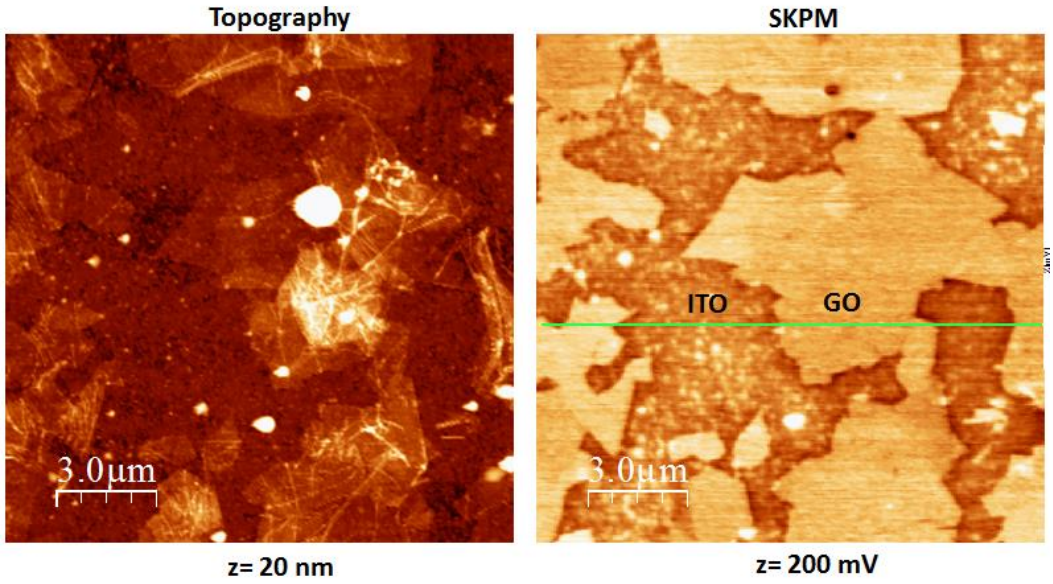

Figure 3.3. Topography and SKPM dark images of the GO on ITO.

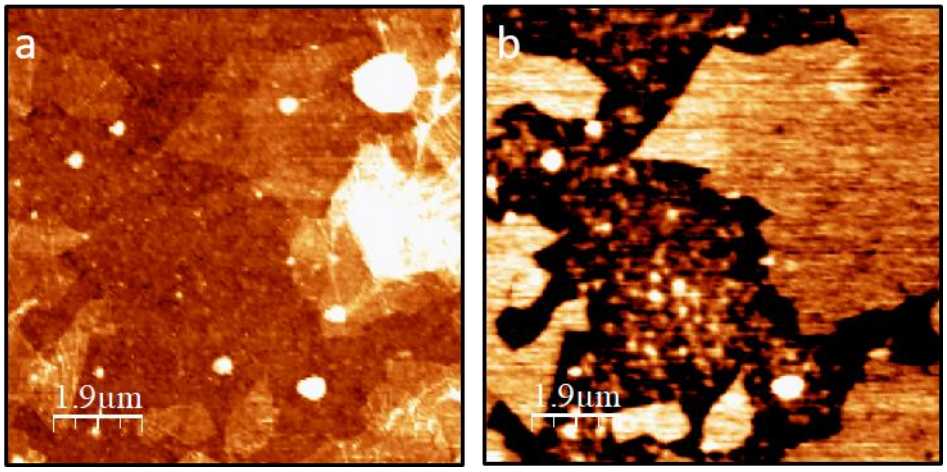

Figure 3.4. (a) Topography (z=15 nm) and (b) SP^{dark} (z=70mV) of the GO on ITO. The z scale of the SP^{dark} image is saturated to highlight the SP differences relative to the ITO substrate depending if one ($\Delta SP_{GO}^{1} = 80mV$), two($\Delta SP_{GO}^{2} = 60mV$) or more GO ($\Delta SP_{GO}^{\geq 2} = 20mV$) sheets are stacked.

The topography of the P3HT$_{NPs}$ (Figure 3.4a) shows spherical nanoparticles ranging from 50-100 nm, which correlates with our previous observations with TEM and AFM in chapter 2. The P3HT$_{NPs}$ presents mostly a bright SP contrast (Figure 3.5b) with respect to the ITO. Additionally, SP^{dark} images also show substructures within P3HT$_{NPs}$. The SP difference between high and low SP regions is as high as 250 mV that is consistent with the existence of different types of polymer chains aggregates in agreement with the work reported Baghgar et. al.[31] The low SP regions can be attributed to higher ordered more planar polymer chain aggregates while the high SP regions corresponds to more disordered aggregates.

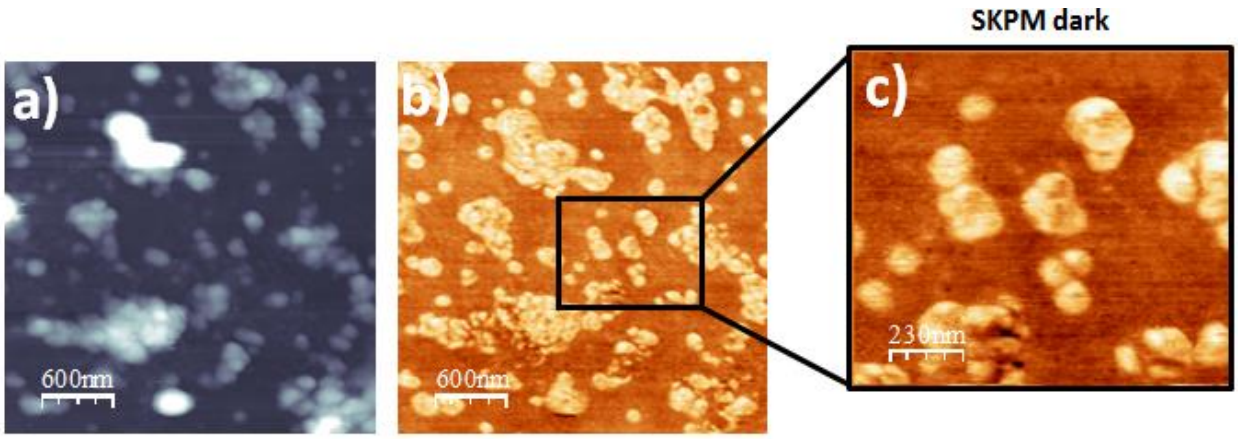

Figure 3.5. a) Topography (z=200 nm) and b)SPdark (z=500 mV) images of the P3HT$_{NPs}$ on ITO.c) englarged SPdark image of P3HT$_{NPs}$

3.3.11. SPV experiments of P3HT$_{NPs}$

Surface photovoltage experiments were carried out on the individual nanoobjects in order to observe photo induced changes of the surface voltage. SPV experiments show that both the GO and the ITO substrates exhibit a null SPV (SP^{dark} =SP^{on}), as expected due to the negligible absorption of the materials at λ=535 nm. On the contrary, under green illumination the SPV of the P3HT$_{NPs}$ is negatively shifted about -50 mV (Figure 3.6). This well-known behavior is characteristic of the P3HT/ITO interface. After photoinduced charge generation and dissociation of excitons at the P3HT/ITO interface, holes are transferred to the ITO and trapped at the interface while electrons are pushed to the external surface. After photoinduced charge generation and dissociation of excitons at the P3HT/ITO interface, electrons are separated toward the external surface, whereas holes are trapped at the ITO surface. This explains the slow character of the relaxation process (SPV≈SPV^{slow}).

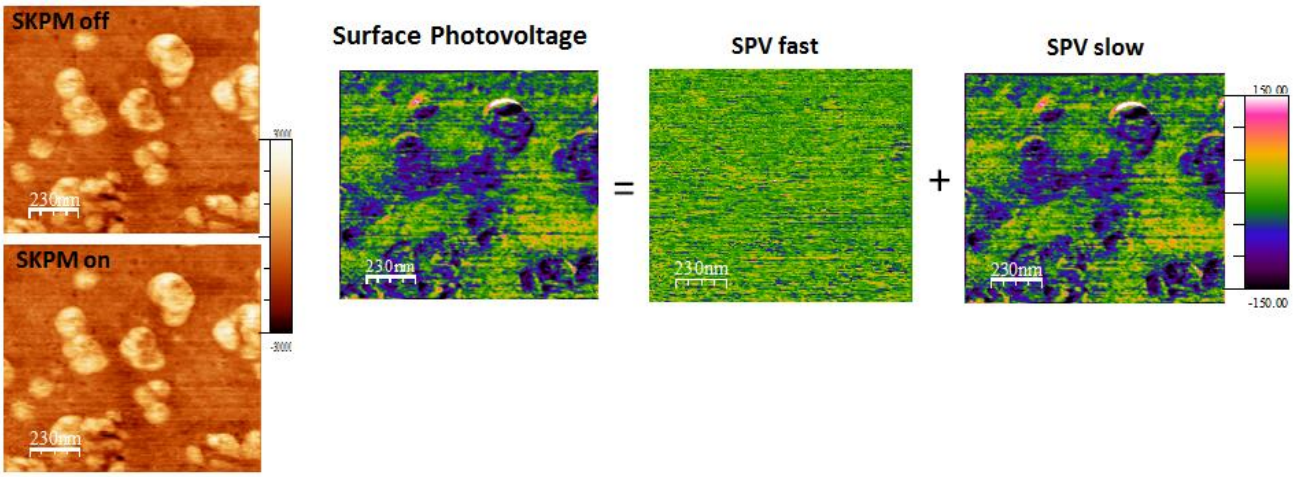

Figure 3.6. SPV performed on P3HT$_{NPs}$ the in the same region as figure 3.5. (z= ± 100mV

3.3.12. Topograpy, SP^{dark} and SPV experiments of ex-situ and in-situ P3HT$_{NPs}$-GO samples

To shed light on the P3HT$_{NPs}$-GO interface charge transfer processes in nanoscale resolution and the influence of in-situ re-precipitation preparation method on the electronic properties, we compare the morphology, the SP^{dark} as well as the SPV experiments both for ex-situ and in-situ P3HT$_{NPs}$-GO samples (Figure 3.8)

As explained in Chapter 2, the differences between the in-situ and ex-situ preparation affect the optoelectronic properties. An already formed aggregation structure within the polymer nanoparticles cannot be modified by ex-situ mixing with a water dispersion of GO. On the contrary, a clear change in aggregate structure of in-situ prepared P3HT$_{NPs}$-GO samples is observed, thus revealing effective formation of P3HT$_{NPs}$-GO nanohybrids as charge-transfer complexes.

Since the main purpose is to clarify the effect of the GO in the P3HT$_{NPs}$-GO hybrid thin film as a function of the preparation method, this study focuses on particles sandwiched between GO layers, that is, particles that are not in direct contact with the ITO substrate.

Firstly, low magnification images show that in the ex-situ sample, the P3HT$_{NPs}$ preserve their original size while in the in-situ sample tends to form larger aggregates (Figure 3.7). This could be attributed to presence of GO during the nanoparticle formation and agglomeration of P3HT$_{NPs}$ on the sp^2 domains of GO due to strong π–π interaction. However, in the ex-situ preparation method the polymer nanoparticle does not agglomerate because they are already formed in the GO free aqueous media and this might weaken the effective π–π interaction.

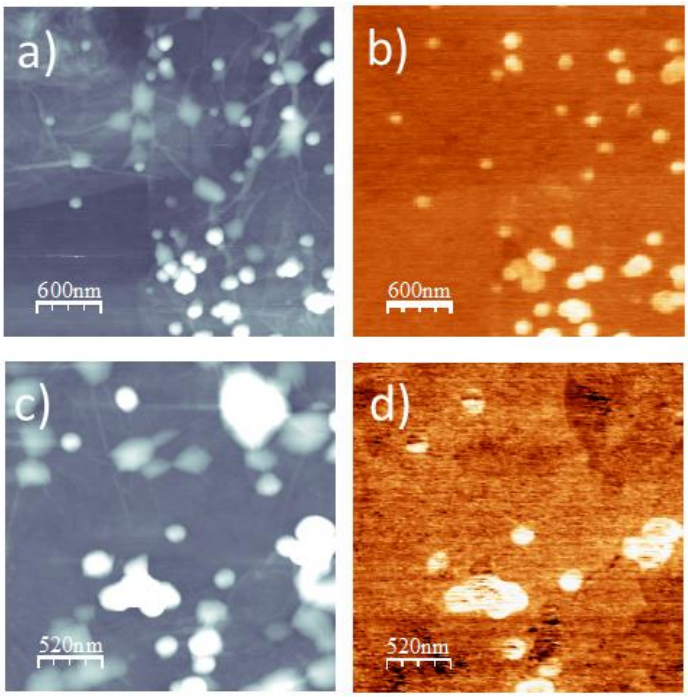

Figure 3.7. Topography low magnification images of the a) and b) ex-situ P3HT$_{NPs}$-GO, c and d) in-situ P3HT$_{NPs}$-GO on ITO.

On the other hand, as it can be seen from Figure 3.7, the polymer nanoparticle can be deposited either on top of the GO or below GO. To understand this phenomena, 3D topography of both samples were also acquired and compared with the SP^{dark} and SPV images.

In both samples (in-situ and ex-situ), from the 3D topography images (Figure 3.8a and Figure 3.8d) and the SP^{dark} (Figure 3.8b and Figure 3.8e), one can distinguish two types of P3HT$_{NPs}$ with a very different SP^{dark}; those above and those below GO sheets (marked with yellow and black circles respectively in Figure 3.8.

Independently of the sample, the P3HT$_{NPs}$ placed on top of the GO always exhibit a large bright SP contrast. For the ex-situ P3HT$_{NPs}$ (Figure 3.8b), the ΔSP value with respect to the GO is about 220±50 mV, similar to the one observed in the P3HT$_{NPs}$ directly deposited on ITO, indicating that the P3HT$_{NPs}$ remains unaltered. On the contrary, this value is reduced to 100 ± 50 mV for the in-situ sample (Figure 3.8e). This is consistent with the previous results, presented in Chapter 2, where it was demonstrated that GO induced the J-like aggregation type during the polymer nanoparticle formation. Consequently, the local work function of P3HT$_{NPs}$ is directly related with the type of aggregation, which is influenced by GO.

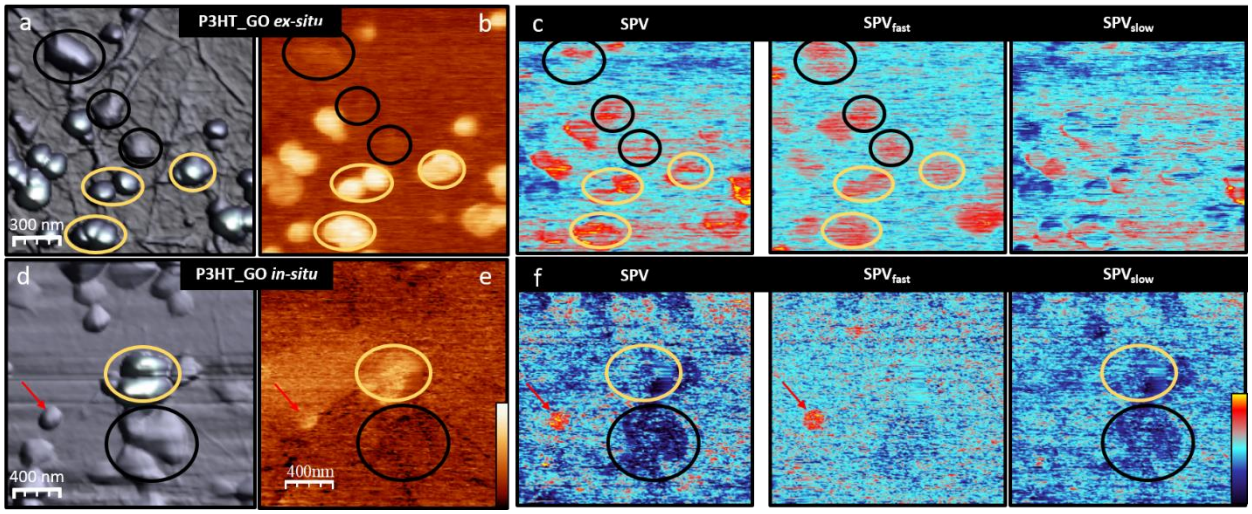

Figure 3.8. (a) and (d) 3D topography images (z scale=, (b) and (d) SP^{dark} (z scale 500mV) and (c) and (f) SPV images (z scale ±200 mV) of the ex-situ and in-situ P3HT$_{NPs}$-GO hybrid samples.

The SP^{dark} difference between ex-situ and in-situ samples is even more drastic when P3HT$_{NPs}$ is covered by GO sheets (dark circles in figure 3.8). The ex-situ nanoparticles show a slightly bright contrast SP^{dark} compared to in-situ nanoparticles contrast due to the screening effect of the high permitivity GO sheet that reduces the apparent SP of the nanoparticle.[32]

However, the P3HT$_{NPs}$ inside the in-situ P3HT$_{NPs}$-GO, exhibit an apparent dark contrast with respect to the GO. This SP^{dark} contrast inversion cannot be explained assuming that the GO plays only a passive role, acting just as a screening layer. Here, one should consider that the charge transfer from P3HT$_{NPs}$ to GO is also taking place, like we observed from Raman and electrochemistry results in Chapter 2. The charge transfer process is even more pronounced in the case of in-situ prepared samples.

Moreover, SPV experiments (Figure 3.8c and 3.8f) also reveal remarkable differences between the in-situ and ex-situ samples photo-response. In the ex-situ samples, independently of the nanoparticle position (above or below GO sheets), the P3HT$_{NPs}$ present a positive SPV of about 100 mV. This behavior is completely opposed in the in-situ samples where the P3HT$_{NPs}$ shows a negative SPV of about -150 mV that is clearer in the particles covered by GO sheets. Additionally, comparing the SPV image together with its corresponding SPV^{fast} and SPV^{slow} components, we find that the in the ex-situ sample, the P3HT$_{NPs}$ almost recover their initial SP^{dark} value "instantly" (in our time scales <2s); that is SPV≈SPV^{fast}. On the contrary, in the in-situ sample SPV≈SPV^{slow}, indicating that the photo-generated charges do not have enough time to relax during the "off" part of the two-pass method.[26] It should be

noticed, that in the in-situ process some particles can present an ex-situ-like behavior (marked with a red arrow in Figure 3.8d, 3.8f and 3.8g.

SPV measurement also gives us valuable information about the interface interaction between the GO and P3HT$_{NPs}$. In the ex-situ sample, the SPV sign as well as the time scale is opposite to the SPV of the P3HT$_{NPs}$ directly deposited on ITO (Figure 3.6). Thus, the SPV differences should be due to presence of low conducting GO sheets in between the ITO and the nanoparticle. In this situation, as schematically represented in figure 3.9a, the origin of the SPV is related with the formation of an effective positive photo-dipole.[31, 23]

The photo-generated charges remain in close proximity at the nanoparticle and can quickly recombine during the in-darkness periods of the "two pass" method leading a small SP^{slow} component. On the contrary, in the in-situ sample the SPV behavior is qualitatively similar to the one observed in the pristine P3HT$_{NPs}$ sample but the SPV value is enhanced from -40 mV to more then -150 mV. This means that holes are effectively transferred to the GO while the particle remains negatively charged (Figure 3.9b).[33] Additionally, the photo-generated charges are far apart and the equilibrium is slowly restored once the sample is brought again into darkness. These SPV results indicates the relaxation processes of photo-generated charges differ depending on the *ex-situ* or *in-situ* P3HT$_{NPs}$-GO hybrid preparation due to different interface interaction between P3HT$_{NPs}$ and GO.

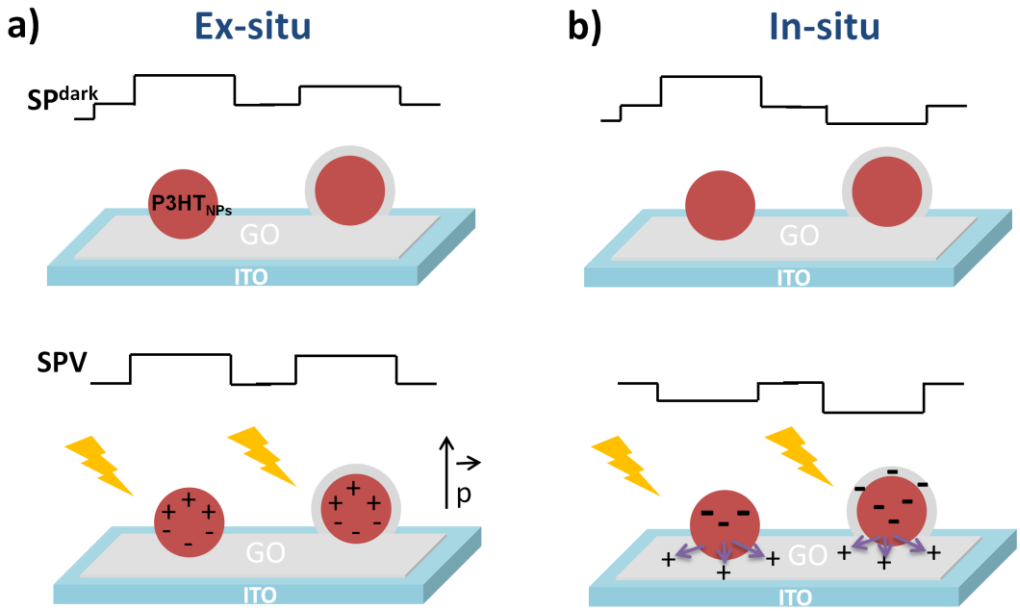

Figure 3.9. Schematic representation of the formations of the photo-induced charges

Furthermore, the study also focuses on the location of polymer nanoparticle with respect to GO, in order to further understanding of the interface interaction of in-situ P3HT$_{NPs}$-GO hybrid. Therefore, two possible locations of P3HT$_{NPs}$ are considered: P3HT$_{NPs}$ below the GO (where the interface directly exposed to the SFM tip) or P3HT$_{NPs}$ above the GO (where the interface is hidden by the polymer nanoparticle itself). A high resolution image in figure 3.10 clearly shows the different location of polymer nanoparticle for in-situ hybrid material, where P3HT$_{NPs}$ above GO is brighter than P3HT$_{NPs}$ below GO. The results show that the dark SP^{dark} of the P3HT$_{NPs}$ below the GO is composed of a SP sub-structure that clearly differs from the surrounding GO (Figure 3.10b). The existence of the low SP domains, relating to a higher local electronegativity, indicates that at these regions, a negative charge transfer from the P3HT$_{NPs}$ to the GO is taking place, modifying the local GO work function. Additionally, under illumination (Figure 3.10c) the whole P3HT$_{NP}$ becomes more electronegative (SP^{on} is downshifted). Moreover, small positively charged patches appear at the surrounding GO confirming that the holes are effectively injected from the P3HT$_{NPs}$ to the surrounded GO sheets.

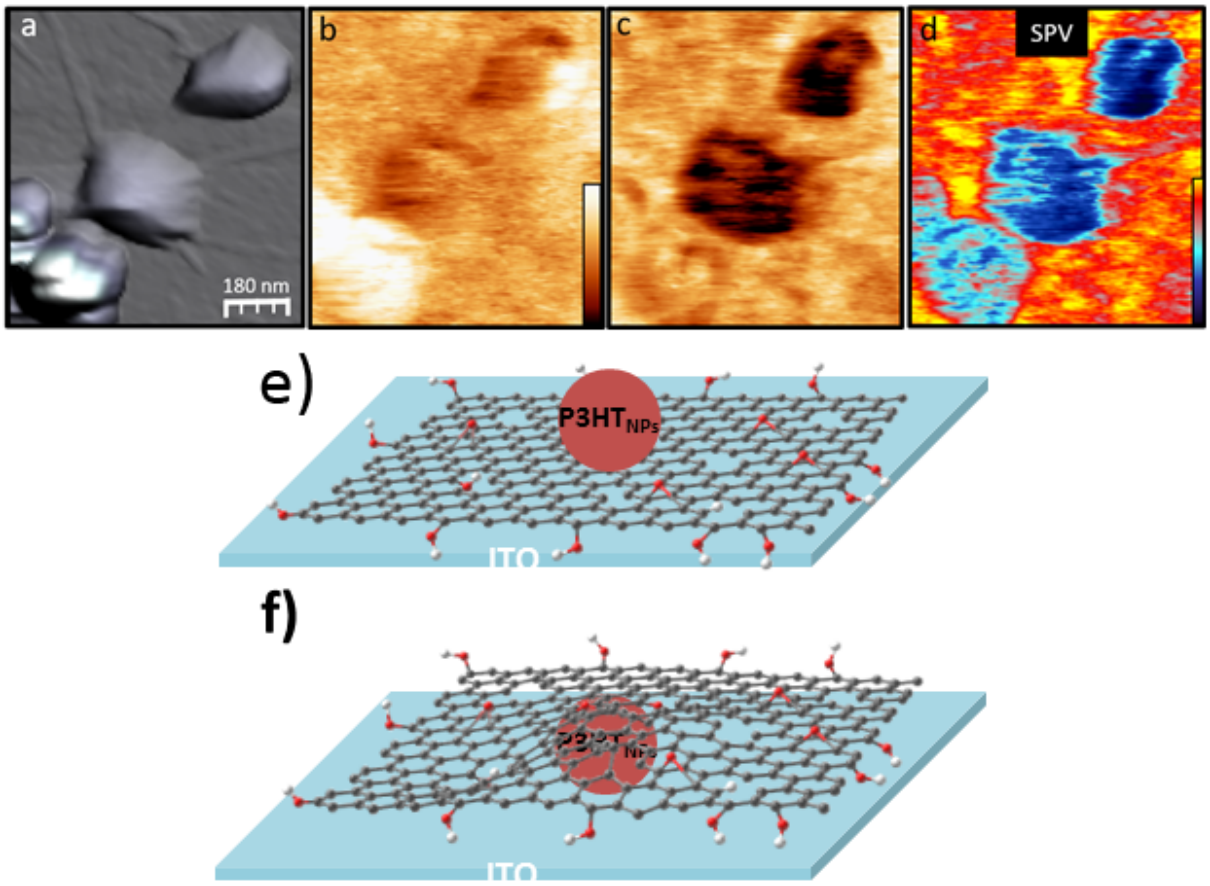

Figure 3.10. High magnification images of a in-situ P3HT$_{NPs}$-GO sample region. (a) Topography (z= 200 nm) (b) SP^{dark} (z= 300 mV) (c) SP^{on} (z= 300mV) and (d) SPV= SP^{on}- SP^{dark} (z= (-230-70 mV). Illustration of the location of P3HT$_{NPs}$ e)P3HT$_{NPs}$ above GO, f) P3HT$_{NPs}$ below GO.

3.4. Conclusion

In conclusion, the nanoscale charge-transfer properties of the P3HT$_{NPs}$- GO charge-transfer complex were studied by SKPM in dark and under illumination, elucidating the SPV characteristics. The results provide important insight for understanding the relation between morphology and electronic properties of the materials. One of the main results, the method we developed "in-situ re-precipitation" has direct impact on charge transfer properties between the P3HT$_{NPs}$ and GO. The ex-situ preparation method was compared with in-situ method and ex-situ SP^{dark} images indicating that the P3HT$_{NPs}$ on the GO shows similar behavior as P3HT$_{NPs}$ alone. This shows P3HT$_{NPs}$ remains unaltered in ex-situ sample.

On the other hand, the ex-situ and in-situ samples effect is even more drastic when P3HT$_{NPs}$ is covered by GO sheets and in-situ samples shows apparent dark contrast which indicates the direct evidence for local electron transfer from P3HT$_{NPs}$ to GO on individual nanoscale objects.

Moreover, SPV experiments reveal remarkable differences between the in-situ and ex-situ samples photo-response. While ex-situ samples present a positive SPV of about 100 mV, the P3HT$_{NPs}$ shows a negative SPV of about -150 mV that is clearer in the particles covered by GO sheets. This result indicates that photo generated charge quickly recombined in ex-situ sample in compare with in-situ sample.

Lastly, the results show that the location of polymer nanoparticle is also important for probing the charge transfer properties. While the polymer nanoparticle below the GO sheets the tip and sample interaction directly effect from the interface interaction between the GO and P3HT$_{NPs}$. In this case dark contast of SP^{dark} was observed and is directly related with higher local electronegativity, indicates that at these regions, a negative charge transfer from the P3HT$_{NPs}$ to the GO is taking place.

This study reveals important insight for morphology-electronic properties correlation of P3HT$_{NPs}$-GO hybrids and its integration for optoelectronic device structure due to efficient for photogenerated electrons which is great relevance for achieving a high device efficiency.

3.5. References

1. G. Haugstad, Atomic Force Microscopy: Understanding Basic Modes and Advanced Applications, (2012), JohnWiley & Sons, Inc

2. Y. Seo and W. Je; Atomic Force Microscopy and Spectroscopy, Rep. Prog. Phys. 71 ,2008, 016101, 23.

3. S.Faranak, Kelvin Probe Force Microscopy on Graphene Thin Films for Solar Cell and Biosensing Applications, The University of Western Ontario, 2014, *Electronic Thesis and Dissertation Repository*. 2597

4. V. L. Mironov, Foundamentals of Scanning Probe Microscopy, 2004, The Russian Academy of Sciences, Institute of Physics of Microstructures, The textbook for students of the senior courses of higher educational institutions.

5. S.H. Xu and M.F. Arnsdorf, Electrostatic Force Microscope for Probing Surface Charges in Aqueous-Solutions, P*roceedings of the National Academy of Sciences of the United States of America*, 1995, 92, 22, 10384-10388.

6. M. Nonnenmacher, M.P. Oboyle and H.K. Wickramasinghe, Kelvin Probe Force Microscopy. *Applied Physics Letters*, 1991, 5825, 2921-2923.

7. U. Hartmann, Magnetic Force Microscopy, *Annual Review of Materials Science*, 1999, 29, 53-87.

8. Zhang, L., T. Sakai, N. Sakuma, T. Ono, and K. Nakayama, Nanostructural Conductivity and Surface-Potential Study of Low-Field Emission Carbon Films with Conductive Scanning Probe Microscopy, *Applied Physics Letters*, 1999, 75(22), 3527-3529.

9. A. Gruverman, O. Kolosov, J. Hatano, K. Takahashi and H. Tokumoto, Domain-Structure and Polarization Reversal in Ferroelectrics Studied by Atomic-Force Microscopy,*Journal of Vacuum Science & Technology B*, 1995, 13(3), 1095-1099.

10. P. Wang, *PhD dissertation*, Synthesis and Characterization of Nanostructured Electro-active Materials, University of Washington, 2016.

11. Saraf, S. and Y. Rosenwaks, Local Measurement of Semiconductor Band Bending and Surface Charge Using Kelvin Probe Force Microscopy, *Surface Science*, 2005. 574, L35-L39.

12. V. Panchal, R. Pearce, R. Yakimova, A. Tzalenchuk and Olga Kazakova, Standardization of Surface Potential Measurements of Graphene Domains, *Scientific Reports*, 2013, 3, 2597.

13. H. Hoppe, T. Glatzel, M. Niggemann, A. Hinsch, M. Ch. Lux-Steiner and N. S. Sariciftci, Kelvin Probe Force Microscopy Study on Conjugated Polymer/Fullerene Bulk Heterojunction Organic Solar Cells, *Nano Lett*., 2005, 5 (2), 269–274.

14. W. Melitz, J. Shen, A. C. Kummel and S. Lee, Kelvin Probe Force Microscopy and Its Application, *Surface Science Reports*, 2011, 66, 1, 1-27.

15. L. Borowik, H. Lepage, N. Chevalier, D. Mariolle and O. Renault O, Measuring the Lifetime of Silicon Nanocrystal Solar Cell Photo-Carriers By Using Kelvin Probe Force Microscopy and X-Ray Photoelectron Spectroscopy, *Nanotechnology*, 2014, 25(26).

16. E. Sengupta, A. L. Domanski, S. A. L. Weber, M. B. Untch, H.-J. Butt, T. Sauermann, H. J. Egelhaaf and Rüdiger Berger, Photoinduced Degradation Studies of Organic Solar Cell Materials Using Kelvin Probe Force and Conductive Scanning Force Microscopy, *Journal of Physical Chemistry C*, 2011, 115(40), 1994-2001.

17. A. Liscio, G. P. Veronese, E. Treossi, F. Suriano, F. Rossell V. Bellani, R. Rizzoli, P. Samorì and V. Palermo, Charge Transport in Graphene–Polythiophene Blends as Studied by Kelvin Probe Force Microscopy and Transistor Characterization, *J. Mater. Chem*., 2011,21, 2924-2931.

18. M.-C. Wu, Y.-J. Wu, W.-C. Yen, H.-H. Lo, C.-F. Lind and W.-F. Su, Correlation Between Nanoscale Surface Potential and Power Conversion Efficiency of P3HT/TiO2 Nanorod Bulk Heterojunction Photovoltaic Devices, *Nanoscale*, 2010,2, 1448-1454.

19. H. Sakaguchi, F. Iwata, A. Hirai, A. Sasaki, and T. Nagamura, Nanometer-Scale Photoelectric Property of Organic Thin Films Investigated by A Photoconductive Atomic Force Microscope, *Jpn. J. Appl. Phys.*, 1999, 38, 3908.

20. D. C. Coffey, O. G. Reid, D. B. Rodovsky, G. P. Bartholomew and S. Ginger, Mapping Local Photocurrents in Polymer/Fullerene Solar Cells with Photoconductive Atomic Force Microscopy, *Nano Lett.* 7, 738 (2007).

21. Z. Schumacher, Y. Miyahara, A. Spielhofer and P. Grutter, Measurement of Surface Photovoltage by Atomic Force Microscopy under Pulsed Illumination, *Phys. Rev. Applied,* 2016, 5, 044018.

22. V.Donchev, K.Kirilov, Ts.Ivanovand K.Germanova, Surface Photovoltage Phase Spectroscopy – A Handy Tool for Characterisation of Bulk Semiconductors and Nanostructures, *Materials Science and Engineering: B*, 2006, 129, 1–3, 15, 186-192.

23. E. Escasain, E. Lopez-Elvira, A. M. Baro, J. Colchero and E. Palacios-Lidon, Nanoscale Surface Photovoltage of Organic Semiconductors with Two Pass Kelvin Probe Microscopy, *Nanotechnology*, 2011, 22, 37.

24. L. Kronik and Y. Shapira, "Surface Photovoltage Phenomena: Theory, Experiment, and Applications, *Surface Science Reports*, 1999, 37, 1–206.

25. L. B.-Nehoshtan, S. Kirmayer, E. Edri, G. Hodes, and D. Cahen, Surface Photovoltage Spectroscopy Study of Organo-Lead Perovskite Solar Cells, *J. Phys. Chem. Lett.*, 2014, 5 (14), 2408–2413.

26. C. Rogero, D. F. Pickup, J.Colchero, E. Azaceta, R. T.Zaera, and E. P.-Lidón, Nanophotoactivity of Porphyrin Functionalized Polycrystalline ZnO Films, *ACS Appl. Mater. Interfaces,* 2016, 8 (26), 16783–16790.

27. M. Chiesa, L. Bürgi, J.-S. Kim, R. Shikler, R. H. Friend and H. Sirringhaus, Correlation between Surface Photovoltage and Blend Morphology in Polyfluorene-Based Photodiodes, *Nano Lett.*, 2005, 5 (4), 559–563.

28. E. Palacios-Lidón, C. Munuera, C. Ocal and J. Colchero, J. Contrast Inversion in Non-Contact Dynamic Scanning Force Microscopy: What Is High and What Is Low? *Ultramicroscopy* 2010, 110 (7), 789–800.

29. E. Istif, J. Hernández-Ferrer , E. P. Urriolabeitia, A. Stergiou, N. Tagmatarchis, G.Fratta M. J. Large, A. B. Dalton, A. M. Benito and W. K. Maser, Conjugated Polymer Nanoparticle–Graphene Oxide Charge-Transfer Complexes, *Adv. Funct. Mater*. 2018, 28, 1707548.

30. K. A. Mkhoyan, A.W. Contryman, J. Silcox, D. A. Stewart, G. Eda, C. Mattevi, S. Miller, S and M. Chhowalla, Atomic and Electronic Structure of Graphene-Oxide. *Nano Letters* 2009, 9 (3), 1058–1063.

31. M. Baghgar and M. D. Barnes, Work Function Modification in P3HT H/J Aggregate Nanostructures Revealed by Kelvin Probe Force Microscopy and Photoluminescence Imaging. *ACS Nano* 2015, 9 (7), 7105–7112.

32. K.S. Kumar, S. Pittala, S. Sanyadanam, P.A. Paik, New Single/Few-Layered Graphene Oxide with a High Dielectric Constant of 10 6 : Contribution of Defects and Functional Groups. *RSC Advances* 2015, 5 (19), 14768–14779.

33. S.-S Li, K.-H Tu, C.-C, Lin, C.-W, Chen and M. Chhowalla, Solution-Processable Graphene Oxide as an Efficient Hole Transport Layer in Polymer Solar Cells. *ACS Nano* 2010, 4 (6), 3169–3174.

4. SELF-ASSEMBLED CORE−SHELL CdTe/P3HT NANOENSEMBLES AS DONOR−ACCEPTOR LIGHT-HARVESTING SYSTEMS

4.1. Abstract

Self-assembly strategies have attracted widespread attention in order to create hetero nanostructures, which contain both donor and acceptor units for efficent charge transfer, such as core-shell nanoparticles.[11] This chapter focuses on the asssembly of a novel core-shell nanostructure composed by $P3HT_{NPs}$ and cadmium telluride quantum dots ($CdTe_{QDs}$) using a re-precipitation technique. The self-assembled nanostructures consist of $P3HT_{NPs}$ of 100 nm as core and semi-conducting $CdTe_{QDs}$ as shell with a thickness of a few tens of nanometers. The microscopic analysis confirms the formation of core-shell type nanoparticle. Optical characterizations reveal photo-induced charge transfer between the $P3HT_{NPs}$ and $CdTe_{QDs}$. Photoelectrochemical assays on $CdTe_{QDs}/P3HT_{NPs}$ films show a reversible on−off photoresponse at a bias voltage of +0.8 V with a 3 times increased photocurrent compared to $CdTe_{QDs}$ alone. In this case, the improved charge separation is directly related to the unique core−shell configuration, in which the outer $CdTe_{QDs}$ shell forces the $P3HT_{NPs}$ core to effectively act as electron acceptor. These findings show the importance of the morphology in the electronic interaction between the donor acceptor units.

4.2. Introduction

4.2.1. Interface Interactions between conjugated polymers and quantum dots

Hybrids of semiconducting inorganic quantum dots and conjugated polymer have attracted widespread attention due to the combined advantages of both materials such as promising photophysical properties and their solution processability. Besides, strong electronic donor-acceptor interactions, between the two materials render them suitable candidates for optoelectronic device structure.

The composition of the CPs-QDs heteronanostructure is often achieved by physically mixing the two materials in a proper solvent or by constructing bilayer or multilayers films, enabling the electron-hole pairs diffuse and separate at the interface of the layers.

So far, various types of electron-donating conjugated polymers are combined with inorganic QDs in order to create hybrid organic-inorganic bulk heterojunction (BHJ) solar cells.

However, device performance relies on development of suitable D/A hybrids. The development of CPs-QDs heteronanostructures may eventually replace the successful CPs-C_{60} (PCBM) photoactive layers in organic solar cells. Importantly, in these hybrid solar cells, both components have the ability to absorb incident light and both can contribute to photocurrent generation, unlike the typical polymer/fullerene system where the fullerene contributes very little to the photocurrent generation.[1, 2]

For example, Ren et. al. reported on CdS quantum dots bound onto crystalline P3HT nanowires through solvent-assisted grafting and ligand exchange methods. The created hybrid solar cell with the corresponding hybrid material shows maximum power conversion efficiency of 4.1% under AM 1.5 solar illumination.[3]

Moreover, the aqueous blend of $P3HT_{NPs}$ with $CdTe_{QDs}$ showed enhanced charge separation and transport in the $P3HT_{NPs}$-CdTe QDs layer are more efficient and. The solar cell performance achieved 4.32% power conversion efficiency.[4]

Moreover, CPs-QDs hybrid materials were also tested in light-emitting-Diodes application.[5, 6] Zorn et. al. [6] reported a hybrid material combining the optical properties of CdSe@ZnS quantum dots (QDs) with the electrical properties of a conjugated polymer (poly(para-methyl triphenylamine-b-cysteamine acrylamide)). They also demonstrated improved light emitting diodes device performance (i.e., 3-fold increase in the external quantum efficiency) compared with the devices prepared by pristine (unmodified) QDs. These examples underline the great potential of CPs-QDs D/A nanostructures for optoelectronic applications.

This chapter describes the synthesis of core-shell nanostructures of $CdTe_{QD}/P3HT_{NPs}$. The electronic communication was studied by photoluminescence together with electrochemistry and photoelectrochemistry studies. The results reveal electron accepting properties of $P3HT_{NPs}$ leading to enhanced photocurrent generation in comparison to bare $CdTe_{QDs}$.

4.3. Experimental Section

4.3.1. Materials

Chemicals, reagents, and solvents were purchased from Sigma-Aldrich and used as received. Dry THF was distilled over benzophenone and sodium.

4.3.2. Characterization

- Electronic absorption spectra (UV−vis) were recorded on a PerkinElmer (Lambda 19) UV−vis−near-infrared spectrophotometer.
- Dynamic light-scattering (DLS) measurements were performed on a ALV/CGS-3 Compact Goniometer System (ALV GmbH, Germany), equipped with a JDS Uniphase 22 mW He− Ne laser, operating at 632.8 nm, interfaced with an ALV-5000/EPP multi-tau digital correlator with 288 channels and an ALV/LSE-5003 light-scattering electronics unit for a stepper motor drive and limiting switch control. The scattering intensity and correlation functions were measured at 90°. Correlation functions were collected for 10 times and analyzed by the cumulant method and the CONTIN software, which provides the apparent hydrodynamic radii distributions by Laplace inversion of the correlation function and with the aid of the Stokes− Einstein relationship.
- Steady-state emission spectra were recorded on a Fluorolog-3 Jobin Yvon-Spex spectrofluorometer (model GL3-21).
- Picosecond time-resolved fluorescence spectra were measured by the time-correlated single photon counting (TCSPC) method on a NanoLog spectrofluorometer (Horiba Jobin Yvon) by using a laser diode as an excitation source (NanoLED, 482 nm). Lifetimes were evaluated with the DAS6 fluorescence-decay analysis software. The experimental calculation of the quantum yield (Φ^{F}_{q}) for $CdTe_{QDs}$ and $P3HT_{NPs}$ in aqueous media was performed with rhodamine B as the reference fluorophore.
- Electrochemical studies were performed using a standard three-electrode cell. Glassy carbon was used as a working electrode, and platinum wires were used as counter and pseudoreference electrodes. Bu_4NPF_6 (98%) was recrystallized three times from acetone and dried in a vacuum at 100 °C before being used as an electrolyte. Before each experiment, the cell was purged with Ar for 30 s. Glassy carbon, platinum mesh, and saturated calomel electrode (SCE) were used as the working, counter, and reference electrode, respectively. Measurements were recorded using an EG&G Princeton Applied Research potentiostat/galvanostat 2273A connected to a personal computer running the PowerSuite software. The working electrode was cleaned before each experiment through polishing with a cloth and 6, 3, and 1 mm diamond pastes. The energy levels are calculated from the electrochemically determined onset redox potentials, which are converted into electronic energies by employing a conversion

potential of 4.70 V (standard hydrogen electrode potential of 4.44 V plus an additional potential of 0.26 V induced by the SCE reference).

- Photoelectrochemical measurements were carried out in a three-electrode cell fitted with a quartz window. Light from a 150 W Xe arc lamp (LOT-Oriel GmbH) illuminated the working electrodes. These consisted of films of P3HTNPs, $CdTe_{QDs}$, and $CdTe_{QDs}/P3HT_{NPs}$ spray-coated on cleaned fluorine-doped tin oxide (FTO) electrodes from an appropriate volume (1 mL) of the corresponding water dispersion, covering a surface area of 1 cm × 1 cm. Data were recorded with an AUTOLAB PGSTAT302N potentiostat. Ag/AgCl electrode and Pt wire were used as reference and counter electrode, respectively. The supporting electrolyte consisted of a 0.1 M $NaClO_4$ solution in acetonitrile. Acetonitrile was dried out using a 3Å molecular sieves, and $NaClO_4$ was dehydrated in an oven at 150 °C overnight before use. The scan rate for cyclic voltammetry (CV) was 20 mV/s, and potentiostatic photocurrent transients were recorded at 0.8 V versus Ag/AgCl.
- For the imaging analyses, an aqueous drop of $CdTe_{QDs}/P3HT_{NPs}$ was deposited on a 3 mm copper grid supporting a very thin carbon membrane. High-resolution scanning transmission electron microscopy (STEM) and energy-dispersive X-rays studies were performed on a probe-corrected STEM FEI Titan-Low-Base operating at 120 and 300 kV (fitted with a X-FEG gun and Cs-probe corrector (CESCOR from CEOS GmbH)).

4.3.3. Synthesis and characterization of P3HT

Synthesis and characterization details of P3HT were shown in chapter 2. The same P3HT batch was used for the experiments in this chapter.

4.3.4. Synthesis of cadmium telluride ($CdTe_{QDs}$)

The $CdTe_{QDs}$ were synthesized in aqueous phase by following a two-step procedure.[7, 8] Initially, NaHTe was prepared by dissolving Te (26 mg, 0.204 mmol) and $NaBH_4$ (100 mg, 2.64 mmol) in distilled water (5 mL) with the aid of bath sonication for 30 minutes. After that period, the solution turned pink and was de-aerated by bubbling with nitrogen for 20 minutes. Subsequently, $Cd(ClO_4)_2$ (650 mg, 2.087 mmol) along with 2-mercaptopropionic acid (0.37 mL, 4 mmol) were dissolved in distilled water (125 mL) under stirring. Then the pH of the solution was adjusted to around 12 by adding dropwise aqueous 1M NaOH, followed by de-aeration by bubbling with nitrogen for 20 minutes. Afterwards, NaHTe was injected to the

above solution with a syringe under stirring and nitrogen atmosphere and the reaction mixture was refluxed at 96 °C for 15 minutes and after that period the reaction mixture was exposed to air while continuing the reflux for 24 hours.

4.3.5. Preparation of $CdTe_{QDs}$/$P3HT_{NPs}$ ensembles

An in-situ reprecipitation technique was also used to synthesize core-shell nanostructures of $CdTe_{QD}$/$P3HT_{NPs}$. Initially, a solution of P3HT in THF (1 mL, at a concentration of 1 mg/mL) was prepared and left stirring overnight at room temperature. Then, P3HT (1 mL) was injected into an aqueous solution of $CdTe_{QDs}$ (10 mL) under vigorous stirring. The dispersion was first stirred for 30 min at room temperature and then heated to 50 °C allowing the evaporation of THF to furnish $CdTe_{QDs}$/$P3HT_{NPs}$. Subsequently, the solution was centrifuged at 3000 rpm for 3 minutes in order to remove residual precipitated polymers and the supernatant used for characterization of $P3HT_{NPs}$/$CdTe_{QDs}$ nanoensembles. The preparation of the hybrid material was also illustrated in figure 4.1.

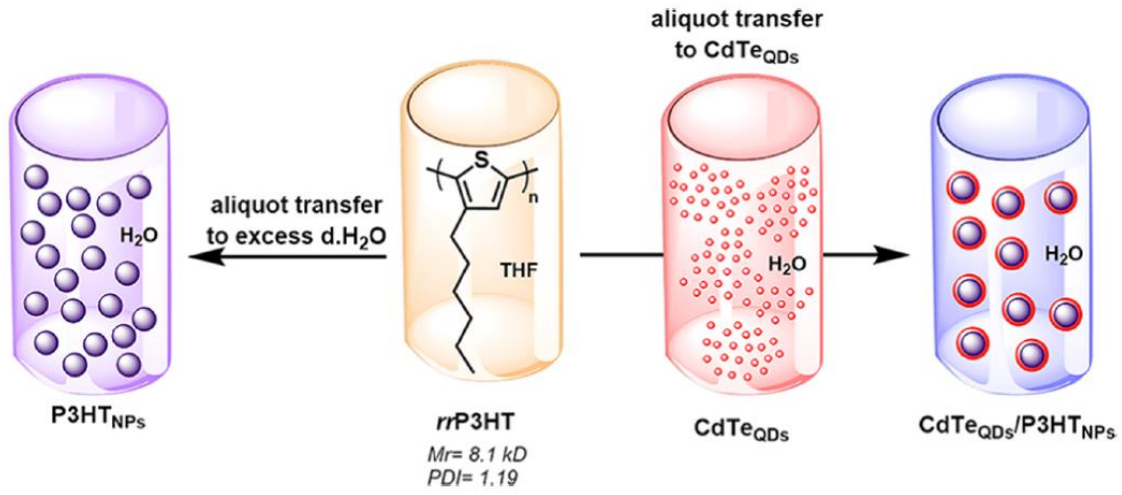

Figure 4.1. Illustrative preparation of $CdTe_{QDs}$/$P3HT_{NPs}$ ensembles by following the reprecipitation technique

4.4. Results and Discussion

The reprecipitation process involves 3 steps as illustrated in figure 4.1.

i. dissolving the polymer (P3HT) in a selective solvent (THF),
ii. mixing the obtained solution with a marginal solvent (water), which has to be completely miscible with the selective solvent,

iii. removal of the organic solvent by evaporation to leave behind water-dispersible nanoparticles

During the second step, as a result of injection of THF into the water, polymer chains fold ona assemble into spheroidal nanoparticles to minimize the contact with water. Subsequently, $CdTe_{QDs}$ are deposited on the as-formed $P3HT_{NPs}$ yielding the $CdTe_{QDs}/P3HT_{NPs}$ assembly, in which $CdTe_{QDs}$ constitute the shell and $P3HT_{NPs}$ the core. Additionally, dipole-dipole interactions between the cadmium and sulphur atom of the thiophene ring unit, were observed by NMR studies[9, 10] critically contribute to stabilize the hybrid in the form of a core-shell nanoparticle.

4.4.1. Morphological characterization

Individual $CdTe_{QDs}$, $P3HT_{NPs}$ and $CdTe_{QDs}/P3HT_{NPs}$ nanoensembles were imaged by scanning transmission electron microscopy (STEM) techniques in order to investigate the morphology of the materials. The aqueous drops of corresponding samples were deposited on a 3 mm copper grid supporting a very thin carbon membrane. The bare $P3HT_{NPs}$ exhibit a size around 80-90 nm around as we have seen in the previous chapter. The spherical nanoparticle shape shows in figure 4.2a confirms the nanoparticle formation during the reprecipitation process.

Bare $CdTe_{QDs}$ usually form small agglomerates with sizes around 10-30 nm. Some individual with sizes around 2-7 nm were also observed. (Figure 4.32) Energy dispersive X-ray spectroscopy (EDS) spectrum was recorded in the red rectangular area in figure 4.2e. Here, it can be clearly seen that $CdTe_{QDs}$ carbon, sulphur, cadmium and telluride atoms. While cadmium and telluride signals come from the inorganic quantum dots themselves as main components, carbon and sulphur atoms appear due to the stabilizer (2-mercaptopropionic acid) which surround the quantum dots surface.

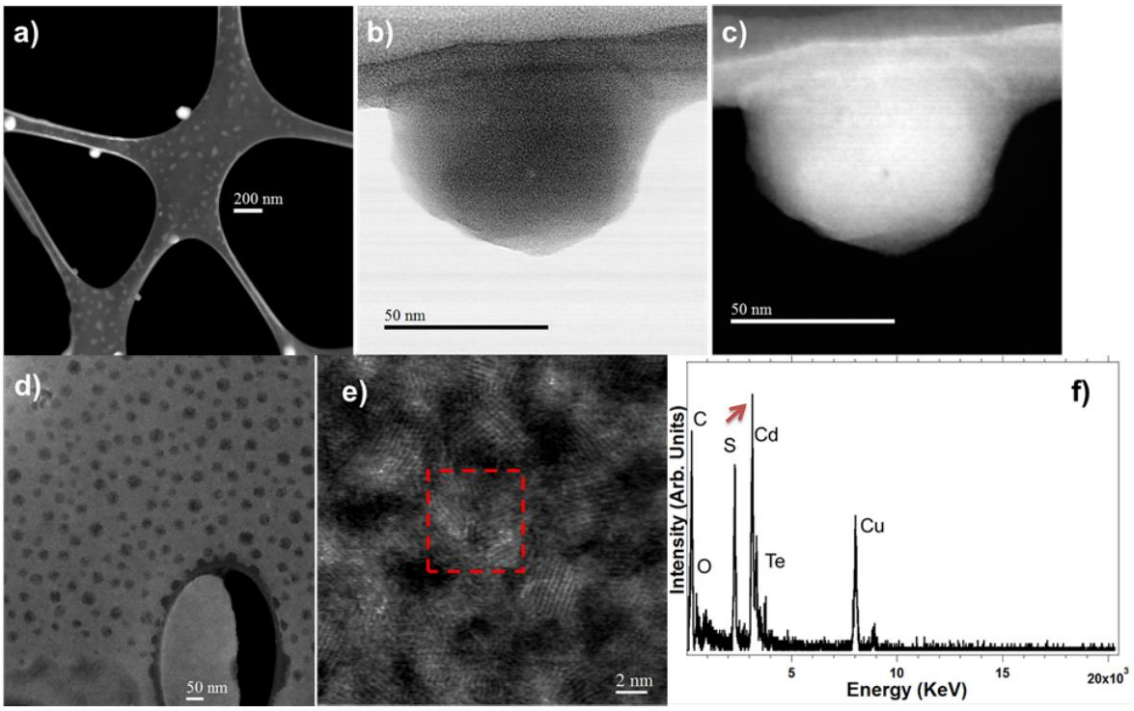

Figure 4.2. a) and (c) High-angle annular dark-field (HADDF)-STEM images of $P3HT_{NPs}$ at lower and higher magnification, respectively. (b) Bright-field (BF)-STEM image of the same $P3HT_{NPs}$ displayed in (c). (d) BF-STEM image of several $CdTe_{QDs}$. (e) High-resolution HAAD HAADF STEM micrograph showing $CdTe_{QDs}$. (f) EDS-STEM spectrum recorded by scanning the electron beam during 20 sec in the red rectangular area highlighted in the HAADF-STEM image shown in (e).

Lastly, STEM (Figure 4.3a) evidenced the formation of core-shell formation of $CdTe_{QDs}/P3HT_{NPs}$ nanoensembles with "bean-like" shape and size around 150−250 nm. Hydrophilic $CdTe_{QDs}$, 2−7 nm in diameter, were found attached onto the surface of the hydrophobic $P3HT_{NPs}$. The EDS spectrum recorded for the $CdTe_{QDs}/P3HT_{NPs}$ nanoensembles show enhanced intensity of the sulphur peak compared to the bare $CdTe_{QDs}$ due to contribution of sulphur atoms of the thiophene ring. (Figure 4.3d)

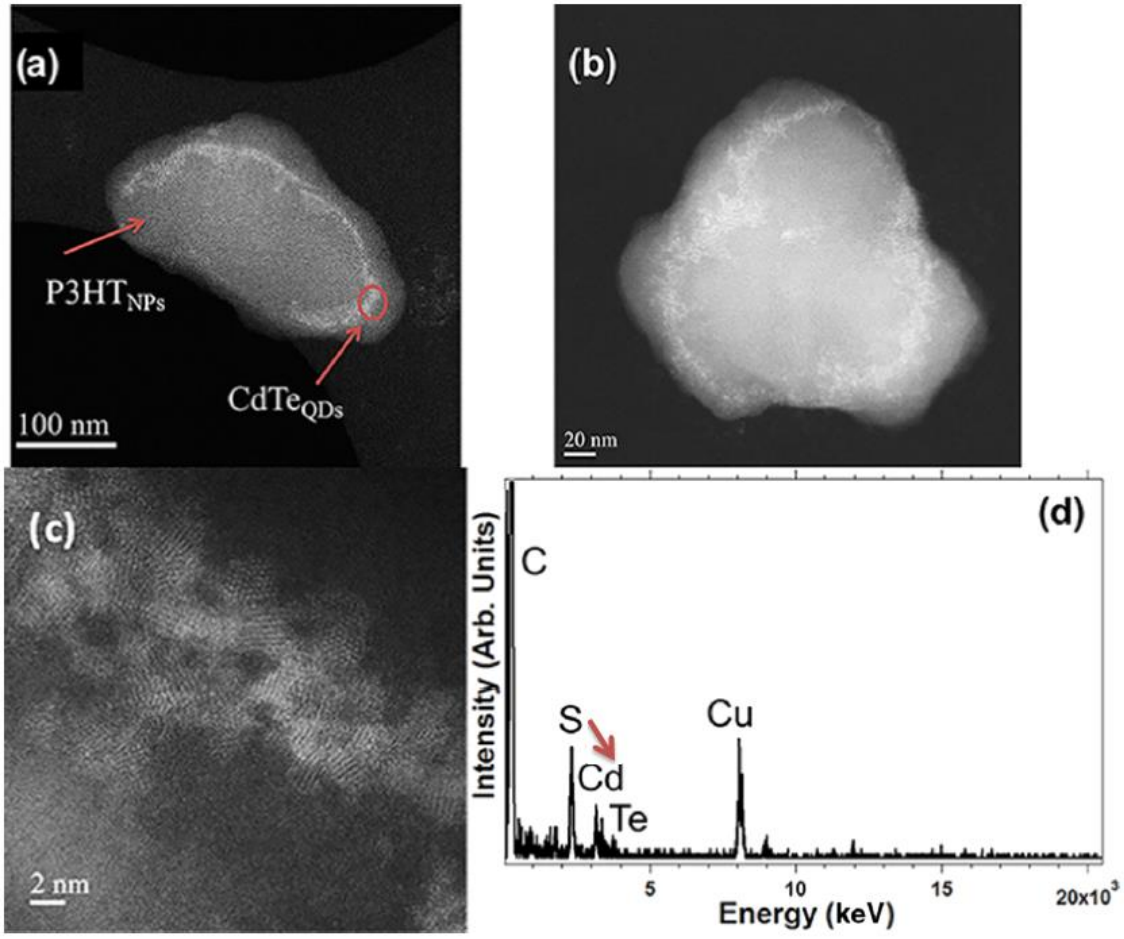

Figure 4.3. (a, b) High-angle annular dark-field (HAADF)-STEM images of two different CdTe$_{QDs}$/P3HT$_{NPs}$ ensembles at lower and higher magnification, respectively. (c) High-resolution HAADF-STEM micrograph showing the CdTe$_{QDs}$ located at the surface of P3HT$_{NPs}$. (d) Energy dispersive X-ray spectroscopy (EDS) spectrum for CdTe$_{QDs}$/P3HT$_{NPs}$ ensembles. Scale bar is 50 nm.

In order to obtain more information about the particle size of CdTe$_{QDs}$, P3HT$_{NPs}$ and CdTe$_{QDs}$/P3HT$_{NPs}$ ensembles, dynamic light-scattering (DLS) experiments were also performed for the corresponding materials in aqueous solution. DLS is a useful characterization technique that can be used to determine the size distribution profile of small particles or polymers in solution as hydrodynamic radius R_h (R_h: the radius calculated from the diffusional properties of the particle). R_h of 53, 17 and 110 nm were measured for individual P3HT$_{NPs}$, CdTe$_{QDs}$ and CdTe$_{QDs}$/P3HT$_{NPs}$ assembles, respectively. (Figure 4.4)

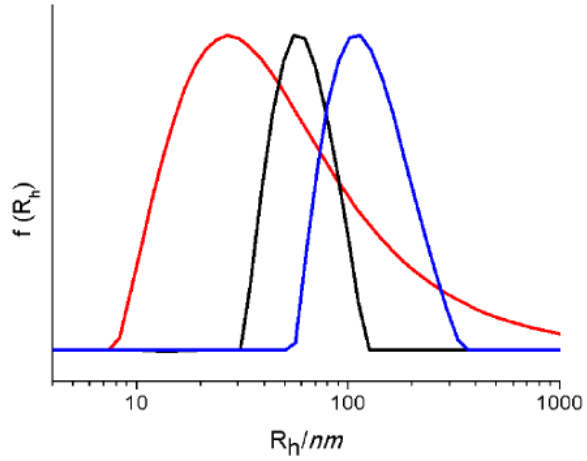

Figure 4.4. Size distribution graphs for $CdTe_{QDs}$ (red), $P3HT_{NPs}$ (black) and $CdTe_{QDs}/P3HT_{NPs}$ (blue).

The R_h of the corresponding materials is in agreement with the sizes observed under STEM conditions. However, in the case of individual $P3HT_{NPs}$, a small increase in their size is identified in the DLS studies compared with STEM images, probably due to swelling of the polymer particles in the liquid phase, whereas in $CdTe_{QDs}/P3HT_{NPs}$ ensembles, this increase is not observed, most likely due to the $CdTe_{QDs}$ shell preventing the polymer particle from swelling. $CdTe_{QDs}$ were found at ca. 34 nm in diameter, corresponding to $CdTe_{QDs}$ agglomerates, observed also with STEM images Figure 4.2d. The local aggregation of $CdTe_{QDs}$ could be due to inability of the small-sized surface stabilizer (2 mercaptopropionic acid) of $CdTe_{QDs}$ to suppress the attraction across the interior bimetallic cores. This observation further clarifies the size difference between bare $P3HT_{NPs}$ (around 85 nm) and $CdTe_{QDs}/P3HT_{NPs}$ (around 200 nm) in the solid state and is also related with the DLS findings, where $CdTe_{QDs}$ is associated with the expansion of the $CdTe_{QDs}/P3HT_{NPs}$ particles (Rh around 110 nm) as compared to bare $P3HT_{NPs}$ (R_h around 50 nm). The observed size differences in both technique DLS and STEM, confirm the formation of $CdTe_{QDs}/P3HT_{NPs}$ core−shell ensembles consisting of a $P3HT_{NPs}$ core about 100 nm in diameter and a shell formed by $CdTe_{QDs}$ with a layer thickness of a few tens of nanometers. DLS and TEM data are summarized in table 6.

Table 4.1. Diameter of the materials as calculated by DLS measurements and observed by TEM imaging

Samples	R_h/diameter[a] (nm)	Diameter by TEM[b] (nm)
$P3HT_{NPs}$	53/106	80-90
$CdTe_{QDs}$	17/34	10-30[c] (2-7)
$CdTe_{QDs}/P3HT_{NPs}$	110/220	150/250

[a]Apparent hydrodynamic radii as calculated by the cumulant analysis method from DLS measurements

[b]Approximate diameter as observed from TEM images.

[c]The size corresponds to $CdTe_{QDs}$ aggregates, value in parenthesis is the size of the single quantum dots.

4.4.2. Optical properties of $CdTe_{QDs}/P3HT_{NPs}$ ensembles

The optical properties of $CdTe_{QDs}/P3HT_{NPs}$ ensembles were investigated by UV-Vis spectroscopy, photoluminescence and time-resolved photoluminescence spectroscopy in order to shed light on the electronic communication between the $CdTe_{QDs}$ and $P3HT_{NPs}$ materials in the hybrid system.

Firstly, the absorption spectroscopy is employed for P3HT, $P3HT_{NPs}$, $CdTe_{QDs}$ and $CdTe_{QDs}/P3HT_{NPs}$. The P3HT in THF exhibits a strong, broad, and featureless π−π* transition around 445 nm due to its conjugated polymer backbone (Figure 4.5). Absence of vibronic transitions shows amorphous morphology of P3HT in THF solution. Upon the formation of $P3HT_{NPs}$, the π−π* transition considerably red-shifts to 505 nm as it was observed in chapter 2 as well. Moreover, the vibronic peaks appear at 505, 550, and 600 nm and are assigned as the A_{0-2}, A_{0-1}, and A_{0-0} peaks, respectively. These vibronic peaks are attributed to crystalline P3HT domains within the $P3HT_{NPs}$. These observations clearly indicate the change in the morphology of the P3HT chains into $P3HT_{NPs}$.

On the other hand, the absorption spectrum of $CdTe_{QDs}$ is characterized by a typical shoulder centered at 520 nm and another peak at 350 nm.

In case of $CdTe_{QDs}/P3HT_{NPs}$, the absorption spectrum exhibits similar features as observed in $P3HT_{NPs}$. However, the maximum absorption of $CdTe_{QDs}/P3HT_{NPs}$ was further red-shifted by about 10 nm compared to individual $P3HT_{NPs}$ (Figure 4.5). The latter indicates electronic communication between $CdTe_{QDs}$ (or aggregates thereof) and $P3HT_{NPs}$ at the core−shell interface.

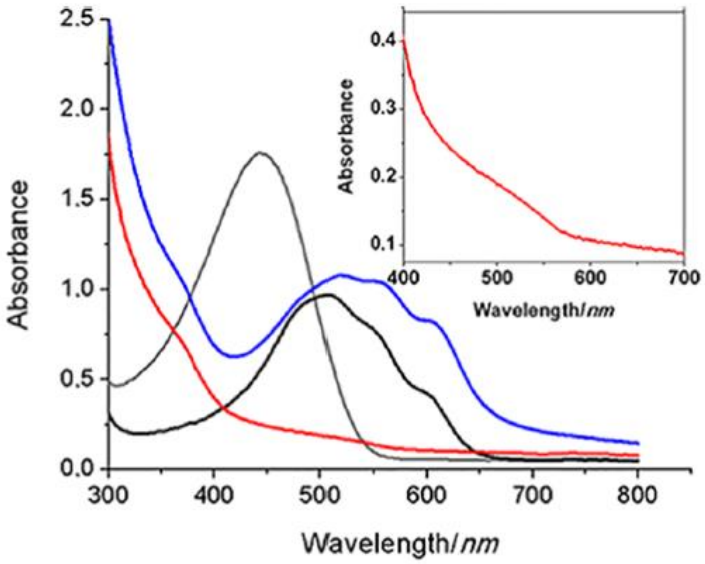

Figure 4.5. UV−vis absorption spectra for P3HT (gray), obtained in THF, and $P3H_{NPs}$ (black), $CdTe_{QDs}$ (red), and $CdTe_{QDs}$/ $P3HT_{NPs}$ (blue), obtained in H_2O. Inset: expanded area of the absorption spectrum of $CdTe_{QDs}$.

Complementary studies have been performed by photoluminescence spectroscopy and time resolved photoluminescence spectroscopy in order to identify possible electronic interaction at the excited states. First, the emission spectrum of $CdTe_{QDs}$ was carried out. The pristine $CdTe_{QDs}$ upon excitation at 490 nm is governed by a broad band centered at 555 nm with a quantum yield of 0.25 (Figure 4.6). Next, the emission spectrum of $P3HT_{NPs}$ upon excitation at 490 nm exhibits a wide emission band at 640−750 nm, showing two peaks at 660 and 720 nm, which can be associated with the 0−0 and 0−1 emissions of $P3HT_{NPs}$. [12, 13] (Figure 4.6) In case of $CdTe_{QDs}$/$P3HT_{NPs}$, the characteristic emission of $CdTe_{QDs}$ is quenched by around 65% for the samples possessing identical concentrations, whereas the emission of $P3HT_{NPs}$ is significantly increased at the same time. (Figure 4.6)

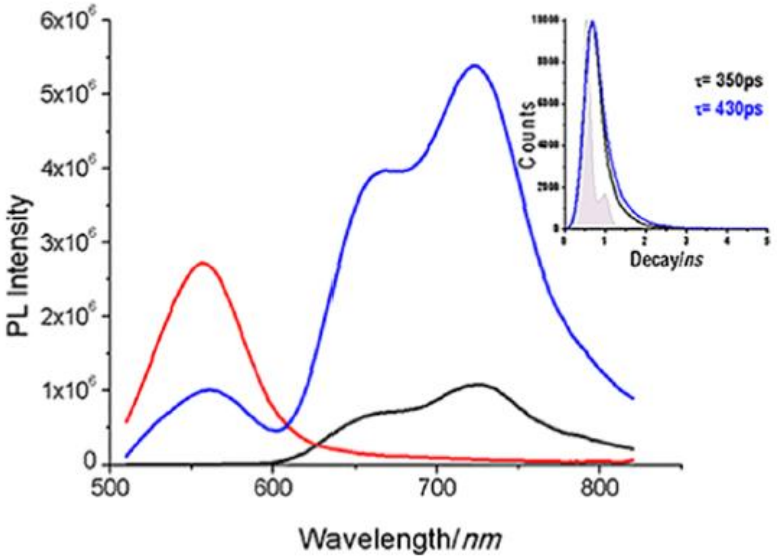

Figure 4.6. Photoluminescence spectra for $P3HT_{NPs}$ (black), $CdTe_{QDs}$ (red), and $CdTe_{QDs}/P3HT_{NPs}$ (blue), obtained upon excitation at 490 nm in H_2O. Inset: fluorescence lifetime decay profiles

The quenching of $CdTe_{QDs}$ indicates strong electronic interactions at the excited state between the two species within $CdTe_{QDs}/P3HT_{NPs}$. The quenching effect can be due to charge transfer as the decay mechanism of the singlet excited state of $CdTe_{QDs}$.

To elucidate the photoluminescence quenching mechanism and the dynamics of the system, time-resolved photoluminescence lifetime assays are also performed for corresponding samples. Time-correlated single-photon-counting measurements are employed to acquire the fluorescence lifetime profiles for $CdTe_{QDs}/P3HT_{NPs}$. The fluorescence-decay profile of bare $CdTe_{QDs}$ is measured and correlated with the one owed to $CdTe_{QDs}/P3HT_{NPs}$. Exciting $CdTe_{QDs}$ at 482 nm, the emission at 555 nm is best monoexponentially fitted. It should be noted that although biexponential fitting is employed for the bare $CdTe_{QDs}$, the analysis of the quenching mechanism is based focusing on the dominant population for convenience. Analysis of the function revealed the fluorescence emission lifetime for pristine $CdTe_{QDs}$ to be 29 ns (Figure 4.7).

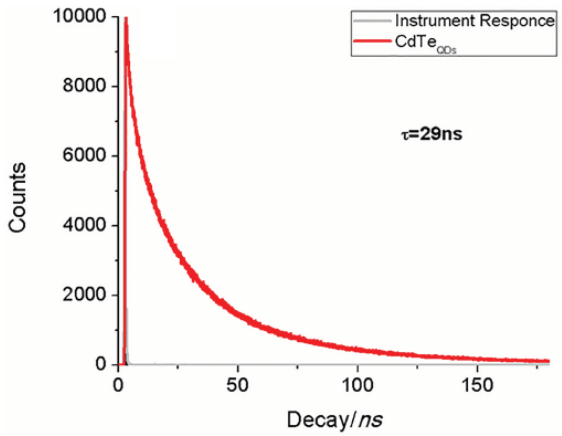

Figure 4.7. Fluorescence lifetime decay profiles for $CdTe_{QDs}$ (excitation 482 nm, emission 555 nm)

However, measurable decay component in $CdTe_{QDs}$/$P3HT_{NPs}$, corresponding to the quenching of the photoluminescence intensity in the steady-state spectra, is not identified, implicitly suggesting that the excited state deactivation of $CdTe_{QDs}$ in $CdTe_{QDs}$/$P3HT_{NPs}$ is faster than the 50 ps resolution of our instrumentation. Then, upon excitation at 482 nm, focusing on the emission of $P3HT_{NPs}$ at 720 nm, within the $CdTe_{QDs}$/$P3HT_{NPs}$ ensemble, the photoluminescence decay is monoexponentially fitted and analysed to be 0.43 ns. The latter value, higher than the one calculated for the bare $P3HT_{NPs}$ (ca. 0.35 ns), is attributed to the excited state of $P3HT_{NPs}$ within $CdTe_{QDs}$/$P3HT_{NPs}$. Overall, these results are in full accordance with the steady-state measurements, showing that the photoluminescence suppression of $CdTe_{QDs}$ is accompanied by a simultaneous enhancement in the emission owed to $P3HT_{NPs}$ (Figure 4.6) for the $CdTe_{QDs}$/ $P3HT_{NPs}$ ensembles. Considering the fast decay value of 50 ps as the upper limit of the actual lifetime attributed to the excited state of $CdTe_{QDs}$ in $CdTe_{QDs}$/$P3HT_{NPs}$, consistent with the strong emission quenching of $CdTe_{QDs}$ by $P3HT_{NPs}$. As identified in the steady-state photoluminescence measurements, and comparing the lifetime values for $CdTe_{QDs}$/$P3HT_{NPs}$ with those for the individual species $CdTe_{QDs}$ and $P3HT_{NPs}$, the minimum value for the quenching rate constant (k^S_q) for the excited state of $CdTe_{QDs}$ and the quenching quantum yield (Φ^S_q) in $CdTe_{QDs}$/$P3HT_{NPs}$ were calculated according to eqs 3 and 4 to be $1.995 \times 108\ s^{-1}$ and 0.998, respectively.

Equation 3: $$k^s_q = (1/\tau_f) - (1/\tau_0)$$

Equation 4: $$\phi^s_q = [(1/\tau_f) - (1/\tau_0)] / (1/\tau_f)$$

τ_f refers to the lifetime of $CdTe_{QDs}$ in $CdTe_{QDs}$/$P3HT_{NPs}$ and τ_0 refers to the lifetime of bare $CdTe_{QDs}$.

All the photophysical properties are summarized in table 7.

Table 4.2. Summarized data for the photophysical properties of P3HT, $P3HT_{NPs}$, $CdTe_{QDs}$ and $CdTe_{QDs}/P3HT_{NPs}$

Samples	abs (nm)	emission (nm)	τ_f (ns)	k^s_q (s^{-1})	ϕ^s_q	ϕ^F_q [a]
P3HT	445	573	0.53	-	-	-
$P3HT_{NPs}$	480, 505, 550, 605	660, 720	0.35	-	-	0.07
$CdTe_{QDs}$	525	555	29	-	-	0.25
$CdTe_{QDs}/P3HT_{NPs}$	485, 515, 555, 610	555, 660, 720	0.43	$1.995x10^8$	0.998	-

[a] Fluorescence quantum yields are experimentally calculated, in aqueous media, with rhodamine B (Φ^F_q = 0.49 in ethanol) as reference.

4.4.3. Electrochemical and photoelectrochemical properties

The corresponding materials are also characterized by cyclic voltammetry (CV) in order to gain information about the conduction and valence band energy levels of the materials. (Figure 4.8) The materials drop casted on glassy carbon (working electrode) from their water dispersion. Only for the case of P3HT, the polymer drop casted from its THF solution. Then, the working electrode was placed into three-electrode electrochemical cell using an electrolyte 0.1 M Bu_4NPF_6 in acetonitrile.

First, the CV curve for $P3HT_{NPs}$ shows two reversible oxidations and one reversible reduction peaks similar to those observed in case of $P3HT_{NPs}$-GO hybrids (Chapter 2). The onset potential for the first oxidation peak of $P3HT_{NPs}$ is found to be at +0.50 V, whereas the onset potential for the reduction peak evolves at −1.80 V. These values result in an electrochemical gap of 2.30 eV, which is slightly narrower than the corresponding one of P3HT registered at 2.42 eV. The first oxidation and reduction onset potentials for P3HT are found to be as high as +0.52 and −1.90 V, respectively. The lower electrochemical gap for $P3HT_{NPs}$ is a consequence of an enhanced degree of crystalline aggregation, which can be easily characterized by vibronic features in UV−vis spectra in figure 4.5. Indeed, the first oxidation peak is indicative of crystalline aggregates, whereas the second one represents the amorphous phases.[14]

For $P3HT_{NPs}$, the first oxidation peak associated with the crystalline aggregations is strongly and it increased ca. by a factor of 2 with respect to the amorphous parts. The increased crystallinity of $P3HT_{NPS}$ equally well is observed at the reduction site. The CV studies on $P3HT_{NPs}$ thus show a response typical for a semicrystalline P3HT with a high degree of crystalline domains.[15]

On the other hand, the CV curve for $CdTe_{QDs}$ reveals two irreversible oxidation steps and one irreversible reduction process at +0.36, and +0.95 and −1.00 V, respectively, with a narrow electrochemical gap of 1.36 eV, in agreement with similar reports in the literature.[16,17]

Lastly, $CdTe_{QDs}/P3HT_{NPs}$ nanoensembles are studied by CV. In the CV curve for the $CdTe_{QDs}/P3HT_{NPs}$ ensembles, two broad irreversible oxidation peaks and a quasi-reversible reduction process appear. The broad shape of the oxidation peaks is characteristic of the $CdTe_{QDs}$ redox properties, and the onset potential at +0.45 V for $CdTe_{QDs}/P3HT_{NPs}$ is associated with the oxidation of $CdTe_{QDs}$, masking the oxidation of $P3HT_{NPs}$. On the other hand, the reduction response reveals a different behavior and supports the formation of a novel $CdTe_{QDs}/ P3HT_{NPs}$ system. The appearance of a quasi-reversible reduction peak at −1.60 V, proper to the new $CdTe_{QDs}/ P3HT_{NPs}$ system, underlines an easier reduction process by 200 mV as compared to the bare $P3HT_{NPs}$, thus highlighting the enhanced stabilization of the core−shell system as also observed in the UV−vis studies. In table 8 the electrochemical properties of P3HT, $P3HT_{NPs}$, $CdTe_{QDs}$, and $CdTe_{QDs}/ P3HT_{NPs}$ ensembles are summarized.

Table 4.3. Summarized data for the electrochemical properties of P3HT, $P3HT_{NPs}$, $CdTe_{QDs}$ and $CdTe_{QDs}/P3HT_{NPs}$.aPotential values are expressed vs the SCE reference electrode at 25 °C.

Samples	Redox Potentials (V)	E_g[a] (eV)
P3HT	+0.52, +0.64, -1.90	2.42
$P3HT_{NPs}$	+0.50, +0.65, -1.80, -1.85	2.35
$CdTe_{QDs}$	+0.36, +0.95, -1.00	1.36
$CdTe_{QDs}/P3HT_{NPs}$	+0.45, +0.86, -1.60, -1.83	2.05

[a] Calculated from the CV data.

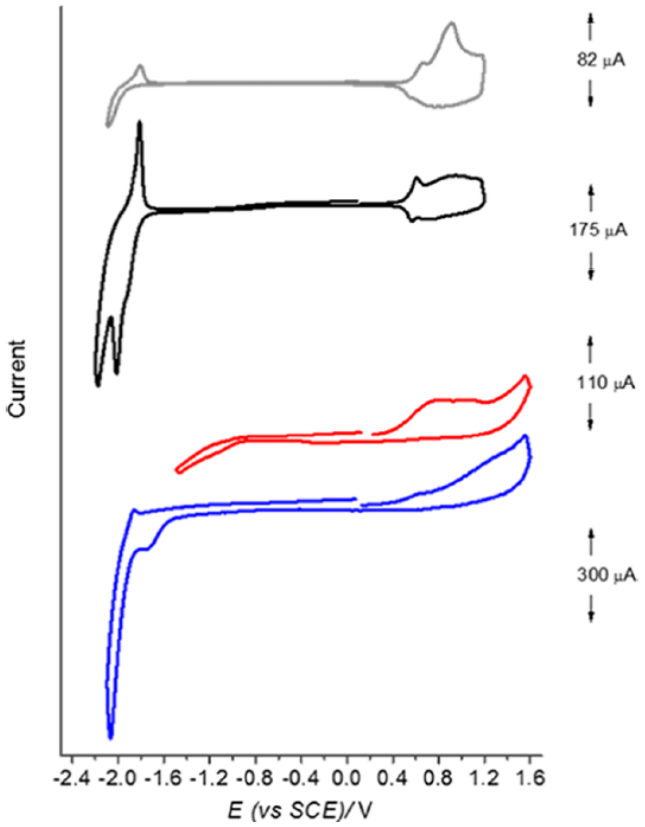

Figure 4.8. Cyclic voltammetry graphs for P3HT (gray), $P3HT_{NPs}$ (black), $CdTe_{QDs}$ (red), and $CdTe_{QDs}/P3HT_{NPs}$ ensembles (blue) recorded in acetonitrile under nitrogen-saturated atmosphere and in the presence of 0.1 M Bu_4NPF_6 as electrolyte.

Finally, photoelectrochemical measurements are performed in a three-electrode cell fitted with a quartz window, in 0.1 M $NaClO_4$ as the redox electrolyte in acetonitrile, employing a Ag/AgCl the reference electrode and a Pt wire as the counter electrode. Briefly, the working electrode consisting of either $P3HT_{NPs}$, $CdTe_{QDs}$, or $CdTe_{QDs}/P3HT_{NPs}$ films fabricated by spray-coating on FTO substrates covering an area of 1 cm × 1 cm is illuminated with white light and the observed photocurrent is measured.

Figure 4.9 shows the differences in the current densities under illumination and dark conditions as obtained from the cyclic voltammograms (I−V characteristics). The $P3HT_{NPs}$/FTO electrode reveals a negative photocurrent in the range from 0 to −0.6 V, where it decreases from 0 to −10 µA/cm^2, indicative of improved charge separation under applied bias voltage. Positive photocurrents are not observed. This photocathodic response is typical for p-type semiconductors and proves that upon bias applied voltage conditions, electrons from $P3HT_{NPs}$ flow to the electrolyte solution, whereas holes transport to the FTO electrode. On the contrary, $CdTe_{QDs}$/FTO and $CdTe_{QDs}/P3HT_{NPs}$/FTO electrodes show a distinct behavior. They exhibit a positive photocurrent in the range from 0 to 0.8 V. Negative photocurrents are not observed. For $CdTe_{QDs}$/FTO, this photoanodic response is typical for n-

type semiconductors and points out that under bias applied voltage, electrons are transported from $CdTe_{QDs}$ to the FTO electrode. As far as $CdTe_{QDs}/P3HT_{NPs}$/FTO is concerned, electrons from $CdTe_{QDs}$ are transferred to $P3HT_{NPs}$ and then to FTO responsible for the anodic photocurrent observed. Being also the case for the $CdTe_{QDs}/P3HT_{NPs}$ film, it is suggested that the interface to the electrolyte is formed by only $CdTe_{QDs}$. The latter is in direct agreement with the STEM observations, which shows that $CdTe_{QDs}$ are tightly deposited on the $P3HT_{NPs}$ to form a shell covering the $P3HT_{NPs}$ core in the $CdTe_{QDs}/P3HT_{NPs}$ ensemble.

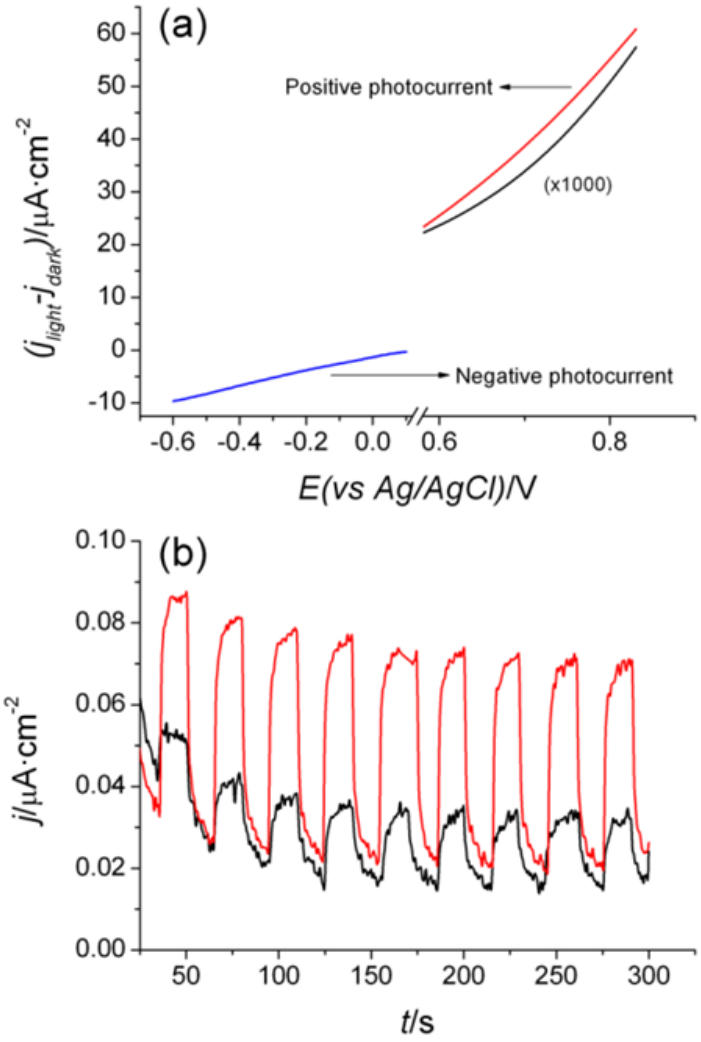

Figure 4.9. (a) Difference in current densities under illumination and dark conditions obtained from the cyclic voltammograms of films of $P3HT_{NPs}$ films (blue), $CdTe_{QDs}$ (black), and $CdTe_{QDs}/P3HT_{NPs}$ (red). (b) Photocurrent generation response of films of $CdTe_{QDs}$ (black) and $CdTe_{QDs}/P3HT_{NPs}$ (red) at an applied voltage of 0.8 V vs Ag/AgCl reference electrode under illumination.

Moreover, the maximum enhancement in the photocurrent, achieved at a bias voltage of around 0.8 V, reaches about 50 nA/cm^2. This is ca. 20% higher with respect to the bare for the $CdTe_{QDs}$/FTO electrode. Hence, electron injection from the reduced $P3HT_{NPs}$, as generated by

charge separation via the singlet excited state of $CdTe_{QDs}$, to the FTO electrode occurs, shows that $P3HT_{NPs}$ tends to accept electron. More insight into the enhancement in the photocurrent is provided by transient photocurrent response measurements. Figure 4.9b shows the transient photocurrent response of $CdTe_{QDs}$ and $CdTe_{QDs}/P3HT_{NPs}$ films under illumination, measured at an applied potential of 0.8 V over several cycles. The photocurrent responses are prompt, steady, and reproducible during repeated on/off cycles of the light illumination. Eliminating short time capacitive currents, the photocurrent for the $CdTe_{QDs}/P3HT_{NPs}$/FTO electrode reaches values that are almost 3 times higher as compared to the ones of the $CdTe_{QDs}$/FTO electrode. This result is also in agreement with the I−V characteristics (Figure 4.9a), thus highlighting the superiority of $CdTe_{QDs}/P3HT_{NPs}$/FTO over $CdTe_{QDs}$/FTO. The improved charge transfer/separation in the $CdTe_{QDs}/P3HT_{NPs}$ system is a direct consequence of the unique self-assembly possibilities of P3HT in the presence of aqueous dispersions and to form a core−shell system.

Lastly, figure 4.10 summarizes the conduction and the valence band for the individual $CdTe_{QDs}$ and the $P3HT_{NPs}$, as well as those for the $CdTe_{QDs}/P3HT_{NPs}$ nanoassembly, respectively, as calculated from redox data. The conduction band of $CdTe_{QDs}$ locates at lower energy as compared to that of $P3HT_{NPs}$, hence making energetically unfavorable the electron flow from the former to the latter component. However, the picture reverses when it comes to $P3HT_{NPs}/CdTe_{QDs}$, namely, the energy level of the conduction band owed to $CdTe_{QDs}$ is increased, thereby allowing diffused photoexcited electrons to travel toward the conduction band of $P3HT_{NPs}$ within the nanoensemble. Even though the real energy levels at the core−shell interface forming a p−n junction cannot be precisely calculated, because redox processes take place at the material−electrode interface.

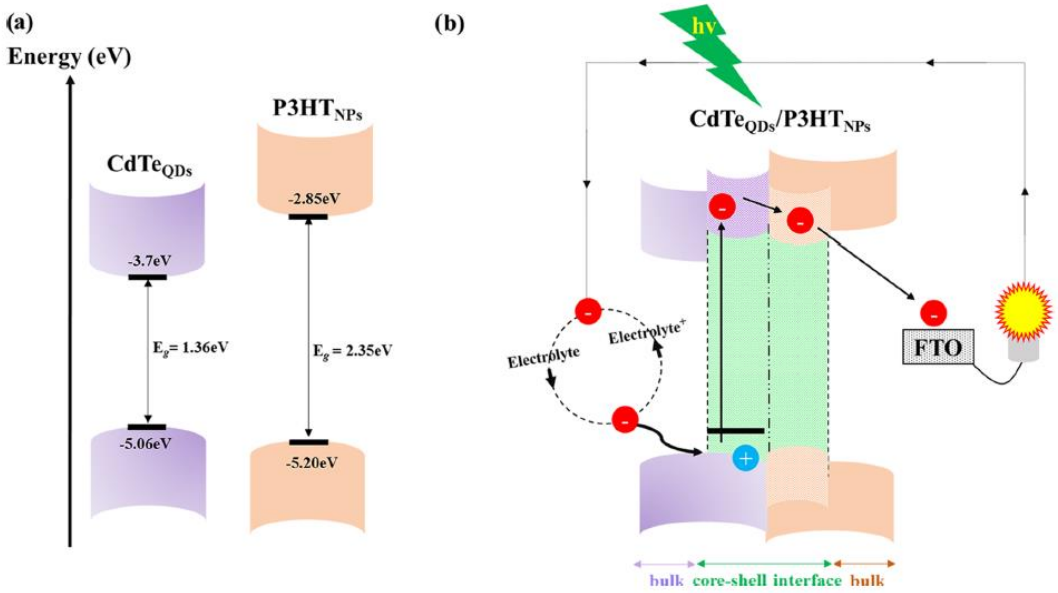

Figure 4.10. Energy diagram for (a) individual CdTe$_{QDs}$ and P3HT$_{NPs}$ as calculated from CV assays, and (b) CdTe$_{QDs}$/P3HT$_{NPs}$ ensembles at the core−shell interface forming a p−n junction.

4.5. Conclusion

Using a re-precipitation approach involving the rapid injection of a P3HT THF solution into an aqueous dispersion of semiconducting CdTe$_{QDs}$, the self-assembly of novel core-shell nanoparticle ensembles was achieved for the first time. The CdTe$_{QDs}$/P3HT$_{NPs}$ core-shell ensembles are characterized by photoluminescence spectroscopy and it yields an effective quenching of the photoluminescence of the shell forming CdTe$_{QDs}$ and thus confirms the existence of charge transfer processes at the interface between the CdTe$_{QDs}$ shell and the P3HT$_{NPs}$ core forming an effective donor-acceptor system, respectively. Moreover, the electrochemical response on films further supports the findings of a stabilized CdTe$_{QDs}$/P3HT$_{NPs}$ core-shell system in the solid state with three times enhanced photocurrent with respect to CdTe$_{QDs}$.

This study presents the possibility to synthesize novel organic-inorganic core shell ensembles with tunable donor-acceptor behavior via simple self-assembly processes employing conjugated polymers and inorganic semiconducting nanoparticles.

4.6. References

1. S.Kazaoui and N.Minami, Intermolecular charge transfer excitons in C70 as compared with C60 films, *Synth. Met*. 1997, 86, 2345-2346

2. M.D. Diener and J. M. Alford, Isolation and properties of small-bandgap fullerenes, *Nature*, 1998, 393, 668–671

3. S. Ren, L. Chang, S. Lim, J. Zhao, M. Smith, N. Zhao, V. Bulović, M. Bawendi, and S. Gradečak, Inorganic–Organic Hybrid Solar Cell: Bridging Quantum Dots to Conjugated Polymer Nanowires, *Nano Lett.* 2011, 11, 3998–4002.

4. S. Yao, Z. Chen, F. Li, B. Xu, J. Song, L. Yan, G. Jin, S. Wen, C. Wang, B. Yang and W. Tian, High-Efficiency Aqueous-Solution-Processed Hybrid Solar Cells Based on P3HT Dots and CdTeNanocrystals. *ACS Appl. Mater. Interfaces* 2015,7, 7146−7152.

5. J. Kwak W. K. Bae M. Zorn H. Woo H. Yoon J. Lim S. W. Kang S. Weber H.Butt R. Zentel S. Lee K.n Char and C. Lee, Characterization of Quantum Dot/Conducting Polymer Hybrid Films and Their Application to Light-Emitting Diodes, *Adv. Mater*. 2009, 21, 5022–5026.

6. M. Zorn, W. K. Bae, J. Kwak, H. Le, C. Lee, R. Zentel and K. Char, Quantum Dot−Block Copolymer Hybrids with Improved Properties and Their Application to Quantum Dot Light-Emitting Devices, *ACS Nano*, 2009, 3, 5, 1063–1068.

7. Y. Zhang, Y. Li and X.P. Yan, Aqueous Layer-by-Layer Epitaxy of Type-II CdTe/CdSe Quantum Dots with Near-Infrared Fluorescence for Bioimaging Applications, *Small*, 2009, 5, 185-189.

8. J. Wang and H. Han, Hydrothermal Synthesis of High-Quality Type-II CdTe/CdSe Quantum Dots with Near-Infrared Fluorescence, *J. Colloid Interface Sci*., 2010, 351, 83-87

9. M. T. Khan, A. Kaur, S.K. Dhawan and S. Chand, In-Situ Growth of Cadmium Telluride Nanocrystals in Poly(3-hexylthiophene) Matrix for Photovoltaic Application, *J. Appl. Phys.* 110, 044509

10. M.J. Chmielewski, M. Pawlicki, N. Sprutta, L. Szterenberg and L.L. Grazynski, L. L. Cadmium(II) and Zinc(II) Complexes of S-Confused Thiaporphyrin. *Inorganic Chemistry*, 45, 21, 2006.

11. T. Hasobe, A. S. D. Sandanayaka, T. Wadac and Y.Arakic, Fullerene-Encapsulated Porphyrin Hexagonal Nanorods. An Anisotropic Donor–Acceptor Composite for

Efficient Photoinduced Electron Transfer and Light Energy Conversion, *Chem. Commun*., 2008, 3372–3374

12. M. Baghgar and M.D. Barnes, Work Function Modification in P3HT H/J Aggregate Nanostructures Revealed by Kelvin Probe Force Microscopy and Photoluminescence Imaging, *ACS Nano*, 2015, 9, 7105−7112.

13. E. T. Niles, J. D. Roehling, H. Yamagata, A. J. Wise, F. C. Spano, A. J. Moulé and J. K. Grey, J-Aggregate Behavior in Poly-3- hexylthiophene Nanofibers. *J. Phys. Chem. Lett.* 2012, 3, 259−263.

14. S. Sweetnam, K. R. Graham, G. O. Ngongang Ndjawa, T. Heumüller, J. A. Bartelt, T. M. Burke, W. Li, W. You, A. Amassian and M.D. McGehee, Characterization of the Polymer Energy Landscape in Polymer:Fullerene Bulk Heterojunctions with Pure and Mixed Phases, *J. Am. Chem. Soc*. 2014, 136, 14078−14088.

15. D. A. M. Egbe, L. H. Nguyen, B. Carbonnier, D. Mühlbacher and N. S. Sariciftci, Thiophene-Containing Poly(arylene−ethynylene)- altpoly(arylene-vinylene)s: Synthesis, Characterisation and Optical Properties, *Polymer* 2005, 46, 9585−9595.

16. M. Amelia, C. Lincheneau, S. Silvi and A. Credi, Electrochemical Properties of CdSe and CdTe Quantum Dots, *Chem. Soc. Rev*. 2012, 41, 5728−5743.

17. S.K. Poznyak, N. P. Osipovich, A. Shavel, D.V. Talapin, M. Gao, A.Eychmüller and N. Gaponik, Size-Dependent Electrochemical Behavior of Thiol-Capped CdTe Nanocrystals in Aqueous Solution, *J. Phys. Chem. B*. 2005, 109, 1094−1100.

5. INTERFACING WATER-SOLUBLE POLYTHIOPHENE WITH TRANSITION METAL DICHALCOGENIDES

5.1.Abstract

In this chapter, covalently functionalized two dimensional transition metal dichalcogenides (2D-TMDs) were hybridized with a water soluble polythiophene derivative in order to profit from electrostatic interactions during the self-assembly approach. Preparation, characterization, and photophysical and electrochemical properties of nano-ensembles are reported. The electrostatic interaction takes place between the positive charges on functionalized MoS_2 and WS_2, owed to the presence of ammonium units, and carboxylate moieties on polymer, yielding poly (3-thiophene sodium acetate)/MoS_2 and poly (3-thiophene sodium acetate)/WS_2 ensembles. The electronic interactions between the species within poly (3-thiophene sodium acetate)/MoS_2 and poly (3-thiophene sodium acetate)/WS_2 ensembles were elucidated from absorption and photoluminescence titration assays. Efficient fluorescence quenching of polythiophene by MoS_2 and WS_2 was observed and attributed to photoinduced electron or/energy transfer. Moreover, under specific photoelectrochemical conditions, poly (3-thiophene sodium acetate)/MoS_2 and poly (3-thiophene sodium acetate)/WS_2 ensembles show enhanced photocurrent compared to individual exfoliated materials, especially in case of WS_2, correspond to electron transfer between the components within the ensembles.

5.2. Interaction of 2D-TMDs with conjugated organic materials

2D-TMDs such as MoS_2 and WS_2 are currently intensively investigated due to their unique electronic and optical properties (including tunable optical bandgaps). Combining 2D-TMDs with organic materials such as organic dyes or polymers offer great promise for the development of materials with superior properties for potential applications. Especially, the combination with organic materials including donors, acceptors, photosensitive polymers and small molecules can lead the establishment of favorable interaction between both classes of material, thus forming the base for optoelectronic device application with improved performance.[1]

For example, an organic dye combining with MoS_2 and taking advantage of the high optical absorption efficiency of organic dyes and the relatively high charge mobility in MoS_2, a high performance photodetector was constructed.[2]

Furthermore, by bring in contact MoS_2 and WS_2, owing to the presence of ammonium units, with an anionic porphyrin bearing a carboxylate moiety, porphyrin/MoS_2 and porphyrin/WS_2 ensembles were prepared. Those ensembles revealed energy transfer from the photoexcited porphyrin to MoS_2 or WS_2.[3]

Moreover, interaction between the 2D-TMDs and conjugated polymers were also reported. For example, a hybrid structure consisting of poly (3, 4-ethylenedioxythiophene) and MoS_2 showed enhanced electrochemical capacitance performance being 4 times higher than a PEDOT electrode itself.[4] In another study, a solution-based approach was developed to grow PPy ultrathin films on 2D MoS_2 monolayers. These sandwich like nanocomposite structures were used as supercapacitor electrodes revealing a high specific capacitance.[5] While these studies focused on the electrochemical energy storage performance, no studies yet are carried out on charge-transfer properties of CPs-TMDs for optoelectronic applications.

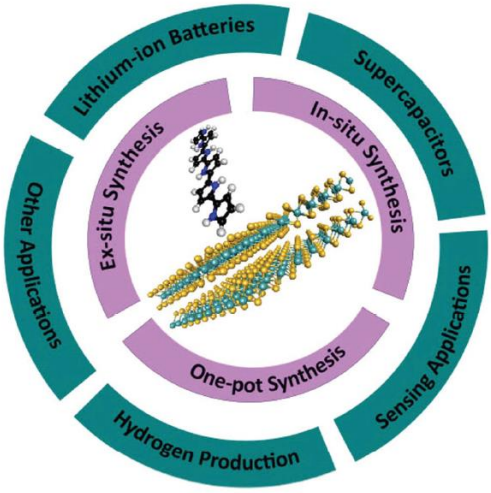

Figure 5.1 Schematic illustration of the synthetic methods and applications of TMDs/CPs hybrid materials. (Nanoscale, 2017, 9, 8052–8065)[15]

In this chapter, the synthesis of a water-soluble polythiophene with TMDs (MoS_2 and WS_2) is descired. To achieve this, (a) polythiophene was specifically modified to graft carboxylic units on its skeleton, which can be easily ionized to the corresponding carboxylates, and (b) exfoliated MoS_2 and WS_2 were initially exfoliated from the bulk and subsequently modified to carry ammonium units. The newly formed ensembles were characterized via complementary spectroscopic and imaging techniques and their optical properties were investigated. More importantly, the charge transfer between the materials was also elucidated by photoelectrochemistry experiments and exhibits enhanced cathodic photocurrent in case of WS2-polythiopene ensembles.

5.3. Experimental Section

5.3.1. Materials

3-Thiophene acetic acid, iron (III) chloride ($FeCl_3$), dry $CHCl_3$, acetonitrile, sulphuric acid (H_2SO_4) were purchased from Sigma-Aldrich and were used as received. MeOH dried over 3Å molecular sieves for overnight. $NaClO_4$ was dried overnight at 130^0C in vacuum oven before use. Ammonium functionalized MoS_2 and WS_2 were synthesized a research stay at in National Hellenic Research Foundation in Athens in collaboration with group of Dr. Nikos Tagmatarchis.

5.3.2. Characterization

- ^{1}H-NMR spectra were recorded in $CDCl_3$ solutions at 25 ºC on a Bruker AV500 spectrometer (δ in ppm and J in Hz) at a ^{1}H NMR operating frequency of 500.13 MHz.
- Steady-state UV-Vis electronic absorption spectra were recorded on a PerkinElmer (Lambda 19) UV-Vis-NIR spectrophotometer.
- Steady-state emission spectra were recorded on a Fluorolog-3 JobinYvon-Spex spectrofluorometer (model GL3-21).
- Picosecond time-resolved fluorescence spectra were measured by the time-correlated-single-photon-counting (TCSPC) method on a Nano-Log spectrofluorometer (Horiba JobinYvon), by using a laser diode as an excitation source (NanoLED, 375 nm) and a UV-Vis detector TBX-PMT series (250-850 nm) by Horiba JobinYvon. Lifetimes were evaluated with the DAS6 Fluorescence-Decay Analysis Software.
- Mid-infrared spectra in the region 500−4500 cm^{-1} were obtained on a Fourier transform IR spectrometer (Equinox 55 from Bruker Optics) equipped with a single reflection diamond ATR accessory (DuraSamp1IR II by SensIR Technologies). A drop of the solution was placed on the diamond surface, followed by evaporation of the solvent, in a stream of nitrogen, before recording the spectrum. Typically, 100 scans were acquired at 2 cm^{-1} resolution.
- Micro-Raman scattering measurements were performed at room temperature in the backscattering geometry using a Renishaw inVia Raman microscope equipped with a CCD camera and a Leica microscope. A 2400 lines mm^{-1} grating was used for all measurements, providing a spectral resolution of ± 1 cm^{-1}. As an excitation source the Ar+ laser (633 nm with less than 2.65 mW laser power) was used. Measurements were

taken with 15 seconds of exposure times at varying numbers of accumulations. The laser spot was focused on the sample surface using a long working distance 50x objective. Raman spectra were collected on numerous spots on the sample and recorded with Peltier cooled CCD camera. The data were collected and analyzed with Renishaw Wire and Origin software.

- Thermogravimetric analysis was performed using a TGA Q500 V20.2 Build 27 instrument by TA in a nitrogen (purity >99.999%) inert atmosphere.
- Scanning electron microscope (SEM) imaging and energy dispersive X-ray spectroscopy (EDS) were performed using a FE-SEM (model JSM-7610F) equipped with an EDAX (X-ACT, Oxford instrument).
- Zeta potential studies were carried out using a Zeta-sizer NanoZS (Malvern instruments Ltd, UK).
- The electrochemical experiments were performed with a AUTOLAB PGSTAT302N potentiostat. Cyclic voltammetry were carried out from spray-coated samples on FTO under nitrogen in a three- electrode cell using 0.1 M $NaClO_4$ in dry acetonitrile as a supporting electrolyte. Scan rates of 20 mV/s were employed. (For all the samples the concentration carefully adjusted in order to better comparison. The concentration of MoS_2 and WS_2 in 3a and 3b were adjusted where the most effective quenching observed in PL measurement; +160μl).
- Photoelectrochemical measurements were carried out spray-coated samples on FTO substrates covering an area of 1 cm^2 as working electrode, which were illuminated through a quartz window by a 150 W Xenon arc lamp (LOT-Oriel GmbH, Germany).

5.3.3. Synthesis and characterization of poly (3-thiophene sodium acetate) (1)

The synthesis of the poly (3-thiophene sodium acetate) **1** was accomplished in three steps. Firstly, 3-thiophene acetic acid was initially esterified to the corresponding methyl acetate derivative, in order to protect the oxidative decomposition of the carboxylic acid side chain of the monomer during the oxidative coupling polymerization reaction.[6] Next, the thiophene ester was polymerized, by employing iron (III) chloride as oxidative coupling agent. Subsequent alkaline hydrolysis of the ester, resulted on the negatively charged water-soluble poly (3-thiophene sodium acetate) **1**, which was further purified by dialysis and obtained in powder form by repetitive freeze-drying cycles**.**

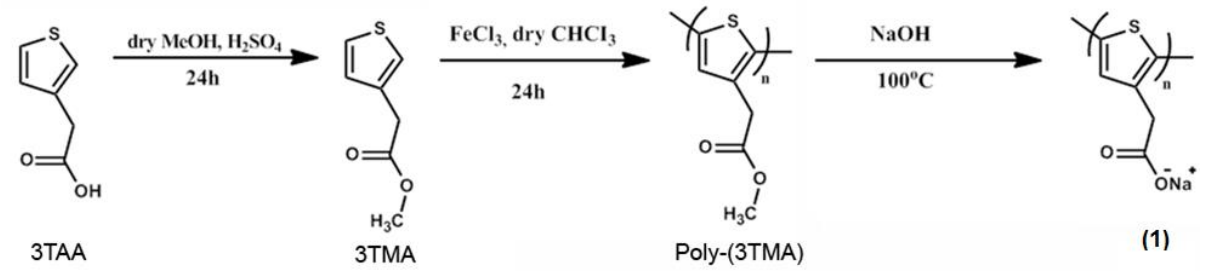

Scheme 5.1. Synthesis of poly (3-thiophene sodium acetate).

5.3.4. Synthesis of 3-thiophene methyl acetate (3TMA)

Thiophene-3-acetic acid (1 g) in dry methanol (20 mL) with a 0.05 mL H_2SO_4 was refluxed for 24 hours. Then, the reaction poured onto the ultrapure water and extracted with dichloromethane. The organic phase was dried over magnesium sulfate and the solvent was evaporated to yield a pale-yellow liquid. Yield: 80 %.

5.3.5. Synthesis of poly (3-thiophene methyl acetate) (Poly-(3TMA)

The monomer 3-thiophene methyl acetate (2 mmol) was dissolved in 10 mL of dry chloroform and $FeCl_3$ (8 mmol) dissolved in 10 mL of chloroform was added dropwise under inert atmosphere. The reaction mixture was stirred at room temperature for 24 hours, then poured into methanol and the precipitate was filtered. The filtered polymer was washed with methanol and water several times to remove unreacted monomer and any $FeCl_3$ residue. The obtained poly (3-thiophene methyl acetate) was dried at room temperature overnight.

5.3.6. Synthesis of poly (3-thiophene sodium acetate) (1)

Poly (3-thiophene methyl acetate) (100 mg), deionized water (50 mL) and 2 M NaOH (10 mL) were placed in a double-neck flask and refluxed overnight. After that period, the reaction mixture was filtered and the supernatant centrifuged at 4000 rpm for 5 min in order to remove any insoluble materials. The collected supernatant was transferred inside a dialysis tubing and dialyzed against deionized water for 3 days at room temperature. Subsequent evaporation of water by freeze-drying technique gave **1** as a reddish solid which can be soluble in water.

Figure 5.2. Solution of poly (3-thiophene sodium acetate) in water.

5.3.7. ^{1}H-NMR characterization

The structure of **3TMA**, **poly-(3TMA)** and **1** was verified by ^{1}H-NMR in figure 5.3. In figure.5.3 a), apart from the thiophene aromatic signals located between 7.5-7.0 ppm, the methyl peak at 3.6 ppm labelled as "H_e", indicates the successful esterification of thiophene-3-acetic. In case of poly (3-thiophene methyl acetate), the ^{1}H-NMR signals are broader than the one observed in the corresponding monomer 3-thiophene methyl acetate,due to the interaction of abundant number of protons on the polymer chain. Lastly, after the hydrolysis of the ester from the poly-(3TMA), the integration of the peak shows the presence of only two types of protons in poly (3-thiophene sodium acetate), i.e. the one is from aromatic proton (H_a) and the other is methylene proton (H_b). This indicates that the methyl group in poly-(3TMA) are deprotonated by NaOH base thus confirming the pure structure of poly (3-thiophene sodium acetate).

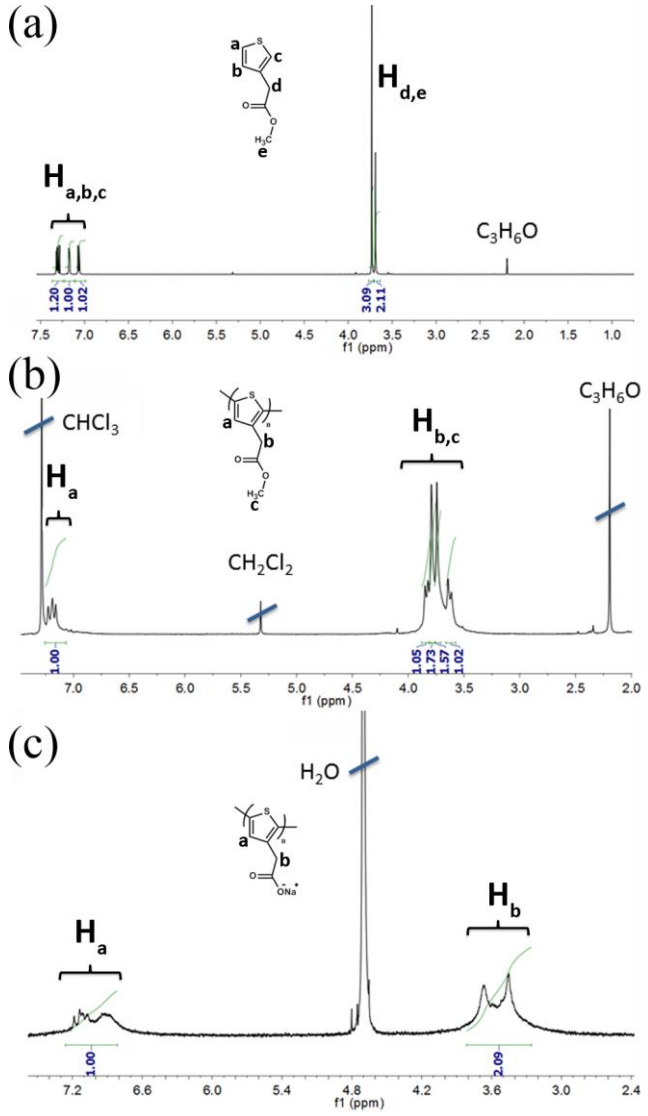

Figure 5.3. ^{1}H-NMR spectrum of poly (3-thiophene sodium acetate) (1) in D_2O (c) as compared to the corresponding spectra due to poly (3-thiophene methyl acetate) in $CDCl_3$ (b), and 3-thiophene methyl acetate in $CDCl_3$ (a).

5.3.8. FTIR characterization

FTIR spectroscopy measurements were carried out for poly (3-thiophene sodium acetate) **1** and for poly (3-thiophene methyl acetate) **poly-(3TMA)** in order to elucidate the functional groups on the polymer structure. (Figure 5.4) Besides, FTIR gives a useful information for alkaline hydrolysis of the ester by downshift of carbonyl peak.

The polymer **1** and **poly-(3TMA)** reveals three important IR absorption regions associated to vibrational modes of the thiophene rings (1450 - 1510 cm^{-1}, and 840 cm^{-1}), carboxylic moieties (1750 -1500 cm^{-1}) and ester groups (1300-1100 cm^{-1}) . The C=C stretch vibrations of the thiophene rings appear at 1435 cm^{-1} and 1378 cm^{-1} for polymer **1** and **poly-(3TMA)** respectively. The band at 840 cm^{-1} corresponds to the out-of skeleton C-H bending mode on

the thiophene ring and the position is the same for both polymers. The band located between 1731 and 1575 cm^{-1} for polymer **1** and **poly-(3TMA),** respectively, is caused by the carbonyl stretching modes. The down-shift of around 200 cm^{-1} of carbonyl peak confirms the successful hydrolysis of the ester to the carboxylate units. Moreover, the C-O related infrared peaks are located at 1325 and 1271 cm^{-1} for polymer **1** and **poly-(3TMA),** respectively**.**

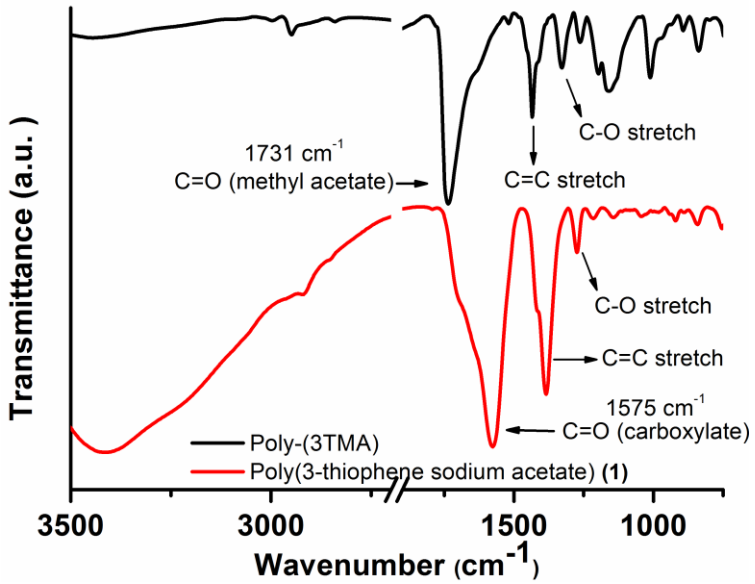

Figure 5.4. FTIR spectrum of poly (3-thiophene methyl acetate) (Poly-(3TMA) and poly (3-thiophene sodium acetate) (1).

5.3.9. Synthesis of ammonium functionalized MoS_2 and WS_2

Firstly, the exfoliation of semiconducting MoS_2 and WS_2 were prepared from the bulk upon chlorosulfonic acid treatment.[7] Based on the general functionalization methodology of exfoliated transition metal dichalcogenides with 1,2-dithiolanes,[8] treatments of exfoliated MoS_2 and WS_2 with 1,2-dithiolane tert-butyl carbamate derivative yielded the butoxycarbonyl (BOC)-modified MoS_2 and WS_2 materials. Subsequent, acidic deprotection ($HCl_{(g)}$) of the BOC group results the ammonium functionalized materials **2a** and **2b** [9, 10] according to scheme 5.2. At this stage, two points should be noted (i) the presence of a solubilizing chain added to the modified MoS_2 and WS_2, in **2a** and **2b**, allowing handling and characterization in liquid media, and (ii) the existence of positive charges due to the incorporated ammonium species, in **2a** and **2b**, which can be exploited for achieving attractive electrostatic interactions. The functionalization of chemically exfoliated MoS_2 with 1,2-dithiolanes takes place at the edges due to high binding affinity of Mo atoms, particularly those located at the edges of the MoS_2 sheets. [9]

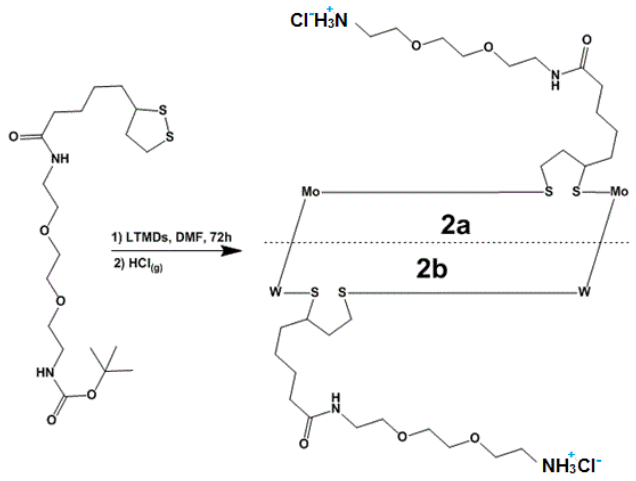

Scheme 5.2. Functionalization of MoS_2 and WS_2 leading to ammonium-modified MoS_2 (2a) and WS_2 (2b), based material

5.3.10. Characterization of ammonium functionalized MoS_2 and WS_2

The functionalization of MoS_2 and WS_2 were proved by several techniques including Infrared spectroscopy (IR), Raman spectroscopy, thermogravimetry (TGA), Kaiser test and ζ-potential assays. IR spectroscopy verified the success for the preparation of BOC-modified MoS_2 and WS_2 and the corresponding ammonium functionalized materials **2a** and **2b**, by observing spectral changes in the characteristic carbonyl vibrations due to the amide and BOC moieties. Before BOC cleavage there are two carbonyls peaks at 1710 cm^{-1} and 1665 cm^{-1}, corresponding to carbamate and amide carbonyl units respectively. As a result of hydrochloric acid (HCl) gas treatment BOC cleavage occurs and only amide carbonyl remained on FTIR spectra (Figure 5.5). This results confirms the ammonium functionalization on MoS_2 and WS_2.

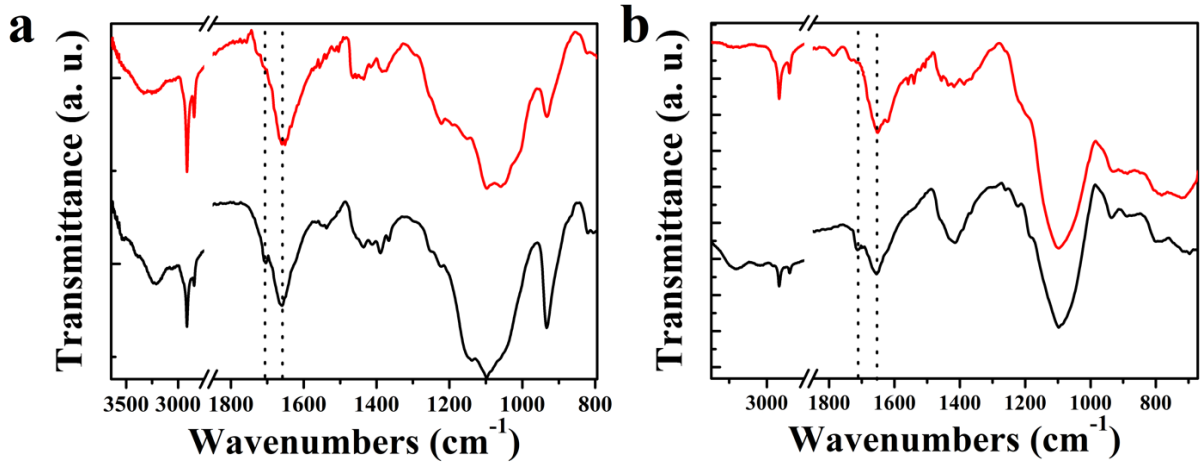

Figure 5.5. ATR-IR spectra of BOC-modified MoS_2 (black – left panel) and WS_2 (black – right panel) and the corresponding ammonium functionalized materials 2a (red – left panel) and 2b (red – right panel).

Raman measurements were carried out under on-resonance conditions (633 nm for MoS_2-based materials and 514 nm for WS_2-based materials) on drop-casted films of the materials. Specifically, the Raman spectrum of MoS_2 is governed by three distinctive modes, namely, the 2LA(M) band located at 460 cm^{-1}, which is associated with sulfur defected sites, the A_{1g} band located at 406 cm-1 which is associated with out-of-plane vibrations, the E^1_{2g} band located at 380 cm-1 which is associated with in-plane vibrations. Importantly, the ammonium modified MoS_2 material (**2a)** was characterized by alterations in intensity of the 2LA(M) mode as compared with that due to exfoliated MoS_2. The intensity ratio $I_{2LA(M)}/I_{A1g}$ decreased from 2.09 to 0.85 for **2a** due to the exfoliated MoS_2 (Figure 5.6a). The decrease in the intensity of the 2LA(M) band for the functionalized material **2a** suggests a reduced number of sulfur defects due to edge functionalization of MoS_2. Similar situation is observed by the Raman spectroscopy in WS_2-based materials. In this case, WS_2 shows Raman features at 350, 355 and 419 cm-1, related with the 2LA(M), E^1_{2g} and A_{1g} modes, respectively. Again, the 2LA(M) band decreased for the modified material (**2b)** as compared to that belonging to exfoliated WS_2.

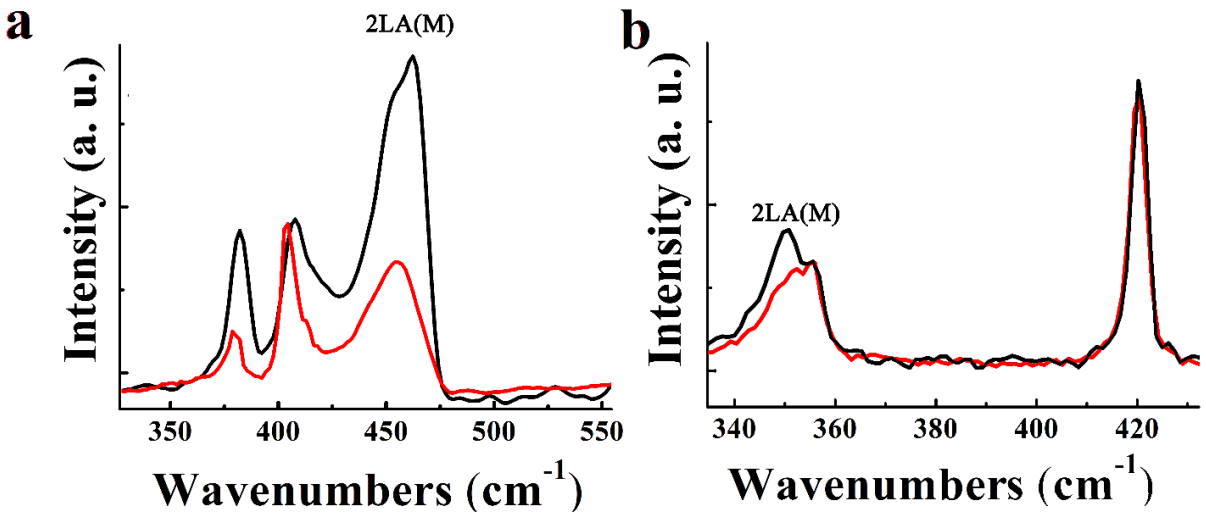

Figure 5.6. a) Raman spectra (633 nm) for exfoliated MoS_2 (black) and 2a (red). b) Raman spectra (514 nm) for exfoliated WS_2 (black) and 2b (red).

Besides, covalent functionalization of MoS_2 and WS_2 with 1,2-dithiolanes were characterized by thermogravimetric analysis (TGA) over the temperature range of 200–800 ^{0}C under a nitrogen atmosphere. TGA results exhibit that the estimation of one ammonium moiety per 48 and 35 units of MoS_2 and WS_2, respectively, by calculating the corresponding mass loss observed in the temperature range 250-540 ^{o}C (which was related to decomposition of the organic part incorporated into MoS_2 and WS_2) as 2.6 and 2.3 % for **2a** and **2b. (**Figure 5.7)

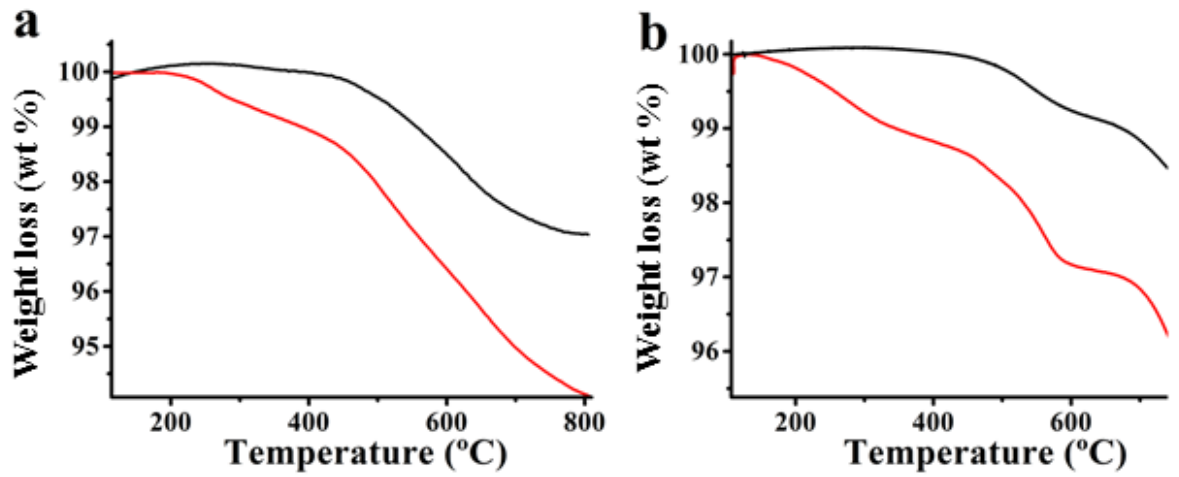

Figure 5.7. TGA of (a) exfoliated MoS_2 (black) as compared with 2a (red) and (b) exfoliated WS_2 (black) as compared with 2b (red), obtained under nitrogen

Lastly, the ζ–potential experiment were also performed and revealed high difference in the values obtained between exfoliated MoS_2 (-25.7 mV) and WS_2 (-31.5 mV) as compared with those due to ammonium modified materials **2a** (10.5 mV) and **2b** (-6.9 mV), respectively. These are consistent with the presence of ammonium functionalities which carry the positive charges.

5.3.11. Synthesis and characterization of water soluble polythiophene (poly (3-thiophene) sodium acetate)-TMDs ensembles

The formation of ensembles of water soluble polythiophene (**1**) with **2a** and **2b** was accomplished by profiting from electrostatic interactions between the positive charges of **2a** and **2b** and the negatively charged polymer **1**. The electrostatic formation of polymer/MoS_2 (**3a**) and polymer/WS_2 (**3b**) ensembles were created upon addition of aqueous **2a** and **2b** to water-soluble **1**. The overall synthesis scheme is illustrated in scheme 5.3.

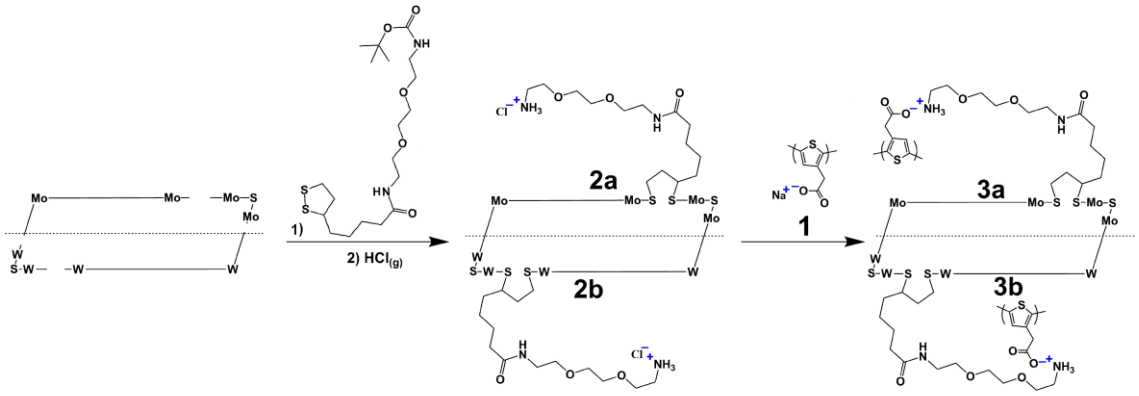

Scheme 5.3. Illustration of the preparation route for ammonium modified transition metal dichalcogenides 2a (ammounium modified MoS_2) and 2b (ammounium modified WS_2) and their ensembles with poly (3-thiophene sodium acetate) (1), furnishing 3a and 3b, respectively.

5.4. Results and Discussions

5.4.1. Optical properties of polymer/MoS_2 (3a) and polymer/WS_2 (3b) ensembles

The electrostatic formation of polymer/MoS_2 **3a** and polymer/WS_2 **3b** ensembles was monitored by absorption and emission spectroscopy techniques, based on titration assays. The polymer concentration keeps constant during the experiment and the changing with addition of **2a** and **2b** were observed from the UV and photoluminescence spectra which **2a** and **2b** background were subtracted.

In more detail, the UV-Vis spectrum of **1** exhibits a strong and broad absorption band around 400 nm due to π-π* transitions of the conjugated polymer backbone, corresponding to the non-aggregated amorphous polymer domains.[11]

Upon incremental additions of **2a** and **2b**, the excitonic bands of MoS_2 at 629 and 687 nm and of WS_2 at 654 nm started to appear. (Figure 5.8)

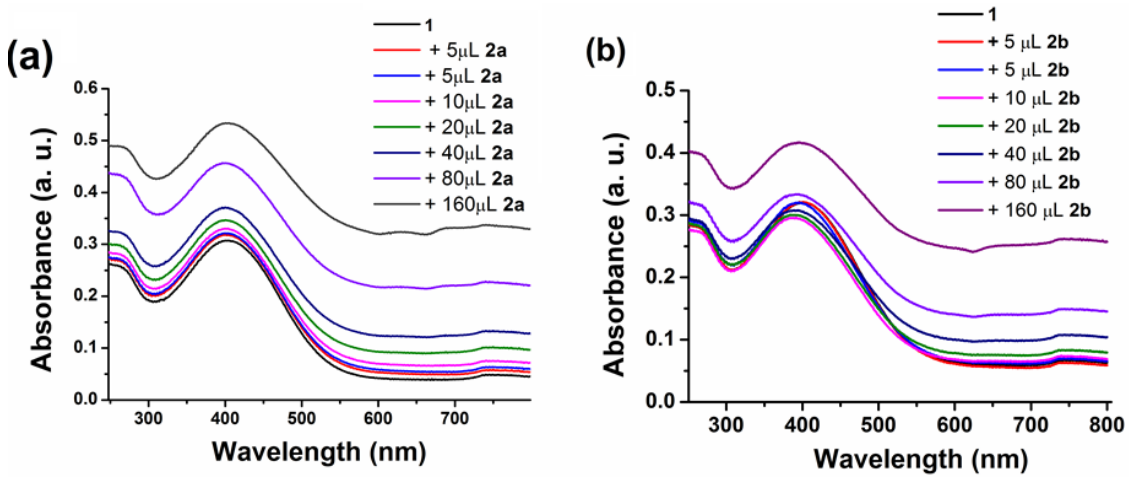

Figure 5.8. Absorption spectra of negatively charged polymer (1) upon incremental additions of positively charged MoS_2 based material 2a and, positively charged WS_2 based material 2b obtained in water.

Subtraction of the absorption background due to MoS_2 and WS_2 allowed a clear observation of the titration effect on the polymer's absorption features, during formation of **3a** and **3b**. (Figure 5.9) Specifically, a blue-shift of 4 and 9 nm of the polymer's band after a total of 290 μL and 40 μL was observed for **3a** and **3b**, respectively (Figure 5.9). This hypsochromic shift corresponds to conformational changes on the structure of **1**, as the long π-π conjugation system of the coplanar polythiophene breaks due to the developed attractive electrostatic interactions with the modified transition metal dichalcogenides **2a** and **2b**. [6] In addition, the absorption band due to **1** was progressively decreased upon interaction with **2a** and **2b**. Considering that the unstacked carboxylate unit absorbs more light in intact polymer **1**, the latter decrease identified in the corresponding absorption band of the ensembles **3a** and **3b** can be safely attributed to efficient interactions developed between the carboxylate units of **1** and the ammonium species of **2a** and **2b**, respectively.

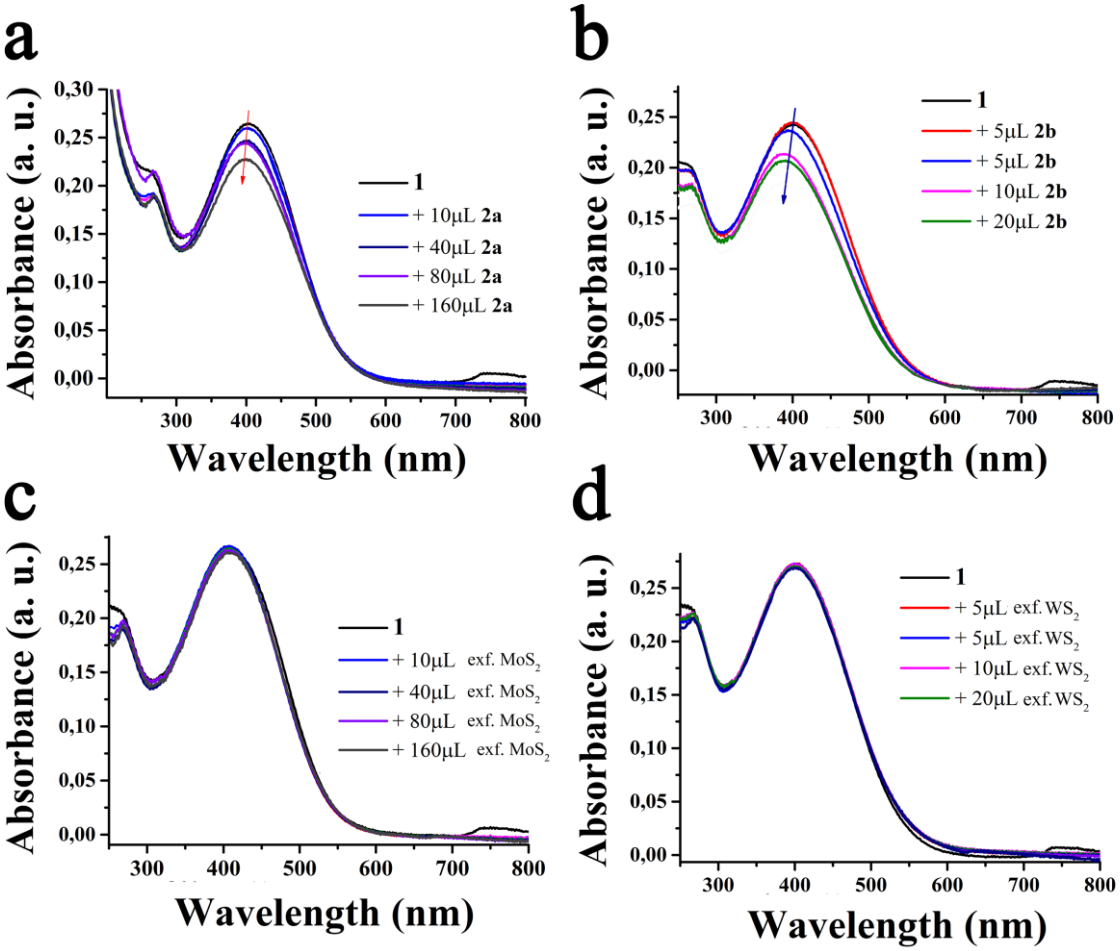

Figure 5.9. Electronic absorption spectra of 1 upon incremental additions of (a) ammonium modified MoS_2 (2a), forming the ensemble material (3a), (b) ammonium modified WS_2 (2b) forming the ensemble material (3b). UV-Vis blank titration assays of (1) upon incremental additions of (c) exfoliated MoS_2, and (d) exfoliated WS_2. (*Absorption background due to MoS_2 and WS_2 are substracted)*

On the other hand, in blank titration assays were performed by employing exfoliated MoS_2 and WS_2 instead of the positively charged **2a** and **2b**. As a result, neither blue-shift nor a decrease in the polymer's absorption features were observed figure 5.9c and 5.9d. This indicates the role of modified MoS_2 and WS_2 with ammonium units for the effective coulombic association with **1**.

Photoluminescence spectroscopy measurements were carried out to elucidate possible interactions between **1** with **2a** and **2b** at the excited states. Aqueous solution of water soluble polythiophene **1,** exhibits broad fluorescence emission spectra with maxima at 555 nm, upon excitation at 395 nm. This broad emission corresponds to conjugated aromatic structures in amorphous morphology of polythiophene and any crystalline aggregate structure was not observed. This photoluminescence band gradually decreases with increasing amounts of ammonium modified MoS_2 **2a** or WS_2 **2b** (Figure 5.10) thereby leading to the realization of **3a** and **3b**, respectively. These findings confirm the effective deactivation of the singlet

excited state of **1** to MoS_2 and WS_2, via energy and/or electron-transfer the decay mechanism. The quenching rate is higher in case of **2b** and this can be attributed to relatively effective electronic interaction in compare to **2a**.

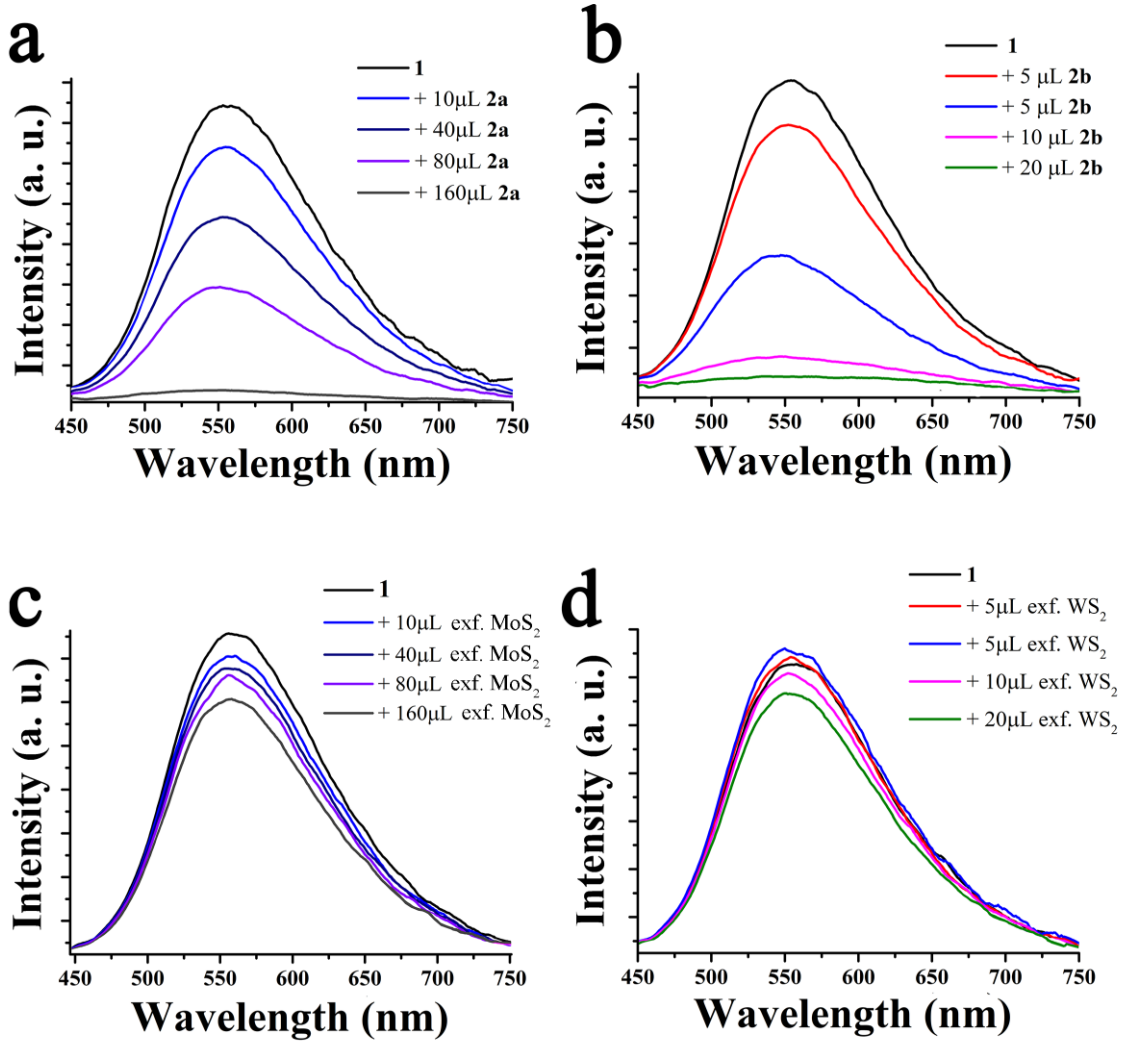

Figure 5.10. Photoluminescence spectra of (1) upon incremental additions of (a) ammonium modified MoS_2 (2a), forming ensemble (3a), (b) ammonium modified WS_2 (2b), forming ensemble (3b). Blank photolumines-cence titration assays of 1 upon incremental additions of (c) exfoliated MoS_2, and (d) exfoliated WS_2. All measurements were conducted upon excitation at 395 nm

On the other hand, when blank assays were investigated, by incorporating exfoliated MoS_2 and WS_2, instead of the positively charged ones, a substantially lower quenching rate for the emission of **1** was observed (Figure 5.10c and 5.10d).

The observation of intraensemble photoinduced processes from poly(3-thiophene sodium acetate) 1 to MoS_2 and WS_2 is consistent with the oxidation potential of the former, precisely the energy of the singlet excited state of 1, that lies above the conduction band of MoS_2 and WS_2. The energy for the singlet excited state of 1 can be easily obtained from the crossing point of the corresponding absorption and emission spectra (Figure 5.11) and found to be 2.50

eV. On the other hand, the conduction band edges for MoS_2 and WS_2 were calcualted to be 4.27 and 3.96 eV below the vacuum level, respectively, as a result of the higher reactivity of Mo vs W.[12]

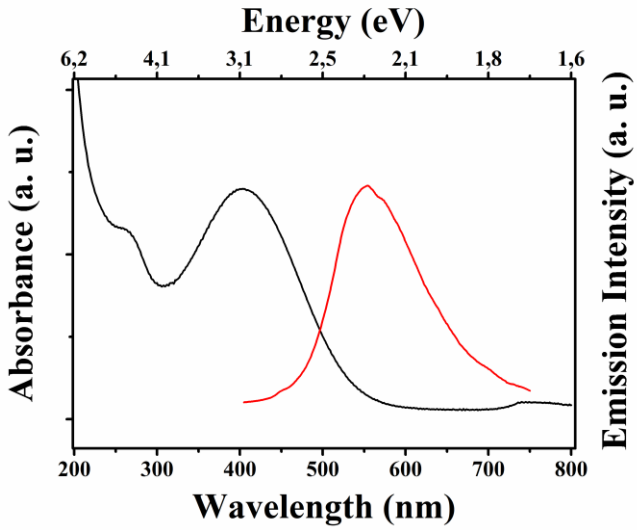

Figure 5.11. UV-Vis absorption and fluorescence emission spectra of poly(3-thiophene sodium acetate) (1). From the crossing point of the two spectra the energy of the singlet excited state of 1 is derived as 2.50 eV.

Hence, photoexcited electron/energy transfer from **1** to both MoS_2 and WS_2 within **3a** and **3b** respectively, is an energetically favored process. Moreover, the degree of fluorescence emission quenching of **1** in the presence of WS_2 is more prominent than that registered by MoS_2. For instance, for the quantitative emission quenching of 1 (2 mL, 10 mM) addition of 290 μL of **2a** (0.33 mg/mL) is required, while only 40 μL of **2b** (0.33 mg/mL) produces similar result (Figure 5.10a and 5.10b). This fact is attributed to the smaller energy difference between the singlet excited state of 1 and the conduction band of WS_2, calculated to be 1.46 eV, as compared to that of MoS_2 which is 1.77 eV.

All these results consistently confirm the advantageous function of electrostatic interactions between the negatively charged polymer **1** and the positively charged transition metal dichalcogenides **2a** and **2b** not only for the realization of the nanoensembles **3a** and **3b** but also for succeeding efficient electronic communication.

In order to get additional insight on the electronic communication between **1** with MoS_2 and WS_2, within **3a** and **3b**, time-resolved photoluminescence assays based on the time-correlated-single-photon-counting method were conducted. Water soluble polythiophene (**1)** shows a decay at 555 nm, which was monoexponentially fitted with a lifetime of 0.6 ns. On the other hand, ensembles **3a** and **3b** were better correlated with a biexponential fitting, which after analysis gave rise to lifetimes of 0.12 and 0.6 ns for **3a** and 0.14 and 0.6 ns for **3b**. While

the slow lifetimes were identical to those due to free polymer **1**, the faster new ones 0.12 and 0.14 ns, for **3a** and **3b**, respectively, correspond to the fluorescence quenching of the emission intensity of the singlet excited state of the polymer within the ensembles **3a** and **3b**. Then, the quenching rate constant and quenching quantum yield were estimated for both **3a** and **3b**. All photophysical parameters are collected and shown in Table 5.1.

Table 5.1. Summary of photophysical data for ensembles 3a and 3b.

Materials	Lifetime τ (ns)[a]	Quenching rate constant k^S_q (s^{-1})[b]	Quenching quantum yield Φ^s_q [c]
3a	0.12 & 0.6	6.67×10^9	0.80
3b	0.14 & 0.6	5.48×10^9	0.78

[a] $\lambda_{(exc)}$ =376 nm; $\lambda_{(em)}$ = 555 nm

[b] The quenching rate constant k^s_q is derived by the following equation: $k^s_q = 1/\tau_f - 1/\tau_o$

[c] The quenching quantum yield Φ^s_q is derived by the following equation: $\Phi^s_q = (1/\tau_f - 1/\tau_o)/(1/\tau_f)$

τ_0 is the lifetime of free polymer **1** and τ_0 is the lifetime of polymer in the corresponding ensemble **3a** and **3b**.

5.4.2. Raman characterization of polymer/MoS_2 (3a) and polymer/WS_2 (3b) ensembles

To further investigate the interactions between **1** with modified MoS_2 and WS_2 within **3a** and **3b**, Raman measurements were carried out under on-resonance conditions (633 nm for MoS_2-based materials and 514 nm for WS_2-based materials) on drop casted films of the materials. The last titration assay both for **3a** and **3b** (+160μl) were drop casted on previously cleaned glass substrate and broad fluorescence background of polymer were substracted from the Raman spectra.

As discussed before in section 5. 2. 10, the material **2a** is governed by three distinctive modes, namely, the 2LA(M) band located at 460 cm^{-1} and associated with sulfur defected sites, the A^1_g band located at 406 cm^{-1} and associated with the symmetry out-for plane, and the E^2_g band located at 380 $cm^{-1.}$ In the case of WS_2, it shows Raman features at 350, 355 and 419 cm^{-1}, related with 2LA(M), E^1_{2g} and A^1_g modes, respectively.

On the other hand, the position of the polymer (**1**) Raman features give us valuable information about the electronic interaction between the materials within the ensembles. The band at 1460 cm^{-1} after subtracting the intense fluorescence of **1** was observed (Figure 5.12). The band is due to the symmetric C=C stretch modes of the thiophene ring.[13]

In case of MoS_2 based material (**3a),** this band found to be red-shifted by 5 cm^{-1} as compared with the corresponding band registered for intact **1**. Similar is the situation with the Raman spectra due to WS_2-based materials. The band due to the C=C of the thiophene was red-shifted by 10 cm^{-1} centred at 1455 cm^{-1}, as compared to intact **1**. These results also confirm the electronic interaction between the materials within the **3a** and **3b**.

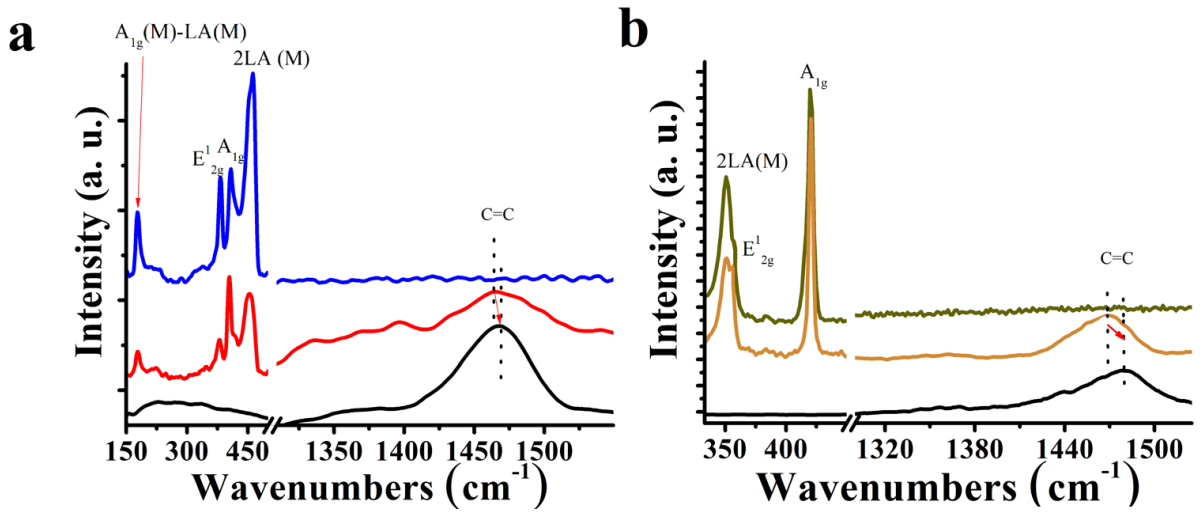

Figure 5.12 Raman spectra for (a) exfoliated MoS_2 (blue), ensemble (3a) (red), (1) (black), obtained upon 633 nm excitation, and (b) exfoliated WS_2 (olive), ensemble (3b) (orange) and (1) (black), obtained upon 514 nm excitation.

5.4.3. Morphology of polymer/MoS_2 (3a) and polymer/WS_2 (3b) ensembles

The morphology of the ensembles was assessed by SEM imaging. Briefly, water dispersions of modified **2a** and **2b** as well as ensembles **3a** and **3b** were used to deposit by drop casting the ensembles onto the sample holder. Oligolayered nanostructures for **2a** and **2b** with sizes between 100-1000 nm and with rectangular shapes were evident (Figure 5.13a, b). Similar images were acquired for **3a** and **3b** (Figure 5.13c, d), though it can be clearly seen that they are covered by amorphous organic matter due to the presence of **1**. This is another indirect evidence for the electrostatic assembly between negatively charged polythiophene **1** and positively charged functionalized MoS_2 and WS_2, yielding the **3a** and **3b** ensembles.

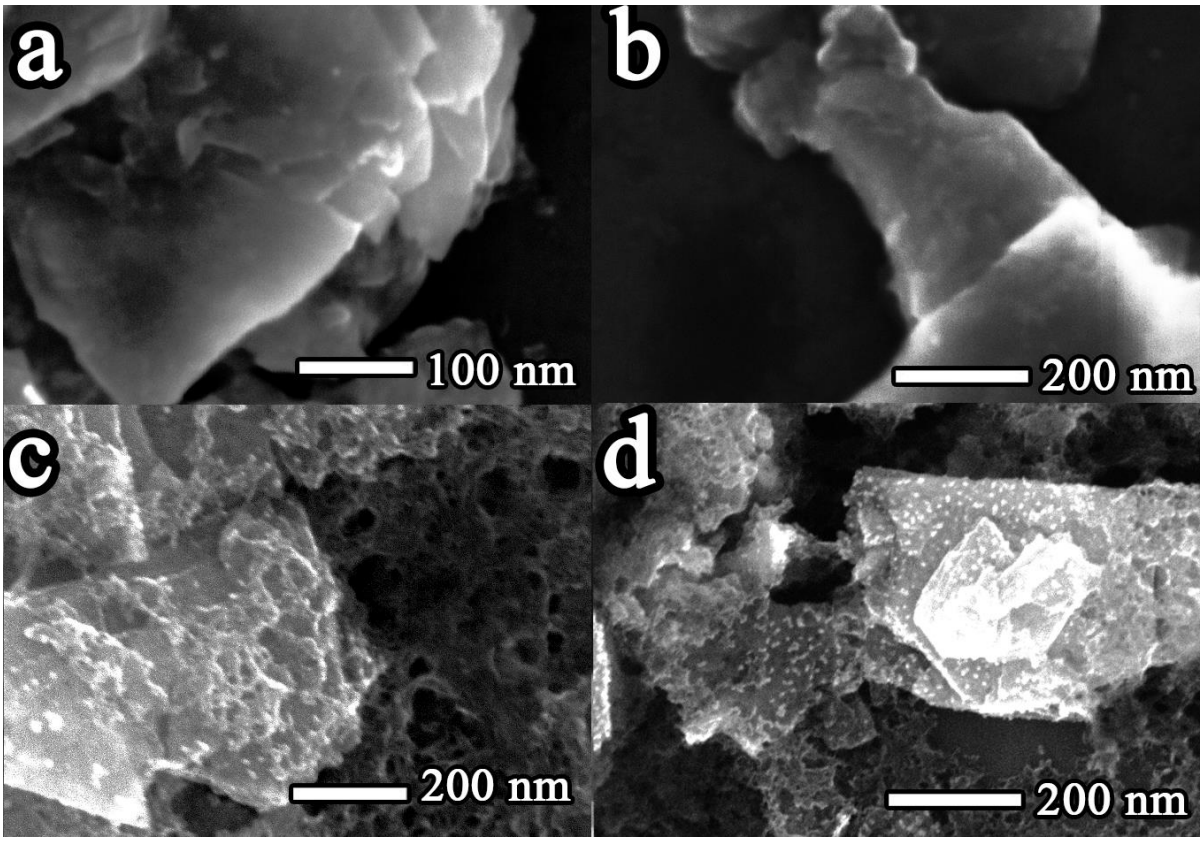

Figure 5.13. Representative FE-SEM images for (a) 2a, (b) 2b, (c) 3a and (d) 3b.

5.4.4. Electrochemical and photoelectrochemical characterization of polymer/MoS_2 (3a) and polymer/WS_2 (3b) ensembles

In order to gain insight of the possible application of the ensembles and the electronic interaction between materials the electrochemical and photoelectrochemical studies were also performed.

Electrochemistry measurements are performed in a three-electrode cell fitted with a quartz window, in 0.1 M $NaClO_4$ as the redox electrolyte in acetonitrile, employing a Ag/AgCl the reference electrode and a Pt wire as the counter electrode. Briefly, the working electrode consisting of either exfoliated MoS_2 or WS_2, water soluble polythiophene (**1)** and **3a** or **3b** films fabricated by spray-coating on FTO substrates covering an area of 1 cm × 1 cm. In case of photoelectrochemistry the samples were illuminated through a quartz window by a 150 W Xenon arc lamp observed photocurrent is measured.

Dark cyclic voltammetry (CV) of **1** showed a voltammogram qualitatively similar to analogous polythiophene derivatives[14], displaying a capacitive region at potentials lower than 0.6 V, corresponding to the bandgap region of the polymer, and a faradaic region, corresponding to the valence band of **1** (Figure 5.14). Besides that, no defined peaks were

observed, indicating a crystalline aggregate structure for **1**. On the other hand, exfoliated WS_2 and MoS_2 dark voltammograms showed a typical capacitive behavior, with no remarkable redox features. The background current for MoS_2 was lower than that for WS_2, which suggests a lower electrochemical active area and/or lower conductivity of the material.[5]

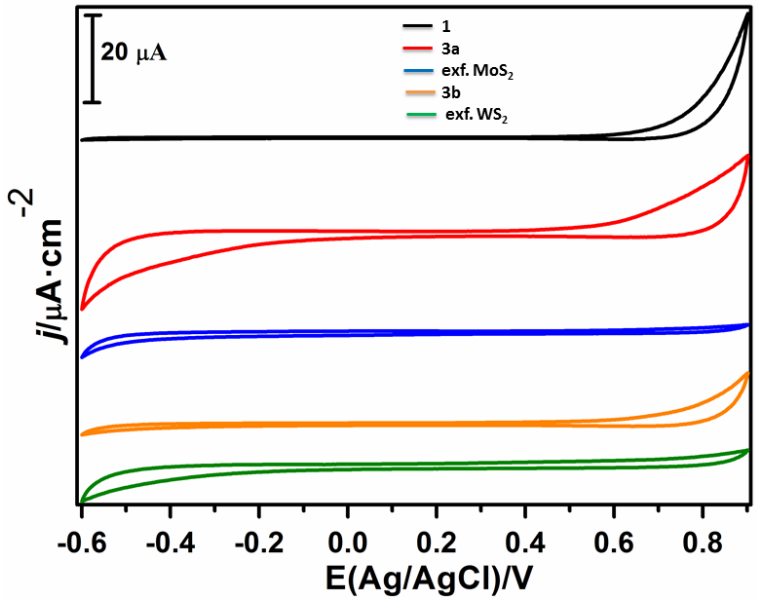

Figure 5.14. Dark cyclic voltammograms of thin films of 1 (black), 3a (red), 3b (orange), exfoliated WS_2 (olive), exfoliated MoS_2 (blue). 0.1 M $NaClO_4$ was used as supporting electrolyte and the scan rate was 0.02 V s^{-1}.

Focusing on ensembles **3a** and **3b**, some differences were observed under dark current assays. In the case of **3b**, the CV was similar to that of free polymer **1**, however, with a higher value for the electrochemical capacitive current in the bandgap region due to the presence of WS_2. On the other hand, **3a** showed an enhancement of the current at negative potential values, indicating a stronger interaction between MoS_2 and **1** at the level of MoS_2 conduction band.

Cyclic voltammograms under illumination (on-off) (Figure 5.15) for **1** revealed a photocathodic response. Cathodic photocurrent started at ca. 0.8 V (Figure 5.15a). The photocurrent reached a maximum value of -1.1 μA.cm^{-2}, while a small anodic photocurrent appeared in the positive scan, at potentials higher than 0.8 V (Figure 5.15b).

In the case of exfoliated MoS_2 and WS_2, both photocathodic and photoanodic currents were observed (Figure 5.15a and 5.15b). Notably, for exfoliated WS_2, the photocathodic current was higher than the photoanodic one, while for exfoliated MoS_2 the opposite phenomenon was observed and the photocathodic response was very low.

The behavior of **3b** was qualitatively similar to that of free **1**, with a very similar photoanodic response in the positive scan. In the negative scan, however, there was observed a decrease of the photocurrent at potentials higher than 0.3 V, and an increase in the photocurrent value at

potentials lower than 0.3 V. The latter finding is indicative of charge transfer between **1** and WS_2, within ensemble **3b**. Particularly, WS_2 accepts photoelectrons from **1**, then transferring them to the solution, increasing cathodic photocurrent at low potentials. At potentials higher than 0.3 V, the current decreased due to the activity of generated photoholes, which start to react with the solution, giving an overall reduction of the net cathodic photocurrent. On the other hand, MoS_2 was not electrochemically active towards photoreduction, therefore, photoelectron transfer from MoS_2 in **3a** yielded a clear decrease in the photocathodic current, since the particular photoelectron was not easily transferred to the solution. Furthermore, photoanodic current, contrary to the case for **3b**, was clearly observed, and even enhanced with respect to MoS_2, since the availability of photoholes for the oxidation was not masked by the presence of active photoelectrons for photoreduction.

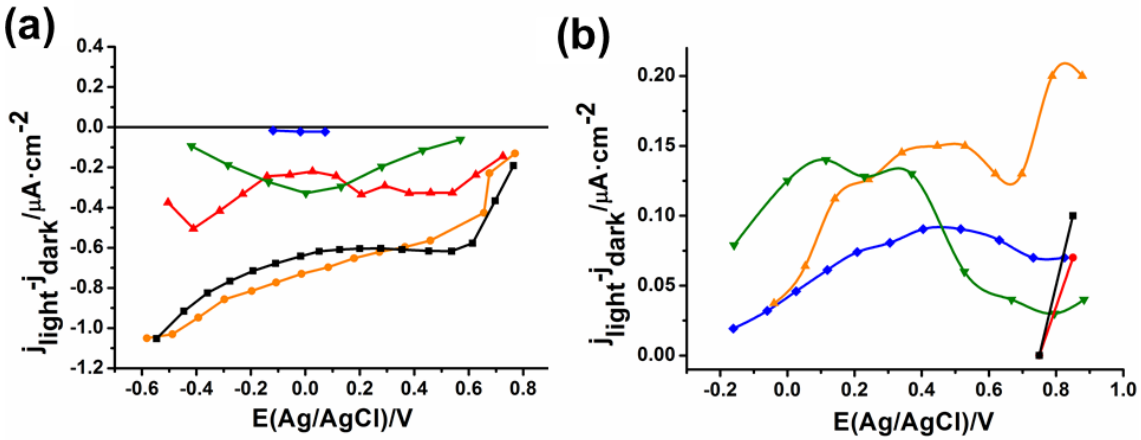

Figure 5.15. Photocurrents obtained by on-off cyclic voltammetry a) photocathodic branch b) photoanodic branch; (1) (black), (3a) (red), (3b) (orange), exfoliated WS_2 (olive), exfoliated MoS_2 (blue) 0.1 M $NaClO_4$ was used as supporting electrolyte and the scan rate was 0. 02 V s^{-1}.

Although beyond the purpose of the current study, another interesting finding is that, depending on the scan direction, positive and negative photocurrent intensities for the same potential value for WS_2, MoS_2 and **3a** (p-type when coming from positive potentials and n-type when coming from negative potentials) were acquired. The latter is a photomemristor behavior, suggesting that charge redistribution, induced by the potential change, is stable during the time when the CV takes place.[16]

5.5. Conclusion

Herein, we developed novel aqueous and stable nanoensembles which consist of polythiophene/MoS_2 and polythiophene/WS_2. The nanoensembles were held together via

electrostatic interaction which takes place between the positively charged ammonium moieties of TMDs and negatively charged carboxylate moieties on polythiophene. Electronic absorption and photoluminescence titration assays, complemented by time-resolved fluorescence studies, confirms the electronic interaction is in charge as well between the components within the ensembles.

Significant quenching of the polymer emission by positively charged MoS_2 and WS_2 were revealed, which prove the effective deactivation of the singlet excited state of polymer to MoS_2 and WS_2, via energy and/or electron transfer as the decay mechanism. Additionally, the electronic interaction was also studied by photoelectrochmical assays. Particularly, WS_2 accepts photoelectrons from polythiophene, then transferring them to the solution, which enhanced the cathodic photocurrent at low potentials.

All these results consistently confirm the advantageous function of electrostatic interactions between the negatively charged polymer and the TMDs not only for the realization of the nanoensembles **3a** and **3b** but also for succeeding efficient electronic communication.

These nanoensembles can also be integrated as alternative water based donor-acceptor complexes in optoelectronic device applications.

5.6. References

1. Y. L. Huang, Y. J. Zheng, Z. Song, D. Chi, T. S. W. Andrew and S. Y. Quek, The Organic-2D Transition Metal Dichalcogenide Heterointerface, *Chem. Soc. Rev*., 2018, 47, 3241—3264.

2. Y. Huang, W. Zheng, Y. Qiu and P. Hu, Effects of Organic Molecules with Different Structures and Absorption Bandwidth on Modulating Photoresponse of MoS2 Photodetector, *ACS Appl. Mater. Interfaces*, 2016, 8 (35), 23362–23370.

3. R. Canton-Vitoria, C. Stangel and N. Tagmatarchis, Electrostatic Association of Ammonium-Functionalized Layered-Transition-Metal Dichalcogenides with an Anionic Porphyrin, *ACS Appl. Mater. Interfaces*, 2018, 10 (28), 23476–23480.

4. J. Wang, Z. Wu, H.Yin, W. Lia and Y. Jiangc, Poly(3,4-ethylenedioxythiophene)/MoS2 Nanocomposites with Enhanced Electrochemical Capacitance Performance, *RSC Adv*., 2014,4, 56926-56932.

5. H. Tang, J. Wang, H. Yin, H. Zhao, D. Wang and Z. Tang, Growth of Polypyrrole Ultrathin Films on MoS2 Monolayers as High-Performance Supercapacitor Electrodes, *Adv. Mater*. 2015, 27, 1117–1123.

6. B.S. Kim, L. Chen, J. Gong and Y. Osada, Titration Behavior and Spectral Transitions of Water-Soluble Polythiophene Carboxylic Acids, *Macromolecules*,1999, 32, 3964-3969.

7. G. Pagona, C. Bittencourt, R. Arenal and N. Tagmatarchis, Exfoliated Semiconducting Pure 2H-MoS2 and 2H-WS2 Assisted by Chlorosulfonic Acid, *Chem. Commun*., 2015, 51, 12950—12953.

8. R. Canton-Vitoria, Y. Sayed-Ahmad-Baraza, M. Pelaez-Fernandez, R. Arenal, C. Bittencourt, C. P. Ewels and N. Tagmatarchis, N. Functionalization of MoS2 with 1,2-dithiolanes: Toward Donor-Acceptor Nanohybrids for Energy Conversion, *NPJ 2D Mater. Appl.* 2017, 1, 13.

9. R. Canton-Vitoria, L. Vallan, E. Urriolabeitia, A. M. Benito, W. K. Maser and N. Tagmatarchis, Electronic Interactions in Illuminated Carbon Dot/MoS2 Ensembles and Electrocatalytic Activity towards Hydrogen Evolution, *Chem. Eur. J*., 2018, 10, 10468-104674.

10. E. Istif, J. Hernández-Ferrer, E. P. Urriolabeitia, A. Stergiou, N. Tagmatarchis, G.Fratta M. J. Large, A. B. Dalton, A. M. Benito and W. K. Maser, Conjugated

Polymer Nanoparticle–Graphene Oxide Charge-Transfer Complexes, *Adv. Funct. Mater*. 2018, 28, 1707548.

11. C. Gong, H. Zhang, W. Wang, L. Colombo, R. M. Wallace and K. Cho, Band Alignment of Two-Dimensional Transition Metal Dichalcogenides: Application in Tunnel Field Effect Transistors. *Appl. Phys. Lett*. 2013, 103, 053513.

12. W. C. Tsoi, D. T. James, J. S. Kim, P. G. Nicholson, C. E. Murphy, D. D. C. Bradley, J. Nelson and J. S. Kim, The Nature of In-Plane Skeleton Raman Modes of P3HT and Their Correlation to the Degree of Molecular Order in P3HT:PCBM Blend Thin Films, *J. Am. Chem. Soc.*, 2011, 133, 9834-9843.

13. M. L. Braunger, A. Barros, M. Ferreira and C. A. Olivati, Electrical and Electrochemical Measurements in Nanostructured Films of Polythiophene Derivatives, *Electrochim. Acta*, 2015, 165 1-6.

14. F. Fabregat-Santiago, I. Mora-Seró, G. Garcia-Belmonte and J. Bisquert, Cyclic Voltammetry Studies of Nanoporous Semiconductors. Capacitive and Reactive Properties of Nanocrystalline TiO_2 Electrodes in Aqueous Electrolyte, *J. Phys. Chem. B*, 2003, 107, 758-768.

15. S. Moghaddam, E. S. Iranizad E, M. Pumera, Two-dimensional transition metal; dichalcogenide/conducting polymer composites: synthesis and applications, *Nanoscale*, 2017, 9, 8052–8065.

16. W. Wang, G.N. Panin, X. Fu, L. Zhang, P. Ilanchezhiyan, V. O. Pelenovich, D. Fu and W. T. Kang, MoS_2 Memristor With Photoresistive Switching. *Sci. Rep.* 2016, *6*, 31224.

6. GENERAL CONCLUSION AND OUTLOOK

6.1. General conclusion

This thesis focused on development of advanced water-dispersible donor-acceptor hybrid nanostructures based on conjugated polymers (CPs) and three different kinds of nanomaterials of great actual scientific and technological interest, namely, 2D sheets of graphene oxide (GO), transition metal dichalcogenides (TMDs), and 0D quantum dots of ($CdTe_{QDs}$).

The general synthesis strategy is based on self-assembly approaches using polythiophene (PTh) derivatives (poly-(3-hexylthiophene), P3HT, and functionalized PTh) as prominent model prototypes for CPs. Re-precipitation processes have been applied in case of P3HT. These result in the formation of P3HT nanoparticles ($P3HT_{NPs}$), which can be easily dispersed in water. This synthesis route has been successfully exploited for the first time for the preparation of $P3HT_{NPs}$-GO charge-transfer complexes and of $P3HT_{NPs}$-$CdTe_{QDs}$ donor-acceptor core-shell particles. Additionally, a self-assembly synthesis route favoring electrostatic interactions between a novel water dispersable PTh derivative with charged functional end-groups and charged TMD derivatives based on MoS_2 and WS_2 has been employed to create successfully PTh-TMD donor-acceptor complexes.

Extensive morphological, spectroscopic and electrochemical characterization has been carried out in the liquid and solid state, covering even studies on the level of the individual nanohybrids itself. This provided deep insight on the unique interface properties of the ensemble hybrid materials.

Finally, photoelectrochemical studies demonstrated the value of the prepared charge-transfer hybrid complexes in the form of thin films for improved optoelectronic applications.

The specific conclusions for each type of hybrid material, described in chapters two to five are summarized in the following:

- ***Chapter two: $P3HT_{NPs}$-GO Charge-Transfer Nanohybrids***

Novel hybrid nanostructures of $P3HT_{NPs}$ and GO sheets were prepared for the first time by employing an in-situ re-precipitation approachs of P3HT in the presence of GO sheets dispersed in water. This results in the formation of $P3HT_{NPs}$ of 90-150 nm in size in intimate contactd with individual sheets of GO. It is shown that during the liquid phase assembly process already lowest amounts of GO lead to a significant change of the crystalline aggregate

structure of the forming $P3HT_{NPs}$. This result in a shift from H-type of aggregates in the original $P3HT_{NPs}$, to a H/J or even J type dominated aggregate structure in the $P3HT_{NPs}$ of the in-situ prepared $P3HT_{NPs}$-GO hybrids. This implies a significantly reduced excitonic coupling, facilitating intramolecular charge-transport along the P3HT chains. Concomittantly, the in-situ assembly process establishes effective π-π interface interactions between the forming $P3HT_{NPs}$ and the GO sheets. This enables the formation of stable of stable charge-transfer complexes exhibiting significantly reduced bandsgaps by several hundredth of meV, compared to the original $P3HT_{NPs}$. Additionally, $P3HT_{NPs}$-GO hybrids processed into thin films reveal photoinduced charge-transfer. As a function of GO concentration, major and minor charge pathways can be controlled, rendering this material of special interest as photoactive layer for thin film optoelectronic devices. In this sense, it remains to mention, that all the optoelectronic properties observed in the form of films are entirely established in the liquid phase self-assembly process and thus do not depend anymore on extrinsic film processing parameters, as the case for "traditional" systems. These findings are of general character and can be easily transferred to other kinds of conjugated polymers of interest for optocelectronic applications and beyond.

- ***Chapter three: $P3HT_{NP}$-GO: Nanoscale Charge-Transfer Properties***

Nanoscale charge-transfer properties of individual nanoobjects of the $P3HT_{NPs}$-GO hybrid materials were probed by Kelvin Probe Microscopy (KPM) under dark and illuminated conditions. The studies were carried out on ex-situ (i.e. mixed) $P3HT_{NPs}$-GO samples and in-situ self-assembled $P3HT_{NPs}$-GO charge-transfer complexes. It clearly can be seen that ex-situ $P3HT_{NPs}$-GO samples consisting of non-interacting $P3HT_{NPs}$ deposited on GO sheets, do not reveal any charge-transfer properties. However, in-situ $P3HT_{NPs}$-GO hybrids effectively reveal charge-transfer and photo-induced electron transfer from $P3HT_{NPs}$ to the GO sheets. This can be impressively seen when $P3HT_{NPs}$ are covered by a GO sheet, which is directly probed by the AFM tip. Here the internal substructure of the $P3HT_{NPs}$, indicative of the crystalline aggregate structure as well as the spatial distribution of the photo-induced electron transfer to the GO sheet, even beyond zones in direct contact with the $P3HT_{NPs}$ is clearly observed. The results on the individual nanoobjects, underline the importance of the in-situ self-assembly process responsible for the important changes of the aggregate structure and the resulting favorable charge-transport properties. Moreover, the results are of critical importance for the better understanding and optimization of thin films optoeelctronic device

structures based on charge-transfer hybrid complexes of nanoparticles of conjugated polymer and graphene oxide.

- ***Chapter four: $P3HT_{NPs}$-$CdTe_{QDs}$ Core-Shell Nanohybrids***

Novel core-shell nanohybrid ensemblies of $P3HT_{NPs}$ and semiconducting CdTe quantum dots ($CdTe_{QDs}$) were prepared for the first time by employing an in-situ re-precipitation approach of P3HT in the presence of $CdTe_{QDs}$ dispersed in water. During the liquid phase process, $P3HT_{NPs}$ are formed first and serve as core-structure, onto which $CdTe_{QDs}$ deposit, thus forming a stable shell structure. Spectroscopic and electrochemical studies consistently reveal the existence of charge-transfer processes taking place at the interface between the $CdTe_{QDs}$ shell and the $P3HT_{NPs}$ core thus indicating the formation of an effective donor-acceptor system. Moreover, films of the $P3HT_{NPs}$-$CdTe_{QDs}$ film reveal a prompt, steady and reproducible on-off photoresponse with a three-times enhanced photocurrent with respect to $CdTe_{QDs}$ thus underlining its value for the development of improved optoelectronic device structures. Finally, it should be underlined that the developed synthesis approach is of general character and can be easily transferred to other types of conjugated polymers and semiconducting quantum dots.

- ***Chapter five: Polythiophene-Transition Metal Dichalcogenide Donor-Acceptor Nanohybrids***

Novel water-dispersible hybrid nanostructures consisting of a polythiophene (PTh) and transition metal dichalcogenides (TMDs) were prepared by a self-assembly process. This process profits from electrostatic interactions between negatively charged carboxylate groups present on a newly synthesized PTh material and positively charged ammonium moieties attached in a novel functionalization process on two types of TMDs, i.e. MoS_2 and WS_2. Optical characterization of the novel hybrid materials, obtained in a series of titration studies, reveals that an electronic interaction takes place between the PTh and the two types of TMDs, facilitated by conformational changes of the polymer backbone. Moreover, effective quenching of the polymer emission by positively charged TMDs prove the effective deactivation of the singlet excited state of PTh by energy and/or electron transfer to the TMDs, as the decay mechanism. Importantly, this process only is observed when employing charged TMDs in the self-assembly process. Finally, photoelectrochemical studies on thin films of the nanohybrids reveal improved cathodic photocurrents at low potentials, particularly for the case of the PTh-WS_2 ensemble. All these results consistently underline the

importance of electrostatic interactions, not only for the stabilization of the water-dispersible PTh-TMDs nanoensembles, but also for achieving successful electronic communication between the PTh and TMDs. Finally, the operational performance of these PTh-TMDs donor acceptor hybrid systems in the form of thin films offers promise for their use as component in optoelectronic devices.

6.2. Outlook

The results obtained in this thesis reveal the value of self-assembly processes for obtaining advanced functional nanohybrid assemblies of conjugated polymers with 2D and 0D nanomaterials of great actual scientific and technological interest. Using this strategy, in this thesis novel donor-acceptor charge-transfer complexes were successfully developed. These revealed their value for improved thin film optoelectronic device structures. This thesis thus paves the way for further optimization of the developed structures with respect to their interface charge-transfer properties, their processing characteristics and their direct use in final thin film optoelectronic device structures, such as organic solar cells, organic light emitting devices or organic field effect transistors, or other types of thin film applications, such as (bio-) sensors or energy storage applications.

The specific outlook for each type of hybrid material are commented in the following:

- ***P3HT$_{NPs}$-GO Charge-Transfer Nanohybrids***

Optimization of the charge-separation and charge-transfer characteristics of this new class of nanohybrids may be achieved by further research on the effects of the region-regularity of P3HT and the size of the GO sheets on the aggregate structure of P3HT$_{NPs}$. The ultimate goal here may consist in the preparation of P3HT$_{NPs}$-GO core-shell particles, which can be effectively being used to complement/substitute the commonly used P3HT-PCBM system as photoactive layer in organic optoelectronic devices. Furthermore, the transfer of the synthesis approach to other types of conjugated polymers may open further possibilities towards improved optoelectronic devices.

- ***P3HT$_{NPs}$-CdTe$_{QDs}$ Core-Shell Nanohybrids***

The developed synthesis approach can be easily applied to other types of semiconducting quantum dots, as well as to other types of conjugated polymers. This may result in a wide

class of novel core-shell nanohybrids with different and well-defined optoelectronic characteristics thus broadening their possibilities for optoelectronic applications and beyond.

- ***Polythiophene-Transition Metal Dichalcogenide Donor-Acceptor Nanohybrids***

The concepts of the synthesis approach may be applied to other types of dichalcogenides, beyond MoS_2 and WS_2 and other types of conjugated polymers, thus broaden-up this new class of donor-acceptor nanohybrids for exploiting their possibilities for optoelectronic applications and beyond.

Finally, all the developed nanohybrid materials constitute model systems of specific interest to characterization techniques focusing on individual nanoobject itself, such as high-resolution transmission microscopy techniques (including electron energy loss spectroscopy (EELS), cathodoluminescence), scanning probe microscopy techniques (AFM, KPM). These techniques not only offer important feedback for synthesis optimization, but even more provide critical complementary information thus contributing to improved understanding of the optoelectronic processes and performance of thin film device structures.

6.3. Conclusiones Generales

Esta tesis está enfocada en el desarrollo de nanoestructuras avanzadas de tipo dador-aceptor dispersables en agua. Estos sistemas están basados en combinaciones de polímeros conjugados (CPs) y tres tipos de nanomateriales distintos, de gran interés científico y tecnológico, como son las láminas 2D de óxido de grafeno (GO), dicalcogenuros de metales de transición (TMDs) y puntos cuánticos 0D de CdTe ($CdTe_{QDs}$)

La estrategia general de síntesis está basada en principios de autoensamblado utilizando derivados de politiofeno (PTh), tales como el poli-(3-hexiltiofeno), P3HT, y politiofenos funcionalizados como modelo prototipo de polímeros conductores. En el caso del P3HT se han llevado a cabo procesos de reprecipitación, dando como resultado la formación de nanopartículas de P3HT ($P3HT_{NPs}$), fácilmente dispersables en agua. Esta ruta sintética ha sido empleada con éxito por primera vez en esta tesis para la preparación de complejos de transferencia de carga de $P3HT_{NPs}$-GO y de partículas *core-shell* de tipo dador-aceptor de $P3HT_{NPs}$-$CdTe_{QDs}$.

Además, se han sintetizado con éxito complejos dador-aceptor PTh-TMD empleando otra ruta sintética de autoensamblado basada en el establecimiento de interacciones electrostáticas entre un nuevo derivado de politiofeno dispersable en agua funcionalizado con grupos terminales con carga y derivados de MoS_2 y WS_2.

Se ha llevado a cabo una caracterización completa de las propiedades electroquímicas, espectrocópicas y morfológicas en estado líquido y sólido de los materiales sintetizados, incluyendo a los nanohíbridos individuales. Esto nos ha permitido una comprensión profunda de las propiedades interfaciales únicas del conjunto de los materiales híbridos.

Finalmente, estudios fotoelectroquímicos han demostrado el valor de los complejos híbridos de transferencia de carga preparados y dispuestos en películas delgadas para aplicaciones optoelectrónicas mejoradas.

Las conclusiones específicas para cada tipo de material híbrido, descrito en los capítulos dos a cinco se resumen a continuación:

Capítulo 2: Nanohíbridos $P3HT_{NPs}$-GO con transferencia de carga.

Por primera vez, han sido preparados materiales que combinan nanoestructuras de P3HT ($P3HT_{NPs}$) y láminas de GO empleando un método de reprecipitación *in situ* en presencia de

láminas de GO dispersadas en agua. Esto ha dado lugar a la formación de $P3HT_{NPs}$ con tamaños de entre 90 y 150nm en contacto con láminas individuales de óxido de grafeno. Se demuestra que durante el proceso de ensamblado en fase líquida incluso las cantidades más pequeñas de GO utilizadas dan lugar a un cambio significativo de la estructura cristalina de los agregados de las $P3HT_{NPs}$ formadas. Se ha demostrado que se produce un cambio de los agregados de tipo H en las $P3HT_{NPs}$ originales a una mezcla de agregados H/J, o incluso del tipo J en las nanopartículas de politiofeno del híbrido $P3HT_{NPs}$-GO preparadas *in situ*.

Simultáneamente, los procesos de ensamblado *in situ* favorecen el establecimiento de interacciones efectivas de tipo π-π entre las superficies de las $P3HT_{NPs}$ formadas y las láminas de GO. Esto permite la formación de complejos estables de transferencia de carga que exhiben una reducción notable de la banda prohibida (bandgap) en varios cientos de meV comparado con las $P3HT_{NPs}$ originales.

Adicionalmente, se demostró la transferencia de carga fotoinducida en los híbridos $P3HT_{NPs}$-GO procesados y transformados en películas finas. Entonces, dependiendo de la concentración de GO, se puede controlar el establecimiento de caminos principales y secundarios para la carga, convirtiendo a este material especialmente interesante como lámina fotoactiva para dispositivos optoelectrónicos en película fina. En este sentido, cabe destacar que todas las propiedades optoelectrónicas observadas en la formación de películas quedan completamente definidas en el proceso de autoensamblado en fase líquida y por lo tanto no dependen de los parámetros del procesado de las películas, cosa que sí ocurre en los sistemas más "tradicionales". Estos descubrimientos son de carácter general y pueden ser fácilmente extrapolados a otros tipos de polímeros conjugados para aplicaciones optoelectrónicas.

Capítulo 3: $P3HT_{NP}$-GO: propiedades de transferencia de carga a escala nanométrica.

Las propiedades de transferencia de carga a escala nanométrica de nanoobjetos individuales de materiales híbridos $P3HT_{NP}$-GO se comprobaron mediante microscopía de fuerza de sonda Kelvin (KPM) en oscuridad y en condiciones de iluminación. Los estudios se llevaron a cabo tanto en muestras de $P3HT_{NPs}$-GO preparadas *ex situ* (i.e. simplemente mezcladas) como en los complejos de transferencia de carga $P3HT_{NPs}$-GO preparados *in situ*. Se puede comprobar claramente que las muestras de $P3HT_{NPs}$-GO preparadas *ex situ* consisten en $P3HT_{NPs}$ depositadas sobre láminas de GO sin ninguna interacción y que no revelan ninguna propiedad de transferencia de carga. Sin embargo, los híbridos $P3HT_{NPs}$-GO preparados *in situ* revelan una transferencia de carga efectiva y una transferencia electrónica fotoinducida de las

$P3HT_{NPs}$ a las láminas de GO, lo que se pudo ver directamente con la punta del AFM. Así pues, se observa con claridad la subestructura interna de las $P3HT_{NPs}$, indicativa de la estructura cristalina de agregados interna, así como la distribución espacial de la transferencia electrónica fotoinducida hacia la lámina de GO, incluso en zonas en contacto directo con las $P3HT_{NPs}$. Estos resultados con nanobjetos individuales subrayan la importancia del proceso de autoensamblado *in situ que* es responsable de los importantes cambios observados en la estructura de agregados y las propiedades de transporte de carga resultantes. Además, los resultados son de una importancia crítica para una mejor comprensión y optimización de dispositivos optoelectrónicos en película fina basados en complejos de transferencia de carga de nanopartículas híbridas de polímeros conjugados y óxido de grafeno.

Capítulo 4: $P3HT_{NPs}$-$CdTe_{QDs}$ nanohíbridos de tipo core-shell

Nuevos híbridos de tipo *core-shell* usando nanopartículas $P3HT_{NPs}$ y puntos cuánticos semiconductores de CdTe ($CdTe_{QDs}$) han sido preparados por primera vez empleando el método de reprecipitación *in situ* de P3HT en presencia de $CdTe_{QDs}$ dispersados en agua. Durante el proceso en fase líquida se forman primero $P3HT_{NPs}$, que sirven de núcleo sobre el cual $CdTe_{QDs}$ se deposita, formando así un recubrimiento estable. Los estudios espectroscópicos y electroquímicos revelan de manera consistente la existencia de procesos de transferencia de carga que ocurren en la interfase entre el núcleo de $P3HT_{NPs}$ y el recubrimiento $CdTe_{QDs}$, lo que indica la formación de un sistema efectivo dador-aceptor. Además, el estudio de las películas de $P3HT_{NPs}$-$CdTe_{QDs}$ revela una fotorrespuesta on-off rápida, regular y reproducible, con una fotocorriente tres veces superior a la medida en los $CdTe_{QDs}$, lo cual acentúa su valor para el desarrollo de dispositivos optoelectrónicos mejorados.

Finalmente, cabe destacar que el proceso de síntesis desarrollado es de carácter general y puede transferirse fácilmente a otros tipos de polímeros conjugados y puntos cuánticos semiconductores.

Capítulo 5: Nanohíbridos dador-aceptor Politiofeno-Dicalcogenuro de metales de transición.

Se han preparado nuevas nanoestructuras híbridas dispersables en agua, consistentes en politiofeno (PTh) y dicalcogenuros de metales de transición (TMDs) mediante un proceso de autoensamblado. Este proceso aprovecha las interacciones electrostáticas entre los grupos

carboxilato negativamente cargados de un nuevo PTh sintetizado expresamente para este estudio y las unidades de amonio positivamente cargadas unidas a dos tipos de TMDs (MoS_2 y WS_2) en un nuevo proceso de funcionalización desarrollado en el laboratorio.

La caracterización óptica de estos nuevos materiales híbridos, obtenida en una serie de estudios de valoración, revelan que la interacción electrónica tiene lugar entre el PTh y los dos tipos de TMDs, facilitada por los cambios conformacionales del esqueleto del polímero. Además, la extinción de la emisión fluorescente del polímero debido a la acción de los TMDs cargados positivamente prueba la desactivación efectiva del estado excitado singlete del PTh debido a la transferencia energética y/o electrónica hacia los TMDs como mecanismo de extinción. Es importante destacar que este proceso sólo se observa cuando se emplean TMDs cargados en el proceso de autoensamblado.

Finalmente, los estudios fotoelectroquímicos sobre películas delgadas de los nanohíbridos revelan la existencia de fotocorrientes catódicas mejoradas a potenciales bajos, especialmente en el caso del PTh-WS_2. Todos estos resultados subrayan de manera sólida la importancia de las interacciones electrostáticas, no sólo para la estabilización de los nanohíbridos PTh-TMDs, sino también para conseguir una comunicación electrónica efectiva entre el PTh y los TMDs. Así pues, el rendimiento de estos sistemas híbridos PTh-TMDs dador-aceptor en forma de películas delgadas ofrece un futuro prometedor para su uso como componente en dispositivos optoelectrónicos.

6.4. Perspectiva

Los resultados obtenidos en esta tesis revelan el valor de los procesos de autoensamblado para la obtención de nanohíbridos avanzados y funcionales de polímeros conjugados con nanomateriales 2D y 0D de gran interés real científico y tecnológico. Usando esta estrategia, se han desarrollado en esta tesis nuevos complejos dador-aceptor con transferencia de carga. Esto reveló su valor como películas finas para dispositivos optoelectrónicos mejorados. Esta tesis también abre el camino para una futura optimización de las estructuras desarrolladas respecto a sus propiedades de transferencia de carga interfacial, sus características de procesado y su uso directo en dispositivos optoelectrónicos de película fina, como celdas solares orgánicas, OLEDs, transistores de efecto campo orgánicos u otros tipos de aplicaciones de película fina tales como biosensores o aplicaciones de almacenamiento de energía.

La perspectiva específica para cada tipo de material híbrido se comenta a continuación.

Nanohíbridos P3HT$_{NPs}$-GO de transferencia de carga.

La optimización de las características de separación y transferencia de carga de este tipo de nuevos materiales deberá ser llevada a cabo en una futura investigación en la que se estudie el efecto de la regiorregularidad del P3HT y el tamaño de las láminas de GO en la estructura de los agregados de las P3HT$_{NPs}$. el objetivo aquí podría consistir en la preparación de partículas de P3HT$_{NPs}$-GO de tipo *core-shell*, las cuales pueden ser usadas de manera efectiva para complementar o sustituir al sistema P3HT-PCBM, que es usado comúnmente como lámina fotoactiva en los dispositivos optoelectrónicos orgánicos. Además, la transferencia del procedimiento sintético a otros tipos de polímeros conjugados puede abrir nuevas posibilidades hacia dispositivos optoelectrónicos mejorados.

P3HT$_{NPs}$-CdTe$_{QDs}$ nanohíbridos de tipo core-shell

El procedimiento sintético desarrollado puede ser fácilmente aplicado a otro tipo de puntos cuantícos semiconductores, así como a otros polímeros conjugados. Esto puede llevar a un amplio desarrollo de nuevos nanohíbridos de tipo *core-shell* con diferentes características optoelectrónicas bien definidas, lo que expandiría las posibilidades para su uso en aplicaciones optoelectrónicas y de otros tipos.

Nanohíbridos dador-aceptor Politiofeno-Dicalcogenuro de metales de transición.

Los conceptos aplicados en la síntesis pueden ser aplicados a otros tipos de dicalcogenuros, además de MoS_2 and WS_2, aumentando enormemente esta nueva clase de nanohíbridos dador-aceptor para aprovechar sus posibilidades para aplicaciones optoelectrónicas y derivadas.

Finalmente, todos los materiales nanohíbridos desarrollados constituyen sistemas modelo de especial interés para el uso de técnicas de caracterización individual, como las técnicas de microscopía de transmisión del alta resolución (incluyendo espectroscopía de pérdida de energía del electrón (EELS), luminiscencia de cátodo,…) o técnicas de microscopía de fuerzas atómicas (AFM) y de sonda Kelvin (KPM). Estas técnicas no sólo ofrecen una importante ayuda para la optimización de la síntesis, sino que proporcionan información crítica para contribuir a mejorar la comprensión de los procesos optoelectrónicos y el rendimiento de los dispositivos

LIST OF SCIENTIFIC CONTRIBUTIONS

Publication 1: Self-Assembled Core−Shell CdTe/Poly(3-hexylthiophene) Nanoensembles as Novel Donor−Acceptor Light-Harvesting Systems

Emin Istif, Antonia Kagkoura, Javier Hernandez-Ferrer, Anastasios Stergiou, Theodosis Skaltsas, Raul Arenal, Ana M. Benito, Wolfgang K. Maser, and Nikos Tagmatarchis

ACS Appl. Mater. Interfaces 2017, 9, 44695−44703

Contribution*:* Synthesis and characterization of P3HT and hybrid material. Involved in the writing of the first draft and was involved in the final editing of the paper.

Publication 2: Conjugated Polymer Nanoparticle–Graphene Oxide Charge-Transfer Complexes,

Emin Istif, Javier Hernández-Ferrer, Esteban P. Urriolabeitia, Anastasios. Stergiou, Nikos Tagmatarchis, Giuseppe Fratta Matthew J. Large, Alan B. Dalton, Ana M. Benito and Wolfgang K. Maser,

Adv. Funct. Mater. 2018, 28, 1707548

Contribution*:* Synthesis and characterization of P3HT and hybrid material. Wrote the first draft and was involved in the final editing of the paper.

Publication 3: Integrating Water-Soluble Polythiophene to Transition Metal Dichalcogenides for Managing Photoinduced Processes ***(to be submitted to ACS Appl. Mater. Interfaces)***

Ruben Canton-Vitoria, Emin Istif, Javier Hernández-Ferrer, Esteban Urriolabeitía, Ana M. Benito, Wolfgang K. Maser, Nikos Tagmatarchis

Contribution*:* Synthesis of polythiophene. Involved in characterizations of the hybrid materials and in writing the first draft. Equal contribution of first and second author

---

Publication 4: Nanoscale Photogenerated Charge-Transfer Study of P3HT Nanoparticles/Graphene Oxide Complexes ***(in preparation)***

Elisa Palacios-Lidón, Emin Istif, Ana Benito, Wolfgang M. Maser, Jaime Colchero

Contribution*:* Synthesis of P3HT and hybrid material. Thin film preparation of individual nano objects by spray coating. Involved in the writing of the first draft.